SYNTHESIS OF LARGE-AREA TWO-DIMENSIONAL MATERIALS FOR VERTICAL HETEROSTRUCTURES

A Dissertation
Presented to
The Academic Faculty

by

Philip Michael Campbell

In Partial Fulfillment
of the Requirements for the Degree
Doctorate of Materials Science and Engineering in the
School of Materials Science and Engineering

Georgia Institute of Technology
May 2017

© 2017 PHILIP MICHAEL CAMPBELL

SYNTHESIS OF LARGE-AREA TWO-DIMENSIONAL MATERIALS FOR VERTICAL HETEROSTRUCTURES

Approved by:

Dr. Eric M. Vogel, Advisor
School of Materials Science and Engineering
Georgia Institute of Technology

Dr. W. Jud Ready
Electronic Systems Laboratory
Georgia Tech Research Institute
Georgia Institute of Technology

Dr. P. Doug Yoder
School of Electrical and Computer Engineering
Georgia Institute of Technology

Dr. Seung-Soon Jang
School of Materials Science and Engineering
Georgia Institute of Technology

Dr. Matt McDowell
School of Materials Science and Engineering
Georgia Institute of Technology

Date Approved: March 30, 2017

To my father

ACKNOWLEDGEMENTS

I would like to express my thanks to Eric Vogel and Jud Ready for their support and guidance over the last four years as I pursued my studies at Georgia Tech. I would also like to thank members of the Vogel group, past and present. In particular, I would like to recognize Tania Roy and Zohreh Razavi-Hesabi for providing training and input during my first several months in the group. I am also thankful to Alexey Tarasov, Corey Joiner, and Meng-Yen Tsai who were instrumental in working with me to develop our synthesis processes. I would also like to recognize Chris Perini, Jake Smith, Spyros Pavlidis, and Brian Beatty for their help and collaboration.

I am thankful for the support of the GTRI Shackelford Fellowship, which has provided me access to equipment and resources which were vital to my research. I would like to particularly recognize Stephan Turano for training and assistance with the EvoVac. As well, Brent Wagner's knowledge was instrumental in configuring the MBE and developing low temperature growth processes. I must also recognize Tyler Colling, who has always been willing to lend a helping hand in lifting heavy turbopumps.

Finally, I would like to recognize my family, whose unwavering support enabled me to pursue my dreams. I would especially like to recognize my parents for instilling in me the drive and motivation that has carried me this far. In addition, I owe a special thanks to my wife, Courtney, who has been by my side for all of the long hours over the last four years.

TABLE OF CONTENTS

	Page
ACKNOWLEDGEMENTS	iv
LIST OF TABLES	ix
LIST OF FIGURES	x
LIST OF SYMBOLS AND ABBREVIATIONS	xxiii
SUMMARY	xxv

CHAPTER

1 Introduction	1
1.1 Layout of this Thesis	1
1.2 Applications of 2D Materials	3
1.2.1 Optoelectronics	3
1.2.2 Flexible Electronics	4
1.2.3 Sensing	5
1.2.4 Beyond-CMOS Devices	6
1.3 History of 2D Materials	8
1.4 Structure and Properties of TMDs	9
1.5 Synthesis Techniques for Thin-Film TMDs	15
1.6 Nature of Metal-TMD Contacts	20
1.7 Applications of 2D Vertical Heterostructures	22
1.7.1 The Symmetric Field-Effect Transistor (symFET)	24
1.7.2 Conduction-to-Valence Band Tunneling	27
1.7.3 TMD-based Vertical Heterostructures using Exfoliated Material	30

1.7.4 Direct Growth of TMD-based Heterostructures 31

2 Theoretical Model for 2D Vertical Heterostructures 34

2.1 Determination of Band Alignment 34

2.2 Calculation of Tunneling Current 38

2.3 Effect of Non-Idealities 41

2.3.1 Formation of Band Tail States 42

2.3.2 Formation of Defect Energy Bands 44

3 Resonant Tunneling in Symmetric Vertical Heterostructures 46

3.1 Enhanced Resonant Tunneling in the symFET 46

3.2 Band Structure Effects on Resonant Tunneling 56

4 Steep-slope operation in the MoS_2-WSe_2 System 68

4.1 The WSe_2-$SnSe_2$ System 70

4.2 The MoS_2-WSe_2 System 72

4.3 TFET Scaling and Performance Tuning 76

4.3.1 Device Size 76

4.3.2 Rotational Misalignment 79

4.3.3 Lattice Constant Mismatch 80

4.3.4 Dopant Density 82

4.3.5 Applied Bias Voltages 84

4.4 Non-Ideal Systems 86

4.5 ITFET Benchmarking 89

5 Synthesis of Large-Area 2D Materials 92

5.1 Large-Area Growth of MoS_2 92

5.2 Large-Area Growth of WSe_2 103

5.3 Considerations for High Temperature Heterostructure Synthesis 115

6 Low Temperature Synthesis of TMDs 117

6.1 Low Temperature Growth Methods 117

6.2 Conversion of MoO_x to MoS_2 120

6.2.1 Remote Plasma 120

6.2.2 Direct Plasma 126

6.3 Vapor Phase Growth of MoS_2 127

6.4 Low Temperature Growth of MoS_2 using Metallic Sources 134

6.5 Comparison of Low Temperature Growth Methods 136

7 Structure and Defects in TMDs 138

7.1 MoS_2-Al_2O_3-MoS_2 138

7.2 MoS_2-WS_2 146

7.3 Fermi Level Pinning in Low-Temperature TMDs 152

8 Performance of 2D Vertical Heterostructures 156

8.1 Tunneling in MoS_2-Al_2O_3-MoS_2 Heterostructures 157

8.2 MoS_2-WS_2 Heterostructures 163

9 Summary and Future Work 166

9.1 Future Work 169

9.1.1 Optimization of Low Temperature Growth 169

9.1.2 In-Depth Defect Characterization 170

9.1.3 Heterostructures with Lateral Transport 170

9.1.4 Interlayer Coupling in Heterostructures 171

Appendix A Experimental Background 172

A.1 High Temperature Tube Furnaces 172

A.2 Molecular Beam Epitaxy 173

A.3 Characterization Techniques 177

A.3.1 Physical Characterization Methods 177

A.3.2 Electrical Characterization 181

REFERENCES 186

VITA 211

LIST OF TABLES

Page

Table 4.1: Device parameters for MoS_2-WSe_2 ITFETs 76

Table 6.1: Conditions explored for conversion of MoO_x to MoS_2. 121

LIST OF FIGURES

Page

Figure 1.1: Possible stacking configurations of TMDs, depending on the coordination between the transition metal atom and the chalcogen atoms in the adjacent layers. The 2H form, which is semiconducting, represents the room temperature stable form for many TMDs. In contrast, the 1T stacking configuration is characteristic of semimetals. Reprinted by permission from Macmillan Publishes Ltd: Nature Nanotechnology, reference 74, copyright 2012. 10

Figure 1.2: Relationship between MoS_2 thickness and band structure. Bulk MoS_2 has an indirect band gap of 1.2 eV. However, as the thickness decreases, the valence band maximum transitions from the Γ-point to the K-point, resulting in a direct 1.9 eV band gap in monolayer MoS_2. Reprinted figure with permission from A. Kuc, N. Zibouche, and T. Heine, *Physical Review B*, vol. 83, p. 245213. Copyright 2011 by the American Physical Society. 12

Figure 1.3: Evolution of the MoS_2 PL with thickness. The thinnest samples display a large PL intensity due to a more favorable direct band gap transition. As the thickness increases, the direct band gap transition becomes less favorable and the PL intensity is diminished. Reprinted with permission from G. Eda, H. Yamaguchi, D. Voiry *et al.*, *Nano Letters*, vol. 11, p. 5111. Copyright 2011 American Chemical Society. 13

Figure 1.4: Schematic of a 2D vertical heterostructure transistor. Reprinted from P. M. Campbell, A. Tarasov, C. A. Joiner, W. J. Ready, and E. M. Vogel, *Journal of Applied Physics*, vol. 119, p. 024503, 2016, with the permission of AIP Publishing. 23

Figure 1.5: Demonstration of negative differential resistance at low temperature in graphene-based symFETs. Reprinted with permission from L. Britnell, R. V. Gorbachev, A.K. Geim, L. A. Ponomarenko, A. Mischenko *et al.*, *Nature Communications,* vol. 4, p. 1794. Copyright 2013 by Macmillan Publishers Ltd. 25

Figure 1.6: Band alignment of the ITFET in the (a) OFF state and (b) ON state. 28

Figure 2.1: Band diagram of the symFET structure. and represent the biases applied to the top and bottom gates, respectively. is the applied source-drain voltage. are the voltages across the top, bottom, and interlayer dielectrics, respectively. represents the Fermi level in the top (bottom) electrode, is the electron affinity of the top (bottom) layer, EG,B is the band gap of the bottom layer and ΦM,T(B) is the work function of the top (bottom) gate metal. The dashed line represents the vacuum level and the dotted line represents the Fermi level of the structure at zero bias. 35

Figure 2.2: Density of states created by band tails in TMDs. 42

Figure 3.1: Simulated J-V_{DS} characteristics for (a) graphene, (b) MoS_2, and (c) $MoTe_2$ symFETs. There is no doping in either layer of the devices. Each curve represents a different back-gate voltage, ranging from -0.2 V to 1 V in 0.2 V steps. The top gate remains fixed at -1.5 V. The top and back gates are 40 layers of hBN, with a capacitance of 3 μF/cm^2. The interlayer consists of two layers of hBN (0.6 nm), with a capacitance of 6.2 μF/cm^2. We assume $|M_{B0}| = 0.01\,\text{eV}$, $\kappa = 3.8\text{x}10^7\,\text{cm}^{-1}$, n = 1.5, and $q_C^{-1} \approx 10\,\text{nm}$. 49

Figure 3.2: Simulated *J-V* characteristics of $ZrSe_2$, $HfSe_2$, $MoTe_2$, and MoS_2. Simulations were performed with $V_{TG} = -1.5\,\text{V}$ and $V_{BG} = 1.5\,\text{V}$ and $C_{TOX} = C_{BOX} = 3$ μF/cm^2. The work functions of the top and back gates were adjusted for each material so that the difference between the gate work function and the conduction or valence band was equivalent. The interlayer consists of two layers of h-BN (0.6 nm), with a capacitance of 6.2 μF/cm^2. We assume $|M_{B0}| = 0.01\,\text{eV}$ and $\kappa = 3.8\text{x}10^7\,\text{cm}^{-1}$. 50

Figure 3.3: (a,b) Tunneling current density in graphene and MoS_2 with varying coherence lengths q_C^{-1}. (c) Comparison of the PVR dependence on coherence length in graphene and MoS_2 symFETs. Valley currents were measured 0.1 – 0.2 V above the NDR peak because the background current increases as a function of V_{DS}. (d) Comparison of the shift in NDR peak position (referenced to 100 nm value) at varying coherence lengths. There is almost no shift for MoS_2, while the graphene peak position has a large shift at small coherence lengths. Simulations were performed with $V_{TG} = -1.5\,\text{V}$ and $V_{BG} = 1.5\,\text{V}$, with $C_{TOX} = C_{BOX} = 3$ μF/cm^2. The interlayer consists of two layers of hBN (0.6 nm), with a capacitance of 6.2 μF/cm^2. We assume $|M_{B0}| = 0.01\,\text{eV}$ and $\kappa = 3.8\text{x}10^7\,\text{cm}^{-1}$. 52

Figure 3.4: Different contributions to the tunneling current in graphene symFETs. (a-c) the density of states of the top (g_{top}) and the bottom layer (g_{bot}), and the Fermi function overlap of both layers $(|f_{bot} - f_{top}|)$versus the energy, referenced to the bottom layer Dirac point. The dark shaded area shows the portion of states capable of tunneling. (d-f) The spectrum of the scattering potential (solid line, left axis) and the contribution to the current density at each energy (red shaded area, right axis). Simulations were performed with $V_{TG} = -1.5\,\mathrm{V}$ and $V_{BG} = 1.5\,\mathrm{V}$, with $C_{TOX} = C_{BOX} = 3$ μF/cm^2. The interlayer consists of two layers of hBN (0.6 nm), with a capacitance of 6.2 μF/cm^2. We assume $|M_{B0}| = 0.01\,\mathrm{eV}$, $\kappa = 3.8\mathrm{x}10^7$ cm^{-1}, n = 1.5, and $q_C^{-1} \approx 10\,\mathrm{nm}$. 54

Figure 3.5: Different contributions to the MoS_2 tunneling current at three source-drain bias conditions. (a-c) the density of states of the top (g_{top}) and the bottom layer (g_{bot}), and the Fermi function overlap of both electrodes $(|f_{bot} - f_{top}|)$ versus the energy referenced to the bottom layer conduction band. The dark shaded area shows the portion of states capable of tunneling. (d-f) The spectrum of the scattering potential (solid line, left axis) and the contribution to the current density at each energy (red shaded area, right axis). Simulations were performed with $V_{TG} = -1.5\,\mathrm{V}$ and $V_{BG} = 1.5\,\mathrm{V}$, with $C_{TOX} = C_{BOX} = 3$ μF/cm^2. The interlayer consists of two layers of hBN (0.6 nm), with a capacitance of 6.2 μF/cm^2. We assume $|M_{B0}| = 0.01\,\mathrm{eV}$, $\kappa = 3.8\mathrm{x}10^7$ cm^{-1}, n = 1.5, and $q_C^{-1} \approx 10\,\mathrm{nm}$. 56

Figure 3.6: Possible band alignments leading to resonant tunneling in III-V devices. Alignment of any pair of subbands results in development of an NDR peak. 58

Figure 3.7: Comparison of (a) MoS_2/hBN/MoS_2 and (b) GaAs/AlGaAs/GaAs symFETs. The peaks in the GaAs symFET are labeled in the form *i-j*, where *i* represents the subband involved in transport in the bottom layer and *j* represents the subband involved in transport in the top layer. The MoS_2 symFET has a single NDR peak with a large PVR of 130, while the GaAs symFET exhibits multiple NDR peaks with a maximum PVR of 1.71 for the 2-1 peak. 59

Figure 3.8: (a) Density of states for an MoS_2 system without subbands, characterized by a single step at the conduction band edge. (b) Density of states for a theoretical MoS_2-like system with a subband 0.1 eV above the conduction band edge. (c) Total transmission coefficient (*T(E)*), for an MoS_2 system without subbands. (d) Total transmission coefficient (*T(E)*) for the theoretical MoS_2-like system. (e) Current density as a function of energy for the MoS_2 system (shown by the black shaded area). (f) Current density as a function of energy in the theoretical system with a subband. The black shaded area represents conduction-to-conduction band tunneling and is identical to that of the single band case. The red shaded area represents tunneling from the conduction band in the bottom layer to the subband in the top layer, resulting in additional valley current in the system containing the subband. Simulations were performed with V_{TG} = -1.5 V and V_{BG} = 1.5 V and C_{TOX} = C_{BOX} = 3 μF/cm^2. The interlayer consists of two layers of hBN (0.6 nm), with a capacitance of 6.2 μF/cm^2. We assume $|M_{B0}|$=0.01eV for all transitions, *n* = 1.5, and $q_c^{-1} \approx 10$ nm for all transitions. 61

Figure 3.9: (a) Effect of subband location on *J-V* response in an MoS_2/hBN/MoS_2 system with an imaginary subband. The top and bottom electrodes are assumed to have identical band structures. (b) PVR as a function of subband location. For small spacing between the conduction band edge and the subband, the PVR is significantly reduced. For large spacing, the PVR in the subband structure approaches the PVR in the absence of any subbands (depicted by the red dashed line). Simulations were performed with V_{TG} = -1.5 V and V_{BG} = 1.5 V and C_{TOX} = C_{BOX} = 3 μF/cm^2. The interlayer consists of two layers of hBN (0.6 nm), with a capacitance of 6.2 μF/cm^2. We assume $|M_{B0}|$=0.01eV for all transitions, *n* = 1.5, and $q_c^{-1} \approx 10$ nm for all transitions. 64

Figure 3.10: (a, b) Current density versus drain-source bias voltage for a variety of conduction band heights (CBH) for symFETs using a material without subbands (a) and with subbands (b) as the electrodes. (c, d) Dependence of PVR on the CBH for the symFETs without subbands (c) and with subbands (d). Simulations were performed with V_{TG} = -1.5 V and V_{BG} = 1.5 V and C_{TOX} = C_{BOX} = 3 μF/cm^2. The interlayer consists of two layers of hBN (0.6 nm), with a capacitance of 6.2 μF/cm^2. We assume $|M_{B0}|$=0.01eV for all transitions, *n* = 1.5, and $q_c^{-1} \approx 10$ nm for all transitions. 65

Figure 4.1: Comparison of the simulated performance of WSe_2-$SnSe_2$ system with a single direct band gap at the K-point for the $SnSe_2$ (simplified) and including secondary band minima and lattice constant mismatch between WSe_2 and $SnSe_2$ (realistic). In the simplified system (black, solid curve), the tunneling current is determined by the density of states overlap of the WSe_2 and $SnSe_2$, resulting in a steep-slope operation and current saturation. However, when the lattice constant mismatch is considered (red, dashed curve), the requirement for momentum conservation dominates the current-voltage response, resulting in a current that increases with increasing bias. 71

Figure 4.2: (a) Comparison of the simulated transfer curve for simplified versus realistic structure in the MoS_2-WSe_2 system. The small lattice constant difference between the two materials results in a slight decrease in the tunneling current. (b) Effect of top-gate work function on the turn-on voltage in MoS_2-WSe_2 ITFETs. As the top gate work function increases, the turn-on voltage shifts to more positive values without changing the subthreshold slope or the saturation current. (c) Simulated transfer curves demonstrating both p-TFET and n-TFET behavior in the MoS_2-WSe_2 system. The simulation uses 10 meV width extended band tail states, with the other device parameters given in Table 1. N- and P-type behavior is possible with only small changes to the device structure, suggesting the possibility for complementary logic out of a single material system. For these simulations, a value of 0.02 eV is used for M_{B0}, the coherence length is 10 nm, and κ is 5.2 nm^{-1}. 74

Figure 4.3: Effect of device size (coherence length) on the transfer characteristic of MoS_2-WSe_2 ITFETs. There is not a significant effect on the saturation current or turn-on voltage of the device until the coherence length is less than 5 nm. The circled region indicates an inflection in the current-voltage characteristic due to the stricter momentum conservation requirements as the coherence length increases. Similarly, the inset shows the subthreshold region of the device, demonstrating a small increase in the subthreshold swing as the coherence length increases. 77

Figure 4.4: Effect of rotational misalignment on tunneling in ITFETs. For a misalignment angle greater than approximately 2 degrees, the device performance is significantly degraded. 80

Figure 4.5: (a) Current-voltage characteristic for lattice constant mismatch ranging from 0% to 21%. While the turn-on voltage and steep-slope behavior of the device are independent of the lattice mismatch, increasing lattice mismatch decreases the device current and changes the slope of the curve in the saturation region. (b) Derivative of the current-voltage characteristic for a value of V_{TG} = -0.3 V, normalized by the current density The slope is near zero for no lattice constant mismatch, but quickly increases to a maximum of approximately 20 for a small lattice constant mismatch. 81

Figure 4.6: Threshold voltage shift due to doping in the ITFET. Doping of the top layer results in a symmetric response for both p-type (closed black squares) and n-type (open black squares) dopants. Doping of the bottom layer is similar to the top layer for p-type doping (closed red circles). However, a smaller effect is observed for n-type doping of the bottom layer (open red circles), with a reduced shift in the threshold voltage compared to the other doping conditions. In all cases, a doping density of larger than 10^{12} cm^{-2} is necessary to observe a significant effect on the threshold voltage. 83

Figure 4.7: (a) Influence of V_{DS} on the transfer curve of an MoS_2-WSe_2 ITFET. For V_{DS} greater than 0.2 V, the turn-on characteristic does not change significantly. Continued increases to the bias voltage only minimally increase the saturation current of the device. (b) Effect of V_{BG} on the threshold voltage of the device. Positive values of V_{BG} have a diminishing effect on the threshold voltage, while negative values can more strongly tune the device behavior. 85

Figure 4.8: Comparison of the relationship between subthreshold swing and band tail width for both localized and extended band tail states. Both types of band tail states increase the subthreshold swing and decrease the ITFET performance. However, localized states appear to more strongly affect the subthreshold swing. For current synthesis techniques, it is expected that wide band tails will result in subthreshold swings greater than 60 mV/decade. 88

Figure 4.9: Benchmarking of the MoS2-WSe2 ITFET. (a) Comparison of the transfer curve of the MoS2-WSe2 ITFET to high-performance (HP) and low-power (LP) CMOS devices. The saturation current of the MoS2-WSe2 ITFET is higher than for either CMOS device with a steeper turn-on. (b) Comparison of the energy and switching delay for the MoS2-WSe2 ITFET with HP/LP-CMOS devices, as well as a number of other proposed tunneling devices. Based on this comparison, the MoS2-WSe2 ITFET has the potential for better performance than other proposed devices. 90

Figure 5.1: (a) Schematic of the process flow used for growth of large-area MoS_2 films. (b) Overview of the high-temperature sulfurization used to convert the evaporated MoO_x thin film to MoS_2. 93

Figure 5.2: Influence of synthesis temperature on the stoichiometry of synthetic Mo films. 94

Figure 5.3: (a) Raman spectra from a 5 nm Mo layer after sulfurization at different growth temperatures (532 nm laser). Typical MoS_2 double peak is visible around 400 cm– 1. The E_{2g}^1 peak represents the in-plane vibrations of Mo and S atoms, and A_{1g} denotes the out-of-plane vibrations of sulfur atoms. The spectra were normalized to the A_{1g} peak intensity and are shown vertically offset for clarity. The MoS_2 peaks become narrower with increasing growth temperature, and their intensity relative to the Si peak increases. b) The full-width at half-maximum (FWHM) of the E_{2g}^1 and A_{1g} peaks as a function of temperature. The peak width decreases as the temperature goes up and reaches the bulk values (dashed lines) only above 1000 °C. 95

Figure 5.4: The thinnest MoS_2 sample (1 nm Mo, sulfurized at 1050 °C) was used for device fabrication following a wafer-scale UV lithography process. a) The optical image shows a wafer die after device fabrication. b) Raman spectra from 15 different areas of the sulfurized wafer align perfectly on top of each other. c) The peak separation between the E_{2g}^1 and $A_{1g}$of 23.53±0.04 cm−1 is smaller than for the bulk material (25 cm^{-1}) and corresponds to 3 layers of MoS_2. The thickness uniformity is ~0.1 monolayers (or ~0.07 nm) across the whole wafer. 97

Figure 5.5: (a) An optical image of a trilayer MoS_2 transistor with Ti/Au contacts before the topgate deposition. Inset: Raman maps were taken across the area of a transistor. The peak separation was 23.5 ± 0.1 cm^{-1}, showing excellent uniformity. (b–d) The thickness was confirmed by cross-sectional STEM, performed on a transistor after fabrication. b) A bright-field (BF) image across the contact region in (a) shows a thin MoS_2 layer between the SiO_2 substrate and the Ti/Au contact material. MoS_2 appears darker than SiO_2 or Ti because of the higher atomic number of Mo. c) A BF image at higher magnification reveals good stacking of 3 layers of MoS_2 (Mo layers are darker than S). (d) The same area is also shown as a dark-field image. The total MoS_2 thickness is around 2 nm. This matches well with our expectation because we deposited 1 nm Mo which should yield 3 layers of MoS_2 after sulfurization. 98

Figure 5.6: (a) Schematic of a dual-gated trilayer MoS_2 transistor (not to scale). The drain-source voltage V_{ds} is applied to the Ti/Au contacts on top of MoS_2. The channel is covered with 30 nm Al_2O_3 and a Ti/Au top gate electrode. The drain current I_d through the MoS_2 channel is measured as a function of the back gate voltage V_{bg} and the top gate voltage V_{tg}. (b) Drain current I_d through the MoS_2 channel as a function of the applied back-gate voltage V_{bg} (transfer curve) at constant drain-source voltage V_{ds} = 1 V, with the top-gate grounded (V_{tg} = 0 V). The transfer curve on the semi logarithmic scale (left vertical axis) shows both gate sweep directions, indicated by arrows. The hysteresis is negligible. The linear transfer curves (right axis) compare one sweep direction for two different transistors, FET 1 (solid circles) and FET 2 (empty circles). Both curves align very well on top of each other. The transistors are several centimeters apart, suggesting high uniformity of the film. (c) The output curves I_d vs V_{ds} are linear and symmetric around V_{ds} = 0 V (Ohmic behavior). The applied drain-source voltages $V_{ds} \leq 1$ V are well inside the linear regime of operation. 100

Figure 5.7: (a) Transfer curves ($I_{d,corr}$ vs V_{bg}) at $V_{tg} = 0$ V after subtracting the extrinsic resistance $2R_{ext}$. (b) From the slope of the curves in (a), the intrinsic field effect mobility μ_{FE}^{int} can be estimated for all measured transistors. 13 devices were randomly chosen across the whole die area of >10 cm^2. 102

Figure 5.8: (a) Schematic of the experimental setup used for selenization. Se pellets are loaded into a crucible which is placed in the furnace with the 1 nm W/WO_3 film. The furnace is heated to 800º C at 3 Torr under 30 sccm Ar and 10 sccm H_2 flows. After 1 hour, the furnace is purged an additional 30 minutes at 800º C under Ar flow before cooling. (b-c) XPS spectra of the resulting WSe_2 films. (b) W 4f spectrum. The main peaks present are the $4f^{7/2}$ and $4f^{5/2}$ doublet resulting from the WSe_2 (red lines). A second set of peaks are present due to the formation of WO_3 on the WSe_2 film or at the grain boundaries (blue lines).[1, 2] The magenta line represents the W $5p^{3/2}$ peak. (c) Se 3d spectrum. Only a single set of Se peaks are present in the XPS spectrum, indicating that all of the Se within the film is contained in the WSe_2. 104

Figure 5.9: (a) Sample Raman spectrum for WSe_2, measured with 488 nm illumination. The main peak (250.2 cm^{-1}) is composed of contributions from the E_{2g}^1, the A_{1g}, and the $2LA(M)$ modes. The presence of the E_g^1 peak (~175 cm^{-1}), the B_{2g}^1 (~307 cm^{-1}), and the three second order modes between 350 cm^{-1} and 410 cm^{-1} indicate the few-layer nature of the synthesized film. (b) Peak position and (c) full-width at half-maximum (FWHM) of the main Raman peak at each point measured on the small Raman map (black squares) and the large Raman map (gray circles). The small variation across large and small scales indicates the excellent uniformity of the synthetic WSe_2. 106

Figure 5.10: (a) Atomic force microscopy (AFM) image of a pre-patterned WSe_2 step. (b) Height profile measured across the WSe_2 step. The thickness was estimated by taking the difference between the mean height on either side of the WSe_2 step. Based on this measurement, the thickness of the WSe_2 is approximately 2.5 nm. 109

Figure 5.11: (a) Optical image of a portion of the measured FET array. (b) Schematic of a back-gated FET used for electrical measurements. (c) Linear (black) and logarithmic (red) scale plots of the source-drain current as a function of back-gate voltage (transfer curve) for one of the measured FETs at a source-drain voltage (V_{ds}) bias of 1 V. The arrows indicate the voltage sweep direction. (d) Transfer curves of a WSe_2 FET transistor measured at several different V_{ds} values. (e) Source-drain current (I_{ds}) versus source-drain voltage (V_{ds}), measured at several back-gate voltages (V_{bg}). Over the entire range measured, the curve is linear, confirming that the measured transfer curves remained within the linear regime. 110

Figure 5.12: (a) Superposition of the reverse sweep transfer curves for several FETs, measured across an area of several square centimeters. The electrical performance of all devices measured is similar, demonstrating the uniform nature of the WSe_2 film. (b) Measurement of the voltage at which the current equals 1 nA (V_{1nA}), for the forward (red circles) and reverse (black squares) directions for each device, showing electrical uniformity between the measured FETs. 111

Figure 5.13: (a) Extrinsic resistance R_{ext} as a function of applied back-gate voltage, measured using the 4-point probe structure shown in the inset, as explained in the text. (b) R_{tot} (black solid line) and intrinsic channel resistance, $R_{tot} - R_{ext}$ (blue dashed line), for a two-terminal FET (see Figure 5.13) as a function of back-gate voltage. (c) Corrected drain-source currents ($I_{d,corr}$) for two FETs from Figure 5.13 (c). The current is corrected using the calculated intrinsic resistance for each device. (d) Field-effect mobility as a function of carrier concentration for the synthetic WSe_2. 113

Figure 5.14: (a) Raman and (b) photoluminescence measurements for $MoSe_2$ flakes before (black lines) and after (red curves) exposure to sulfur vapor at high temperature. 116

Figure 6.1: Schematic of the MoS_2 synthesis process explored. (a) Process used for remote plasma conversion. The Ar/H_2S gas mixture flows into the ASTRONi plasma source which contains the plasma. H and S radicals flow from the outlet of the plasma source into the chamber and react with the MoO_s film. (b) MBE chamber containing the direct plasma process. The chamber is outfitted with both a thermal and plasma H_2S source, as well as an effusion cell containing MoO_3 for the vapor phase growth method. 118

Figure 6.2: (a) Representative Raman spectra for each of the synthesis conditions explored. Samples labeled as "A" have no pre-treatment, while samples labeled as "B" underwent an H_2 plasma pre-treatment prior to H_2S exposure. Samples marked with an asterisk (*) were exposed to remote plasma H_2S, while those without an asterisk underwent the thermal H_2S process. (b) Mo3d and S2p XPS spectra for the samples without pre-treatment. The remote plasma H_2S results in effective conversion to MoS_2, while the thermal process results in minimal sulfur incorporation in the sample. (c) Mo3d and S2p XPS spectra for samples with pre-treatment. Both the thermal and plasma process result in effective conversion to MoS_2. 122

Figure 6.3: (a) Raman spectrum after conversion of MoO_x film to MoS_2 using direct plasma. (b) Mo 3d spectrum of the sample converted using direct plasma. The red curves represent the Mo $3d^{5/2}$ and Mo$3d^{3/2}$ from MoS_2 bonding and the blue curves represent the Mo $3d^{5/2}$ and Mo $3d^{3/2}$ due to MoO_3 bonding. The green curve represents the S 2s peak. (c) S 2p spectrum from the direct plasma sample. The sulfur spectrum is characterized by only two peaks, confirming that all sulfur in the sample has reacted with molybdenum. 126

Figure 6.4: (a) Comparison of the Mo3d spectra for the plasma (solid lines) and thermal (dashed lines) vapor phase processes. While both samples exhibit a prominent peak resulting from MoO_3 in the sample, the plasma sample has a smaller MoO_3 peak, confirming that the plasma-based process results in a greater extent of reaction. (b) Comparison of the S2p spectra for the plasma and thermal processes. The red curve represents sulfur bonded to molybdenum, while the blue curve represents excess sulfur on the sample surface. The plasma sample has stronger peak intensity, indicating that more sulfur has been incorporated into the sample. 128

Figure 6.5: Comparison of the Raman spectra for the thermal (a) and plasma (b) vapor phase processes. Both processes result in the formation of MoS_2 on the sample surface. However, the peak separation is larger for the plasma process than the thermal process, indicating thicker MoS_2 on the plasma sample. Because the total amount of MoO_3 supplied to the sample is identical in both cases, the larger peak separation indicates that the use of plasma processing resulting in a larger extent of reaction between sulfur and MoO_3. 130

Figure 6.6: RHEED patterns measured on the thermal and plasma-assisted growths at 800 °C. The presence of streaks indicates the two-dimensional growth mode of the MoS_2. The spacing between the streaks corresponds to a lattice constant of 3.13 Å. 131

Figure 6.7: (a) Comparison of Mo3d for the pulsed MoO_3 process at 400 °C (solid) and 800 °C (dashed). The spectra are identical, suggesting that plasma processing enables low temperature processing without sacrificing material quality. (b) Comparison of S2p spectra for the low and high temperature pulsed MoO_3 processes. The high temperature sample exhibits a small amount of excess sulfur on the surface. Aside from the excess sulfur, the spectra are similar. 133

Figure 6.8: Results of Raman mapping on low-temperature pulsed MoO_3 samples. (a) Peak separation between the E_{2g}^1 and A_{1g}peaks versus point number. The peak separation is relatively uniform across the sample surface, indicating a uniform sample thickness over a large area. (b) E_{2g}^1 and (c) A_{1g} full width at half maximum (FWHM) versus peak position, indicating uniform quality of MoS_2 across the sample surface. 134

Figure 6.9: Raman spectrum of the MoS_2 grown using a sputtered Mo source and direct H_2S plasma. 135

Figure 6.10: (a) Mo 3d and (b) S 2p XPS spectra for the MoS_2 grown by cyclical growth based on sputtered Mo and direct H_2S plasma at low substrate temperature. 136

Figure 6.11: Comparison of PL response for different low temperature growth methods, including the sputtered-Mo based method (black curve), the pulsed MoO_3 method (red curve), and conversion of a thin MoO_x film using direct plasma (green curve). The PL response of a high temperature sample grown by conversion of MoO_x in sulfur vapor (blue curve) is included for comparison. 137

Figure 7.1: (a,b) Representative Raman spectra for growths on SiO_2 (black curve), gold (red curve), and sapphire (green curve) for the (a) 10 min MoO_3 and (b) 5 min MoO_3 pulsed growths. (c) FWHM of the Raman peaks on each substrate for the two growth methods. The FWHM for the 5 min MoO_3 pulsed growth with the addition of an MoO_3 seed layer is included as well. 140

Figure 7.2: Comparison of the PL response of the 5 minute MoO_3 (black curve) and 10 minute MoO_3 (red curve) growth methods. 141

Figure 7.3: XPS comparison of the (a) Mo 3d and (b) S 2p spectra at different steps during growth of the MoS_2-Al_2O_3-MoS_2 heterostructure. The black curve was measured after deposition of the bottom layer MoS_2, the red curve represents the bottom layer of MoS_2 with the addition of a MoO_3 seeding layer, and the green curve was measured after growth of the top layer of MoS_2 143

Figure 7.4: XPS depth profiling of the MoS_2-Al_2O_3-MoS_2 heterostructure. 145

Figure 7.5: (a) Raman spectra of the individual WS_2 film (black curve), the individual MoS_2 film (red curve), and the MoS_2-WS_2 heterostructure (green curve). (b) Raman FWHM comparison of grown of the MoS_2 and WS_2 films used for the heterostructure on SiO_2, sapphire, and gold substrates. 147

Figure 7.6: PL measurements taken on individual WS_2 (black curve) and MoS_2 (red curve) films, as well as the MoS_2-WS_2 heterostructure (green curve). 149

Figure 7.7: XPS comparison of the (a) Mo 3d, (b) W 4f, and (c) S 2p spectra in the MoS_2/WS_2 heterostructure. The black (red) curve represents an individual WS_2 (MoS_2) film, while the green curve was measured on the heterostructure. 150

Figure 7.8: Capacitance versus DC bias voltage measured at several frequencies for the 10 min MoO_3 pulsed samples. 152

Figure 7.9: Temperature dependence of conductivity for 5 minute MoO_3 (black squares), 10 minute MoO_3 (red circles), and sputtered Mo (green triangles) based synthesis methods for MoS_2. The dashed lines indicate linear fits to the data to extract the value of T_0. 154

Figure 8.1: Schematics of the heterostructures explored for the (a) MoS_2/Al_2O_3/MoS2 and (b) MoS_2/WS_2 heterostructures. 156

Figure 8.2: (a) Size dependence of the current density measured for the MoS_2-Al_2O_3-MoS_2 heterostructures. (b) Measured current density for various device sizes for an Au-Al_2O_3-Ti control sample. 158

Figure 8.3: Comparison of experimentally measured (green line) with simulated transfer curves (red dotted and black dashed lines) on MoS_2-Al_2O_3-MoS_2 heterostructures. The black dotted line represents a 1 nm coherence length indicative of low quality devices and matches the experimental data well. The red dotted line uses a 20 nm coherence length to predict the performance of higher-quality devices. 160

Figure 8.4: Simulation of the current-voltage characteristic for vertical MoS_2-Al_2O_3-MoS_2 heterostructures using different combinations of contact metals. The NDR peak position is tunable based on Fermi level pinning at the metal-MoS_2 interface. 162

Figure 8.5: Experimentally measured current-voltage characteristics for two MoS_2-WS_2 heterostructure devices. (a) Tunneling current measured at 300 K. (b) Tunneling current measured at 77 K. 164

Figure A.1: Schematic of the MBE system used for TMD growth. 174

Figure A.2: Ewald sphere representation of a RHEED pattern. The intersections of the Ewald sphere with the reciprocal lattice determine the pattern of streaks which will occur. 176

Figure A.3: (a) Schematic of back-gated field-effect transistor structure (FET) used for mobility evaluation. (b) Schematic of metal-oxide-semiconductor capacitor (MOSCAP) structure used for defect characterization 181

Figure A.4: (a) Capacitance and (b) Conductance measurements used to extract band tail states in MoS_2 samples. (c) Extracted density and time constants of type M and type B traps. (d) The extracted band tails in the MoS_2. Reprinted by permission from Macmillan Publishers Ltd: Nature Communication, reference 97, copyright 2014. 183

LIST OF SYMBOLS AND ABBREVIATIONS

AFM	Atomic Force Microscopy
ALD	Atomic Layer Deposition
BF	Bright Field
BP	Black Phosphorus
BTBT	Band-to-Band Tunneling
CMOS	Complementary Metal Oxide Semiconductor
CVD	Chemical Vapor Deposition
CVT	Chemical Vapor Transport
DFT	Density Functional Theory
DMS	Dimethyl Sulfide
FET	Field-Effect Transistor
FIB	Focused Ion Beam
FWHM	Full width at half maximum
GIXRD	Grazing Incidence X-ray Diffraction
ITFET	Interlayer Tunnel Field-Effect Transistor
LED	Light emitting diode
LP CMOS	Low power CMOS
HP CMOS	High performance CMOS
MBE	Molecular Beam Epitaxy
ML	Monolayer
MOSCAP	Metal Oxide Semiconductor Capacitor
MOSFET	Metal Oxide Semiconductor Field-Effect Transistor
NDR	Negative Differential Resistance

PL	Photoluminescence
PVD	Physical Vapor Deposition
PVR	Peak-to-Valley Ratio
RF	Radio frequency
RHEED	Reflection High-Energy Electron Diffraction
RSF	Relative Sensitivity Factor
RTD	Resonant Tunneling Diode
RTT	Resonant Tunneling Transistor
SS	Subthreshold Swing
STEM	Scanning Transmission Electron Microscopy
symFET	Symmetric Field-Effect Transistor
TFET	Tunnel Field-Effect Transistor
TMD	Transition Metal Dichalcogenide
UV	Ultraviolet
vdW	van der Waals
VRH	Variable Range Hopping
XPS	X-ray Photoelectron Spectroscopy

SUMMARY

Transition metal dichalcogenides (TMDs) have recently emerged as a class of two-dimensional materials relevant for use in electronic devices. TMDs have an intrinsic bandgap, making these materials appealing for applications in digital and analog electronics, flexible electronics, optical applications, and sensors. Several synthesis methods for TMDs have been explored, ranging from chemical vapor deposition (CVD) to thin film alloying methods. CVD methods result in large grain sizes, but high uniformity films require long growth times. Conversely, thin-film based methods result in wafer-scale coverage albeit with small grain sizes on the order of tens of nanometers. A common drawback to both methods is the high synthesis temperature required, ranging from roughly 550 – 1050 °C.

2D vertical heterostructures composed of TMDs have a number of interesting applications, including digital logic, analog communications, and optoelectronics. However, the quality of currently available synthetic materials is not sufficient to realize many of these applications. Further, the impact of defects and layer-to-layer interactions on the electronic behavior of heterostructures is not well understood. In this work, the behavior of these heterostructures is explored using a theoretical model based on the Bardeen transfer Hamiltonian. Within this framework, the potential for TMD-based heterostructures to exhibit both resonant tunneling and steep-slope operation is explored.

This work demonstrates wafer-scale synthesis of TMDs using high temperature growth methods. In addition, plasma-enhanced synthesis processes are

demonstrated which lower the growth temperature and improve compatibility with the thermal budget of a CMOS process. Physical characterization provides information about the stoichiometry, thickness, and crystallinity of the material, while electrical measurements link electronic transport materials to the material quality. In particular, temperature dependent conductivity measurements for the materials synthesized at low temperature demonstrated conduction through variable range hopping as a result of high defect densities and the nanocrystalline nature of the synthetic films.

MoS_2-Al_2O_3-MoS_2 and MoS_2-WS_2 heterostructures are created using the low temperature, plasma-assisted growth processes. Extensive physical characterization of the films demonstrates good fidelity of the heterostructures, with no evidence of chemical bonding between the layers. Electrical characterization of two-terminal devices based on the MoS_2-Al_2O_3-MoS_2 heterostructure confirms tunneling between the MoS_2 electrodes with a high degree of scattering. The MoS_2-WS_2 heterostructure, which relies only on the van der Waals gap as the tunnel barrier, exhibits a current-voltage characteristic dominated by tunneling through defects.

The work presented in this thesis demonstrates initial first steps toward the realization of complex 2D heterostructure devices. Through a combination of simulation and experiment, the implications of defects and Fermi level pinning on device performance were explored. In particular, this work demonstrates the potential of 2D vertical heterostructures and provides a path toward realizing high performance devices through device design and optimization of synthesis.

CHAPTER 1

INTRODUCTION

Transition metal dichalcogenides (TMDs) are a class of two-dimensional (2D) materials that has recently generated significant interest for devices such as sensors,[3-10] flexible electronics,[9-13] and optical electronics[14-17] due to their thickness-dependent optical and electrical properties. Unlike 3D materials, 2D materials lack out-of-plane bonding, forming as layered materials instead of bulk crystals. As a result, there are a number of applications for 2D materials which are difficult to realize using more traditional 3D materials, including novel device structures which exhibit resonant tunneling or steep-slope behavior. This chapter includes a brief overview of the history of 2D materials, a discussion of the interesting properties of TMDs, a survey of TMD synthesis methods, and a number of interesting applications of 2D materials in electronic devices.

1.1 Layout of this Thesis

The first portion of this thesis (Chapters 2-4) includes the theoretical description of 2D vertical heterostructures. In particular, Chapter 2 describes the theoretical model used to simulate tunneling in heterostructures. The theoretical model is based on the Bardeen transfer Hamiltonian and includes the effects of several non-idealities, including defects and band tails. Chapter 3 applies the theoretical model to explore resonant tunneling within 2D vertical heterostructures. The behavior of TMD-based devices is compared with graphene-based devices and III-V resonant tunneling diodes to understand the performance enhancement when using TMDs. Chapter 4 discusses the potential for

steep-slope operation of 2D vertical heterostructures. In particular, this work includes the first prediction of steep-slope behavior in MoS_2-WSe_2 system. A number of device parameters are explored in order to insight into the design of high-performance devices.

The second portion of the thesis (Chapters 5-7) describes the experimental approach taken to realize large-area TMDs which are applicable to the creation of 2D vertical heterostructures. Chapter 5 describes the large-area, uniform synthesis of few-layer films of both MoS_2 and WSe_2. The synthesis is based on the chalcogenization of evaporated transition metal films at high temperature.

Chapter 6 discusses efforts to reduce the synthesis temperature for TMDs through plasma-assisted processing. Conversion of thin metal films to create MoS_2 and vapor phase transition metal precursors are both explored. Chapter 7 explores the quality of individual low-temperature TMD films and the application of low-temperature films for direct growth of vertical heterostructures. Physical and electrical characterization are used to understand the nature of defects within the individual TMD layers as well as interlayer interaction which occur in vertical heterostructures.

Finally, Chapter 8 describes the electrical performance of directly grown vertical heterostructures. The experimentally determined tunneling behavior is compared with the theoretical model to understand the effects of material defects on device performance. The chapter examines MoS_2-based heterostructures with an oxide interlayer between the 2D electrodes and MoS_2-WS_2 heterostructures without an interlayer.

To provide the necessary background for understanding the results presented in this thesis, the Introduction is organized as follows. First, a general overview of the applications of 2D materials is given, followed by a brief history of the development of

TMDs. An overview of the possible structures for TMDs and the unique properties which result from the structure is included. Next, a number of potential synthesis techniques for TMDs are discussed, including the advantages and drawbacks of each method.

Because understanding the electrical performance of the vertical heterostructures relies on understanding the nature of Fermi level pinning in TMDs, a portion of the Introduction focuses on previous studies which explored Schottky barrier heights and Fermi level pinning at the TMD-metal interface.

The final section of the Introduction contains a literature review of the 2D vertical heterostructures of interest in this thesis. The potential for both resonant tunneling and steep-slope behavior in these structures is discussed. For each application, a discussion of experimental work based on exfoliated material is included. In addition, prior work on the direct growth of 2D vertical heterostructures is discussed.

1.2 Applications of 2D Materials

1.2.1 Optoelectronics

Monolayer TMDs have direct bandgaps within the visible portion of the electromagnetic spectrum,[18, 19] making them applicable to photodetectors, solar cells, and light-emitting devices. In addition, the lower dimensionality of two-dimensional materials compared to three-dimensional materials has been predicted to increase the exciton binding energies in these devices, resulting in enhanced performance in optoelectronic applications.[20]

Photodetectors based on 2D materials have been explored as both phototransistors[21-24] and photodiodes.[25-27] In particular, MoS_2-based phototransistors have been demonstrated to have high responsivities, but suffer from long response times

compared to photodiodes. In contrast, extremely fast photoresponse times are possible in photodiodes, but these have much lower responsivity than the phototransistors.

Solar cells based on TMDs have shown encouraging results, including a power conversion efficiency of ~1% using a few layer MoS_2 flake.[28] Heterostructure devices using a graphene/TMD/graphene sandwich structure has demonstrated an external quantum efficiency as high as 55% at a single wavelength.[24] However, light absorption in these devices is limited by the ultrathin nature of these devices. Therefore, a number of light-trapping techniques are necessary in order to enhance the device performance.[29-32]

A final optoelectronic application of TMDs is the light-emitting diode (LED). Because monolayer TMDs have a direct band gap, these materials are promising for atomically thin, flexible LEDs. Previous studies have explored Schottky junction-based LEDs, though the quantum efficiency of these devices was low.[33] Heterojunctions based on WSe_2 have also been used to create LEDs with efficiency of ~0.2%.[15, 34, 35]

1.2.2 Flexible Electronics

Due to their atomically thin nature, two-dimensional materials are uniquely suited for applications in flexible electronics. Traditionally, there has been a tradeoff between flexibility and the performance of devices used for flexible electronics. In particular, these approaches have relied on techniques such as the thinning of 3D materials in order to increase the flexibility of the material, which is typically accompanied by changes in the electronic structure of the material.[36-38] Another approach has been the development of materials specifically for flexible devices, such as organic or metal oxide thin-film transistors.[39] While these materials have greater flexibility, they also tend to have low

charge carrier mobilities, limiting their use to low performance, low frequency operations.

2D materials have the potential to bridge the gap for flexible devices, providing ultra-thin, highly flexible devices with performance closer to that of silicon-based devices. Combined with the use of a transfer process, recent work has explored the behavior of MoS_2 transistors on flexible substrates.[9-12, 40] These studies suggested that the transfer of MoS_2 to the flexible substrates did not result in any significant degradation in the quality of devices. Most importantly, the mobility of the films was similar on the flexible substrates compared to the rigid substrates, suggesting that TMDs can be used to create high quality flexible electronics.

1.2.3 Sensing

Due to their ultrathin nature, the electrical performance of 2D materials is particularly sensitive to environmental effects. For example, adsorption of atmospheric molecules to MoS_2 has been shown to alter the response of field-effect transistors and increase the hysteresis in device measurements.[41] By tailoring the interface between the TMD surface and the environment, these interactions can be tailored to specific molecules. In field-effect transistors binding of these molecules to the TMD device results in electronic changes to the TMD, causing a shift in the threshold voltage which is proportional to the density of bound molecules. As a result, by evaluating the change in electrical performance, a robust TMD-based sensor can be developed for a wide variety of molecules.[4-8, 10, 42]

A second type of sensor which has been explored in MoS_2 is a strain sensor. The band gap of MoS_2 slightly narrows with increasing tensile strain.[43-48] Due to the change

in the band gap, the current-voltage characteristic of the MoS_2 transistor varies with the strain state. By integrating MoS_2 transistors with a flexible substrate, a device can be created which passes a strain induced in the substrate to the MoS_2 channel.[9, 49, 50] Because of their highly flexible nature, TMD-based strain sensors do not exhibit strong degradation upon strain cycling, making them highly suited for strain sensing.

1.2.4 Beyond-CMOS Devices

Development of current digital technology began in December 1947, when the first transistor, based on Ge, was demonstrated by a team at Bell Labs.[51, 52] As transistor technology began to mature, Si replaced Ge as the material of choice for transistors for a number of reasons.[53] First, the high abundance of Si in the Earth's crust results in low-cost devices. Second, the wider band gap of Si (1.1 eV) compared to Ge (0.67 eV) results in more reliable device operation due to reduced thermal excitation of charge carriers.[54] Finally, processing breakthroughs resulted in easier to fabrication and doping of Si.[53]

In 1959, the metal-oxide semiconductor field-effect transistor (MOSFET) was developed by Bell Labs.[55] This breakthrough was enabled by the high quality interface between Si and SiO_2 which does not incorporate large amounts of trapped charges.[56] Around the same time, Jack Kilby of Texas Instruments demonstrated the first integrated circuit, providing the final building block fo rmoderm electronics.[57] For decades, complementary metal-oxide semiconductor (CMOS) devices have dominated electronics.

Over the last several decades, Moore's law has characterized the constant push for increased device performance and decreased transistor sizes. However, there have been several challenges to overcome in order to continue this device scaling. A primary materials related challenge for scaling of CMOS devices has been increasing OFF-state

and leakage currents due to the scaling of the gate dielectric. In the early 2000s, the industry began to use high-κ dielectrics such as HfO_2 as the gate dielectric in order to combat the increasing leakage current in CMOS devices.[58]

Current CMOS devices are reaching a number of physical limitations which may hinder continued scaling of the devices. Crucially, the subthreshold swing of MOSFETs is limited to 60 mV/decade, which is the slope of the Fermi function at room temperature. This limitation also limits the operating voltage of the device in order to achieve the necessary ON/OFF ratio for high-performance device operation. A second consideration is that devices are approaching length scales where quantization effects occur, which can fundamentally alter the behavior of MOSFET devices.

Two-dimensional materials are an ideal candidate for continued scaling of digital logic devices because they are not subject to the same quantization effects which occur when 3D materials are scaled down to small sizes. Additionally, the different classes of 2D materials exhibit a range of electronic behaviors, including highly conducting (graphene), insulating (hexagonal boron nitride, hBN), and semiconducting. The TMDs generally exhibit semiconducting behavior, making TMDs a potential replacement to Si. Additionally, the band gap of many TMDs is on the same order as that of Si. For example, the band gap of bulk MoS_2 is 1.2 eV, very close to the 1.1 eV band gap of Si. However, processing techniques for 2D materials, especially the TMDs, are only in their infancy, and a large amount of development is necessary in order to unlock the potential of these materials.

1.3 History of 2D Materials

Historically, two-dimensional materials, including TMDs, were explored by the manufacturing industry as industrial lubricants.[59] Because of their layered structures, 2D materials typically possess high in-plane strength, but because they lack out-of-plane bonding, the layers in the material can slip easily against one another. As a result, these materials present excellent candidates for high durability lubricants.

In order to facilitate use as industrial lubricants, a large emphasis was placed on the growth of synthetic TMD crystals. A common method for growth of synthetic crystals of TMDs is the chemical vapor transport (CVT) method. For CVT growth, a transport agent such as Cl,[60, 61] Br,[62, 63] or I[64] reacts with a transition metal source to produce a volatile transition metal compound, which flows downstream in the growth tube. The transition metal compound then reacts with a chalcogen vapor to produce the transition metal dichalcogenide, which condenses to form a large crystal. Through this method, growth of a number of high quality transition metal dichalcogenides is possible.

Following the development of the CVT method, several studies began to explore the optical and electronic properties of bulk TMD crystals.[65-71] One of the most interesting results of these studies was the demonstration of the semiconductor-metal transition which TMDs undergo when subjected to high temperature or high pressure environments. As will be discussed in detail later, this transition occurs as a result of changes in the stacking of the layers within the TMD.

In 2004, development of the so-called "Scotch tape method" for the exfoliation of graphene led to renewed interest in 2D materials.[72] In addition to the initial demonstration for graphene, the Scotch tape method was applied to a number of other materials,

including TMDs such as MoS_2 and dielectrics such as hBN. The Scotch tape method represented a step forward in 2D materials research because of the potential to create flakes of the materials ranging from single-layers to several layers thick. One drawback of these flakes is that at best, they are several micrometers in size, meaning that they are not applicable for large-scale processing. However, combined with e-beam lithography, the Scotch tape method was sufficient to drive exploration of the interesting properties of 2D materials. For example, single layer MoS_2 field-effect transistors have been fabricated using exfoliated material, demonstrating ON/OFF ratios on the order of 10^8.[73]

1.4 Structure and Properties of 2D Materials

An individual layer of a TMD has the formula MX_2 and is composed of a sheet of a transition metal (typically M = Mo or W) sandwiched between two sheets of chalcogen atoms (X = S, Se, Te). Stacking of several layers results in the creation of a bulk crystal which is held together through van der Waals interactions between the individual layers. Within this crystal, each layer consists of only in-plane bonding and the surface of a perfect crystal contains no dangling bonds. As a result, high-quality 2D materials have the potential to form perfect interfaces, in contrast to 3D crystals in which the surface has a number of unsatisfied dangling bonds that can result in poor interfaces. In addition, the lack of out-of-plane bonding between the layers results in anisotropic electronic transport in 2D materials, with high resistance to out-of-plane transport which requires tunneling between layers, and lower resistance to in-plane transport.

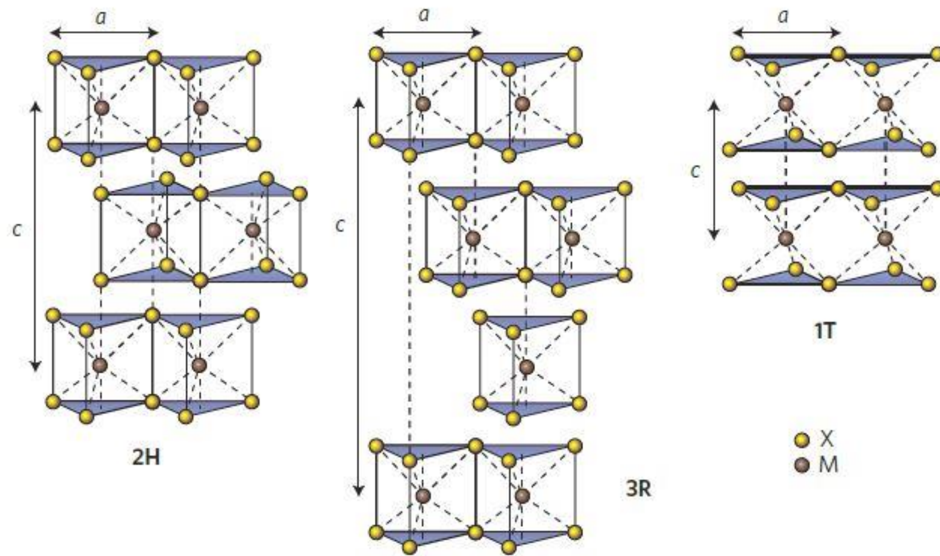

Figure 1.1. Possible stacking configurations of TMDs, depending on the coordination between the transition metal atom and the chalcogen atoms in the adjacent layers. The 2H form, which is semiconducting, represents the room temperature stable form for many TMDs. In contrast, the 1T stacking configuration is characteristic of semimetals. Reprinted by permission from Macmillan Publishes Ltd: Nature Nanotechnology, reference 74, copyright 2012.[74]

For a TMD sample with multiple layers, a number of different stacking configurations are possible depending on the coordination of the metal and chalcogen atoms between multiple layers, as shown in Figure 1.1.[74] For most TMDs, including the transition metal sulfides and transition metal selenides, the room temperature stable stacking configuration is the 2H form, in which the chalcogen atoms in one layer are aligned with the metal atom in the layers above and below that layer. The 2H stacking configuration results in a unit cell composed of a two-layer repeating structure and an overall hexagonal symmetry of the material.

Another common stacking configuration for TMDs is the 1T configuration, in which the metal atoms and chalcogen atoms in one layer lie directly on top of the metal or chalcogen atoms, respectively, in the layers above and below. The 1T (or 1T') phase of

TMDs is orthorhombic, rather than the trigonal prismatic structure of the 2H phase. In particular, the equilibrium phase of WTe_2 at room temperature is the 1T’ phase.[62] This phase is also characterized by a buckled structure of the transition metal layer. Extreme conditions, such as high pressure or high temperature, can result in a shift of the stacking coordination in a material between the 2H and 1T forms,[68, 75] resulting in significant changes in the electrical properties and band structure of the material. In the 2H configuration, the p_z orbitals on the chalcogen atoms are offset from each other, while in the 1T configuration, the chalcogen atoms in different layers lie directly above or below each other, resulting in an overlap of the p_z orbitals on these atoms. Because the p_z orbitals determine a large amount of the valence band structure of the TMDs, the increased interaction between the p_z orbitals in the 1T phase significantly changes the band structure of the materials. For example, for MoS_2 and $MoTe_2$ the 2H configuration is a semiconductor, while the 1T configuration is a semimetal.[68, 75, 76]

Because of their unique structure, TMDs have a number of interesting thickness dependent properties, determined by the interactions between the layers in the sample. Using MoS_2 as a representative material, the valence band structure is derived from the combination of p_z orbitals on the S atoms and *d*-orbitals on Mo atoms.[74] Because the S atoms are exposed to the environment on either side of an MoS_2 layer, and the orbitals are oriented normal to the plane of the layer, the valence band structure is significantly influenced by interlayer interactions. In contrast, the conduction band structure derives from localized *d*-orbitals on Mo atoms, which are sandwiched between sulfur in the S-Mo-S structure and as a result, are relatively protected from interlayer interactions.[74]

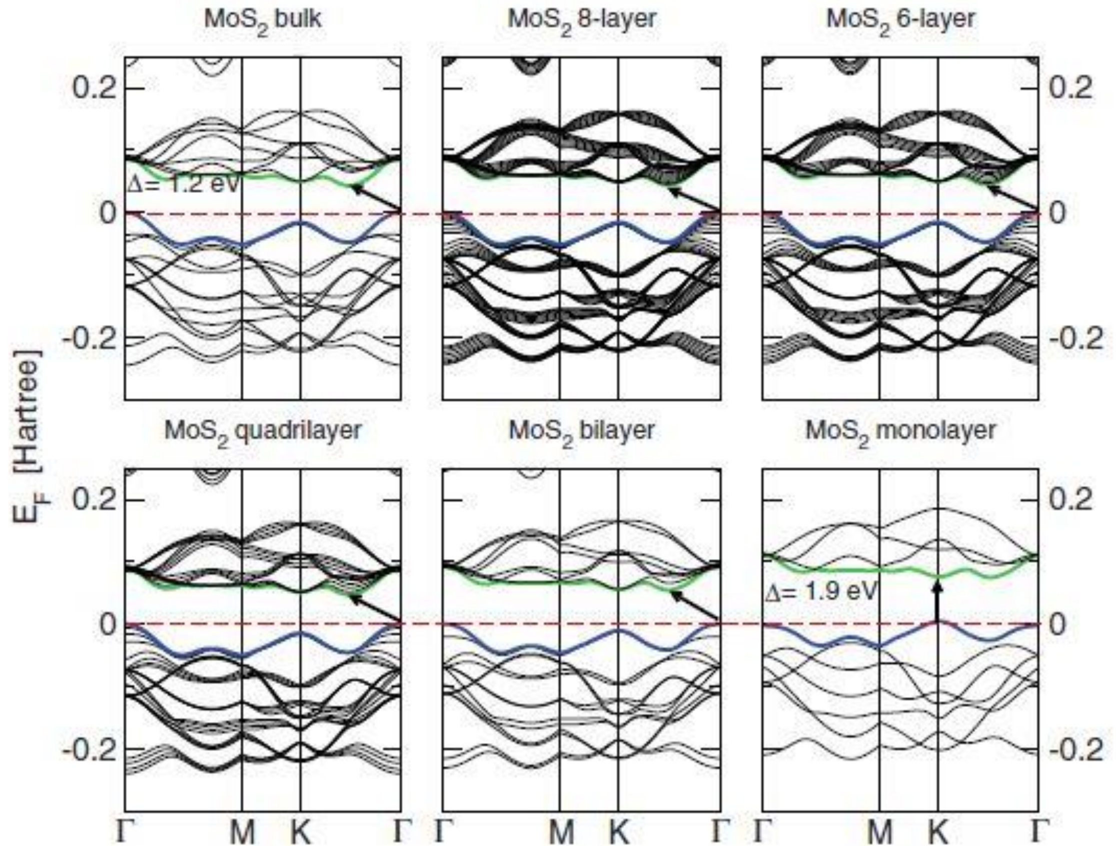

Figure 1.2. Relationship between MoS_2 thickness and band structure. Bulk MoS_2 has an indirect band gap of 1.2 eV. However, as the thickness decreases, the valence band maximum transitions from the Γ-point to the K-point, resulting in a direct 1.9 eV band gap in monolayer MoS_2. Reprinted figure with permission from A. Kuc, N. Zibouche, and T. Heine, *Physical Review B*, vol. 83, p. 245213. Copyright 2011 by the American Physical Society.[77]

Figure 1.2 shows the change in MoS_2 band structure as the thickness decreases from bulk MoS_2 to monolayer MoS_2.[77] As the thickness of MoS_2 decreases, two main changes occur in the band structure: (1) a shift in the valence band maximum from the Γ-point to the K-point, resulting in a change from an indirect band gap to a direct band gap, and (2) a significant widening of the band gap from 1.2 eV to 1.9 eV.[77, 78] Similar changes in band structure occur for other TMDs. Compared to the valence band, there are

only minor changes in the conduction band of the MoS_2 with thickness, with the conduction band minimum shifting to the K-point.

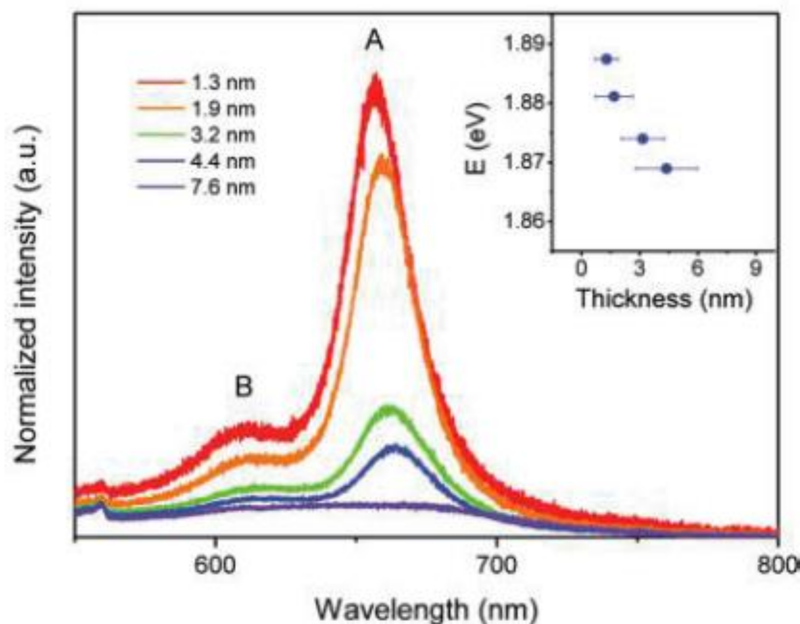

Figure 1.3. Evolution of the MoS_2 PL with thickness. The thinnest samples display a large PL intensity due to a more favorable direct band gap transition. As the thickness increases, the direct band gap transition becomes less favorable and the PL intensity is diminished. Reprinted with permission from G. Eda, H. Yamaguchi, D. Voiry *et al.*, *Nano Letters*, vol. 11, p. 5111. Copyright 2011 American Chemical Society.[79]

The change from a direct to an indirect band gap with increasing MoS_2 thickness can be directly observed through photoluminescence (PL) measurements of the sample. Figure 1.3 shows the evolution of the PL of exfoliated MoS_2 samples with thickness.[79] As shown in the figure, mono- and few-layer MoS_2 samples exhibit much higher PL intensities than thicker samples, with bulk samples displaying essentially no PL signal. This is because the direct band gap transition is the favorable transition for monolayer MoS_2 samples. However, as the band gap transitions to a narrower indirect band gap with

increasing thickness, the direct band gap transition becomes less favorable. As a result, these MoS_2 samples still exhibit photoluminescence, though the intensity is much weaker than in the thinner samples.

The defect structure within a two-dimensional material is important in determining the electrical response of the material. Typical defects that should be considered include point defects from charged impurities and grain boundaries that result from a particular growth method of the material. Each type of defect results in scattering of charge carriers during electronic transport and potentially decreases the mobility of the material.

Density functional theory (DFT) calculations on monolayer MoS_2 explored the formation energies for many common point defects.[80] Of the possible defects considered, S adatoms were found to have the lowest formation energy. In terms of the band structure, S adatoms induce a shallow state near the valence band edge in the MoS_2. Due to the process conditions used to create MoS_2 layers, it is also favorable to form S vacancies in the MoS_2 film. S vacancies have a significant effect on the MoS_2 band structure, resulting in the formation of gap states within the band gap of the MoS_2. Finally, in the case of either sulfur-rich (S-adatoms) or sulfur-deficient (S-vacancies) MoS_2 films, these defects are also expected to dope the MoS_2 film, resulting in p-type and n-type behavior, respectively. These theoretical predictions suggest that understanding the defect structure of MoS_2 films will be necessary to understand and characterize the electrical behavior of the material.

Atomic resolution scanning transmission electron microscopy (STEM) has been used to characterize the intrinsic defects in synthetic MoS_2 films.[81] A number of different

point defects were observed, including various types of sulfur vacancies (mono-, di- and tri-), vacancy complexes involving both molybdenum and sulfur, and antisite defects in which Mo is substituted by S or Mo replaces S. The most common point defect observed was the monosulfur vacancy, consistent with the prediction that monosulfur vacancies have the lowest formation energy of the observed defects. As an explanation for the vacancy complexes, it is observed that the presence of a molybdenum vacancy results in a destabilization of the surrounding sulfur atoms. As a result, molybdenum vacancies appear to preferentially evolve into the vacancy complexes observed. The authors also note the observation of both Mo and S adatoms on the synthetic MoS_2 surface.

The atomic resolution STEM imaging also provides a wealth of information about dislocations and grain boundaries in the MoS_2 film. As with graphene, dislocations consisting of 5/7 member rings are present in MoS_2, but Zhou *et al*.[81] also confirmed the presence of 4/4, 4/6, 4/8, and 6/8 member rings in the dislocation and grain structure of the MoS_2, which had each been previously predicted to exist based on first principles calculations.[82] In addition, the authors explored a 60° grain boundary in the MoS_2 sample, finding that this particular grain boundary exhibits metallic behavior rather than the semiconducting behavior expected for the MoS_2 film. As a result, it is important to understand the relationship between synthesis conditions and defect structure in TMDs in order to effectively design high-performance electronics.

1.5 Synthesis Techniques for Thin-Film TMDs

While exfoliation produces high-quality TMD samples, the resulting flakes are at best only several micrometers in size and obtaining a high degree of control over the thickness of flakes is difficult. In addition, exfoliation is not suitable for large-scale

manufacturing. As a result, exfoliation does not represent a suitable production method for TMDs and alternative methods of synthesis must be developed. An early approach to the creation of thickness-controlled samples was the reaction of transition metal films with chalcogens at high temperature.[2, 83-90] However, these techniques typically produce films too thick for a number of electronic or optical applications. Thinner films produced by this method have documented issues with thickness nonuniformity.[90]

Chemical vapor deposition (CVD) represents a potential solution to these problems in which films of large grain size can be produced on the few-layer scale. In CVD growth methods, two precursors, one containing a transition metal and the other containing a chalcogen, are simultaneously flowed through a tube furnace containing the growth substrate. The two precursors react in the vapor phase to form the TMD, which nucleates on the substrate to begin growth of a TMD flake. Additional TMD molecules approaching the surface either continue the growth of an existing flake or initiate the growth of a new flake. Extended growth times can cause the film to coalesce and result in wafer-scale coverage. As a result of the kinetics of the CVD growth process, factors such as grain size, thickness, and uniformity can in principle be tuned by changing the process parameters, such as temperature, pressure, and ratio of transition metal to chalcogen flows.

A number of studies have explored the CVD growth of TMD thin films. Within these studies, there are a few widely used options for the transition metal source: (1) a metal hexacarbonyl precursor with the general formula $M(CO)_6$, such as molybdenum hexacarbonyl ($Mo(CO)_6$)[91] or tungsten hexacarbonyl ($W(CO)_6$)[92], (2) a transition metal oxide, such as MoO_3[93-100] or WO_3,[1] or (3) a transition metal chloride, such as $MoCl_5$ or

WCl_6.[101] A variety of chalcogen precursors have been investigated, including chalcogen vapor and dimethyl[92] or diethyl[91, 101] chalcogenides.

A drawback of CVD growth processes is that there is a nonzero probability of nucleation of additional TMD layers on the surface of a growing TMD grain. In these processes, additional TMD layers tend to nucleate as the growth of the film approaches coalescence, which leads to localized thickness nonuniformities in the TMD film. Because the electronic and optical properties of few-layer TMDs are highly sensitive to the number of layers of the TMD, this thickness nonuniformity causes significant localized variations in the behavior of CVD-grown samples. One potential solution is limiting the growth rate of the TMD film such that the growth time can be used to reliably control the sample thickness. Recent work on MoS_2 has suggested that stopping the film growth at a time very near complete coalescence of the MoS_2 film results in wafer-scale monolayer MoS_2.[91] By choosing a growth time that is a multiple of the monolayer growth time, controlled thickness multilayer films can be grown at the wafer scale. However, the growth times associated with this process are approximately 24 hours per layer of TMD desired, presenting a significant obstacle to high throughput synthesis of TMDs.

Another method for growing high-quality TMDs is molecular beam epitaxy (MBE).[102-109] In particular, the extremely clean environment within an MBE chamber creates the opportunity to grow some of TMDs whose growth is limited by thermodynamic constraints, including the transition metal tellurides.[104] Typically, this MBE growth uses a hexagonal substrate, such as graphite, MoS_2, or hBN. The chalcogen

source is usually thermally evaporated from a Knudsen cell, while e-beam evaporation is common to provide the transition metal.

MBE growth of 2D materials has several advantages. First, epitaxial growth of TMDs is not restricted by a lattice constant mismatch. Instead, MBE growth of TMDs results in a material with a lattice constant identical to that of an isolated film of the TMD.[102] Second, TMD heterostructures can be grown within a single system, opening an avenue toward the creation of complex heterostructures with extremely clean interfaces. Finally, TMDs can be grown on one another without a significant misorientation between the layers.[102] As a result, MBE growth of TMDs is an interesting technique for continuing to explore the unique properties of these materials.

A final method for TMD film deposition is physical vapor deposition (PVD) sputtering. A recent paper studied the synthesis of thin-film, controlled thickness MoS_2 by radio frequency (RF) sputtering from an MoS_2 target on SiO_2/Si substrates.[110] Following sputtering of the film, the quality of the film is improved through annealing at high temperature (700 °C) in a sulfur and argon containing environment. The measured field-effect mobility of the material is 29 $cm^2 V^{-1} s^{-1}$ for bilayer MoS_2, and up to ~180 $cm^2 V^{-1} s^{-1}$ for thicker films, both of which are significantly higher than most reported mobilities for synthetic MoS_2. After the high temperature annealing step, the authors observe the formation of an $MoSiO_s$ layer, which potentially provides dielectric screening and improves the performance of the material.

One of the important implications of a PVD sputtering process to create high-quality TMDs is the ease of integration into an industrial environment. Because sputtering is already widely used for thin film deposition in industry, PVD sputtering

represents an ideal process for TMD deposition in the back end of a CMOS process. The only drawback to the proposed process is the high temperature annealing step, which alters the thermal budget of the CMOS process. However, optimization of TMD deposition may result in higher quality films before annealing and reduce or eliminate the need for this step.

One of the drawbacks of many current methods for TMD synthesis is the high temperature required to drive the reaction. In an attempt to decrease synthesis temperatures, one study explored plasma-enhanced synthesis in which an e-beam evaporated Mo film was exposed to a direct H_2S plasma.[111] This process resulted in formation of slightly substoichiometric MoS_2 at temperatures of both 150 °C and 300 °C. However, the grain size of the MoS_2, measured using transmission electron microscopy (TEM), was on the order of 5-7 nm and the mobility of the MoS_2 was lower than has been measured for higher temperature CVD grown films. The authors of the study attributed the poor electrical performance to physical sputtering during the plasma processing since the MoS_2 film is exposed to the energetic Ar ions used to sustain the plasma. Therefore, while this study demonstrates the promise of plasma-based to lower synthesis temperatures for TMDs, it also suggests that a remote plasma may present a better option for low-temperature synthesis to create high-quality films.

Despite significant progress in the growth of TMD films over the last few years, several criteria must be met in order for TMDs to be compatible with industrial processes. Primarily, a process is needed that produces large-area films of TMDs with a high level of control over the film thickness and the film uniformity. Second, the growth time must be compatible with the high throughput requirements of semiconductor

manufacturing. Third, the defect concentration in the synthetic films must be controllable and must be small enough such that it does not result in significant intrinsic doping of the film, does not cause scattering of charge carriers that negatively affects the mobility, and does not create large shifts in the threshold voltage of devices due to charge trapping. Fourth, the ideal synthesis process requires temperatures much lower than is possible for the currently explored methods. Finally, the grain size of the resulting films must be large enough that scattering at grain boundaries does not significantly affect electrical transport in the films. The ability to satisfy each of these requirements will result in a synthesis process for TMDs that can be incorporated in a large-scale manufacturing process.

1.6 Nature of the Metal-TMD Interface

An important consideration in the design of TMD-based devices is the metal-TMD interface. Several studies explored the effect of contact metal choice on the carrier injection into MoS_2 transistors, with some conflicting reports on the nature of each contact metal. An early study suggested that most metals for an interface free of chemical bonding, with the measured Schottky barrier suggesting that there is no Fermi level pinning at the interface.[112] More recently, however, Das *et al*. compared the Schottky barrier heights of the metal-MoS_2 junction using Sc, Ti, Ni, and Pt.[113] Based on the theoretical band alignment for these materials, Sc and Ti are expected to provide efficient electron injection into the MoS_2 conduction band, while Ni and Pt are expected to provide hole injection into the MoS_2 valence band. However, the experimental results show only n-type behavior (electron injection) for all of the measured metals, potentially as a result of Fermi level pinning which alters the expected band alignment for these contacts. Further experimental work on Au-MoS_2 contacts suggests that the Schottky

barrier height of the Au contact is much smaller than expected due to Fermi level pinning in the top half of the MoS_2 bandgap.[114] In contrast to these results, the potential for both n- and p-type transport in multilayer MoS_2 flakes has been demonstrated through the combination of Au and Pd contacts.[28] Interestingly, the main difference between the two reports is the use of a thin Cr (Nb) adhesion layer for the Au (Pd) contacts which prevents the Fermi level pinning observed in the previous report.

A large number of electronics applications for TMDs require good control over the Fermi level in the material. Therefore, understanding the mechanisms that give rise to effects such as Fermi level pinning or interface state formation is crucial to designing TMD-based devices. Several recent studies have sought to explain the mechanisms which cause Fermi level pinning in these devices. DFT calculations suggest that even in the absence of covalent bonding between the MoS_2 and a metal layer, interactions between the *d*-orbitals in the metal layer and the Mo *d*-orbitals result in the formation of an interfacial density of states.[115] Further theoretical calculations including many electron effects have successfully captured the experimentally measured dependence of the Schottky barrier height on the metal contact.[116]

The deposition method has also been shown to influence the nature of the TMD-metal interface. For example, the nature of the metal-MoS_2 interface potentially changes drastically depending on the deposition pressure.[117] For some metals, such as Sc, Cr, and Ir, metal deposition on MoS_2 results in the formation of metal sulfide species at the interface. In addition, deposition at higher pressures can result in partial oxidation of the contacts. Due to the sensitivity of thin-film TMDs to interfaces, these reaction byproducts formed during deposition potentially alter the electronic nature of the film.

A final consideration with regard to contacts is the role that defects in the MoS_2 play in determining the nature of the MoS_2 contact. It has been suggested that a potential source of the Fermi level pinning which has been observed experimentally is the presence of chalcogen vacancies in the TMD layer.[118, 119] As discussed previously, chalcogen vacancies result in a gap state near the conduction band edge of TMDs. When a metal contact is formed with the TMD, the gap state formed by the chalcogen vacancies can cause the Fermi level to be pinned close to the conduction band of the TMD. For example, DFT calculations predict that the Fermi level for a Au-MoS_2 contact will be near the middle of the MoS_2 band gap.[115] However, experimental measurements of the Schottky barrier height suggest that the Fermi level is close to the conduction band of the MoS_2,[114] suggesting that the gap states formed by sulfur vacancies in the MoS_2 are the dominant factor in determining the Schottky barrier height of the contact.

1.7 Applications of 2D Vertical Heterostructures

One interesting application of 2D materials is the creation of 2D vertical heterostructures. Because 2D materials exist as conductors (graphene), insulators (hexagon boron nitride, hBN), and semiconductors (TMDs), it is possible to create entire functional devices out of only 2D materials. In a 2013 review paper, Geim and Grigorieva suggested the idea that the assembly of these heterostructures is similar to the assembly of a structure using Lego blocks, in which the chosen two-dimension blocks can be assembled in an arbitrary order.[120]

A common structure considered for 2D vertical heterostructures is shown in Figure 1.4. The active region of these devices consists of a pair of 2D material electrodes separated by an interlayer barrier, such as hBN, a high-κ dielectric, or the van der Waals

(vdW) gap. Under appropriate bias conditions, charge carriers can tunnel between the top and bottom 2D layers, resulting in current flow between the source and drain terminals. Band alignment within the structure is controlled by a combination of the drain-source voltage bias (V_{DS}) and the top and bottom gate biases (V_{TG} and V_{BG}, respectively). The drain-source voltage determines the offset in energy space between the Fermi level of the top layer and the Fermi level of the bottom layer, while the gate voltages tune the carrier concentration in each layer, changing the Fermi level in each layer relative to the conduction and valence bands of that layer.

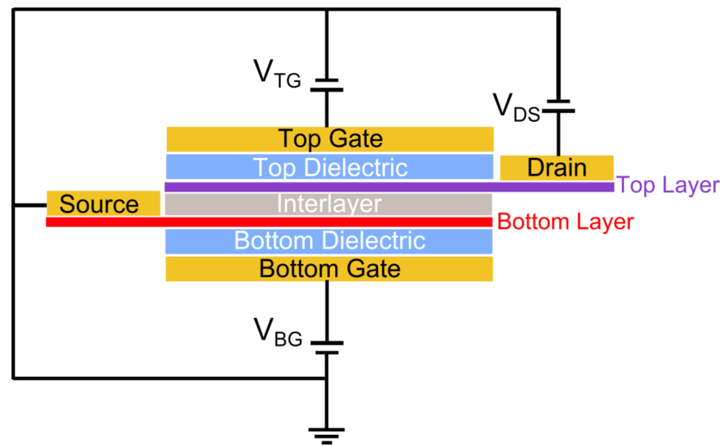

Figure 1.4. Schematic of a 2D vertical heterostructure transistor. Reprinted from P. M. Campbell, A. Tarasov, C. A. Joiner, W. J. Ready, and E. M. Vogel, *Journal of Applied Physics*, vol. 119, p. 024503, 2016, with the permission of AIP Publishing.[121]

2D vertical heterostructures for electronic applications are typically designed around two tunneling transitions in the structure – like-band tunneling (i.e., conduction-to-conduction band or valence-to-valence band) and opposite-band tunneling (i.e., conduction-to-valence band tunneling). Like-band tunneling has been explored for the symmetric field-effect transistor (symFET)[122-125], while opposite-band tunneling has been explored for the tunnel field-effect transistor (TFET)[126, 127] and the Esaki diode.[128-132]

1.7.1 The Symmetric Field-Effect Transistor (symFET)

The symFET consists of two identical (symmetric) 2D materials separated by an insulating tunnel barrier. The probability of tunneling depends on the difference in the momenta of the starting and ending states of a charge carrier. In high-quality devices with a small number of scattering centers, the current in the device is dominated by the probability of tunneling due to necessity for momentum conservation. Due to the symmetric nature of the symFET, the top and bottom electrodes share identical dispersion relations. Therefore, the tunneling probability is maximized when the band structures of the top and bottom electrodes are completely aligned.

Typical operation of the symFET involves sweeping the source-drain voltage bias to change the band alignment of the top and bottom electrodes. As the band structures become closely aligned, a sharp increase in the current occurs due to the increased tunneling probability. As the source-drain voltage bias increases past the point of complete band alignment, the current decreases due to the misalignment of the electrode band structures, resulting in a region of negative differential resistance (NDR) in the device.

Because of the symmetric nature of the 2D electrodes, it is necessary to design the symFET to induce an initial offset between the 2D electrodes. There are two main methods for creating a band offset between the top and bottom layers. The first option is through doping of the TMD layers so that equilibration of the Fermi levels throughout the device results in an offset of the band structures at zero bias voltage. The second option is by unevenly biasing the top and bottom gates to induce different carrier concentrations in

the top and bottom layers, resulting in a band offset between the two electrodes with zero source-drain bias.

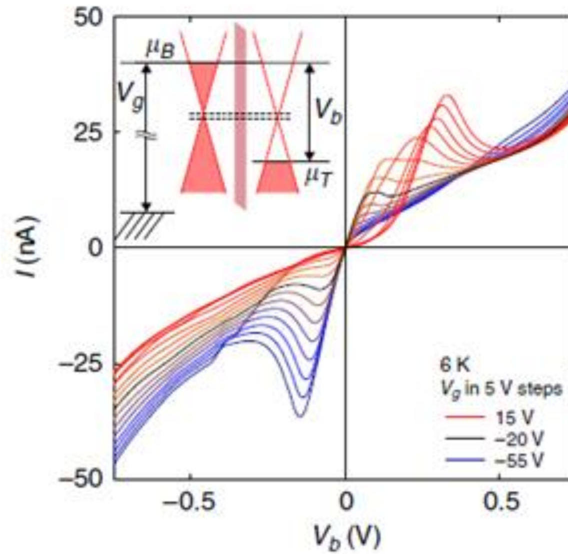

Figure 1.5. Demonstration of negative differential resistance at low temperature in graphene-based symFETs. Reprinted with permission from L. Britnell, R. V. Gorbachev, A.K. Geim, L. A. Ponomarenko, A. Mischenko *et al.*, *Nature Communications,* vol. 4, p. 1794. Copyright 2013 by Macmillan Publishers Ltd.[133]

A great deal of theoretical[122-124] and experimental[133-135] work has been devoted to the study of graphene-insulator-graphene (GIG) symFETs. In particular, Britnell *et al*. experimentally demonstrated the presence of NDR in a graphene-hBN-graphene symFET, as shown in Figure 1.5.[133] The device consisted of exfoliated materials, with the bottom layer graphene placed on a thick hBN substrate to isolate the bottom graphene from the SiO_2 substrate. The use of an hBN underlayer has been shown to screen the active area of the device from charge puddles in the SiO_2, resulting in a lower potential fluctuation and increases the probably of coherent tunneling in the device.[136] Electrical measurements taken at liquid helium temperature demonstrated the presence of NDR,

with a peak-to-valley ratio (PVR) of up to 4. Further, the NDR peak is present in room temperature measurements as well, suggesting that the behavior is due to resonant tunneling behavior rather than a defect-mediated interaction or density of states effects, which would display a temperature-dependent characteristic. Earlier work using an identical device structure failed to demonstrate resonant tunneling,[135] indicating the importance of high-quality materials in creating resonant tunneling devices. Importantly, the authors note that devices were carefully chosen to be free from transfer residues that would interfere with device behavior. Despite these precautions, while multiple devices demonstrated resonant tunneling, the current-voltage characteristics of the devices showed significant device-to-device variation. Related experimental work incorporating CVD graphene and hBN on an SiO_2 substrate showed direct tunneling through the hBN barrier but did not demonstrate NDR.[134] The differences in these experiments emphasize the importance of material quality, interface quality, and substrate-device interactions in determining the performance of tunneling devices.

Several studies have theoretically explored tunneling in the graphene-hBN-graphene system,[122, 125, 133] with the results providing a close match to the experimental results of Britnell *et al.* For the graphene system, the NDR peak occurs at the voltage where the Dirac points of the two graphene electrodes are energetically aligned, resulting in complete alignment of the graphene band structures. At this voltage, every point in energy space has an identical momentum value, resulting in a maximum in the probability of tunneling based on the requirement for momentum conservation. A key parameter which describes the tunneling in the symFET is the coherence length, which represents the lateral decay constant for electron tunneling in the device. As the

coherence length increases, the PVR of the device is predicted to increase, while small coherence lengths result in either small PVRs or the lack of an NDR peak.

Understanding of the coherence length is critical to interpretation of the presence or lack of NDR in symFETs. Contaminants, including polymer residues from the transfer process and material defects, cause increased scattering during carrier transport, resulting in a smaller coherence length and decreasing the likelihood of observing NDR in the device. In addition, potential fluctuations of the substrate also decrease the coherence length, resulting in smaller coherence lengths on SiO_2 than hBN. Therefore, by using an hBN underlayer and measuring devices without transfer residues, Britnell *et al*. were able to maximize the chances of observing NDR.

1.7.2 Conduction-to-Valence Band Tunneling

Two types of behavior are possible related to conduction-to-valence band tunneling: steep-slope operation and Esaki diode behavior. Due to the step-like nature of the 2D density of states in TMDs, steep-slope operation in TMD-based heterostructures has the potential to surpass the 60 mV/decade limit on MOSFETs. The interlayer tunnel field-effect transistor (ITFET) is a device designed to facilitate steep-slope operation at small gate voltages.

Choice of a set of TMDs for the ITFET depends on the band offset between the conduction band of one electrode and the valence band of the other electrode. In order to achieve a small turn-on voltage, a typical approach is to choose two different materials for the electrodes in which this band offset is minimized, referred to as near-broken band gap alignment. During operation of the ITFET, the overlap between the conduction and valence bands of the 2D material electrodes is determined by the applied gate bias. With

a small gate bias, there is no overlap between the conduction and valence bands and tunneling is restricted, as shown in Figure 1.6 (a). As the gate bias increases, an overlap develops between the conduction and valence bands (Figure 1.6 (b)), at which point a sharp increase in the tunneling current occurs. Continued increases in the bias voltage increase the overlap between the conduction and valence bands. However, because tunneling is confined within a limited energy range due to the requirement for momentum conservation, the current no longer increases after a critical overlap is reached and the device enters the saturation region. For ideal TMDs, the band structure is step-like, resulting in an infinite slope in the subthreshold region. However, non-idealities, such as defects or potential fluctuations, result in a spreading of the band edges and a finite subthreshold slope.

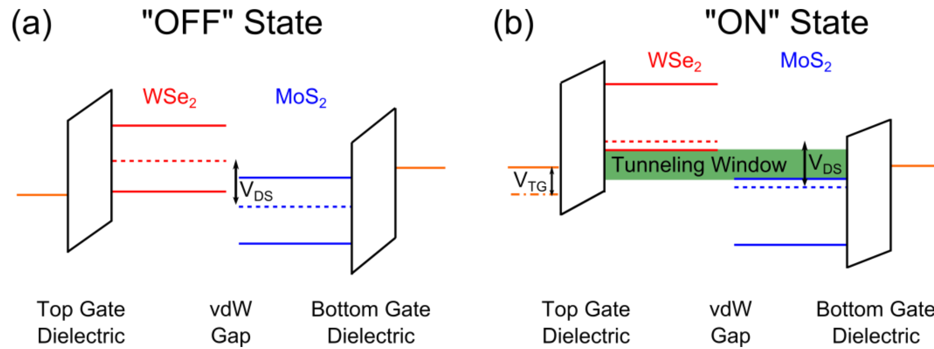

Figure 1.6. Band alignment of the ITFET in the (a) OFF state and (b) ON state.

A number of theoretical studies have explored steep-slope behavior in 2D vertical heterostructures, including the MoS_2/WTe_2[126, 137] system and the $WSe_2/SnSe_2$ system.[127] These studies confirmed the potential for steep-slope operation in 2D material systems, but also suggest that the behavior will be strongly dependent on material quality.

Importantly, Li *et al*. examined the relationship between the width of band tail states caused by potential fluctuations and the subthreshold swing in ITFET devices, finding that a band tail width of approximately 40 meV represents the point at which the subthreshold swing of an ITFET becomes greater than 60 mV/decade.[126]

The second possibility for conduction-to-valence band tunneling is Esaki diode behavior, first demonstrated by Esaki, Chang, and Tsu.[128] Operation of the Esaki diode requires a broken band alignment, in which there is a slight overlap between the conduction band of one electrode and the valence band of the other electrode with zero applied bias. As the source-drain bias voltage increases, a small energy range is created over which tunneling can occur, resulting in a corresponding increase in the current. However, as the bias voltage continues to increase, the energetic overlap between the conduction band of one electrode and the valence band of the other electrode decreases. This decrease in the energetic overlap results in a decrease in the energy range over which charge carriers are able to tunnel and the tunneling current decreases, creating a region of NDR in these devices. After a region of NDR, further increases in the source-drain bias voltage result in an increase in the tunneling current.

It is important to note that both Esaki diode behavior and symFET behavior can result in similar NDR characteristics in TMD-based heterostructures. However, the phenomena which result in the presence of NDR in both types of devices are distinct. Importantly, Esaki diode behavior results only from density of states effects and does not require momentum conservation. In contrast, NDR resulting from resonant tunneling in the symFET requires high quality materials and minimal scattering. In addition, the development of defect bands due to material impurities in TMDs can also create NDR

peaks in TMD-based heterostructures. Therefore, it is important to completely understand band alignment within TMD-based heterostructures in order to correctly classify the tunneling behavior of these devices.

1.7.3 TMD-based Vertical Heterostructures using Exfoliated Material

A number of recent experiments have explored the behavior of TMD-based vertical heterostructures using exfoliated materials. For example, Roy *et al*. explored the behavior of MoS_2/WSe_2 devices using exfoliated materials in a gated structure.[132] This work demonstrated three modes of operation within the MoS_2/WSe_2 structure: (1) Esaki diode behavior with an NDR peak at low temperatures, (2) a backward diode which has large tunneling current, and (3) a forward rectification diode. Because of the ability to control the carrier concentration in each layer independently using the gate voltages, all three modes of operation are possible within a single device.

A second recent experiment explored the behavior of $WSe_2/SnSe_2$ devices.[131] Black phosphorous (BP) was first exfoliated onto an SiO_2/Si substrate, followed by transfer of mechanically exfoliated $SnSe_2$ on top of the BP to create the vertical heterostructure. Ti/Au contacts were evaporated to electrically probe each layer, and the SiO_2/Si substrate provided a way to modulate the behavior of the device using a back-gate. I-V measurements of several of the BP/$SnSe_2$ heterostructures display two interesting characteristics: (1) a large reverse bias current, and (2) NDR in the forward bias current characteristic. Interestingly, the NDR peak in these devices persists at room temperature, as is expected from an Esaki diode behavior which arises due to density of states effects. However, there is still a clear dependence of both the peak current and peak

position on temperature, some of which the authors attribute to changes in the nature of the metal contacts with temperature.

Finally, steep-slope behavior has been demonstrated in a device using a combination of 2D and 3D materials.[138] The active area of the device consists of a vertical heterostructure created by transferring CVD MoS_2 onto p-type Ge substrates, with the vdW gap serving as a tunnel barrier between the two materials. A gate is included on top of the MoS_2 layer to alter the band alignment between the MoS_2 and the Ge substrate. Below the threshold voltage, the band alignment restricts tunneling because the valence band of the Ge aligns with the band gap of the MoS_2. Above the threshold voltage, the valence band of the Ge overlaps with the conduction band of the MoS_2, resulting in band-to-band tunneling (BTBT) between the Ge and MoS_2. For this device, the reported average subthreshold swing (SS) over 4 decades of current is 31.1 mV/decade, demonstrating the potential for 2D materials to continue scaling beyond the 60 mV/decade limit of CMOS devices.

1.7.4 Direct Growth of TMD-based Heterostructures

Direct growth of TMD-based heterostructures is an important step in the development of high-quality, high-performance tunneling devices. As demonstrated for the graphene symFET, contaminants from exfoliation and transfer processes increase scattering in devices and can weaken or eliminate both steep-slope behavior and NDR in these devices.[139, 140] In addition, rotational alignment of the individual layers within a heterostructure also has a significant impact on performance. While a recent study demonstrated the ability to obtain a high degree of rotational alignment when transferring

material,[141] it is not widely applicable due to the polycrystalline nature of many large-area TMD samples.

A variety of approaches have been used for the direct growth of van der Waals heterostructures. Previous studies explored methods for the growth of both vertical and lateral heterostructures of TMDs. For example, Lin *et al.* demonstrated growth of vertical MoS_2/WSe_2 stacks using a sequential CVD growth process on epitaxial graphene on SiC substrates.[142] While this process only results in small flakes of the heterostructure, the growth method resulted in rotational alignment within 1.9°, demonstrating that direct growth of heterostructures is one potential way to achieve high degrees of rotational alignment. Interestingly, conductive AFM measurements on the MoS_2/WSe_2 heterostructure reveal the presence of an NDR peak at room temperature.

Recently, CVD growth has also been used to grow vertical heterostructures of p-type and n-type MoS_2.[143] In this process, an initial layer of n-type MoS_2 was grown at 700 °C using MoO_3 and S. Following the first growth, p-type MoS_2 was grown at 600 °C, resulting in an incomplete reaction between the precursors. The remaining oxygen in the film results in p-type doping of the material. The two different layers of MoS_2 exhibit different emission wavelengths. By transferring the MoS_2 heterostructure to a *p*-GaN, a device with white light emission was created.

An alternative method for the growth of vertical heterostructures is the chalcogenization of a stack of different metals. Choudhary *et al.* grew a MoS_2/WS_2 heterostructure by first sputtering films of Mo and W and then exposing to sulfur at high temperature.[144] TEM imaging reveals horizontal growth of the TMD layers, with a clean interface between the MoS_2 and WS_2. However, the heterostructure consists of some

regions which have good rotational alignment and other regions which are not rotationally aligned. Electrical measurements on the MoS_2/WS_2 heterostructure exhibit the rectification behavior of a diode, while measurements on a single layer of either MoS_2 or WS_2 show a linear current characteristic.

For some applications, such as in-plane *p-n* junctions, lateral growth of heterostructures is preferred to the vertical growth discussed above. Chen *et al*. demonstrated lateral epitaxy of WSe_2/WS_2 heterojunctions on SiO_2 through the use of a modified CVD process.[145] Electrical measurements on the lateral heterojunctions demonstrated gate-tunable rectification behavior indicative of the formation of a *p-n* junction.

Similar lateral heterojunctions have also been demonstrated through the use of patterned transition metal films on SiO_2.[146] Alternating lines of Mo and W were sputtered onto an SiO_2 substrate which was subsequently exposed to high temperature chalcogen sources to result in MoS_2/WS_2 and $MoSe_2/WSe_2$ lateral heterojunctions. Two terminal devices were constructed with electrodes perpendicular or parallel to the line direction to explore the electrical properties of the heterojunctions. With the electrodes perpendicular to the line direction, the current-voltage characteristic is purely resistive because the TMD lines form parallel current paths. However, when the electrodes are parallel to the line direction, current must travel across the *p-n* junctions formed between the TMD heterojunctions, resulting in diode behavior.

CHAPTER 2

THEORETICAL MODEL FOR 2D VERTICAL HETEROSTRUCTURES

A theoretical model was developed to understand the factors that influence tunneling in 2D vertical heterostructures. Specifically, this model captures not only the ideal behavior of 2D materials, but incorporates the behavior of defects within the structure in order to investigate the minimum quality of TMD necessary for enabling the unique applications possible with 2D materials. This chapter describes the basis for the theoretical model, including a method for determining the band alignment between 2D materials within the structure, a description of the tunneling current between ideal 2D materials, and an extension of the model to include common defects in TMDs.

2.1 Determination of Band Alignment[a]

The general schematic of the 2D vertical heterostructure for theoretical exploration is given in Figure 1.4. As discussed in Chapter 1, operation of the device relies upon tunneling between the top and bottom electrodes, composed of 2D materials, through a thin insulator. A voltage (V_{DS}) is applied to the top electrode relative to the bottom and determines the offset between the Fermi levels in the top and bottom

---

[a] Reprinted from P. M. Campbell, A. Tarasov, C. A. Joiner, W. J. Ready, and E. M. Vogel, *ACS Nano*, vol.9, p. 5000-5008. Copyright 2015 American Chemical Society.

electrodes. The top and bottom gates, V_{TG} and V_{BG} , are used to adjust the carrier concentrations in the layers.

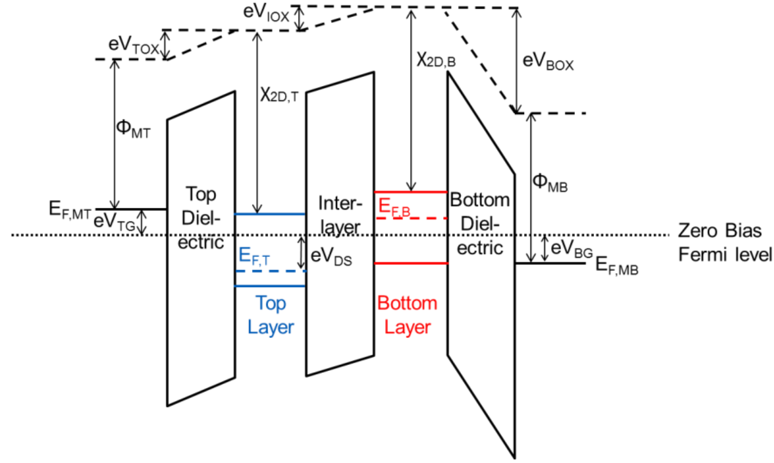

Figure 2.1. Band diagram of the symFET structure. V_{TG} and V_{BG} represent the biases applied to the top and bottom gates, respectively. V_{DS} is the applied source-drain voltage. V_{TOX} , V_{BOX} , and V_{IOX} are the voltages across the top, bottom, and interlayer dielectrics, respectively. $E_{F,T(B)}$ represents the Fermi level in the top (bottom) electrode, $\chi_{2D,T(B)}$ is the electron affinity of the top (bottom) layer, $E_{G,B}$ is the band gap of the bottom layer and $\Phi_{M,T(B)}$ is the work function of the top (bottom) gate metal. The dashed line represents the vacuum level and the dotted line represents the Fermi level of the structure at zero bias.

In order to evaluate the tunneling current in a vertical heterostructure under a given set of bias conditions, the first step is to determine the band alignment throughout the heterostructure. Essentially, the vertical heterostructure behaves like a set of three coupled capacitors, composed of (1) the top gate and top 2D electrode, separated by the top gate dielectric, (2) the top and bottom 2D electrodes, separated by the interlayer dielectric, and (3) the bottom 2D electrode and the bottom gate, separated by the bottom gate oxide. The band alignment within the structure is determined by simultaneously solving this set of coupled capacitors for charge balance. A model to relate the dielectric

voltages and the carrier concentration in the electrodes can be developed based on the band diagram (see Figure 2.1).[126] While the band diagram shown in Figure 2.1 depicts TMDs as the top and bottom electrodes, a similar band diagram can be drawn for graphene-based devices. Based on Gauss' Law, the carrier concentration in the 2D sheets and the oxide voltages are related by

$$C_{TOX}V_{TOX} - C_{IOX}V_{IOX} = -e\left(p_{top} - n_{top} + N_D\right) \tag{2.1}$$

$$C_{IOX}V_{IOX} + C_{BOX}V_{BOX} = -e\left(p_{bot} - n_{bot} - N_A\right) \tag{2.2}$$

where C_{IOX}, C_{BOX} and C_{TOX} are the capacitances for the interlayer, the bottom gate dielectric, and the top gate dielectric, respectively. $p_{top(bot)}$ and $n_{top(bot)}$ represent the concentrations of holes and electrons in the top(bottom) layer, while N_D is the donor concentration in the top layer and N_A is the acceptor concentration in the bottom layer.

Based on the band diagram, the following relationships can be developed relating the voltage drops across the dielectric and the band alignment

$$eV_{TOX} = eV_{TG} + \chi_{2D,T} + e\phi_{n,T} - eV_{DS} - \Phi_{M,T} \tag{2.3}$$

$$eV_{BOX} = eV_{BG} + \chi_{2D,B} + E_{G,B} - e\phi_{p,B} - \Phi_{M,B} \tag{2.4}$$

$$eV_{IOX} = eV_{DS} + E_{G,B} + \chi_{2D,B} - e\phi_{p,B} - e\phi_{n,T} - \chi_{2D,T} \tag{2.5}$$

where $\chi_{2D,T(B)}$ is the electron affinity of the top (bottom) layer, $E_{G,B}$ is the band gap of the bottom layer and $\Phi_{M,T(B)}$ is the work function of the top (bottom) gate metal. For the case of a TMD layer,

$$e\phi_{n,T} = E_{CT} - E_{FT} \tag{2.6}$$

$$e\phi_{p,B} = E_{FB} - E_{VB} \tag{2.7}$$

and the carrier densities are expressed as

$$n(p)=\frac{g_v m_c^*(m_v^*)k_B T}{\pi\hbar^2}\ln\left[\exp\left(-\frac{q\phi_{n(p)}}{k_B T}\right)+1\right] \tag{2.8}$$

where g_v is the valley degeneracy and $m_{c(v)}^*$ is the effect mass of electrons (holes).

For the case of graphene,

$$e\phi_{n,T}=E_{Dirac}-E_{FT} \tag{2.9}$$

$$e\phi_{p,B}=E_{FB}-E_{Dirac} \tag{2.10}$$

and the carrier density is

$$n=\frac{g_v g_s}{2\pi\hbar^2 v_f^2}\int_{E_{Dirac}}^{\infty}\frac{E-E_{Dirac}}{1+\exp\left(\frac{E-E_F}{k_B T}\right)}dE \tag{2.11}$$

which is evaluated using

$$n(p)=\frac{g_v g_s (k_B T)^2}{2\pi\hbar^2 v_f^2}F_1(\eta(-\eta)) \tag{2.12}$$

where $\eta=\frac{-e\phi_n}{k_B T}$ and the Fermi integral can be evaluated using[147]

$$F_1(\eta)\approx\left(\frac{8}{\left[2.41+\eta+\left(|\eta-2.41|^{2.29}+11.73\right)^{0.437}\right]^2}+\exp(-\eta)\right)^{-1} \tag{2.13}$$

Using this set of equations, which can be generally applied to the case of any set of two 2D electrodes, the band alignment within the vertical heterostructure can be determined.

2.2 Calculation of Tunneling Current[b]

Once the band alignment of the structure is determined, the tunneling current can be calculated based on the charge carrier concentration and momentum as a function of energy within the materials. One simple and common approach to modeling tunneling in 2D vertical heterostructures uses the Bardeen transfer Hamiltonian,[123, 126, 148-151] where the current is expressed by

$$I = g_v g_s \frac{2\pi e}{\hbar} \sum_{B,T} |M|^2 (f_B - f_T) \partial(E_B - E_T) \tag{2.14}$$

where g_s and g_v are the spin and valley degeneracies, respectively. The summation is taken over all wave-vectors in the bottom and top layers. $|M|$is the matrix element which is related to the overall probability of tunneling between the bottom and top electrodes. $(f_B - f_T)$ is the difference in the Fermi functions between the bottom and top layers, and $\partial(E_B - E_T)$ restricts the model to elastic tunneling. However, most previous studies describe the tunneling current in momentum space, which makes direct relation of the results to the band structure of the materials somewhat non-intuitive. In order to facilitate easy description of the observed results in terms of band structures of the 2D electrodes, this work transforms the momentum-space description of the tunneling current into energy-space.

Equation 2.14, given in momentum space, is converted to energy space as follows.

---

[b] Reprinted from P. M. Campbell, A. Tarasov, C. A. Joiner, W. J. Ready, and E. M. Vogel, *ACS Nano*, vol.9, p. 5000-5008. Copyright 2015 American Chemical Society.

$$I_{tot} = g_v g_s \frac{2\pi e}{\hbar} \int_{\overrightarrow{k_B}} \int_{\overrightarrow{k_T}} \frac{A_{tot}}{(2\pi)^2} d^2\overrightarrow{k_B} \frac{A_{tot}}{(2\pi)^2} d^2\overrightarrow{k_T} |M|^2 (f_B - f_T) \partial(E_B - E_T) \tag{2.15}$$

$$J_{tot} = g_v g_s \frac{e}{(2\pi)^3 \hbar} \int_{\overrightarrow{k_B}} \int_{\overrightarrow{k_T}} d^2\overrightarrow{k_B} d^2\overrightarrow{k_T} A_{tot} |M|^2 (f_B - f_T) \partial(E_B - E_T) \tag{2.16}$$

with $k_{B(T)}$ representing the wave-vector in the bottom (top) layer.

The matrix element is

$$|M|^2 A_{tot} = |M_{B0}|^2 T_t(E) S_F(\vec{q}) \tag{2.17}$$

$$S_F(|\vec{q}|) = \frac{L_C^2}{\left[1 + \left(\frac{|\vec{q} + \vec{Q}|}{q_C}\right)^2\right]^n} \tag{2.18}$$

$$\vec{q} = \overrightarrow{k_B} - \overrightarrow{k_T} \tag{2.19}$$

where $\vec{q}$ is the difference in wave-vector of the top and bottom states, $\vec{Q}$ describes the additional difference when the top and bottom electrodes are misaligned by a small angle (ω), d is the interlayer thickness, κ is a decay factor, and L_C is the structural coherence length. To include the effects of both direct tunneling and Fowler-Nordheim tunneling, the transverse transmission coefficient ($T_t(E)$) is calculated using the WKB approximation, a technique shown to produce accurate results for ultra-thin oxides,[152] according to the equation

$$T_t(E) = \exp\left[\frac{-2}{\hbar} \int \sqrt{2m_i(E_{ci}(x) - E)} dx\right] \tag{2.20}$$

where $\hbar$ is the reduced Planck's constant, m_i is the effective mass within the dielectric, and $(E_{ci}(x) - E)$ represents the difference in energy between the tunneling carrier and the conduction band edge of the interlayer.

Isotropic bands are assumed so that the momenta in the bottom and top layers can be written in polar coordinates as,

$$\overrightarrow{k_B} = (k_B, \theta_B) \quad \overrightarrow{k_T} = (k_T, \theta_T) \tag{2.21}$$

For no rotational misalignment,

$$\left|\vec{q} + \vec{Q}\right|^2 = \left|\vec{q}\right|^2 = \left|k_T\right|^2 + \left|k_B\right|^2 - 2\left|k_B\right|\left|k_T\right|\cos(\theta) \tag{2.22}$$

where

$$\theta = \theta_B - \theta_T \tag{2.23}$$

is the angular difference between the wave vectors. If the two electrodes are misaligned by a small angle (ω),

$$\left|\vec{q} + \vec{Q}\right| = \left(\left|k_T\right|\sin\theta + \frac{4\pi}{3a_{0,T}}\sin\omega\right)^2 + \left(\frac{4\pi}{3a_{0,T}}\cos\omega - \frac{4\pi}{3a_{0,B}} + \left|k_T\right|\cos\theta - \left|k_B\right|\right)^2 \tag{2.24}$$

After substitution and writing the integrals over wave-vectors as an integral over energy, the current density is given by

$$J_{tot} = \frac{e\left|M_{B0}\right|^2}{\hbar}\int_E g_B(E)g_T(E)e^{-2\kappa d}(f_B - f_T)T(E)dE \tag{2.25}$$

where $T(E) = T_t(E)S_F(\vec{q})$. This form is equivalent to another recently published[35] and is useful for describing tunneling in terms of band diagrams. A particular advantage of this energy-space formulation is that it allows a more intuitive exploration of the mechanisms that give rise to the drastic differences in behavior between graphene symFETs and TMD symFETs, as will be discussed in detail in Chapter 3.

It is important to note the limitations of the Bardeen transfer Hamiltonian model described above. In particular, this model does not account for the non-equilibrium

current distribution which can arise for large currents. An alternative approach is the use of the Wigner transport equation with properly assigned boundary conditions to avoid the creation of unphysical solutions.[153]

As another consideration, this model only considers purely vertical transport between the 2D material electrodes and does not include any effects of lateral transport within the electrodes. It is possible that the presence of large numbers of defects within the 2D materials degrades lateral transport in the devices to a point where the transfer characteristic of the device is dominated by lateral transport effects rather than vertical transport.

Despite these limitations, however, the goal of this study is to understand what factors determine the nature of tunneling within this device and how the vertical transport in the device can be tuned based on material properties. The simpler nature of the Bardeen transfer Hamiltonian lends itself to simpler interpretation of the trends the results are showing. While the model may not completely replicate all aspects of device behavior, it is expected to predict trends that occur based on factors such as material quality and band structure in order to provide insight into promising areas for experimental research.

2.3 Effect of Non-Idealities

Up to this point, only the qualities of ideal materials have been considered in the theoretical model for tunneling. In order to more accurately predict the behavior of realistic devices, some of the common non-idealities of 2D materials should also be incorporated into the model. In particular, the effects of band tail states resulting from both potential fluctuations and defects are considered. In addition, the creation of defect

energy bands within the band gap of the 2D materials can significantly alter device performance.

2.3.1 Formation of Band Tail States

Two types of band tail states are considered within the theoretical model: (1) extended states, and (2) localized states. Extended states form as the result of potential fluctuations within the substrate, resulting in slight shifts in the position of the band structure in energy space. As a result, the step-like density of states of the TMDs become spread out, resulting in the formation of an exponential tail, as shown in Figure 2.2

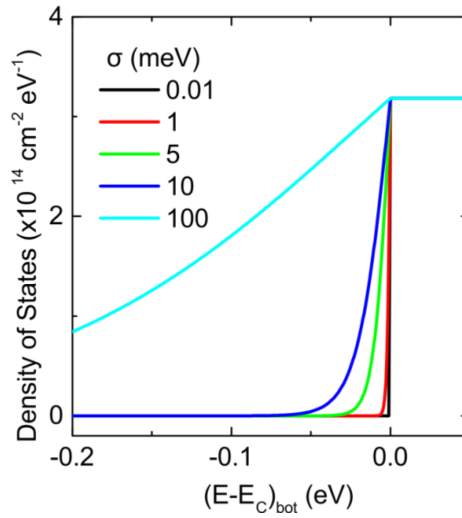

Figure 2.2. Density of states created by band tails in TMDs.

Extended states are modeled similarly to the method used by Li *et al.*[126] The effect of the band tail states is expressed by an energy broadening spectrum S_E, and expressed by

$$S_E(E_T - E_B) = \int_{-\infty}^{\infty} dE P_{vT}[E - E_T] P_{vB}[E - E_B] \tag{2.26}$$

where P_{vT} and P_{vB} represent the potential distribution functions in the top and bottom layers, respectively. In this case, the current density is expressed as

$$J_{tot} = \frac{e|M_{B0}|^2}{\hbar} \int_{E_B} \int_{E_T} g_B(E_B) g_T(E_T)(f_B - f_T) T(E_B, E_T) S_E(E_B - E_T) \, dE_B dE_T \quad (2.27)$$

rather than the form used in Equation 2.25. Importantly, the inclusion of extended states requires integration over both the energy of the top layer and the energy of the bottom layer, rather than the single condensed integral used previously. Interestingly, extended states essentially represent a probability of inelastic tunneling. For this work, $S_E(E)$ is represented by a normalized Gaussian function with a characteristic width, σ. The Gaussian function for $S_E(E)$ results from the assumption of a Gaussian potential distribution, which is the form derived previously for randomly distributed impurities.[154] Under the assumption that the potential distribution functions of the top and bottom layers are identical, $S_E(E)$ is expressed by

$$S_E(E_T - E_B) = \frac{1}{\sqrt{\pi}(2\sigma^2)} \exp\left[-\left(\frac{E_T - E_B}{\sigma}\right)^2\right] \quad (2.28)$$

Band tail states resulting from localized defects within the material are treated as trap states which lack momentum. Two models are used in this work to simulate the effect of localized band tail states. The first assigns a value of $S_F = 2\pi L_C^2$ to states within the band tails, resulting in a current-voltage contribution that scales with the coherence length. While this approach is not completely correct, it is computationally simple and allows for a general comparison of the effects of different band tail widths on the tunneling current. In order to break the link between the response of the band tail states and the coherence length, $S_F(E)$ is replaced with the capture cross section, σ. At a given temperature, the capture cross section is expressed as

$$\sigma(T) = \sigma_\infty e^{-\frac{E_B}{kT}} \tag{2.29}$$

where σ_∞ is a constant and E_B is the activation energy of the trap state.

2.3.2 Formation of Defect Energy Bands

As discussed in Chapter 1, the presence of point defects can result in significant changes in the electronic structure of TMDs. In particular, chalcogen vacancies tend to introduce additional densities of states within the band gap of the material. Proper treatment of defect energy bands requires two changes to the calculations used for ideal materials: (1) the charge balance equations must be updated to include the occupancy of defect energy states, and (2) the contribution of defect energy bands to the tunneling current must be calculated.

Depending on whether each defect energy level behaves as a donor or acceptor, each defect level either contributes positive or negative charge to the charge balance equations. In this case, Equations 2.1 and 2.2 are modified to

$$C_{TOX}V_{TOX} - C_{IOX}V_{IOX} = -e\left(p_{top} + P_{defect,top} - n_{top} - N_{defect,top} + N_D\right) \tag{2.30}$$

$$C_{IOX}V_{IOX} + C_{BOX}V_{BOX} = -e\left(p_{bot} + P_{defect,bot} - n_{bot} - N_{defect,bot} - N_A\right) \tag{2.31}$$

To determine the values of N_{defect} and P_{defect}, a binomial approximation of the Gauss-Fermi integral was used.[155] The electron density of states for acceptor-type defects (N_{defect}) is represented by

$$N_{defect} = \frac{N_0}{\sigma\sqrt{2\pi}} G(\zeta, s) \tag{2.32}$$

where N_0 represents the defect density and σ represents the width of the defect energy level. For donor-type defects, $P_{defect} = 1 - N_{defect}$. $G(\zeta, s)$ is given by

$$G(\zeta, s) =$$

$$\sigma\sqrt{\frac{\pi}{2}}\lim_{N\to\infty}\sum_{i=0}^{N}F_i(-1)\left[e^{-\frac{(1+i)\left(2\zeta+s^2(1+i)\right)}{2}}Erfc\left(\frac{s^2(i+1)-\zeta}{s\sqrt{2}}\right)+e^{-\frac{i\left(2\zeta+s^2 i\right)}{2}}Erfc\left(\frac{s^2 i+\zeta}{s\sqrt{2}}\right)\right] \tag{2.33}$$

where $\zeta = (\varepsilon_0 - \varepsilon_F)/kT$ and $s = \sigma/kT$. ε_0 is the energy level of the defect and ε_F is the Fermi level.

Similar to the case for localized band tail states, the capture cross section of the trap replaces $S_F(E)$ for the purposes of calculating the current. Individual defect densities of states are represented using a Gaussian shape. The defect is characterized by the peak density of states, the energy level of the defect state, and the energetic width of the defect level. The contribution to the current density from defects is represented by

$$J_{defect} = \frac{e|M_{B0}|^2}{\hbar}\int_E g_{2D}(E)n_{defects}(E)(f_B - f_T)\sigma(T)dE \tag{2.34}$$

where $n_{defects}$ represents the defect density of states and g_{2D} represents the density of states for the 2D material electrode involved in tunneling. Finally, the total current density is calculated as

$$J_{total} = J_{ideal} + J_{defect} \tag{2.35}$$

CHAPTER 3

RESONANT TUNNELING IN SYMMETRIC VERTICAL HETEROSTRUCTURES

This chapter focuses on the application of the theoretical model described in Chapter 2 to understand some of the unique applications of 2D vertical heterostructures. The first section consists of a discussion of the potential for NDR in TMD-based symFETs and compares the performance of TMD symFETs to graphene based symFETs. The second section compares TMD symFETs to previously explored III-V-based resonant tunneling diodes, specifically comparing the effect of quantized subbands and tunnel barrier height on the performance of resonant tunneling devices.

3.1 Enhanced Resonant Tunneling in the symFET[c]

Since the 1970s, resonant tunneling transistors have attracted significant attention for their potential in a variety of applications including low multi-valued logic, high frequency radar and communication systems, analog-to-digital conversion and signal processing.[156] Devices such as the Esaki diode,[128-130] the resonant tunneling diode (RTD),[157-161] and the resonant tunneling transistor (RTT)[162-164] have all been proposed. The defining property of these devices is NDR in the current-voltage (*I*-*V*) characteristics. The presence of NDR creates a peak in the *I*-*V* characteristics that is defined by the ratio

---

[c] Reprinted from P. M. Campbell, A. Tarasov, C. A. Joiner, W. J. Ready, and E. M. Vogel, *ACS Nano*, vol.9, p. 5000-5008. Copyright 2015 American Chemical Society.

between the peak current and the current beyond the NDR region (valley current), known as the peak-to-valley ratio (PVR). However, despite intensive research efforts exploring a range of material systems, including Si/SiGe[159, 160] and III-V quantum well systems,[157, 161] the PVR has been limited. A limited PVR degrades the performance of digital, high frequency and power systems with integrated resonant devices.[156, 165, 166]

The valley current in conventional 3D semiconductor resonant devices has three primary mechanisms. First, 3D semiconductor quantum wells have multiple longitudinal sub-bands due to quantization.[167] Each sub-band produces a distinct NDR peak and the overlapping contributions to the current from each sub-band increases the valley current. Furthermore, the transverse dispersion relations for the sub-bands are typically not identical.[167, 168] Therefore, at voltages above the primary resonance, the non-zero transverse momentum states of the sub-bands are more strongly coupled, increasing the number of tunneling channels that contribute to the current.[167, 169] Second, the need for lattice matching during epitaxy limits the range of barrier materials and achievable band offset of the barrier. The lower band offset can result in thermionic emission which contributes to the valley current.[169, 170] Optimized AlGaN based resonant devices with larger band offset barriers improve the valley current.[169] However, valley current in AlGaN is still limited by transport associated with higher sub-bands. Finally, the resonant states are effectively broadened due to a variety of possible scattering mechanisms. This broadening increases with energy so that the contribution of valley current due to higher sub-bands is enhanced.[168, 169, 171]

Vertical heterostructures consisting of two-dimensional materials such as graphene, hexagonal boron nitride (hBN) and transition metal dichalcogenides (TMDs)

have a variety of properties which can potentially overcome some of the limitations of epitaxial 3D semiconductor heterostructures for resonant tunneling devices. 2D materials do not have additional longitudinal sub-bands that can contribute to valley current. Also, the van der Waals bonding between 2D materials in vertical heterostructures allows for a wider range of materials. For example, hBN with a large bandgap can be used for the tunneling barrier, limiting valley current associated with thermionic emission. Beyond the potential for improved performance, devices fabricated with 2D materials can be transferred to arbitrary substrates permitting direct integration with other technologies such as in the back-end of a CMOS process.[11, 12] Finally, the peak current of resonant devices depends exponentially on the barrier thickness, and the peak voltage depends on the quantization associated with nanometer thickness of the quantum wells. While molecular beam epitaxy of 3D semiconductors has matured to improve thickness control and uniformity, obtaining reproducible device characteristics still remains a challenge.[172] The lack of covalent bonding between layers of 2D materials can potentially lead to monolayer thickness control and improved reproducibility.

Figure 3.1 compares the tunneling behavior of symFETs using graphene (a), MoS_2 (b) and $MoTe_2$ (c) as the top and bottom layers, with two layers (0.6 nm) of hBN as the interlayer tunneling barrier. In each case, we consider equivalent top and bottom gate dielectrics with a capacitance of 3 μF/cm^2, and the top gate voltage is fixed at -1.5 V for each of the sweeps. Because there is a difference in the values of V_{TG} and V_{BG}, the carrier concentrations in the top and bottom layers are unequal. Therefore, at $V_{DS} = 0$ V, there is an offset between the band edges in the two electrodes, which we refer to as the zero bias offset.

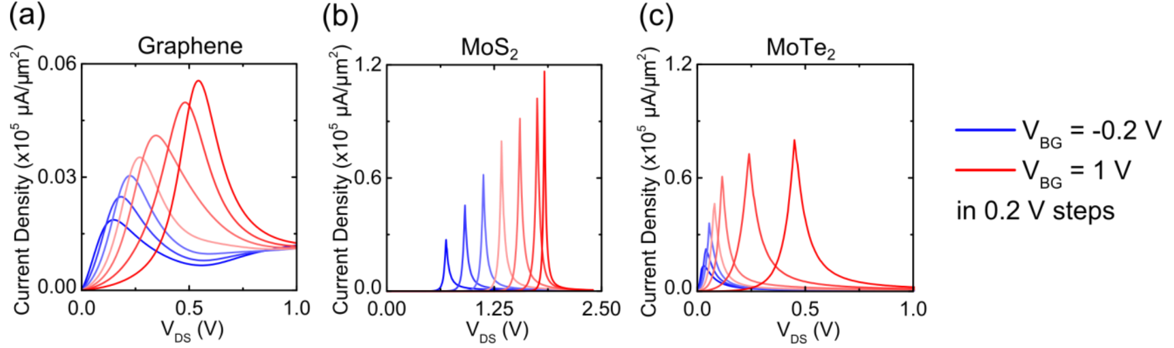

Figure 3.1. Simulated J-V_{DS} characteristics for (a) graphene, (b) MoS_2, and (c) $MoTe_2$ symFETs. There is no doping in either layer of the devices. Each curve represents a different back-gate voltage, ranging from -0.2 V to 1 V in 0.2 V steps. The top gate remains fixed at -1.5 V. The top and back gates are 40 layers of hBN, with a capacitance of 3 μF/cm^2. The interlayer consists of two layers of hBN (0.6 nm), with a capacitance of 6.2 μF/cm^2. We assume $|M_{B0}| = 0.01\,\text{eV}, \kappa = 3.8\text{x}10^7\,\text{cm}^{-1}$, n = 1.5, and $q_C^{-1} \approx 10\,\text{nm}$.

For all three materials, the NDR peak shifts to higher V_{DS} values as the bottom gate voltage increases, depending on the zero bias offset between the top and bottom layers. In TMD symFETs where the top and bottom electrodes have carrier concentrations of opposite sign, the Fermi level in one layer will be near the conduction band, and the Fermi level in the other will be near the valence band. The size of the band gap will therefore affect the magnitude of the zero bias offset and a higher V_{DS} is required to reach the NDR peak. Because MoS_2 has a larger bandgap, the MoS_2 NDR peak occurs at a higher V_{DS} than in $MoTe_2$ (1.8 eV for MoS_2 versus 0.9 eV for $MoTe_2$). For graphene, the density of states available for tunneling is smaller than for MoS_2 and $MoTe_2$, causing a lower magnitude of current in the graphene device. There is a lower density of states in $MoTe_2$ and consequently, a lower current density than in MoS_2.

To examine the effect of the bandgap on the NDR response of TMD symFETs, simulations were performed for $ZrSe_2$ and $HfSe_2$. To ensure equivalent electrostatic conditions for each material, the work functions of the top and bottom gates were

adjusted for each material to ensure the same offset between the gate work functions and the conduction band of the material. Figure 3.2 shows the results of these simulations.

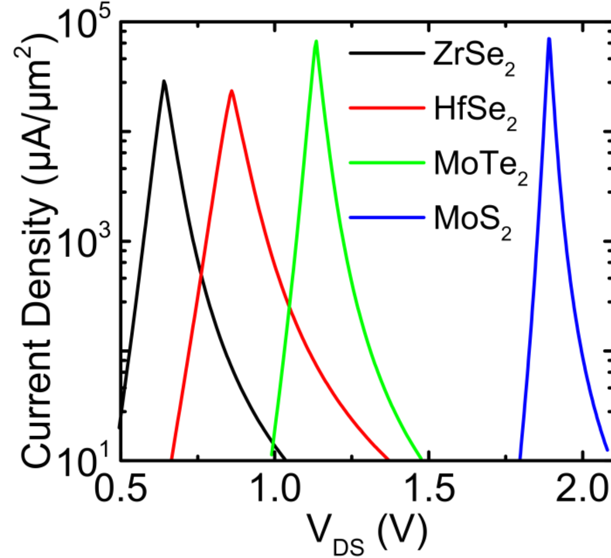

Figure 3.2. Simulated *J-V* characteristics of $ZrSe_2$, $HfSe_2$, $MoTe_2$, and MoS_2. Simulations were performed with $V_{TG} = -1.5$ V and $V_{BG} = 1.5$ V and $C_{TOX} = C_{BOX} = 3$ μF/cm^2. The work functions of the top and back gates were adjusted for each material so that the difference between the gate work function and the conduction or valence band was equivalent. The interlayer consists of two layers of h-BN (0.6 nm), with a capacitance of 6.2 μF/cm^2. We assume $|M_{B0}| = 0.01$ eV and $\kappa = 3.8\text{x}10^7$ cm^{-1}.

As predicted, decreasing the bandgap of the TMD causes the NDR peak to shift to lower voltages. In these simulations, the gate conditions ensure that the top layer is p-type, while the bottom layer is n-type. As a result, the Fermi level in the top layer is near the valence band, while the Fermi level in the bottom layer is near the conduction band so that the zero bias offset is approximately equal to the value of the bandgap. Consequently, the source-drain bias required to cause alignment of the conduction and valence bands is lower for the materials with a smaller bandgap.

In addition to the bandgap effect, Figure 3.2 shows that the width of the NDR peak depends on the material. Specifically, MoS_2 has the narrowest peak while $HfSe_2$ has the widest peak, due to the difference in the density of states in the materials. The density of states affects how quickly the current decays on the higher bias side of the NDR peak, causing a narrower peak in materials with a larger density of states. In addition, the density of states also affects the magnitude of the current density in symFETs. According to Equation 2.8, the density of states in TMDs depends on the effective mass of charge carriers in the TMD. Therefore, the desired current-voltage response of symFETs can be tailored by choosing materials based on bandgap and effective mass to determine the position and shape of the NDR peak.

Figure 3.3 shows the effect of coherence length on the tunneling current in graphene versus MoS_2 symFETs, with a value of $V_{TG} = -1.5$ V and $V_{BG} = 1.5$ V. Comparing the J - V_{DS} characteristics with varying coherence lengths, it is clear there are two main differences between the two materials. First, for a given coherence length and value of n, there is a much higher PVR in MoS_2 than in graphene. At large coherence lengths, the PVR in MoS_2 approaches 10^9, while the PVR in graphene is limited to a few hundred. The NDR peak in MoS_2 is present at smaller coherence lengths than in graphene, suggesting that MoS_2 symFETs could be scaled to smaller device sizes than graphene symFETs. Second, at small coherence lengths, the voltage at which the peak occurs for graphene shifts significantly, whereas the peak in MoS_2 shifts minimally.

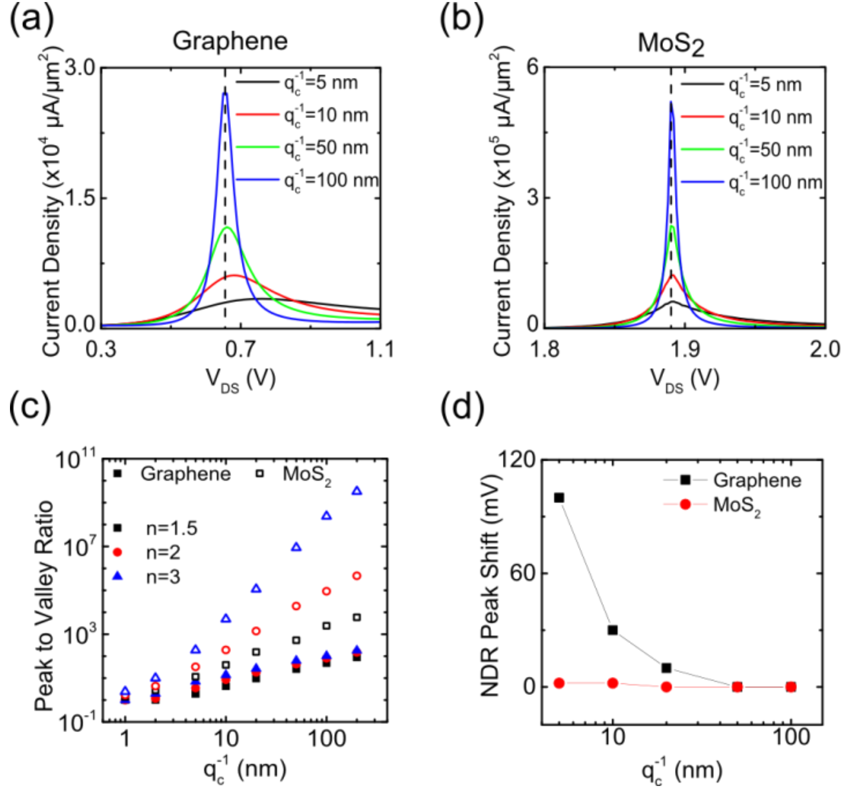

Figure 3.3. (a,b) Tunneling current density in graphene and MoS_2 with varying coherence lengths q_C^{-1}. (c) Comparison of the PVR dependence on coherence length in graphene and MoS_2 symFETs. Valley currents were measured 0.1 – 0.2 V above the NDR peak because the background current increases as a function of V_{DS}. (d) Comparison of the shift in NDR peak position (referenced to 100 nm value) at varying coherence lengths. There is almost no shift for MoS_2, while the graphene peak position has a large shift at small coherence lengths. Simulations were performed with $V_{TG} = -1.5$ V and $V_{BG} = 1.5$ V, with $C_{TOX} = C_{BOX} = 3$ μF/cm^2. The interlayer consists of two layers of hBN (0.6 nm), with a capacitance of 6.2 μF/cm^2. We assume $|M_{B0}| = 0.01\,\text{eV}$ and $\kappa = 3.8\text{x}10^7\,\text{cm}^{-1}$.

To further explain the differences in behavior for TMD symFETs compared to graphene symFETs, we explore how each of the components of the tunneling current changes as a function of source-drain bias. First, we consider the case of graphene. Figure 3.4 (a-c) compares the density of states (dashed lines) and Fermi level difference (solid line) contributions to the graphene tunneling current for source-drain bias conditions less than the peak (a), at the peak (b) and greater than the peak (c). The dark shaded areas in

each graph represent the density of states at each energy that are available for tunneling. As the source-drain bias increases, the dark shaded area in Figure 3.4 (a-c) increases non-linearly, causing the background current to increase non-linearly.

Figure 3.4 (d-f) show the evolution of $S_F(|\vec{q}|)$ with source-drain bias for graphene (black curve). The red shaded area represents the current density at a given E, with the total current density given by the integral of the red shaded area. When the Dirac points in the two electrodes are not aligned, there is a single energy where the magnitude of the wave-vector in the top layer and the magnitude of the wave-vector in the bottom layer are equivalent and a small range of energies where the momentum difference is small enough that there is still a high probability of tunneling. For most values of energy, there is a large wave-vector difference and the probability of tunneling is small. Because tunneling can only occur for a narrow range of energies, the current density is also small. In contrast, at the NDR peak (Figure 3.4 (e)) there is a small difference in the magnitude of the wave-vector and high tunneling probability for all energies. At a given coherence length, as V_{DS} changes, the Dirac points of the two graphene layers move gradually relative to one another and the current increases to a maximum at the NDR peak before decreasing again. The smooth transition for graphene is due to the linearly increasing density of states as a function of energy. As the coherence length decreases, the width of the $S_F(|\vec{q}|)$ function increases. Because the density of states and Fermi function difference are always increasing as a function of source-drain bias and the current density depends on the product of $S_F(|\vec{q}|)$ with these terms, the NDR peak position is a function of coherence length (Figure 3.3 (d)).

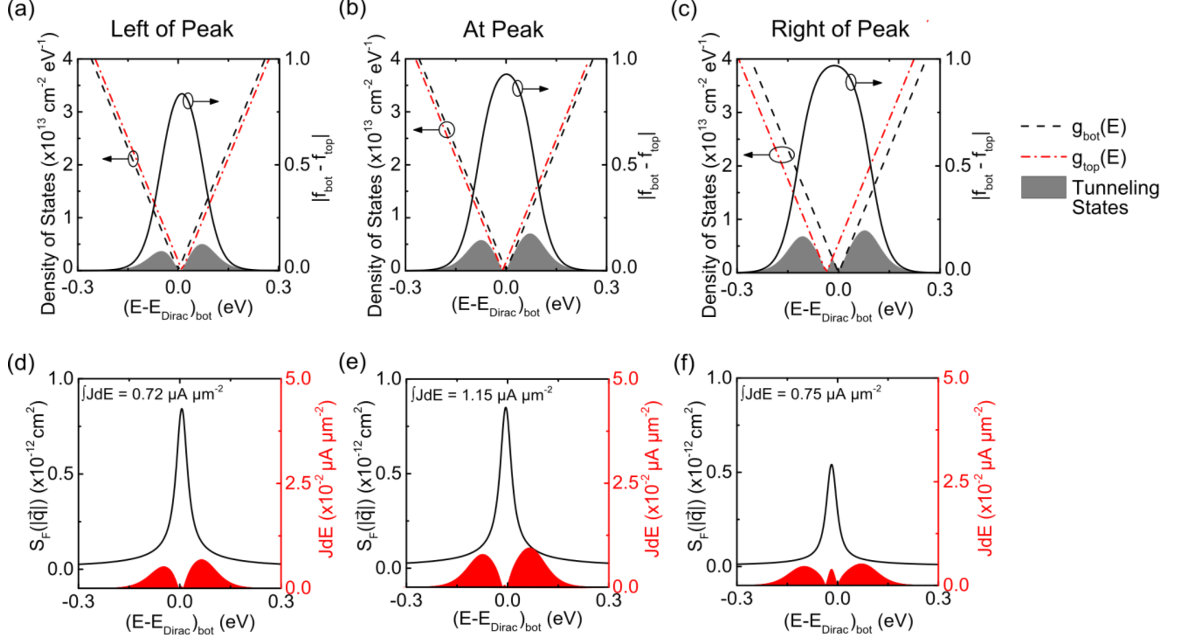

Figure 3.4. Different contributions to the tunneling current in graphene symFETs. (a-c) the density of states of the top (g_{top}) and the bottom layer (g_{bot}), and the Fermi function overlap of both layers $(|f_{bot} - f_{top}|)$ versus the energy, referenced to the bottom layer Dirac point. The dark shaded area shows the portion of states capable of tunneling. (d-f) The spectrum of the scattering potential (solid line, left axis) and the contribution to the current density at each energy (red shaded area, right axis). Simulations were performed with $V_{TG} = -1.5\,\text{V}$ and $V_{BG} = 1.5\,\text{V}$, with $C_{TOX} = C_{BOX} = 3$ μF/cm^2. The interlayer consists of two layers of hBN (0.6 nm), with a capacitance of 6.2 μF/cm^2. We assume $|M_{B0}| = 0.01\,\text{eV}, \kappa = 3.8\text{x}10^7\,\text{cm}^{-1}$, n = 1.5, and $q_C^{-1} \approx 10\,\text{nm}$.

In 2D TMDs such as MoS_2 and $MoTe_2$, the characteristics of the NDR peak are significantly altered by the differences in band structure compared to graphene. The theoretical density of states for TMDs is constant within the valence and conduction bands, with zero states available within the band gap. Because tunneling can only occur at points where both densities of states are nonzero, tunneling is restricted to two energy ranges: one within the conduction band, and the other within the valence band.

To the left of the resonance peak, only a small number of states can tunnel, governed by the tail of the Fermi functions in each layer (solid line in Figure 3.5 (a)). As

the bias voltage increases, the band edges move closer together and more of the Fermi function difference overlaps with the density of states, causing large increases in the tunneling current with small changes in bias voltage. The NDR peak occurs at the V_{DS} where the band edges of the TMD layers are aligned (Figure 3.5 (b)). To the right of the resonance peak, the contribution from the density of states is constant and the current only changes due to the Fermi level (Figure 3.5 (c)). This suppresses the valley current and contributes to the increased PVR observed in TMD symFETs.

Figure 3.5 (d-f) shows $S_F(|\vec{q}|)$ for MoS_2 to MoS_2 tunneling. At source-drain values far from the resonance peak, the tunneling probability is small resulting in low values of valley current. Near the band edge, $S_F(|\vec{q}|)$ decreases due to the $\sqrt{E}$ dependence of the momentum in each layer. Far from the band edge, the change in wave-vector with energy is small so that the difference between the magnitude of the wave-vectors $(|\vec{q}|)$of each layer is constant. When the band edges are offset, the magnitude of the wave-vector near the band edge producing the cutoff varies more quickly than in the other layer, causing a larger difference in momentum between the top and bottom layers. At the resonance peak, the contribution from $S_F(|\vec{q}|)$ enters the peaked region and the decrease in $S_F(|\vec{q}|)$ near the band edge disappears because the band edges are aligned and the momentum difference is a minimum. This results in a steep, narrow peak in the current-voltage characteristic.

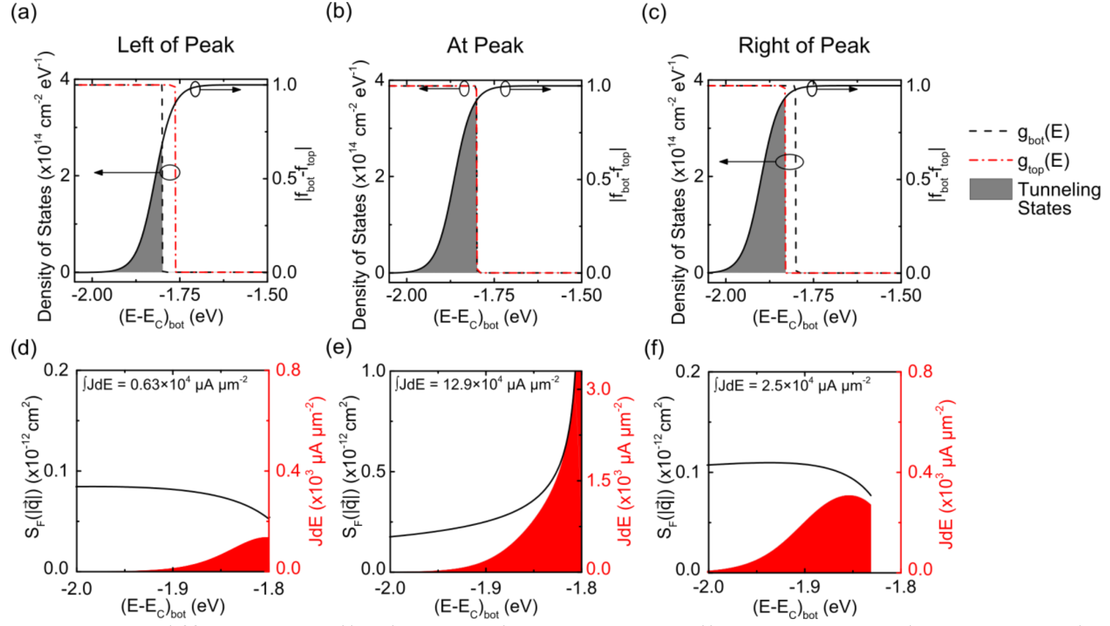

Figure 3.5. Different contributions to the MoS_2 tunneling current at three source-drain bias conditions. (a-c) the density of states of the top $\left(g_{top}\right)$ and the bottom layer $\left(g_{bot}\right)$, and the Fermi function overlap of both electrodes $\left(\left|f_{bot} - f_{top}\right|\right)$ versus the energy referenced to the bottom layer conduction band. The dark shaded area shows the portion of states capable of tunneling. (d-f) The spectrum of the scattering potential (solid line, left axis) and the contribution to the current density at each energy (red shaded area, right axis). Simulations were performed with $V_{TG} = -1.5\,\text{V}$ and $V_{BG} = 1.5\,\text{V}$, with $C_{TOX} = C_{BOX} = 3$ $\mu\text{F/cm}^2$. The interlayer consists of two layers of hBN (0.6 nm), with a capacitance of 6.2 $\mu\text{F/cm}^2$. We assume $\left|M_{B0}\right| = 0.01\,\text{eV}$, $\kappa = 3.8\text{x}10^7\ \text{cm}^{-1}$, $n = 1.5$, and $q_C^{-1} \approx 10\,\text{nm}$.

3.2 Band Structure Effects on Resonant Tunneling[d]

The structure of the symFET is similar to previously explored RTDs with the addition of gates to provide additional control of the electrostatics. Due to the 2D parabolic dispersion relation for TMDs and III-V quantum wells, the densities of states for both types of materials are step-like. In TMDs, there is only a single band edge for

---

[d] Reprinted from P. M. Campbell, A. Tarasov, C. A. Joiner, W. J. Ready, and E. M. Vogel, *Journal of Applied Physics*, vol. 119, p. 024503, 2016, with the permission of AIP Publishing.

both the conduction and valence bands, separated by the band gap. Complete band alignment results in the formation of an NDR peak.

In III-V quantum wells, quantization of energy levels leads to the development of additional subbands at higher energies corresponding to the excited states within the quantum well.[167] When any of these subbands becomes aligned with energetic states in the emitter, a sharp increase in the transmission coefficient occurs, creating an NDR peak. Three possible band alignment conditions leading to the formation of an NDR peak in III-V devices are shown in Figure 3.6. Specifically, the three cases shown arise due to: (1) alignment of the conduction band edge in the top layer with the first excited subband in the bottom layer, denoted as the 2-1 transition; (2) complete alignment of the band structures of the top and bottom layers, denoted as the 1-1 transition; and (3) alignment between the first excited subband in the top layer and the conduction band edge in the bottom layer, denoted as the 1-2 transition. In addition, the subbands typically do not have identical transverse dispersion relations, leading to a stronger coupling of the non-zero transverse momentum states above the primary resonance and increasing the number of tunneling channels.[167, 169] As a result, III-V RTDs are characterized by the presence of several NDR peaks occurring at different bias voltages. However, the overlap of the tails of the NDR peaks and the stronger coupling between higher energy subbands result in an increase in the valley current in RTDs, lowering the achievable PVR in III-V based devices.

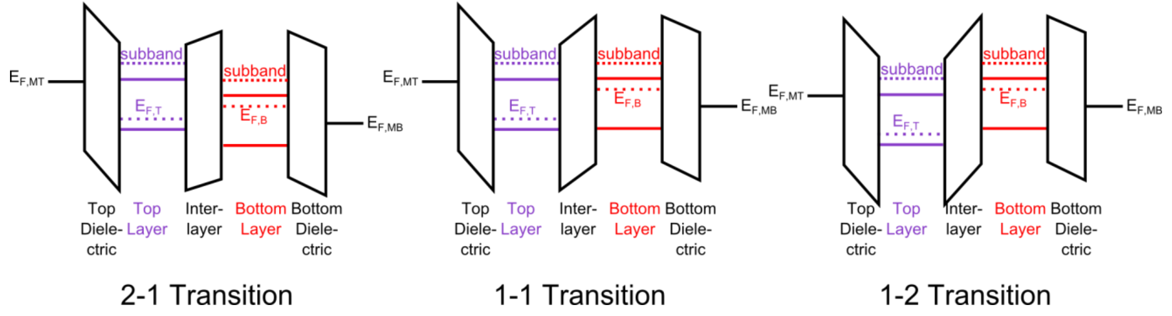

Figure 3.6. Possible band alignments leading to resonant tunneling in III-V devices. Alignment of any pair of subbands results in development of an NDR peak.

The implications of the difference in band structure between 2D materials and III-V materials are shown in Figure 3.7. Figure 3.7 (a) shows the simulated current density versus drain-source bias for an MoS_2 – hBN – MoS_2 symFET. In this device, the interlayer consists of two layers of hBN, while the electrodes are monolayer MoS_2. The top and bottom gate dielectrics consist of four layers of hBN each, resulting in a gate capacitance of 3 μF cm^{-2}. A band gap of 1.8 eV is used for the MoS_2, with a conduction band effective mass of $0.378m_0$. For comparison, Figure 3.7 (b) shows the simulated current density versus drain-source bias voltage for a symFET containing GaAs quantum wells as the electrodes with AlGaAs as the interlayer. For the GaAs device, the top and bottom layers are composed of 10.2 nm GaAs quantum wells, while the barrier is 10.2 nm $Al_{0.3}Ga_{0.7}As$. The band gap used for the GaAs quantum wells is 1.46 eV, with the first excited subband located 0.11 eV above the conduction band edge. An effective mass of $0.063m_0$ is used for both the conduction band and the first excited subband. This device structure matches previously explored GaAs RTDs. In both sets of devices, a work function of 5.2 eV is used for the bottom gate electrode and a work function of 4.17 eV is used for the top gate electrode. Several differences are evident between the tunneling

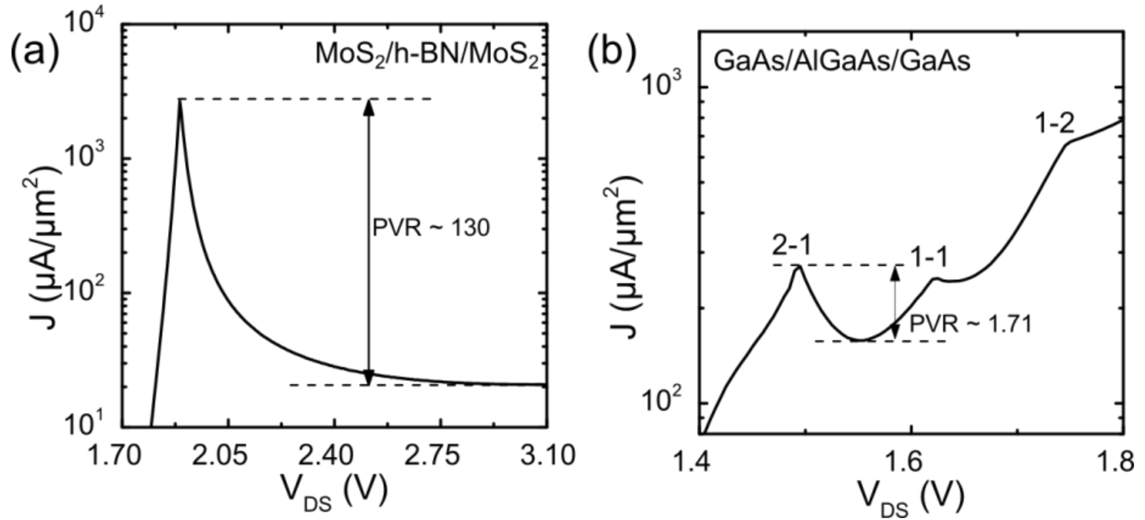

Figure 3.7. Comparison of (a) MoS_2/hBN/MoS_2 and (b) GaAs/AlGaAs/GaAs symFETs. The peaks in the GaAs symFET are labeled in the form *i-j*, where *i* represents the subband involved in transport in the bottom layer and *j* represents the subband involved in transport in the top layer. The MoS_2 symFET has a single NDR peak with a large PVR of 130, while the GaAs symFET exhibits multiple NDR peaks with a maximum PVR of 1.71 for the 2-1 peak.

behavior of the two material systems. The MoS_2 symFET only has a single NDR peak, while the GaAs symFET has three visible peaks. From low to high bias voltages, these peaks are due to the 2-1 transition (bottom excited subband to top conduction band), the 1-1 transition (complete band alignment) and the 1-2 transition (bottom conduction band to top excited subband). Due to the overlap of the tails of these three NDR peaks and the lower barrier height in the GaAs device, the tunneling characteristic of the GaAs symFET shows a much stronger dependence of the valley current on the source-drain bias than the MoS_2 symFET. As a result of these differences, the GaAs symFET has a maximum PVR of less than 2, while the MoS_2 symFET has a PVR greater than 100. To understand the relative impacts of both the presence of subbands and the barrier height on lowering the PVR in III-V devices, each of these factors were investigated independently.

To investigate the effect of subbands on the valley current, the MoS_2 symFET was compared to a symFET using a theoretical MoS_2-like material with a subband 0.1 eV above the conduction band edge. Aside from the presence of the subband, the rest of the electronic structure of the theoretical MoS_2-like material is identical to MoS_2 so that differences in performance are a result of only the subbands. Figure 3.8 shows energy diagrams describing the impact that subbands have on the tunneling characteristics of resonant devices. Figure 3.8 (a) and (b) show the density of states for the top and bottom layers ($g_T(E)$ and $g_B(E)$, depicted as the dashed lines) and the difference in Fermi functions between the top and bottom layers ($|f_B - f_T|$, solid lines) for MoS_2 without and with a subband, respectively. The energy diagrams are shown with a source-drain bias in the valley region located on the higher bias side of the primary NDR peak. In the case of MoS_2 with a subband, this source-drain bias lies between the primary (1-1) and secondary (1-2) NDR peaks. As a result of these bias conditions, there is a slight offset in the band structures of the top and bottom electrodes. For the single-band MoS_2 case (Figure 3.8 (a)), only a single step is present in the density of states, resulting in tunneling that occurs between the conduction band of the top layer and conduction band of the bottom layer. However, for the MoS_2 with a subband (Figure 3.8 (b)), a second step is present in the density of states spaced 0.1 eV above the first step, representing the location of the first excited subband. As a result, there are additional tunneling channels in the material with the subband, which can increase the overall current.

Figure 3.8 (c) shows the current density as a function of energy for MoS_2 with a single band while Figure 3.8 (d) shows the current density for MoS_2 with a subband 0.1 eV above the conduction band. The black shaded area in each part of the figure represents

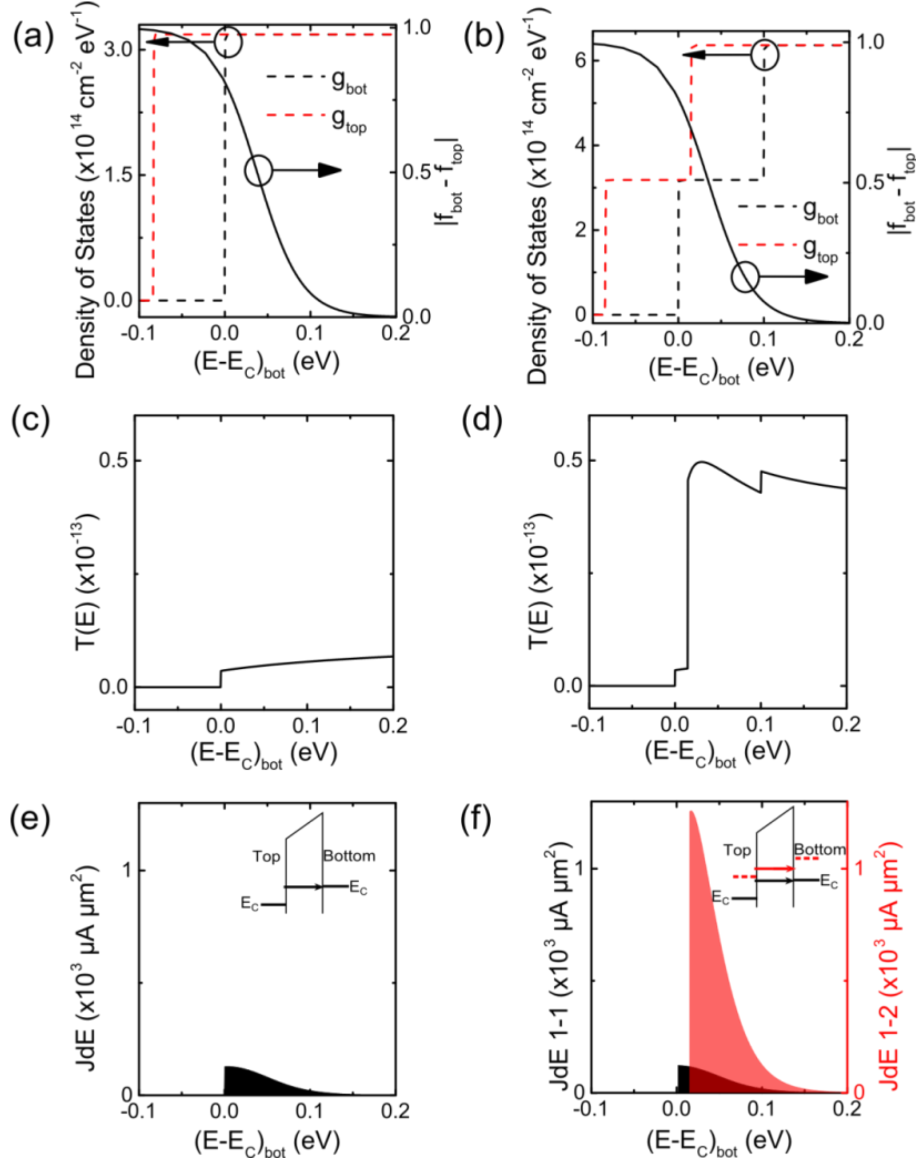

Figure 3.8. (a) Density of states for an MoS_2 system without subbands, characterized by a single step at the conduction band edge. (b) Density of states for a theoretical MoS_2-like system with a subband 0.1 eV above the conduction band edge. (c) Total transmission coefficient (*T(E)*), for an MoS_2 system without subbands. (d) Total transmission coefficient (*T(E)*) for the theoretical MoS_2-like system. (e) Current density as a function of energy for the MoS_2 system (shown by the black shaded area). (f) Current density as a function of energy in the theoretical system with a subband. The black shaded area represents conduction-to-conduction band tunneling and is identical to that of the single band case. The red shaded area represents tunneling from the conduction band in the bottom layer to the subband in the top layer, resulting in additional valley current in the system containing the subband. Simulations were performed with V_{TG} = -1.5 V and V_{BG} = 1.5 V and C_{TOX} = C_{BOX} = 3 μF/cm^2. The interlayer consists of two layers of hBN (0.6 nm), with a capacitance of 6.2 μF/cm^2. We assume $|M_{B0}|$=0.01eV for all transitions, n = 1.5, and $q_c^{-1} \approx 10$ nm for all transitions.

the portion of the current arising from tunneling between the ground states in the conduction band for each material (the 1-1 transition). Because the density of states and the momenta are identical in both cases, the contribution to the current from the energy state at the conduction band edge is identical regardless of the presence of a subband. However, when a subband is present (Figure 3.8 (d)), tunneling between the ground state in one layer and the first excited subband in the other layer (the 1-2 transition) results in an additional contribution to the current, shown as the red shaded area. Under the bias conditions shown, the integral of the current density with respect to energy ($\int JdE$) gives the valley current. Therefore, the presence of subbands in the material results in a higher valley current compared to a material without subbands. Consequently, higher PVRs should be achievable in TMDs compared to III-V materials.

To further investigate the impact of a subband on the tunneling behavior in the device, the position of the subband relative to the conduction band edge in an MoS_2-like material with an added subband was varied and the PVR for each of subband position was calculated. Figure 3.9 (a) shows the conduction band *J-V* characteristic for several subband positions. Because the subband results in a second NDR peak of similar shape to the primary peak, the contribution to the current drops off quickly within a narrow voltage range around the secondary peak. Increasing the spacing between the subband and the conduction band edge increases the voltage required to align the subband in the top layer with the conduction band edge in the bottom layer, causing the secondary NDR peak to move to the right. Because the current is only strongly affected by the subbands

in a narrow voltage range around the secondary NDR peak, the shift in the secondary NDR peak follows the profile of the primary NDR peak.

Figure 3.9 (b) shows the PVR for each of the simulated subband positions, with the dashed line indicating the PVR in the absence of subbands (the PVR in the case of perfect MoS_2). The PVR was calculated as the maximum value of the current for the primary NDR peak divided by the minimum value of the current in the valley between the primary peak and the secondary peak caused by the subband. For small spacing between the conduction band edge and the subband, the additional NDR peaks created due to the subbands occur at a voltage close to the primary NDR peak. As a result, the valley current is significantly increased by the subband NDR peak and the PVR is reduced. As the spacing between the subband and the conduction band edge grows, the overlap between the primary NDR peak and the secondary NDR peak is reduced and the PVR approaches the PVR in the single band case. In typical III-V materials, the first quantized subband is roughly 0.1 eV above the conduction band edge, resulting in a significant reduction in the maximum NDR compared to a material without any subbands.[157, 168] Therefore, because they lack quantized subbands that are detrimental to the achievable PVR, TMDs can potentially exhibit higher PVRs than has been previously observed in III-V materials.

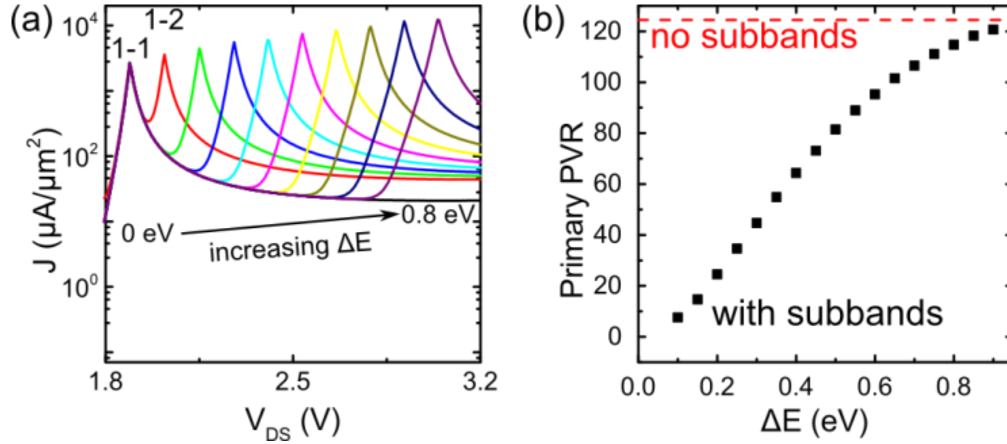

Figure 3.9. (a) Effect of subband location on *J-V* response in an MoS_2/hBN/MoS_2 system with an imaginary subband. The top and bottom electrodes are assumed to have identical band structures. (b) PVR as a function of subband location. For small spacing between the conduction band edge and the subband, the PVR is significantly reduced. For large spacing, the PVR in the subband structure approaches the PVR in the absence of any subbands (depicted by the red dashed line). Simulations were performed with V_{TG} = -1.5 V and V_{BG} = 1.5 V and $C_{TOX} = C_{BOX}$ = 3 μF/cm^2. The interlayer consists of two layers of hBN (0.6 nm), with a capacitance of 6.2 μF/cm^2. We assume $|M_{B0}|$=0.01eV for all transitions, n = 1.5, and $q_c^{-1} \approx$ 10 nm for all transitions.

A second difference in TMD symFET versus RTD performance lies in the height of the potential barrier created at the interface between the quantum well and the interlayer. In III-V devices, the requirement for lattice matching during epitaxial growth restricts the choices for barrier material, limiting the barrier height to only a fraction of an eV. In 2D materials, the effect of strain arising from a lattice mismatch within the structure is minimal because there is no out-of-plane bonding in the structures. As a result, a wide range of 2D material choices exists for the interlayer and large barrier heights are possible through use of materials such as hexagonal boron nitride (hBN). For example, the potential barrier created between hBN and MoS_2 is approximately 3 eV, higher than has been achieved in III-V structures.[169, 173]

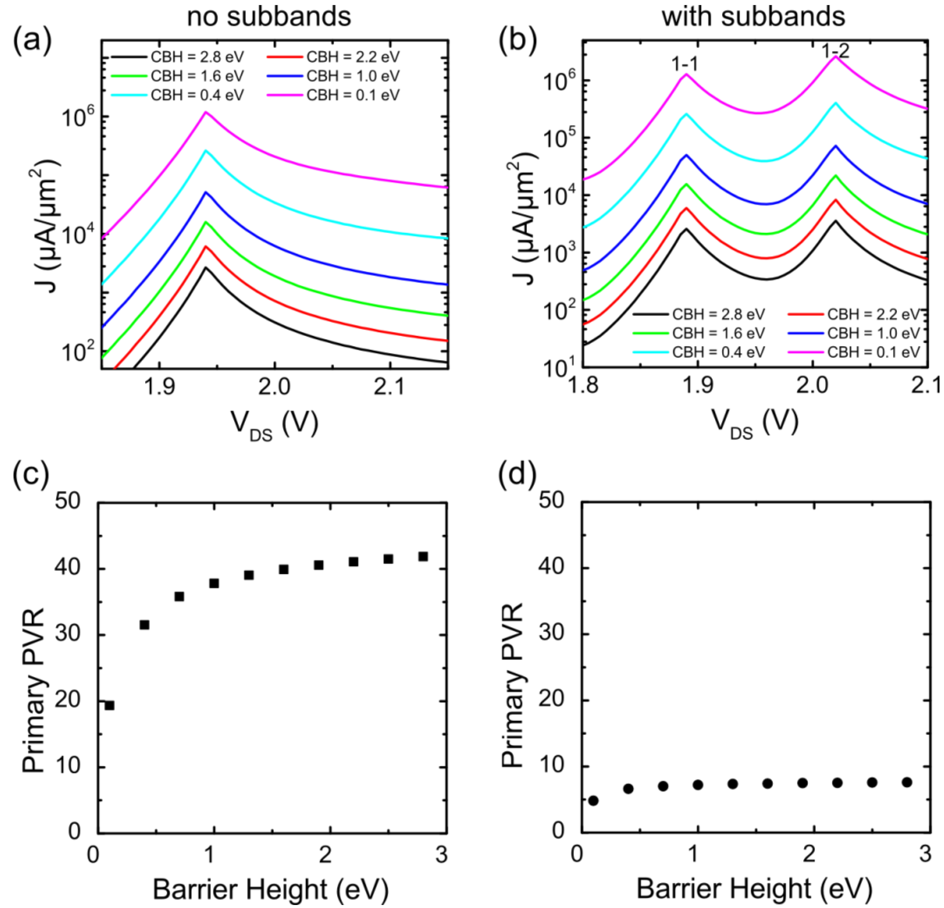

Figure 3.10. (a, b) Current density versus drain-source bias voltage for a variety of conduction band heights (CBH) for symFETs using a material without subbands (a) and with subbands (b) as the electrodes. (c, d) Dependence of PVR on the CBH for the symFETs without subbands (c) and with subbands (d). Simulations were performed with V_{TG} = -1.5 V and V_{BG} = 1.5 V and C_{TOX} = C_{BOX} = 3 μF/cm^2. The interlayer consists of two layers of hBN (0.6 nm), with a capacitance of 6.2 μF/cm^2. We assume $|M_{B0}|$=0.01eV for all transitions, n = 1.5, and $q_c^{-1} \approx$ 10 nm for all transitions.

The influence of the conduction band barrier height was explored in a series of MoS_2 symFETs using hBN as the interlayer. The tunneling current was simulated while varying the electron affinity of the interlayer for a device without subbands and a theoretical device with a subband located 0.1 eV above the conduction band edge to match the typical case for III-V materials. Figure 3.10 (a) shows the results for the single-

band device, while Figure 3.10 (b) presents the tunneling current in devices with a subband. In both types of devices, lowering the conduction band barrier height results in an increased transmission coefficient and a higher current. However, the general shape of the current-voltage characteristic remains the same at all barrier heights, as both the peak and valley currents increase as a result of the lower barrier. For the material with a subband, the ratio between the maximum current for the primary and secondary peaks changes with the barrier height. Because the transmission coefficient has an exponential dependence on the barrier height, the 0.1 eV difference in the barrier height for the two bands causes a larger change in the current from the subband than for the current from the ground state.

The PVR was extracted from the tunneling current density as explained previously. Figures 3.10 (c) and (d) present the extracted PVR as a function of conduction band barrier height for the single energy band and multiple energy band devices, respectively. The main difference between the two systems is that the maximum PVR in the case with only a single energy band saturates at roughly 40, while the PVR for the case of a subband saturates around 8, indicating that simply the presence of the subband has significantly reduced the performance of the device. For large barrier heights, the PVR is relatively unaffected by the barrier height, remaining close to the saturation value. However, for both systems, the effect of barrier height is more pronounced when the barrier height drops below 1 eV, and the PVR is strongly reduced by as much as a factor of 2 for a barrier height of less than 0.5 eV. In both TMD- and III-V- based devices, the band structure can be engineered through material choice to have a barrier of 1 eV or greater, causing barrier height not to limit either system strongly.

By independently exploring the effects of both subbands and barrier height on the *J-V* characteristic of symFETs, the results presented here demonstrate that TMD materials have the potential to create resonant tunneling devices with better performance than III-V materials. The primary reason for this is the presence of subbands, which increase the valley current in III-V devices and significantly reduce the PVR. While the barrier height can also contribute to the reduction in PVR, both TMD and III-V structures can be optimized to have a barrier height greater than 0.5 eV, eliminating most of the effect of barrier height on the PVR.

While these results demonstrate one of the important factors distinguishing III-V resonant devices from TMD devices, this model does not include other factors that may affect the performance of these devices. In particular, the effects of inelastic scattering are not considered in this work. While inelastic scattering is a relatively minor contributor to the valley current in high-performance RTDs,[167] the high defect densities in currently available TMDs may cause inelastic scattering to play a large role in determining the performance of current experimental devices. Further work is necessary to understand the influence of defects and inelastic scattering on the predicted tunneling characteristic of TMD devices.

CHAPTER 4

STEEP-SLOPE OPERATION IN 2D VERTICAL HETEROSTRUCTURES

Due to the continued scaling of logic devices over the past several decades, several physical limitations have emerged that require the development of novel device structures. In particular, the MOSFET architecture is limited to a subthreshold swing of 60 mV/decade by the slope of the Fermi function at room temperature. In order to continue scaling the bias voltage and power consumption of these devices, smaller subthreshold swings are necessary, requiring alternative device architectures. Additionally, device scaling has been accompanied by increased OFF state currents and increased power density.[174] Each of these considerations complicates scaling of devices for future technology nodes.

The tunnel field-effect transistor (TFET) has been proposed as a potential successor to the MOSFET. In general, TFET operation relies on strong gate control over the band alignment to transition from a state with low tunneling probability to a state with high tunneling probability over a narrow voltage range. While a number of TFET designs have been explored, only a few studies have experimentally demonstrated sub-60 mV/decade subthreshold swing.[138, 175-182] The interlayer tunnel field-effect transistor (ITFET) is one particularly promising design, as described in Chapter 1.

Steep-slope operation of the ITFET relies on valence-to-conduction band tunneling, with the band alignment determined by the applied gate bias. With a small gate bias, there is no overlap between the conduction and valence bands and tunneling is

restricted. As the gate bias increases, an overlap develops between the conduction and valence bands, at which point a sharp increase in the tunneling current occurs. Continued increases in the bias voltage increase the overlap between the conduction and valence bands. However, because tunneling is confined within a limited energy range due to the requirement for momentum conservation, the current no longer increases after a critical overlap is reached and the device enters the saturation region. For ideal TMDs, the band structure is step-like, resulting in an infinite slope in the subthreshold region. However, non-idealities, such as defects or potential fluctuations, result in a spreading of the band edges and a finite subthreshold slope. Understanding the relationship between non-idealities and subthreshold slope is critical to designing ITFET devices which outperform conventional CMOS transistors.

A number of theoretical studies have explored the behavior of the ITFET. In particular, Li *et al*. explored the MoS_2-WTe_2 system[126] and the WSe_2-$SnSe_2$ system,[127] suggesting the potential for a low turn-on voltage and steep subthreshold slope in both systems. In this prior work, each of these systems was selected because of the small intrinsic band offset between the conduction band/valence band of the two materials. In addition, nFET and pFET behavior were both demonstrated within the WSe_2-$SnSe_2$ system, indicating the potential for complementary logic using only a single set of 2D materials.[127]

The previous studies on TMD-based ITFETs used only a simplified material structure to predict the tunneling behavior. This work explores the impact of including the full electronic and physical structure of the 2D electrodes on device performance. Importantly, the difference in lattice constants is found to be a critical factor in overall

device performance. Further, this work demonstrates the potential for steep-slope behavior with low turn-on voltages in the MoS_2-WSe_2 system. A number of device parameters are explored to identify promising methods for device performance tuning. Finally, the performance of MoS_2-WSe_2 TFETs is benchmarked against other proposed 2D TFETs as well as traditional CMOS devices.

4.1 The WSe_2-$SnSe_2$ System

Previous investigations into the behavior of the WSe_2-$SnSe_2$ system used a simplified band structure which did not account for two potential characteristics of the materials that play a critical role in determining the overall device behavior: (1) the presence of additional valleys in both the conduction and valence bands of the 1T-$SnSe_2$ monolayer at the M-point, and (2) the large lattice constant mismatch between $SnSe_2$ and WSe_2. To evaluate the impact of these two factors on the performance of WSe_2-$SnSe_2$-based devices, the current-voltage characteristic was explored for the simplified versus complete band structure, as shown in Figure 4.1. The black solid curve represents the case of a single direct band gap in the $SnSe_2$ and a perfectly matched lattice constant between the top and bottom materials with only a single direct bandgap in the $SnSe_2$ layer (simplified structure), while the red dashed curve includes the lattice constant mismatch between $SnSe_2$ (a_0 = 3.82 Å) and WSe_2 (a_0 = 3.25 Å) and the additional valleys in the conduction and valence band of the $SnSe_2$ (realistic structure).

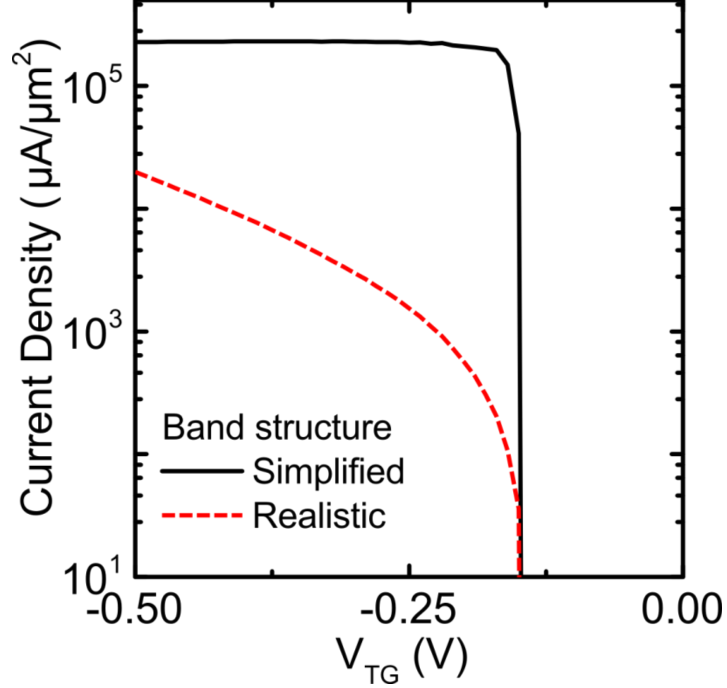

Figure 4.1. Comparison of the simulated performance of WSe_2-$SnSe_2$ system with a single direct band gap at the K-point for the $SnSe_2$ (simplified) and including secondary band minima and lattice constant mismatch between WSe_2 and $SnSe_2$ (realistic). In the simplified system (black, solid curve), the tunneling current is determined by the density of states overlap of the WSe_2 and $SnSe_2$, resulting in a steep-slope operation and current saturation. However, when the lattice constant mismatch is considered (red, dashed curve), the requirement for momentum conservation dominates the current-voltage response, resulting in a current that increases with increasing bias.

The differences in tunneling behavior between the simplified structure and the realistic structure arise mainly because of the lattice constant mismatch between the WSe_2 and $SnSe_2$, which creates an additional momentum offset between the states involved in tunneling in the top and bottom electrodes. Essentially, the difference in lattice constant results in the K-points in the 2D materials existing at different locations in momentum space, which decreases the probability of tunneling. As a result, tunneling is suppressed for small values of V_{TG}, where the overlapping states in the WSe_2 and $SnSe_2$ have similar momenta relative to their band edges ($|\vec{q}|$ is small, but $|\vec{q} + \vec{Q}|$ is large). As

the magnitude of V_{TG} increases, the number of overlapping states increases, accompanied by an increasing relative momentum difference between these states. This increased relative momentum difference compensates the fixed momentum difference associated with the lattice constant difference, resulting in the increasing current with increasing magnitude of gate voltage observed in Figure 4.1.

These results demonstrate the importance of considering a variety of material parameters when evaluating combinations of materials for use in tunneling devices. While the previous approach has mainly focused on the identification of materials with a small intrinsic band offset (near broken gap), it is important to understand the implications of the band structure on the tunneling response. For example, it is important that the conduction band minimum and valence band maximum of the opposing materials exist at the same point in momentum space (typically the K-point) and the materials have similar lattice constants to create a high probability of momentum conservative tunneling. In general, it is necessary to select a pair of materials for which the density of states determines the tunneling current through the device rather than having momentum conservation considerations serve as the dominant factor. Using these considerations as a starting point, the remainder of this chapter explores how different aspects of device design and material choices affect the current-voltage behavior of an ITFET.

4.2 The MoS_2-WSe_2 System

A large amount of experimental work has focused on the synthesis of thin-films of MoS_2 [90, 91, 98, 111, 183, 184] and WSe_2,[1, 92, 101, 185] demonstrating the ability to grow wafer-scale films of both materials. As a result of the more sophisticated synthesis techniques for MoS_2 and WSe_2 compared to other 2D materials, MoS_2-WSe_2 is an interesting system

to consider for the ITFET. Additionally, there is only a small lattice constant difference between MoS_2 (a_0 = 3.14 Å) and WSe_2 (a_0 = 3.25 Å), resulting in a tunneling current which is controlled by the density of states.

Despite these advantages of the MoS_2-WSe_2 system, the small intrinsic offset between the conduction band of MoS_2 and the conduction band of WSe_2 presents a challenge for device design. Experimental measurements have identified the valence band of WSe_2 to be offset by 0.83 eV from the valence band of MoS_2 and the conduction bands to be offset by 0.56 eV, placing the conduction band of the MoS_2 within the bandgap of the WSe_2.[186] As a result, steep-slope operation in the MoS_2-WSe_2 system has not been considered up to this point. However, the intrinsic band offset between the top and bottom electrodes is not the only parameter that determines the threshold voltage for a ITFET. For example, one potential solution to achieve small threshold voltage for MoS_2-WSe_2 ITFETs is tailoring of the top and bottom gate work functions to achieve a small zero-bias offset between the MoS_2 conduction band and the WSe_2 valence band. In this situation, only a small applied bias voltage is necessary to achieve device turn on, resulting in a threshold voltage similar to that observed for material systems with an intrinsic small band offset. Figure 4.2 (a) demonstrates the potential for steep-slope operation in the MoS_2-WSe_2 system. For these simulations, a value of 0.02 eV was used for M_{B0}, the coherence length (L_C) was 10 nm, and the decay constant for tunneling, κ, was 5.12 nm^{-1}. The black solid curve represents the simulated transfer characteristic for the case of a simplified structure (same lattice constant, only a single band minimum/maximum), while the red dashed curve represents the realistic structure. The small lattice constant mismatch between MoS_2 and WSe_2 results in a small decrease in

the tunneling current, but there is still a clear saturation region. The saturation current in the devices is on the order of 10^5 μA $μm^{-2}$, suggesting that current densities large enough for high performance applications are possible in an ITFET.

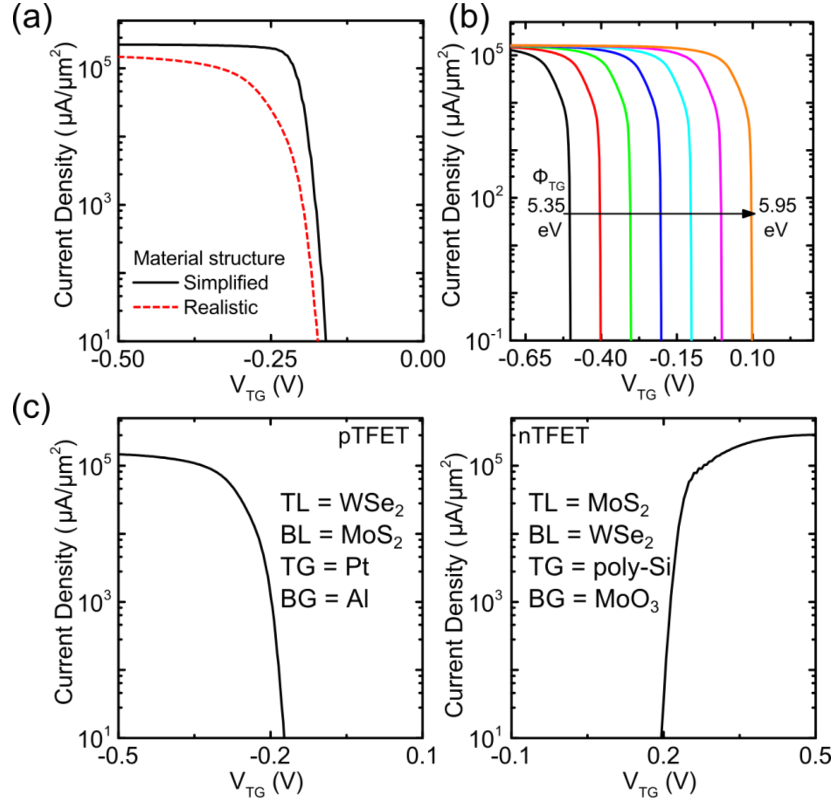

Figure 4.2. (a) Comparison of the simulated transfer curve for simplified versus realistic structure in the MoS_2-WSe_2 system. The small lattice constant difference between the two materials results in a slight decrease in the tunneling current. (b) Effect of top-gate work function on the turn-on voltage in MoS_2-WSe_2 ITFETs. As the top gate work function increases, the turn-on voltage shifts to more positive values without changing the subthreshold slope or the saturation current. (c) Simulated transfer curves demonstrating both p-TFET and n-TFET behavior in the MoS_2-WSe_2 system. The simulation uses 10 meV width extended band tail states, with the other device parameters given in Table 1. N- and P-type behavior is possible with only small changes to the device structure, suggesting the possibility for complementary logic out of a single material system. For these simulations, a value of 0.02 eV is used for M_{B0}, the coherence length is 10 nm, and κ is 5.2 nm^{-1}.

To further explore the potential of the MoS_2-WSe_2 system the relationship between the current-voltage characteristic and top gate work function was explored. Figure 4.2 (b) shows the effect of work function on the *J-V* curve of an MoS_2-WSe_2 p-TFET. As the work function is varied from a value of 5.35 eV to 5.95 eV, the *J-V* curve shifts uniformly. Importantly, there is no change in the subthreshold slope or saturation current as the work function changes. Essentially, a change in the gate work function of 0.1 eV is equivalent to a change of the applied gate voltage of 0.1 V. As a result, the control gate work function represents an excellent method for performance tuning in ITFETs.

Finally, in order to build logic circuits, it is essential to be able to create complementary logic using ITFETs. Ideally, this complementary behavior should occur in a single materials system to simplify processing and device design. Figure 4.2 (c) shows the transfer curve of both an MoS_2-WSe_2 pTFET and a WSe_2-MoS_2 nTFET, according to the device parameters given in Table 4.1. Both devices display similar saturation currents and magnitudes of the threshold voltage. The main difference between the devices is that the gate work functions are changed in order to tune the device performance. While the top and bottom layers are inverted to simulate the nTFET, this is because the simulation applies the drain-source bias voltage to the top layer. In a real device, the nTFET could also be created using MoS_2 as the bottom layer and WSe_2 as the top layer, with the gate materials also switched.

Table 4.1. Device parameters for MoS_2-WSe_2 ITFETs

Parameter	**pTFET**	**nTFET**
Top Layer	WSe_2	MoS_2
Bottom Layer	MoS_2	WSe_2
Φ_{TG}	5.65 eV (Pt)	4.17 eV (poly-Si)
Φ_{BG}	4 eV (Al)	6.55 eV (MoO_3)
V_{DS}	-0.4 V	0.4 V
V_{BG}	0 V	0 V
I_{DSAT}	1.56×10^5 µA µm^{-2}	2.89×10^5 µA µm^{-2}

4.3 TFET Scaling and Performance Tuning

In addition to creating a device with a low turn-on voltage, large saturation current, and high ON/OFF ratio, an understanding of the factors that affect 2D TFET behavior is critical for tailoring the performance to specific device applications. This section discusses the effects of device size, rotation misalignment, lattice constant mismatch, doping, and applied bias voltages on TFET performance.

4.3.1 Device Size

In the limit of ideal 2D materials, the lateral dimension of a ITFET limits the coherence length for vertical transport (L_C).[123] That is, the coherence length in a device composed of ideal 2D materials can be represented as $L_C = \sqrt{A}$, where A represents the device area. Therefore, varying the coherence length represents a simple way to investigate the impact of device size on tunneling in the ideal MoS_2-WSe_2 system.

The MoS_2-WSe_2 pTFET described above was simulated with a coherence length ranging from 1 nm to 100 nm to assess the scalability of ITFET devices, with the *J-V* characteristics shown in Figure 4.3 As the results show, for a coherence length of 5 nm or greater, the saturation current of the pTFET does not vary significantly. However, the subthreshold slope decreases slightly as the coherence length increases, as shown in the inset in Figure 4.3. These results suggest that the ITFET can be scaled to at least the 5 nm node without significantly affecting the device behavior.

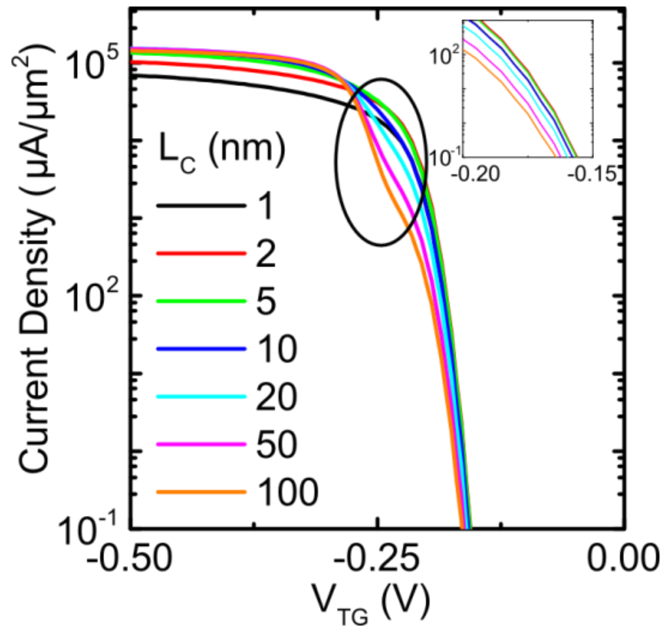

Figure 4.3. Effect of device size (coherence length) on the transfer characteristic of MoS_2-WSe_2 ITFETs. There is not a significant effect on the saturation current or turn-on voltage of the device until the coherence length is less than 5 nm. The circled region indicates an inflection in the current-voltage characteristic due to the stricter momentum conservation requirements as the coherence length increases. Similarly, the inset shows the subthreshold region of the device, demonstrating a small increase in the subthreshold swing as the coherence length increases.

Interestingly, there is a brief inflection that appears in the device turn-on characteristic as the coherence length increases, shown in the circled region in Figure 4.3.

This effect, as well as the decreasing subthreshold swing, appears as a result of the stricter requirements for momentum conservation as the coherence length increases. In the turn-on region, there is a small overlap between the conduction and valence bands of the top and bottom 2D electrodes, in which the total momentum difference ($|\vec{q} + \vec{Q}|$) is due to a combination of the momentum relative to the band edge in each material and the lattice constant mismatch between the MoS_2 and WSe_2. As the coherence length increases, energetic states with a small or zero momentum difference have increased tunneling probability, while states with larger momentum difference have a decreased probability of tunneling. Because most of the states which can tunnel in the turn-on region have a relatively large momentum difference, this results in the observed decrease in current.

At larger values of gate voltage, the energetic overlap between the MoS_2 conduction band and the WSe_2 valence band increases. In this energy range, the momentum difference during tunneling has a zero value in the middle of the energy range and a large value towards the edges. Based on the value of the coherence length, there is a finite width around this zero point which strongly contributes to the tunneling current. For large bias voltages, the entire energy range which contributes to tunneling is contained entirely within the energy overlap. As a result, the value of the saturation current is relatively independent of the coherence length. For small values of the coherence length (<5 nm), the tails of the energy range over which tunneling occurs extend outside of the band overlap, resulting in the observed decrease in saturation current in extremely small devices.

4.3.2 Rotational Misalignment

An important aspect in the creation of 2D vertical hetetostructure devices is the ability to ensure close rotational alignment of the 2D material electrodes. As stated in Equation 2.24, a rotational misalignment between the top and bottom 2D electrodes results in a small fixed momentum difference between the K-points of the materials. As the angle increases, the momentum difference increases as well, resulting in a decreased likelihood of tunneling and a corresponding decrease in the tunneling current density.

In order to estimate the necessary degree of rotational alignment for high performance in the ITFET, the MoS_2-WSe_2 ITFET was simulated with varying amounts of rotational misalignment (ω), with the simulated current densities shown in Figure 4.4. For small values of ω, there is only a small decrease in the tunneling current due to the rotational misalignment. However, for larger values of ω, the tunneling current significantly decreases as a result of the large momentum difference during tunneling. Based on these simulations, a rotational misalignment of only 5 degrees results in a decrease in the saturation current of the device by approximately an order of magnitude. In addition, large rotational misalignments increase the subthreshold swing of the device. Together, these factors suggest that high performance ITFETs incorporating 2D materials will require a maximum rotational misalignment of only a few degrees. Recent work has suggested that direct synthesis of TMDs on top of one another has the potential to create heterostructures with rotational misalignment as small as 1.9°, providing one possible path for achieving the necessary rotational alignment in ITFET devices.[142]

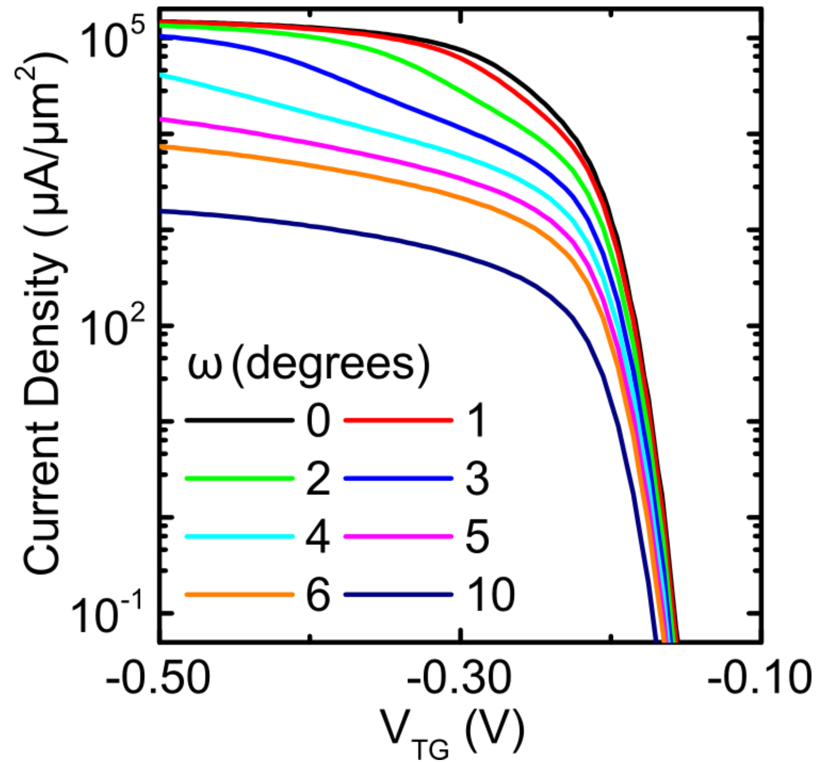

Figure 4.4. Effect of rotational misalignment on tunneling in ITFETs. For a misalignment angle greater than approximately 2 degrees, the device performance is significantly degraded.

4.3.3. Lattice Constant Mismatch

As discussed previously for the WSe_2-$SnSe_2$ system, a lattice constant mismatch between the 2D electrodes can significantly impact the performance of an ITFET. As the lattice constant mismatch increases, the additional momentum offset that must be accommodated during tunneling also increases and the tunneling behavior departs farther from ideal ITFET behavior. With large mismatches, such as that in the WSe_2-$SnSe_2$ system, the saturation region of the device disappears as the low probability of momentum conservative tunneling becomes the dominant factor in determining the tunneling behavior of the device.

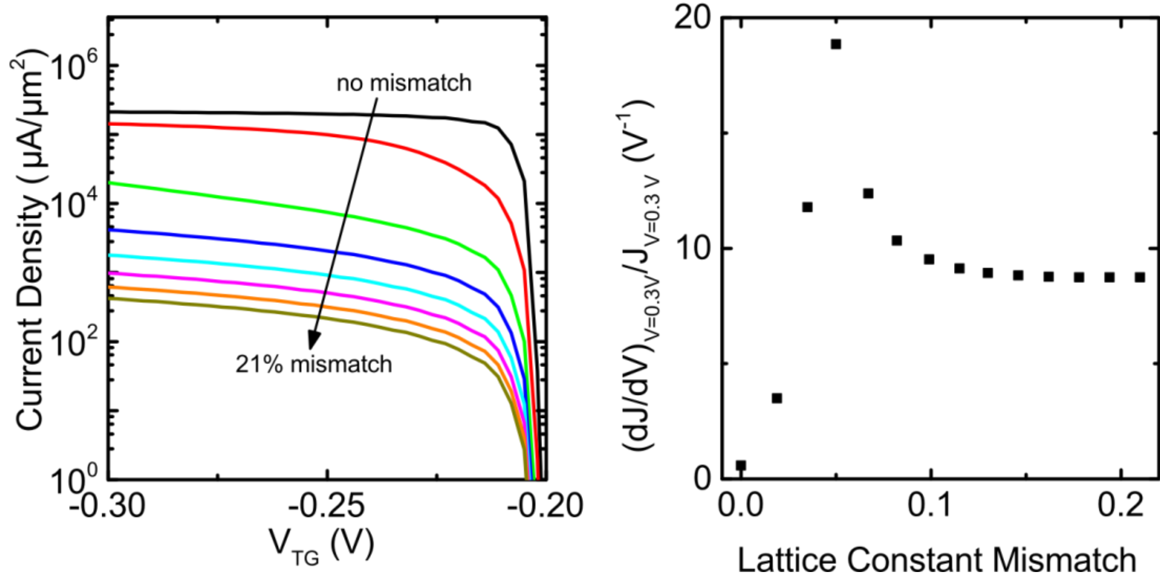

Figure 4.5. (a) Current-voltage characteristic for lattice constant mismatch ranging from 0% to 21%. While the turn-on voltage and steep-slope behavior of the device are independent of the lattice mismatch, increasing lattice mismatch decreases the device current and changes the slope of the curve in the saturation region. (b) Derivative of the current-voltage characteristic for a value of V_{TG} = -0.3 V, normalized by the current density The slope is near zero for no lattice constant mismatch, but quickly increases to a maximum of approximately 20 for a small lattice constant mismatch.

To estimate the amount of lattice constant mismatch that can be tolerated while retaining a saturation region in the current-voltage characteristic, a series of simulations was carried out in which the lattice constant of the WSe_2 layer in an MoS_2-WSe_2 pTFET was varied from exactly matched with MoS_2 to a 21% mismatch. The resulting *J*-*V* curves, shown in Figure 4.5 (a), demonstrate two important effects of the lattice constant mismatch: (1) a decrease in the device current at a given value of V_{TG}, and (2) a change in the slope of the *J*-*V* curve in the saturation region as the lattice constant mismatch changes.

Figure 4.5 (b) plots the derivative of the *J*-*V* curve at a value of V_{TG} = 0.3 V, within the saturation region in the case of a matched lattice constant. As shown in the

figure, the slope in this region increases quickly as the lattice constant mismatch increases, peaking when the lattice constant is roughly 5%. Above 5%, the slope decreases again and saturates. As these results show, high performance ITFETs must incorporate materials with closely matched lattice constants.

Based on these results, the maximum lattice constant mismatch which can be tolerated for high performance devices can be estimated as 3-4%, as is the case for the MoS_2-WSe_2 system. When the lattice constant mismatch is greater than this, there is a significant decrease in the tunneling current due to the low probability of momentum conservation.

4.3.4 Dopant Density

Understanding the relationship between dopant density and device performance is important to ensure proper device operation and robustness of the design to small device-to-device variations. Primarily, doping allows a way to tailor the current-voltage characteristic to specific applications. As another consideration, most techniques for 2D material synthesis result in defects, such as chalcogen vacancies in TMDs, which unintentionally induce doping in the 2D electrodes.[187] Therefore, it is also important to understand how dopant density changes device performance to evaluate the robustness of the devices to these defects. Of particular concern in these devices is the shift in threshold voltage that occurs as a result of the change in the Fermi level of the 2D electrodes due to doping.

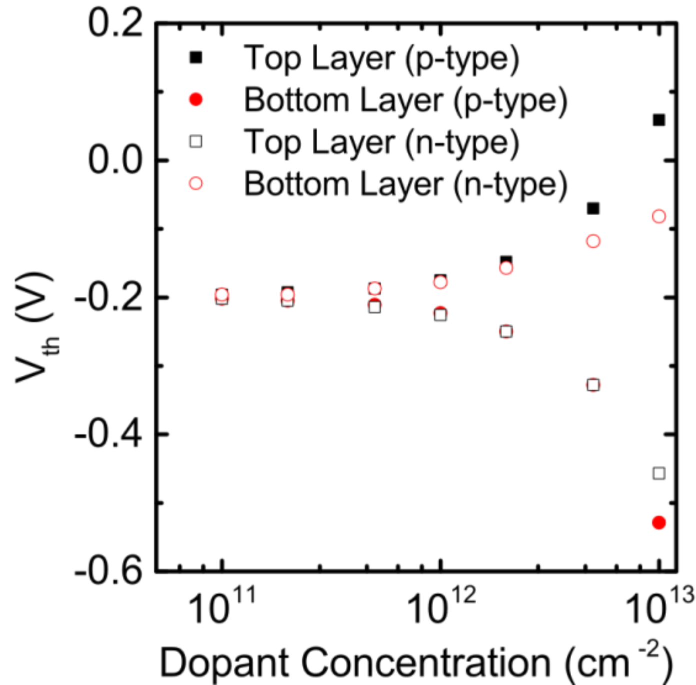

Figure 4.6. Threshold voltage shift due to doping in the ITFET. Doping of the top layer results in a symmetric response for both p-type (closed black squares) and n-type (open black squares) dopants. Doping of the bottom layer is similar to the top layer for p-type doping (closed red circles). However, a smaller effect is observed for n-type doping of the bottom layer (open red circles), with a reduced shift in the threshold voltage compared to the other doping conditions. In all cases, a doping density of larger than 10^{12} cm^{-2} is necessary to observe a significant effect on the threshold voltage.

Figure 4.6 shows the shift in threshold voltage as the doping concentration is varied in an MoS_2-WSe_2 p-TFET. These simulations consider both p-type (closed markers) and n-type (open markers) doping of the top (black squares) and bottom (red circles) 2D layers. As the figure shows, doping of the top layer results in a symmetric shift in the threshold voltage with n- and p-type doping. As a result, doping presents another method aside from the use of the top gate work function to tune the threshold voltage of a device. This is because both doping and changing the top gate work function similarly affect the Fermi level of the top 2D electrode in the device, which changes the

alignment of the band structures of the top and bottom 2D electrodes. As a result, the top gate voltage required for band alignment also changes.

It is important to note that doping of the bottom layer is not symmetric between n- and p-type dopants. P-type doping of the bottom layer results in a threshold voltage shift comparable to that observed for doping of the top layer. However, n-type doping results in a much smaller threshold voltage shift. This asymmetric effect is because the Fermi level in the bottom layer (MoS_2) is close to the conduction band edge during normal operation. Therefore, while p-type doping can effectively move the Fermi level closer to mid-gap, n-type doping does not result in a large shift in the Fermi level towards the conduction band and does not significantly alter the device performance.

Based on these results, it can be estimated that unintentional doping due to defects on the order of 10^{12} cm^{-2} can be tolerated before significantly affecting the tunneling characteristic of the device. However, this only considers doping effects due to these defects and does not consider the implications of scattering due to defects or the effect of any energetic states that develop due to defects, which could potentially increase the subthreshold swing of the device.

4.3.5 Applied Bias Voltages

A final consideration for the performance of an ITFET is the relationship between the applied source-drain and back gate voltage biases and device performance. Within a specific device structure, including gate work function and doping densities, the applied bias voltages provide a way to actively adjust device performance. To understand how much the bias voltages can affect device performance, V_{DS} and V_{BG} were varied in an MoS_2-WSe_2 p-TFET.

Figure 4.7 (a) shows *J-V* curves for several different values of V_{DS}. With the exception of a value of V_{DS} = -0.2 V, the major characteristics of the transfer curve remain the same. That is, the threshold voltage does not strongly depend on V_{DS} and the turn-on characteristic of the device is unchanged. However, the saturation current of the device does depend on the source-drain bias voltage, with the effect saturating as the voltage increases. Once the magnitude of V_{DS} is greater than 0.4 V, the increase in the saturation current becomes minimal and further increasing the source-drain bias voltage only increases power consumption with no benefit to performance.

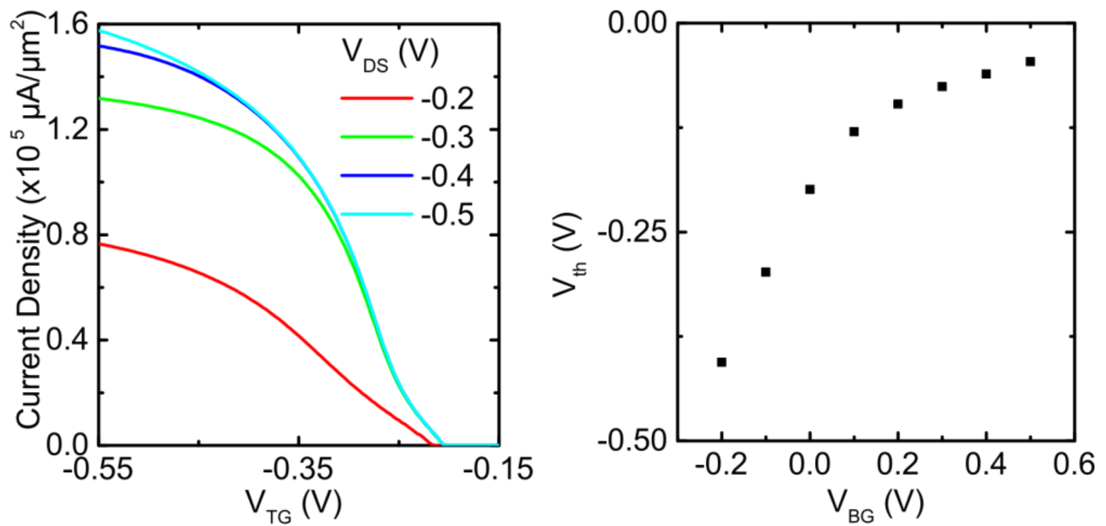

Figure 4.7. (a) Influence of V_{DS} on the transfer curve of an MoS_2-WSe_2 ITFET. For V_{DS} greater than 0.2 V, the turn-on characteristic does not change significantly. Continued increases to the bias voltage only minimally increase the saturation current of the device. (b) Effect of V_{BG} on the threshold voltage of the device. Positive values of V_{BG} have a diminishing effect on the threshold voltage, while negative values can more strongly tune the device behavior.

Figure 4.7 (b) shows the threshold voltage of the ITFET for different back-gate voltages, V_{BG}. As was the case with doping, the dependence of the threshold voltage on

the back-gate voltage bias is non-symmetric. For positive values of V_{BG} the threshold voltage approaches zero, but the magnitude of the change quickly decreases due to the Fermi level of the MoS_2 moving towards the conduction band at a decreasing rate. Conversely, for negative values of V_{BG}, the magnitude of the threshold voltage increases in a linear fashion. This suggests that some amount of performance tuning can be achieved using the value of V_{BG}. However, it is also important to note that similar effects on the performance of ITFETs are possible using either dopants or the back gate work function. Either of these other approaches has the advantage that device operation is simplified by not requiring a separate back gate bias. In contrast, however, the use of a back gate voltage bias allows for dynamic tuning of the device during operation.

4.4 Non-Ideal Systems

A final consideration for TFET performance is the impact of non-ideal materials on device performance. For example, both exfoliated [188] and chemical vapor deposited[97] MoS_2 films have been shown to have significant band tail states. In general, these band tail states arise from factors such as potential fluctuations on the substrate or defects in the material, such as chalcogen vacancies. As previously discussed by Li *et al*.,[126] a large width of band tail states arising from potential fluctuations increases the subthreshold swing in ITFETs. Therefore, it is necessary to understand the relationship between band tail width, device performance, and material properties to accurately predict the performance of real devices.

To assess the impact of band tail states on the MoS_2-WSe_2 system, two types of band tail states were considered: (1) band tail states arising from potential fluctuations, referred to as extended states, and (2) band tail states due to localized defects. Because

potential fluctuations result in a shift in the electronic structure of the 2D layers, the band tail states due to potential fluctuations are assumed to be part of the conduction and valence band of the 2D electrodes and are treated as momentum conservative states. The band tail states are represented by a Gaussian function, $S_E(E)$, which has been previously described in detail by Li *et al.*[126] In this case, the tunneling current is calculated as

$$J_{tot} = \frac{e|M_{B0}|^2}{\hbar} \int_{E_B} \int_{E_T} g_B(E_B) g_T(E_T)(f_B - f_T) T(E_B, E_T) S_E(E_B - E_T)\, dE_B dE_T \quad (4.1)$$

Band tail states due to localized defects are treated as trap states with zero momentum and a value of $S_F = 2\pi L_C^2$. Additionally, because localized defects are unlikely to be spatially aligned, tunneling is only allowed between the localized band tail states and states in the conduction or valence band of the 2D material electrodes. Tunneling is not allowed between localized band tail states in the top 2D electrode and localized band tail states in the bottom 2D electrode. In this simplistic model, the current contribution due to the defects depends on the coherence length, rather than incorporating a more complex defect model. However, it is still a useful model in order to compare the relative effect of different band tail widths on the tunneling characteristic. Future work will investigate the use of more accurate models for band tail states.

Figure 4.8 compares the effects of localized and extended band tail states on the subthreshold swing of an MoS_2-WSe_2 ITFET. Based on the models used, localized states have a more significant impact on the subthreshold swing than extended states. However, for either type of band tail state, a relatively small width (~10meV) results in a subthreshold swing close to or greater than 60 mV/decade, suggesting that narrow band tails will be necessary for high performance devices. Current synthesis techniques result

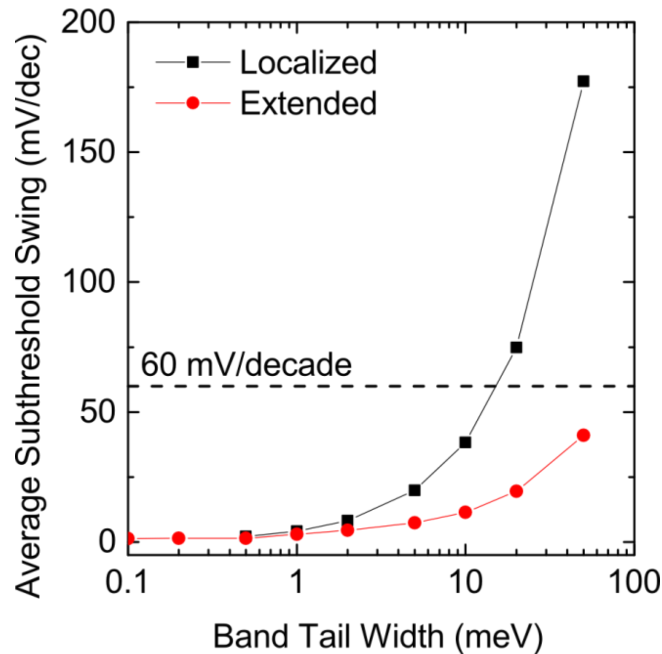

Figure 4.8. Comparison of the relationship between subthreshold swing and band tail width for both localized and extended band tail states. Both types of band tail states increase the subthreshold swing and decrease the ITFET performance. However, localized states appear to more strongly affect the subthreshold swing. For current synthesis techniques, it is expected that wide band tails will result in subthreshold swings greater than 60 mV/decade.

in band tails larger than 10 meV, suggesting that high-quality synthesis methods are critical to realize the full potential of the ITFET.

In addition to band tail states, the presence of defects in 2D materials can result in the development of defect energy bands which change the performance of the device. The effect of these defect bands depends on their energetic position, but could include an increase in the OFF state current of the device, a shift in the threshold voltage, or the creation of additional features in the current-voltage characteristic. Further work is necessary to understand the influence of common defects in 2D materials on device performance and to assess the implications for device performance.

4.5 ITFET Benchmarking

To further evaluate the performance of MoS_2-WSe_2 ITFETs, benchmarking was performed to compare the MoS_2-WSe_2 system to conventional CMOS technology. The specific MoS_2-WSe_2 ITFET considered is the nFET shown in Figure 4.3 (c), with 10 meV band tail states and a source-drain voltage bias of V_{DS} = -0.4 V. Similar to the comparison made by Seabaugh for TFETs previously,[189] Figure 4.9 (a) shows a comparison of the transfer curves of the MoS_2-WSe_2 ITFET (solid red line), a low-power (LP) CMOS device (dashed blue line) and a high-performance (HP) CMOS device (dashed black line). As was done for the Thin-TFET previously,[127] the value of I_D/w was computed using a gate length of 10 nm. It is evident from this comparison that the MoS_2-WSe_2 ITFET has a much steeper subthreshold slope than the CMOS-based devices. Additionally, the predicted saturation current for the ITFET is higher than for the HP-CMOS, further suggesting that higher performance is possible for the ITFET than in HP-CMOS devices.

As another metric for benchmarking the ITFET, the switching energy and intrinsic switching delay of the MoS_2-WSe_2 ITFET were compared to CMOS devices and other emerging device architectures, as shown in Figure 4.9 (b). This benchmarking methodology is similar to that adopted by Nikonov and Young for evaluating post-CMOS devices.[190] For this evaluation, the switching delay is calculated as

$$t_{switching} = \frac{C_{G,avg} V_{DS}}{I_{DS,sat}} \tag{4.2}$$

and the switching energy is calculated as

$$E_{switching} = C_{G,avg} W V_{DS}^2 \tag{4.3}$$

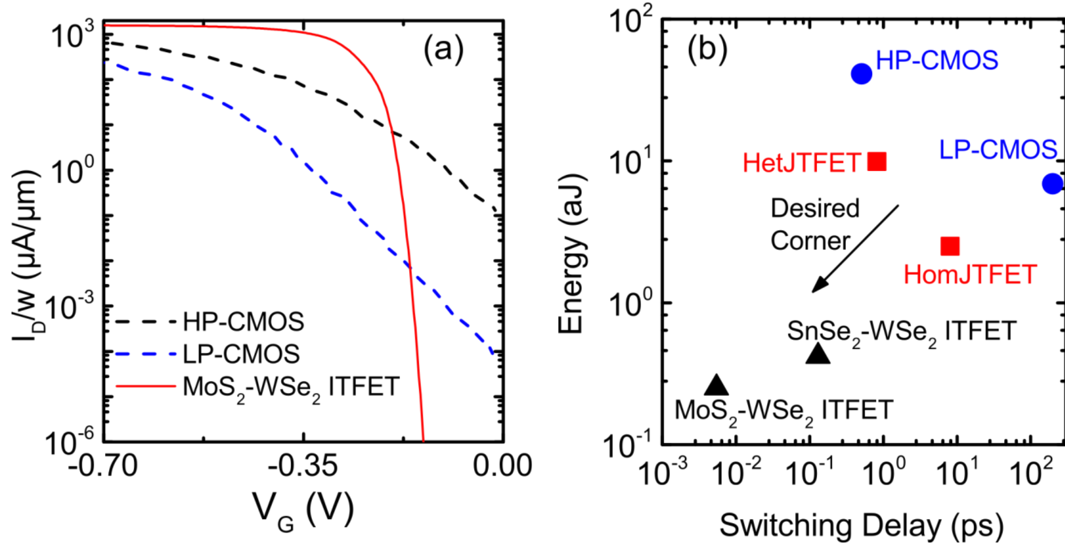

Figure 4.9. Benchmarking of the MoS2-WSe2 ITFET. (a) Comparison of the transfer curve of the MoS2-WSe2 ITFET to high-performance (HP) and low-power (LP) CMOS devices. The saturation current of the MoS2-WSe2 ITFET is higher than for either CMOS device with a steeper turn-on. (b) Comparison of the energy and switching delay for the MoS2-WSe2 ITFET with HP/LP-CMOS devices, as well a number of other proposed tunneling devices. Based on this comparison, the MoS2-WSe2 ITFET has the potential for better performance than other proposed devices.

where $C_{G,avg}$ represents the average gate capacitance, $I_{DS,sat}$ is the saturation current, and W the device width. The values for these calculations were collected for the MoS_2-WSe_2 ITFET where $V_{GS} = V_{DS} = -0.4$ V. In the figure, the performance values for HP CMOS, LP CMOS, HetJTFET and HomJTFET are those used by Nikonov and Young.[190] The value for the WSe_2-$SnSe_2$ ITFET is taken from Li *et al.*[127]

Based on the benchmarking of the MoS_2-WSe_2 ITFET, the material system has the potential to outperform existing CMOS devices, with both faster operation and lower power consumption. However, there are several aspects of realistic device operation that will increase the switching delay or increase the energy used for switching. In particular, this model does not include lateral transport in the 2D materials which will increase the

overall resistance of the device, potentially decreasing the saturation current and increasing the power consumed by the device. The resistance due to lateral transport for current synthetic materials is expected to dominate the device operation due to the typically low mobility in these materials. Similarly, contact resistance will result in decreased device performance, as previously discussed in the WSe_2-$SnSe_2$ system.[127]

An additional consideration related to the device structure is fringing capacitance. Because the lateral transport length must be minimized in order to maximize the device performance, there is the possibility for additional capacitance between the drain or source contacts and the top or bottom gates. This parasitic capacitance increases the switching delay of the device.

The combination of the extrinsic resistance and capacitance in the ITFET moves the device performance away from the ideal corner and towards that of conventional CMOS devices. Ultimately, the extent to which these factors can be reduced will determine how significant of an improvement over existing CMOS technology the MoS_2-WSe_2 ITFET presents.

CHAPTER 5

SYNTHESIS OF LARGE-AREA 2D MATERIALS

This chapter describes multiple methods which have been used for the growth of TMDs, using the equipment described in Appendix A. The first section details optimization of the growth process for few-layer MoS_2, work which was performed in close collaboration with Dr. Alexey Tarasov and Meng-Yen Tsai. My role in the described work largely involved aspects of process design and sample synthesis, XPS characterization, and involvement in transistor fabrication and electrical measurements. Section 5.1 presents selected portions of the work related to the choice of synthesis temperature, film structure and uniformity, and mobility measurements, as these details influenced the approach taken for synthesis of WSe_2. Section 5.2 includes the synthesis method developed for synthesis of highly uniform, few-layer WSe_2, including physical and electrical characterization of the films. Dr. Alexey Tarasov assisted in the collection of Raman data on the synthetic WSe_2.

5.1 Large-Area Growth of MoS_2[e]

Large area growth of MoS_2 on SiO_2 substrates was demonstrated according to the growth process sketched in Figure 5.1 (a). Highly doped silicon wafers were thermally oxidized to create a 300 nm thick SiO_2. Prior to Mo deposition, the substrate was cleaned

---

[e] Adapted with permission from A. Tarasov, P. M. Campbell, M.-Y. Tsai, Z. R. Hesabi, J. Feirer, S. Grahan, W. J. Ready, and E. M. Vogel, *Advanced Functional Materials*, vol. 24, p. 6389-6400. Copyright 2014 WILEY-VCH

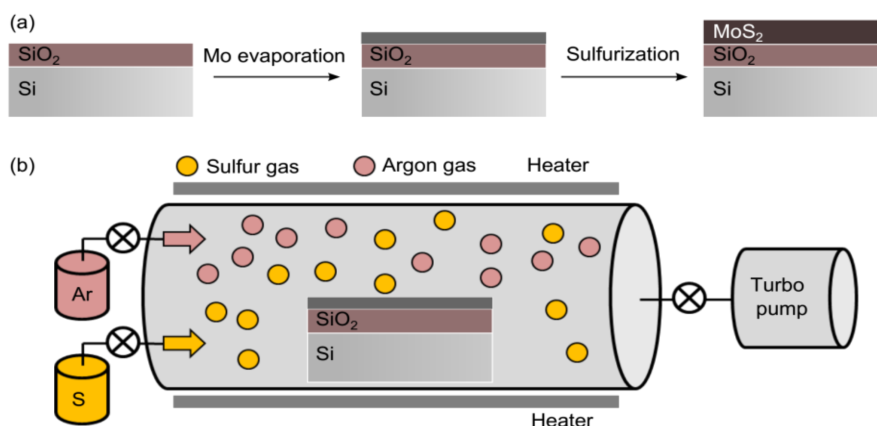

Figure 5.1. (a) Schematic of the process flow used for growth of large-area MoS_2 films. (b) Overview of the high-temperature sulfurization used to convert the evaporated MoO_x thin film to MoS_2.

with organic solvents and piranha solution. A thin Mo layer was deposited by e-beam evaporation at a rate of 0.3 Å/s, with the thickness ranging from 1- 5 nm. The Mo films were then directly sulfurized in a furnace for 1 h in an Ar/S atmosphere at temperatures between 550 °C and 1050 °C, with the best results at the highest temperature. The schematic of the sulfurization furnace is provided in Figure 5.1 (b). The sulfur vapor pressure is controlled by preheating a separate sulfur container. After evacuating the chamber, the samples were first annealed in an Ar/H_2 (4:1) atmosphere for 30 min at 300 °C to eliminate possible oxygen contamination. Meanwhile, the sulfur was preheated to 160 °C to generate a sufficient vapor pressure. Afterwards, the chamber was soaked with sulfur gas (20 mTorr) and argon carrier gas (5 Torr). The chamber was heated to the final temperature and remained for 1 h with all valves closed. The chamber was then purged with Ar and cooled down under a constant Ar flow.

To evaluate the stoichiometry of the synthetic MoS_2, X-ray photoelectron spectroscopy (XPS) measurements were performed and are summarized in Figure 5.2.

The stoichiometry, defined as the ratio of the peak areas of the S 2p to the Mo 3d peaks, is plotted in Figure 5.2 as a function of growth temperature. The bulk value measured on a geological crystal is represented by the dashed line. The stoichiometry of the grown MoS_2 clearly improves with temperature and saturates at the bulk value above 750 °C, suggesting that MoS_2 with stoichiometry equivalent to bulk can be achieved if the growth temperature is sufficiently high.

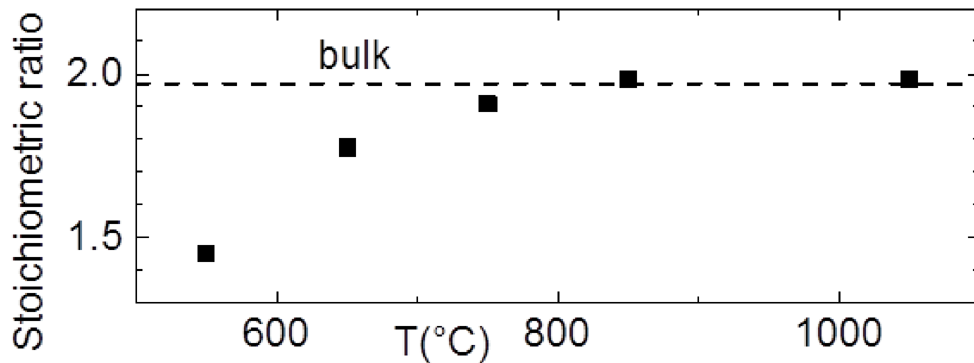

Figure 5.2. Influence of synthesis temperature on the stoichiometry of synthetic Mo films.

Further structural analysis is performed using Raman spectroscopy. Raman spectra of the synthetic MoS_2, made by sulfurization of a 5 nm thick Mo film at different temperatures, are depicted in Figure 5.3 (a). The typical MoS_2 double peak is visible around 400 cm^{-1}. The measured E_{2g}^1 position is at ~ 382 cm^{-1} and A_{1g} is at ~ 407 cm^{-1}, independent of the growth temperature. This corresponds to a peak separation Δ ~ 25 cm^{-1} and agrees well with the previous measurements on exfoliated bulk flakes.[191, 192] The full-width at half-maximum (FWHM) of the E_{2g}^1 and A_{1g} peaks decreases as the growth temperature rises (Figure 5.3 (b)). The peak width reaches the bulk values

(indicated by dashed lines) only above 1000 °C. This shows that the structural quality of the synthesized MoS_2 greatly improves at higher growth temperatures and is similar to geological MoS_2 if grown at temperatures > 1000 °C. The relative intensity of the MoS_2 signal vs. Si background peak at 520 cm^{-1} also tends to increase with temperature. Similarly, Laskar *et al*. showed that the intensity of the MoS_2 peaks grown on sapphire strongly increases with growth temperature.[193] The authors attributed this effect to the improved structural quality of the material.

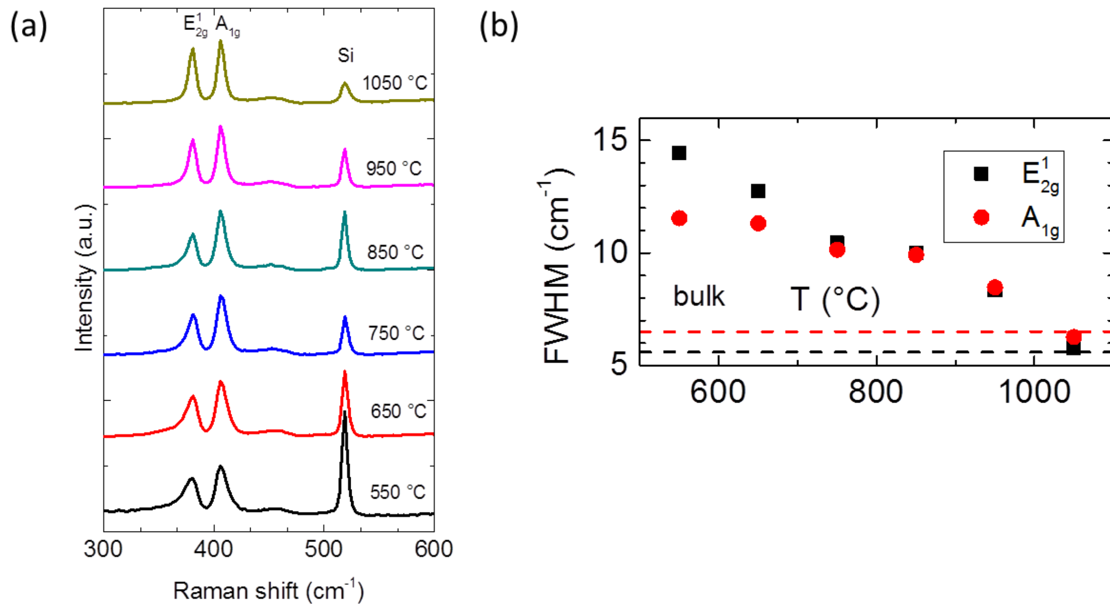

Figure 5.3. (a) Raman spectra from a 5 nm Mo layer after sulfurization at different growth temperatures (532 nm laser). Typical MoS_2 double peak is visible around 400 cm^{-1}. The E_{2g}^1 peak represents the in-plane vibrations of Mo and S atoms, and A_{1g} denotes the out-of-plane vibrations of sulfur atoms. The spectra were normalized to the A_{1g} peak intensity and are shown vertically offset for clarity. The MoS_2 peaks become narrower with increasing growth temperature, and their intensity relative to the Si peak increases. b) The full-width at half-maximum (FWHM) of the E_{2g}^1 and A_{1g} peaks as a function of temperature. The peak width decreases as the temperature goes up and reaches the bulk values (dashed lines) only above 1000 °C.

After optimizing the growth temperature, the synthesis method described above was applied to the creation of few-layer MoS_2. To do so, 1 nm Mo was evaporated and sulfurized at the highest possible temperature (1050 °C, limited by the furnace). Note that natural oxidation either during deposition or exposure to atmosphere results in the formation of an MoO_x film. Following sulfurization, dual-gated field-effect transistors were fabricated using a wafer-scale UV lithography process to study the electrical properties of the material. Figure 5.4 (a) shows a photograph of a wafer die after device fabrication. This thickness of Mo (1 nm) is expected to give approximately 2 nm or 3 layers of MoS_2. To study the film uniformity, Raman measurements were collected at 15 different positions across the whole sample area (Figure 5.4 (b)). All spectra align perfectly on top of each other. The separation between the characteristic MoS_2 peaks (E_{2g}^1 and A_{1g}) is 23.53±0.04 cm^{-1} (Figure 5.4 (c)), which corresponds to trilayer MoS_2.[191, 192] Around a trilayer MoS_2 thickness, a change in Raman peak separation by ∼ 1 cm^{-1} corresponds to ∼ 1 monolayer (ML) thickness difference. We show a uniformity of ∼ 0.04 cm−1 which corresponds to ∼ 0.04 ML. As a conservative estimate, the film uniformity is 3 ML ±0.1 ML across the entire area of the chip (> 10 cm^2). Assuming a monolayer thickness of ∼7 Å, this uniformity corresponds to ±0.7 Å. For comparison, the CVD growth of MoS_2 produces films with large variations in thickness from monolayer to > 4 layers over an area < 1 cm^2.

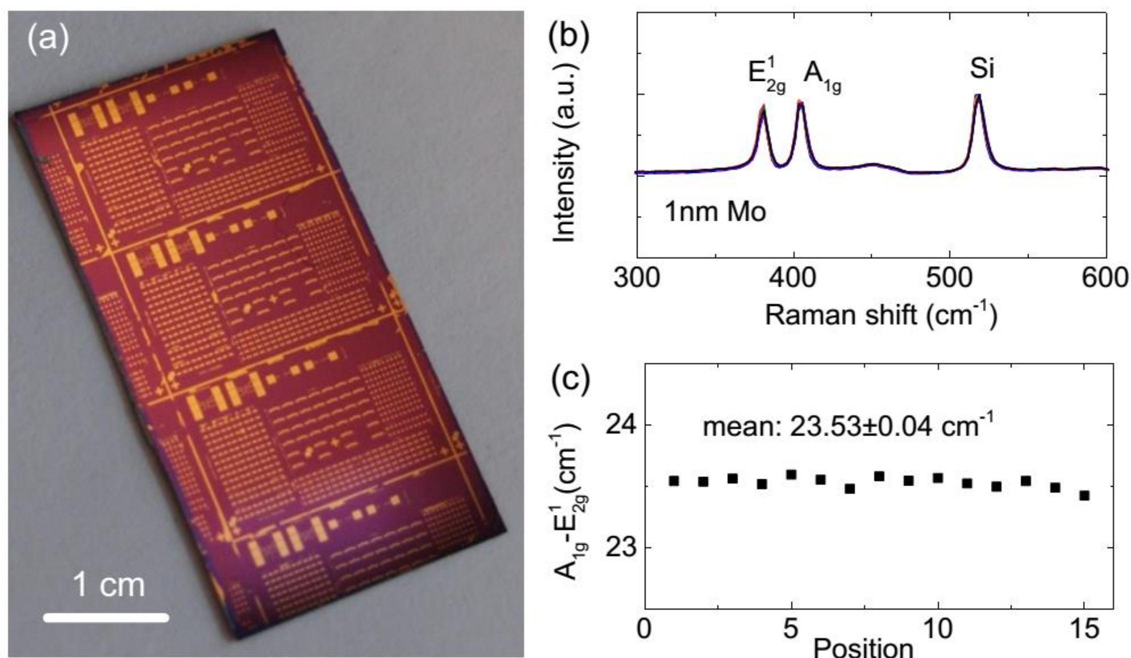

Figure 5.4. The thinnest MoS_2 sample (1 nm Mo, sulfurized at 1050 °C) was used for device fabrication following a wafer-scale UV lithography process. a) The optical image shows a wafer die after device fabrication. b) Raman spectra from 15 different areas of the sulfurized wafer align perfectly on top of each other. c) The peak separation between the E^1_{2g} and A_{1g} of 23.53±0.04 cm^{-1} is smaller than for the bulk material (25 cm^{-1}) and corresponds to 3 layers of MoS_2. The thickness uniformity is ~0.1 monolayers (or ~0.07 nm) across the whole wafer.

Small-area Raman maps were collected across the area of a transistor (in 5 µm steps). Figure 5.5 (a) provides an optical microscope image of a single transistor. The inset shows the peak separation between the E^1_{2g} and A_{1g}at 36 different positions. The mean value is again very close to 23.5 ± 0.1 cm^{-1} and extremely uniform across the area of the transistor (3 ML ±0.1 ML). In addition, cross-sectional scanning transmission electron microscope images (STEM) were performed on a transistor after fabrication to resolve the layered structure of the material (Figure 5.5 (b)-(d)). The sample was prepared using a focused ion beam (FIB) system prior to imaging. In Figure 5.5 (b), a

lower magnification image of the contact region is shown, acquired in transmitted electron mode (bright-field). The image reveals a thin layer of MoS_2 between the SiO_2 substrate and the titanium and gold (Ti/Au) contacts. At higher magnification (c), good stacking of 3 MoS_2 layers is resolved. Molybdenum layers appear darker than the sulfur layers because of the higher atomic number of Mo. The total MoS_2 thickness is around 2 nm. This value matches surprisingly well with our expectations and the Raman data. The same area is also shown in atomic number contrast mode (part d), with the color scale inverted (dark-field, Mo appears lighter than S).

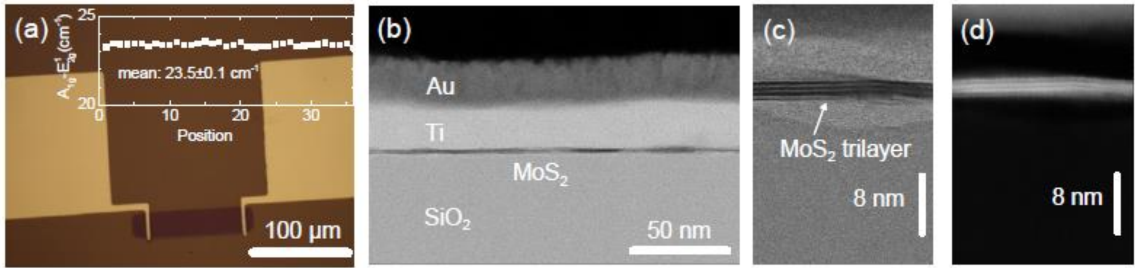

Figure 5.5. (a) An optical image of a trilayer MoS_2 transistor with Ti/Au contacts before the topgate deposition. Inset: Raman maps were taken across the area of a transistor. The peak separation was 23.5 ± 0.1 cm^{-1}, showing excellent uniformity. (b–d) The thickness was confirmed by cross-sectional STEM, performed on a transistor after fabrication. b) A bright-field (BF) image across the contact region in (a) shows a thin MoS_2 layer between the SiO_2 substrate and the Ti/Au contact material. MoS_2 appears darker than SiO_2 or Ti because of the higher atomic number of Mo. c) A BF image at higher magnification reveals good stacking of 3 layers of MoS_2 (Mo layers are darker than S). (d) The same area is also shown as a dark-field image. The total MoS_2 thickness is around 2 nm. This matches well with our expectation because we deposited 1 nm Mo which should yield 3 layers of MoS_2 after sulfurization.

Using UV lithography, several samples with hundreds of transistors each were fabricated from the synthetic MoS_2. The transistor channels were defined by dry etching the MoS_2 with an SF_6/O_2 mixture. The source and drain contacts were formed by e-beam evaporation of 30 nm titanium (Ti) and 30 nm of gold (Au). Several tens of back-gated

transistors were first tested after this step. The yield was 100%. Then, 30 nm of alumina (Al_2O_3) were grown by atomic layer deposition (ALD) at 250 °C, followed by the evaporation of a Ti/Au top gate electrode. Thirteen transistors were measured again after ALD in a dual-gated configuration (Figure 5.6 (a)). The transistors were randomly chosen from the entire die area of ~ 10 cm^2 (see Figure 5.4 (a)). All measurements were done using a Keithley 4200-SCS parameter analyzer and a Cascade Microtech probe station at room temperature and ambient conditions. Figure 5.6 (a) shows the schematic of a dual-gated transistor and the measurement circuit. In part (b), the measured drain current I_d is plotted vs. the applied back-gate voltage V_{bg} at fixed source-drain voltage V_{ds} = 1 V (transfer curve). The top-gate is grounded (V_{tg} = 0 V) to avoid spurious coupling effects between the top-gate and the back-gate that have been observed if the top gate was left floating.[194] The transfer curve on a semi-logarithmic scale (left vertical axis) shows both gate sweep directions, indicated by arrows. The hysteresis is negligible because the top dielectric protects the MoS_2 channel from environmental factors such as humidity and oxygen, as has been previously studied.[41, 195-197] The linear transfer curves (right axis) compare one sweep direction for 2 different transistors, FET 1 (solid symbols) and FET 2 (empty symbols). Both curves align very well on top of each other. These transistors are several centimeters apart, suggesting good film uniformity. The output curves I_d vs. V_{ds} are plotted in Figure 5.6 (c) for different back-gate values. The curves are linear and symmetric around V_{ds} = 0 V, usually indicative of Ohmic behavior. The applied drain-source voltages $V_{ds} \leq 1$ V are well inside the linear regime of operation. However, it has been shown that a linear output characteristic can occur due to thermally assisted

tunneling in atomically thin materials even if a significant Schottky barrier is present at the semiconductor-metal interface.[113]

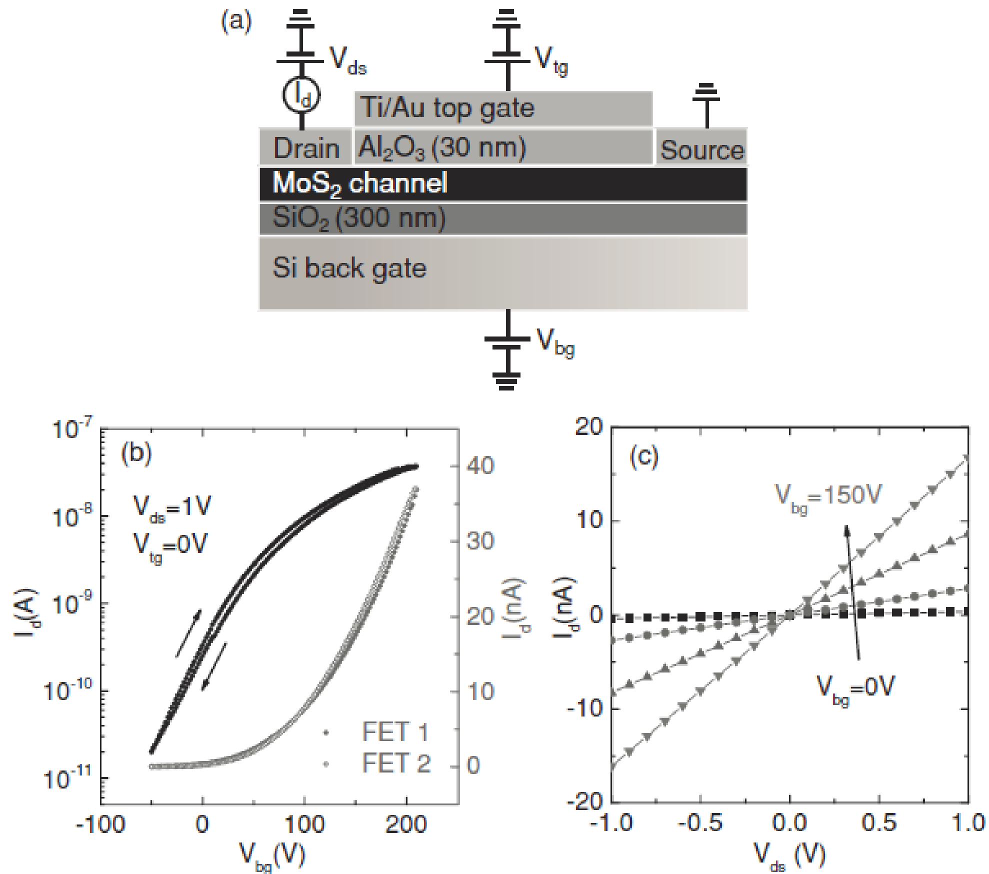

Figure 5.6. (a) Schematic of a dual-gated trilayer MoS_2 transistor (not to scale). The drain-source voltage V_{ds} is applied to the Ti/Au contacts on top of MoS_2. The channel is covered with 30 nm Al_2O_3 and a Ti/Au top gate electrode. The drain current I_d through the MoS_2 channel is measured as a function of the back gate voltage V_{bg} and the top gate voltage V_{tg}. (b) Drain current I_d through the MoS_2 channel as a function of the applied back-gate voltage V_{bg} (transfer curve) at constant drain-source voltage V_{ds} = 1 V, with the top-gate grounded (V_{tg} = 0 V). The transfer curve on the semi logarithmic scale (left vertical axis) shows both gate sweep directions, indicated by arrows. The hysteresis is negligible. The linear transfer curves (right axis) compare one sweep direction for two different transistors, FET 1 (solid circles) and FET 2 (empty circles). Both curves align very well on top of each other. The transistors are several centimeters apart, suggesting high uniformity of the film. (c) The output curves I_d vs V_{ds} are linear and symmetric around V_{ds} = 0 V (Ohmic behavior). The applied drain-source voltages $V_{ds} \leq 1$ V are well inside the linear regime of operation.

The maximum drain currents measured here are comparatively low, suggesting a strong contribution from the contact resistance, which can dramatically lower the drain current.[113, 198] The contact resistance is mainly determined by two key factors: (1) a Schottky barrier as a result of the work function difference between the semiconductor and the contact metal; (2) a significant number of interface states which is influenced by the material quality, fabrication process, sample cleanliness etc.[113, 198-200] High contact resistance is a major issue for transistors based on two-dimensional semiconductors because the source/drain regions are not heavily doped like in conventional semiconductors. Well-established techniques such as ion implantation are difficult to use because of the atomically thin structures. Therefore, several systematic studies have been conducted to minimize the Schottky barrier formation by using low work function metals such as titanium[201] and scandium,[113] or using a tunnel barrier (MgO[200] or TiO_2 [202]) between a ferromagnetic metal and MoS_2. Contact doping with nitrogen dioxide, potassium, and polyethylenimine has also been demonstrated in TMDs.[201] Despite this progress, the influence of the contact resistance remains an issue and it is important to have a reliable method to quantify its contribution.

Dual-gated measurements allow extraction of the contact resistance, similar to the approach presented by Liu et al.[203] The full details of the contact resistance determination for the MoS_2 films are presented in reference 183. Figure 5.7 (a) shows the same transfer curves as in Figure 5.6 (b) after subtracting the extrinsic resistance, $2R_{ext}$. The corrected maximum drain current $I_{d,\ corr}$ has increased by approximately 4 times, emphasizing the large influence of the contacts. From the slope of these transfer curves, the intrinsic field-effect mobility μ_{FE}^{int} can be estimated using the following expression

$$\mu_{FE}^{int} = \frac{dI_{d,corr}}{dV_{bg}} \frac{L}{WC_{bg}V_{ds}} \quad (5.1)$$

with $\frac{dI_{d,corr}}{dV_{bg}}$ being the transconductance (derivative of the transfer curve), L = 100 μm the channel length, W = 10 μm the channel width, $C_{bg} \approx 10^{-4}$ F/m^2 the estimated back-gate capacitance per unit area, and V_{ds} = 1 V the source-drain voltage. The results are summarized in Figure 5.7 (b) for all measured transistors. The mean value is 6.5 ± 2.2 cm^2/Vs.

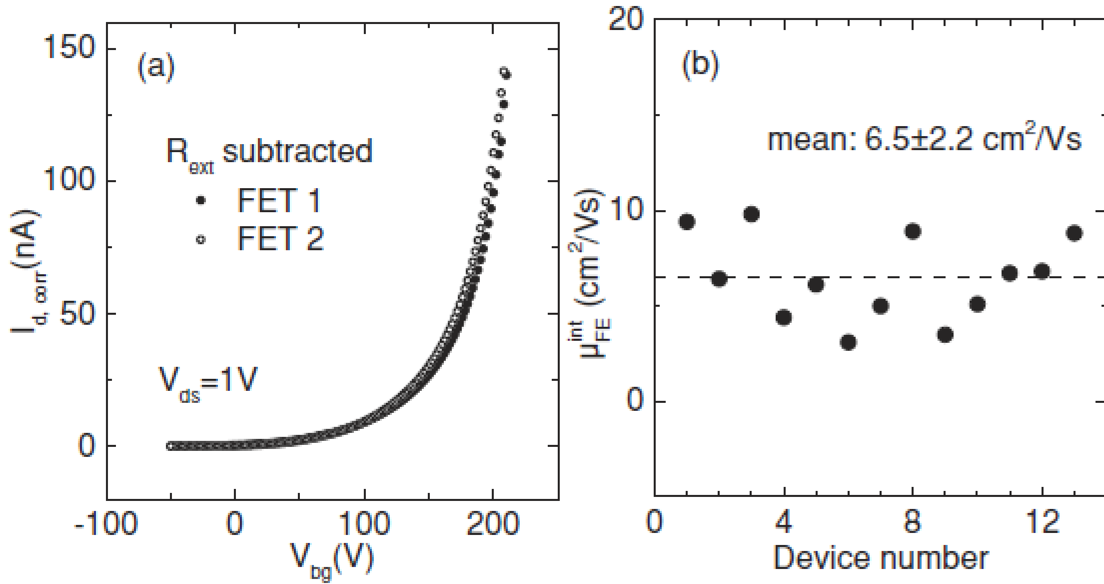

Figure 5.7. (a) Transfer curves ($I_{d,corr}$ vs V_{bg}) at V_{tg} = 0 V after subtracting the extrinsic resistance 2R_{ext}. (b) From the slope of the curves in (a), the intrinsic field effect mobility μ_{FE}^{int} can be estimated for all measured transistors. Thirteen devices were randomly chosen across the whole die area of >10 cm^2.

5.2 Large-Area Growth of WSe_2[f]

A schematic of the growth process used for large-area WSe_2 is shown in Figure 5.8 (a). The first step in sample preparation was thermal growth of a 300 nm SiO_2 on low-resistivity (0.1 – 0.5 Ω-cm, Boron-doped) silicon wafers. Following solvent cleaning, 1 nm of W was deposited on the thermal oxide via e-beam evaporation at a rate of 0.3 Å/s. Natural oxidation of the W film resulted in a combination of WO_3 and W in the thin film, which was confirmed using XPS measurements. To selenize the tungsten film, the samples were loaded into a furnace along with a crucible containing Se pellets. The furnace chamber was pumped down to approximately 10^{-6} Torr to remove atmospheric contaminants. Following this, the chamber was stabilized at 30 sccm Ar and 10 sccm H_2 with a pressure of 3 Torr to provide a flow of gas across the Se pellets and W film. After gas stabilization, the furnace was heated to 800 °C at a heating rate of 80 °C/min and the samples were annealed under the Ar/H_2 flow for 1 hour, incorporating the Se into the film to create the WSe_2. After 1 hour, the chamber was purged at 800 °C for 30 minutes under 200 sccm Ar flow to remove excess selenium from the samples. Finally, the furnace was allowed to cool to room temperature under 2 slm Ar flow. The resulting film is expected to be three layers of WSe_2 based on the starting thickness of 1 nm evaporated W.

To determine the stoichiometry of the WSe_2 samples, XPS measurements were performed and are summarized in Figure 5.8 (b) and (c). Figure 5.8 (b) shows the W 4f

[f] Reproduced from Reference 185 with permission from The Royal Society of Chemistry.

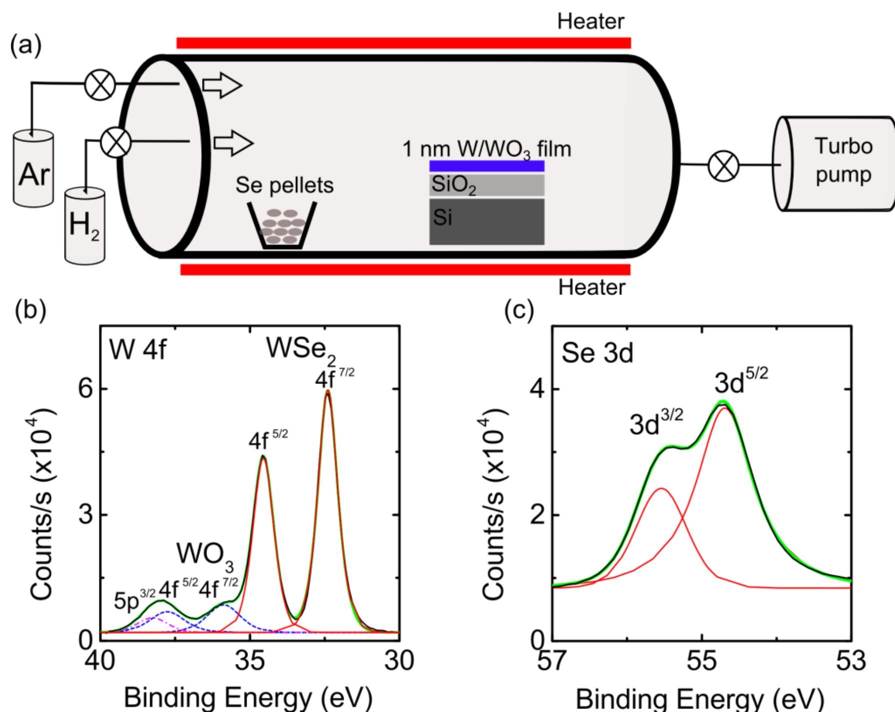

Figure 5.8. (a) Schematic of the experimental setup used for selenization. Se pellets are loaded into a crucible which is placed in the furnace with the 1 nm W/WO_3 film. The furnace is heated to 800º C at 3 Torr under 30 sccm Ar and 10 sccm H_2 flows. After 1 hour, the furnace is purged an additional 30 minutes at 800º C under Ar flow before cooling. (b-c) XPS spectra of the resulting WSe_2 films. (b) W 4f spectrum. The main peaks present are the $4f^{7/2}$ and $4f^{5/2}$ doublet resulting from the WSe_2 (red lines). A second set of peaks are present due to the formation of WO_3 on the WSe_2 film or at the grain boundaries (blue lines).[1, 2] The magenta line represents the W $5p^{3/2}$ peak. (c) Se 3d spectrum. Only a single set of Se peaks are present in the XPS spectrum, indicating that all of the Se within the film is contained in the WSe_2.

scan, consisting of five peaks. The doublet present at 32.4 eV and 34.5 eV (shown by the red solid lines) represents the W 4f electrons from the $4f^{7/2}$ and the $4f^{5/2}$, respectively, in the WSe_2. A second set of peaks are present at 35.7 eV and 38 eV (blue dashed lines). In previous reports, these peaks have been assigned to WO_3 in the film,[1, 2, 88] suggesting some oxidation of the WSe_2 thin film to form WO_3, possibly at the WSe_2 domain edges.[1, 204] A previous study found that oxidation of WSe_2 results in electron transfer to the WO_3, causing hole doping of the WSe_2.[205] Based on the ratio of the area of the WO_3 peaks to

the total area of the W 4f spectrum ($WO_3 + WSe_2$), the amount of oxide in the film is estimated as 16%. The final peak (magenta dash-dotted line) represents the W $5p^{3/2}$ peak, which overlaps with the $4f^{5/2}$ peak of the WO_3. Part (c) shows the Se 3d scan, characterized by a doublet with peaks at 54.7 eV ($3d^{5/2}$) and 55.5 eV ($3d^{3/2}$), shown by the green lines in the figure. Fittings were performed using a Voigt function with a Shirley background, using five peaks for the W 4f spectrum and two peaks for the Se 3d spectrum. To estimate the WSe_2 stoichiometry, the area of the 4f (3d) peaks for W (Se) was computed based on the fitting results and normalized using empirical relative sensitivity factors (RSFs) of 2.75 for W and 0.67 for Se.[206] The stoichiometry of the WSe_2 in the samples was calculated by taking the ratio of the normalized area of the Se 3d doublet to the normalized area of the WSe_2 W 4f doublet. In these samples, the ratio of Se:W in the WSe_2 was 1.99±0.06.

To assess the thickness uniformity of the WSe_2 film, Raman measurements were performed under 488 nm illumination as shown in Figure 5.9 (a). 488 nm illumination was chosen because the Raman spectrum of WSe_2 supported on SiO_2 has a number of lower intensity first- and second-order peaks that can be used to distinguish between monolayer, few-layer, and bulk samples.[207, 208] Unlike the Raman spectra observed for transition metal sulfides (MoS_2 and WS_2), the E_{2g}^1 and A_{1g} modes for WSe_2 are degenerate.[209] As a result, the bulk WSe_2 Raman spectrum is characterized by a single strong peak around 252 cm^{-1}, formed by the overlap of the E_{2g}^1 and A_{1g} vibrational modes. At 488 nm excitation WSe_2 samples with less than four layers show a small secondary peak slightly above this main peak, due to the $2LA(M)$ secondary resonance mode,[210] accompanied by a shift of the main peak to 250.2 cm^{-1}.[209-211] The 488 nm

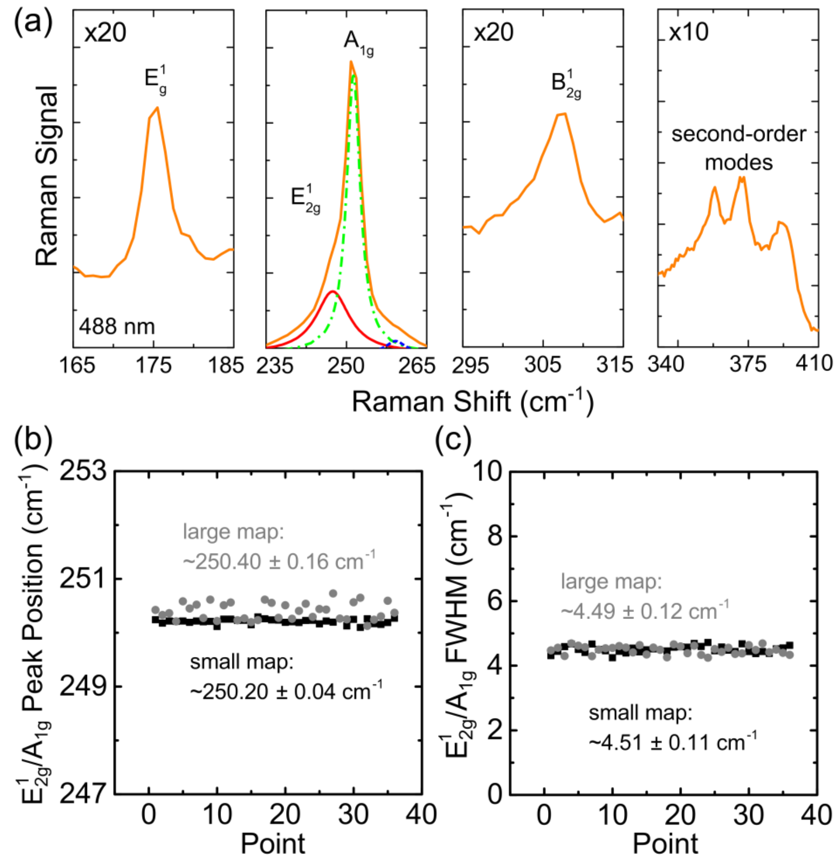

Figure 5.9. (a) Sample Raman spectrum for WSe_2, measured with 488 nm illumination. The main peak (250.2 cm^{-1}) is composed of contributions from the E^1_{2g}, the A_{1g}, and the $2LA(M)$ modes. The presence of the E^1_g peak (~175 cm^{-1}), the B^1_{2g} (~307 cm^{-1}), and the three second order modes between 350 cm^{-1} and 410 cm^{-1} indicate the few-layer nature of the synthesized film. (b) Peak position and (c) full-width at half-maximum (FWHM) of the main Raman peak at each point measured on the small Raman map (black squares) and the large Raman map (gray circles). The small variation across large and small scales indicates the excellent uniformity of the synthetic WSe_2.

experimental data in Figure 5.9 (a) shows the main peak at 250.2 cm^{-1} and a visible shoulder at 259 cm^{-1}, suggesting that these samples are composed of 3-4 layer WSe_2. The red solid, green dash-dotted, and blue dashed curves under the main peak represent peak fits corresponding to the E^1_{2g}, the A_{1g}, and the $2LA(M)$ modes, respectively. Further confirmation of the few-layer nature of the WSe_2 films is provided by the presence of

several additional resonance modes in the Raman spectrum, each of which is shown in Figure 5.9 (a). The peak shown at approximately 176 cm^{-1} is the E_{1g} mode, which does not appear in the Raman spectra for bulk or monolayer WSe_2 but does appear for few-layer WSe_2 samples.[208] The presence of the B_{2g}^{1}peak around 307 cm^{-1} in the 488 nm spectrum also indicates that the film is composed of few-layer WSe_2. Under 488 nm illumination, the B_{2g}^{1} peak cannot be observed in bulk WSe_2, but is observable in few-layer samples.[208, 210, 212, 213] Finally, few-layer WSe_2 samples show a set of three second-order resonance modes at 360 cm^{-1}, 375 cm^{-1}, and 395 cm^{-1}.[207] In reference 207, these peaks are assigned to combinations of the main vibrational modes with acoustical phonon modes to form secondary Raman peaks. In bulk samples, these second order peaks have low intensities and are essentially not present. The presence of all of these peaks in the 488 nm Raman spectrum confirms that these synthetic films are composed of few-layer WSe_2. Additionally, the presence of these few-layer peaks in the Raman spectra suggests that the WSe_2 is horizontally aligned. In this material, the grains are estimated to be on the order of tens of nanometers, which is large enough that the WSe_2 would behave similarly to bulk WSe_2. Therefore, if the WSe_2 consisted of vertically aligned layers, the Raman spectrum would be characteristic of bulk, rather than few-layer WSe_2. The structure of these WSe_2 films as a few-layer, horizontally aligned film is consistent with the evaporated W thickness.

Raman mapping confirms the uniformity of the WSe_2 over a large area. Both small maps (50 µm x 50 µm, 36 spectra, 10 µm steps) and large maps (1 cm x 1 cm, 36 spectra, 2 mm steps) were taken with the 488 nm laser to demonstrate uniformity throughout individual devices and over the entire die area. Figure 5.9 (b) shows the peak

positions of the 250.2 cm^{-1} main peak for the synthetic WSe_2, while Figure 5.9 (c) shows the full-width at half-maximum (FWHM) for the main Raman peak. Over the small map, the Raman peak is present at 250.2 ± 0.04 cm^{-1} with a FWHM of 4.51 ± 0.11 cm^{-1}, while for the larger map the peak position is 250.4 ± 0.16 cm^{-1} with a FWHM of 4.49 ± 0.12 cm^{-1}. In few-layer WSe_2, the main peak position depends on the number of layers and changing the number of layers from monolayer to roughly five layers (bulk) results in a shift of the main peak of several wavenumbers.[209, 212] A change in thickness of only a single layer can therefore result in a shift in peak position of up to 1 cm^{-1}. Therefore, nonuniformities in sample thickness are expected to result in significant variations in the main peak position. Additionally, because the spacing between the E_{2g}^1 and A_{1g} modes depends on the WSe_2 thickness,[209, 210] the FWHM of the main Raman peak formed by the overlap of these two modes will also vary with thickness. The small variation in the peak position and FWHM over both maps indicates the excellent uniformity of the synthesized WSe_2. Because this method relies on e-beam evaporation of the starting material, the area over which the selenization can be performed is determined only by the physical limitations of the equipment used. As a result, the direct selenization approach represents a wafer-scale method for producing uniform thickness WSe_2 relevant for use in the industry.

To confirm the thickness of the WSe_2 samples, 1 nm of W was patterned onto an SiO_2 substrate using a lift-off process. These samples were subsequently selenized using the previously described process to provide a clean step edges for an accurate thickness measurement. The resulting WSe_2 steps were imaged by atomic force microscopy (AFM) to measure the WSe_2 thickness. Figure 5.10 (a) shows a representative AFM image of one

of the patterned WSe_2 steps. A line profile (Figure 5.10 (b)) was taken diagonally across this step to provide a large distance over which to accurately measure the height on either side of the step. To obtain a measurement of the step height, the difference between the mean height on the left and right sides of the step was used. Based on this measurement, the estimated thickness of the WSe_2 is 2.5 nm, corresponding to approximately 3 layers of WSe_2.

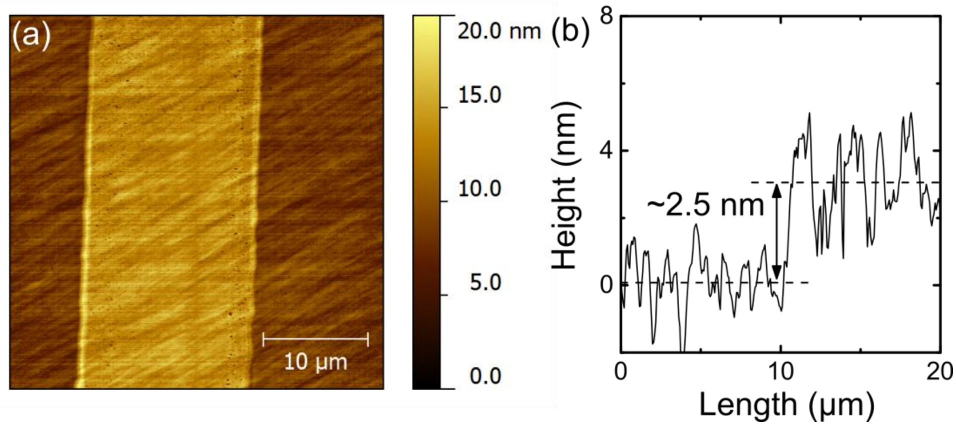

Figure 5.10. (a) Atomic force microscopy (AFM) image of a pre-patterned WSe_2 step. (b) Height profile measured across the WSe_2 step. The thickness was estimated by taking the difference between the mean height on either side of the WSe_2 step. Based on this measurement, the thickness of the WSe_2 is approximately 2.5 nm.

In addition to the physical characterization of WSe_2, the electrical properties were evaluated using back-gated FETs fabricated with conventional UV photolithography. Figure 5.11 (a) shows an optical image of a portion of the FET array. Individual transistors within a single die block are separated by approximately 500 μm. The fabricated devices consisted of several die blocks, with the transistor arrays in each die block separated by more than 1 cm. Figure 5.11 (b) shows a schematic of the transistors, with a channel width of 13 μm and length of 100 μm. More than ten transistors were

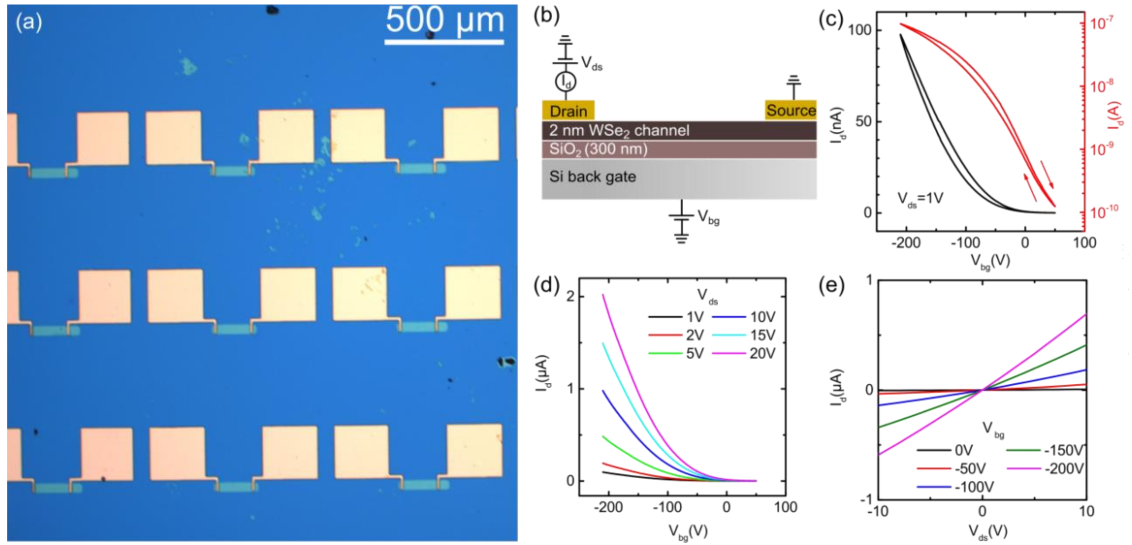

Figure 5.11. (a) Optical image of a portion of the measured FET array. (b) Schematic of a back-gated FET used for electrical measurements. (c) Linear (black) and logarithmic (red) scale plots of the source-drain current as a function of back-gate voltage (transfer curve) for one of the measured FETs at a source-drain voltage (V_{ds}) bias of 1 V. The arrows indicate the voltage sweep direction. (d) Transfer curves of a WSe_2 FET transistor measured at several different V_{ds} values. (e) Source-drain current (I_{ds}) versus source-drain voltage (V_{ds}), measured at several back-gate voltages (V_{bg}). Over the entire range measured, the curve is linear, confirming that the measured transfer curves remained within the linear regime.

measured under vacuum conditions to protect them from atmospheric effects, with all transistors exhibiting similar behavior. Most of these transistors were within a single die block, covering an area of several mm^2. However, to ensure the electrical uniformity of the film, transistors from separate die blocks were also measured, indicating that the electrical response of the film is consistent over an area of several cm^2. A representative I_d-V_{bg} measurement (transfer curve) on a linear and logarithmic scale is shown in Figure 5.11 (c). With a V_{ds} value of 1 V, the source-drain current density is higher than 10^{-8} A/μm, which is comparable to previously reported values on exfoliated few-layer WSe_2 FETs.[214] In these devices, only p-type behavior is observed because of the choice of Au as the contact metal. The work function of gold is well-aligned with the valence band of

the WSe_2, resulting in efficient hole injection from the contacts, but preventing electron injection. Figure 5.11 (c) shows the transfer curve in both the forward and reverse direction, demonstrating negligible hysteresis in these devices when protected from atmospheric effects by the vacuum environment. Such protection could be achieved by encapsulation in a dielectric rather than a vacuum environment, as has been studied previously for MoS_2 transistors.[73, 183] Figure 5.11 (d) shows the transfer curve measured at several different values of V_{ds}, demonstrating that the source-drain current scales with the applied bias. To ensure that transistor operation remained within the linear regime, the I_d-V_{ds} response was measured for a variety of back-gate voltages, with the curves plotted in Figure 5.11 (e). The response remains linear over the entire range shown (-10 V to 10 V), confirming that the measurements presented in this paper remain well within the linear regime.

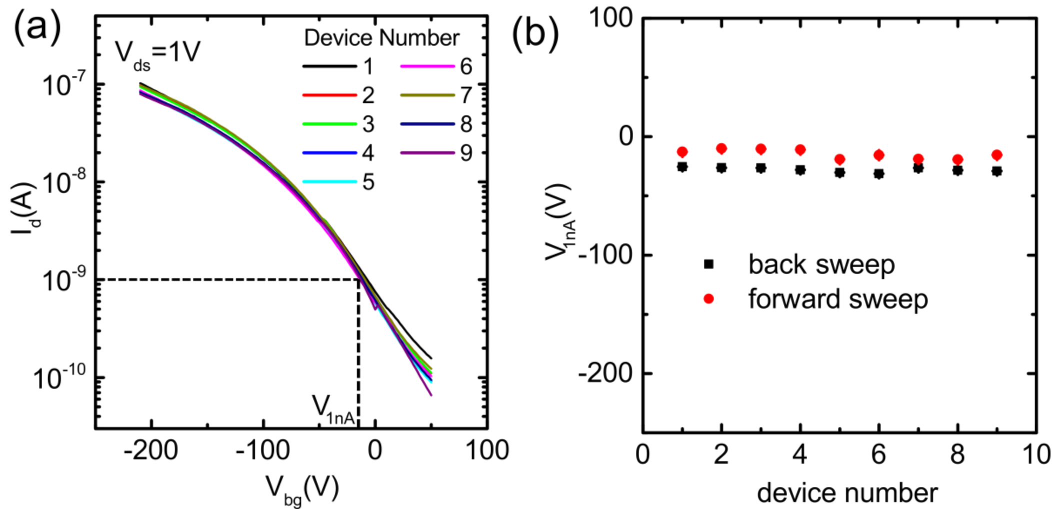

Figure 5.12. (a) Superposition of the reverse sweep transfer curves for several FETs, measured across an area of several square centimeters. The electrical performance of all devices measured is similar, demonstrating the uniform nature of the WSe_2 film. (b) Measurement of the voltage at which the current equals 1 nA (V_{1nA}), for the forward (red circles) and reverse (black squares) directions for each device, showing electrical uniformity between the measured FETs.

Electrical uniformity of the WSe_2 layer was verified by measuring more than ten transistors over the area of a die. Figure 5.12 (a) contains a superposition of the reverse sweep transfer curves for a subset of the transistors measured, located across the entire die area, demonstrating the consistency of the electrical behavior of the WSe_2 devices. Figure 5.12 (b) shows the back-gate voltage where the source-drain current crosses 10^{-9} A. The standard deviation in these voltages is less than 5 V, demonstrating excellent electrical uniformity of the WSe_2 film.

To estimate the intrinsic mobility of the synthetic WSe_2, the extrinsic resistance was removed from the transfer curves. This extrinsic resistance includes contributions due to current injection from the contacts into the WSe_2, characterized by the barrier formed at the contact, and the formation of interfacial states between the metal and WSe_2, which can pin the Fermi level under the contacts, as has been studied for MoS_2.[113, 115] Due to the lack of doping in the contact regions, there is a large contribution to the extrinsic resistance from the high resistance of the WSe_2 under the contacts. As the back-gate voltage is changed, the resistance of the WSe_2 under the contacts is also affected by changes in the WSe_2 carrier concentration, which causes the extrinsic resistance to be a function of the back-gate voltage.[183] Using four-point probe measurements, the extrinsic resistance (R_{ext}) was calculated as described below, with the results shown in Figure 5.13 (a). The inset shows the four-point probe structure, consisting of contacts numbered from 1 to 4. Using a V_{ds} value of 1 V, the I_d-V_{bg} transfer curve was measured between contacts 1 and 4 while simultaneously measuring the voltage difference between contacts 2 and 3. The total resistance of the FET is given by $R_{tot} = \frac{V_{ds}}{I_d}$. Similarly, the resistance between

contacts 2 and 3 (R_{23}) can be calculated as $R_{23} = \frac{V_{23}}{I_{\mathrm{d}}}$, a value which is then normalized to determine the total WSe_2 resistance between contacts 1 and 4 according to $R_{23\mathrm{norm}} = R_{23}\left(\frac{L_{14}}{L_{23}}\right)$, where L_{14} and L_{23} represent the distance between contacts 1 and 4 and contacts 2 and 3, respectively. Finally, the extrinsic resistance is the difference between the R_{tot} and $R_{23\mathrm{norm}}$, shown in Figure 5.13 (a). Over the full range of back gate voltages measured, the value of R_{ext} varies by approximately 2 orders of magnitude mainly as a result of changes in the resistance of the WSe_2 under the contacts.

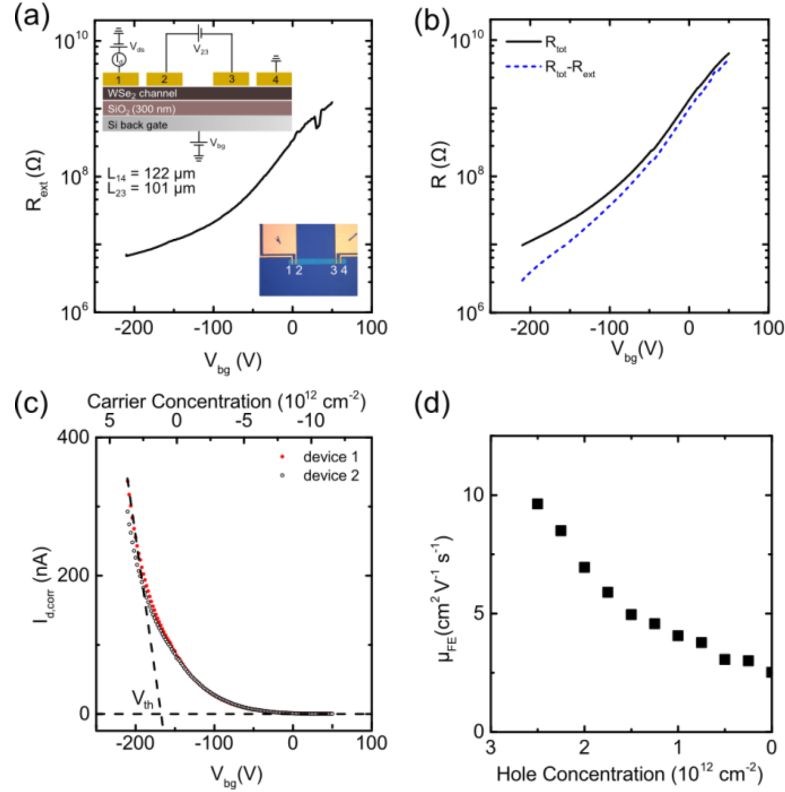

Figure 5.13. (a) Extrinsic resistance R_{ext} as a function of applied back-gate voltage, measured using the 4-point probe structure shown in the inset, as explained in the text. (b) R_{tot} (black solid line) and intrinsic channel resistance, $R_{\mathrm{tot}} - R_{\mathrm{ext}}$ (blue dashed line), for a two-terminal FET (see Figure 5.13) as a function of back-gate voltage. (c) Corrected drain-source currents ($I_{\mathrm{d,corr}}$) for two FETs from Figure 5.13 (c). The current is corrected using the calculated intrinsic resistance for each device. (d) Field-effect mobility as a function of carrier concentration for the synthetic WSe_2.

Using the extracted dependence of R_{ext} on V_{bg}, the intrinsic mobility of WSe_2 in the two-terminal FETs can be calculated. Figure 5.13 (b) shows the correction to the resistance, where the black line represents the total resistance for the two-terminal FET device. The corrected resistance (blue dashed line) is calculated by subtracting the curve for R_{ext} from the total resistance, resulting in a measure of the resistance only due to the WSe_2 channel. Figure 5.13 (c) shows $I_{d,corr}$, the corrected drain-source current, for two devices. Following this correction, the drain-source current has increased by a factor of approximately 3 and the ON/OFF ratio is at least 10^4. Based on these corrected transfer curves, the intrinsic field-effect mobility is calculated as $\mu_{FE}^{int} = \frac{dI_{d,corr}}{dV_{bg}} \frac{L}{W C_{bg} V_{ds}}$, where $\frac{dI_{d,corr}}{dV_{bg}}$ represents the transconductance (derivative of the transfer curve), L and W are the channel length and width, respectively, C_{bg} is the back-gate capacitance (approximately 10^{-4} F m^{-2}), and V_{ds} is the source-drain voltage bias (1 V). In the measured gate voltage range, the maximum field-effect mobility observed is around 10 cm^2 V^{-1} s^{-1}. This value of the mobility is comparable to previous work on CVD-grown WSe_2, which has shown mobility in few-layer WSe_2 on the order of 10 to a few 10's cm^2 V^{-1} s^{-1}.[215] For better comparison to other studies, the back-gate voltage was converted to carrier concentration using the expression $n = \frac{(V_{bg} - V_{th})}{eC_{ox}}$, where e represents the electron charge. The threshold voltage (V_{th}) was calculated by extrapolating the slope of the transfer characteristic in the linear regime to 0 A, shown by the dashed lines in Figure 5.13 (c). This transformation allows the mobility to be plotted as a function of carrier concentration, shown in Figure 5.13 (d). In the synthetic WSe_2, the carrier concentration at the maximum mobility was approximately 3×10^{12} cm^{-2}. For exfoliated WSe_2 flakes, the peak in mobility was

observed at a back gate voltage corresponding to a carrier concentration of roughly $5x10^{12}$ cm^{-2}, much higher than the carrier concentration observed in our measurements.[214] Therefore, we expect that the maximum mobility in our synthetic WSe_2 could be several times higher (~50 cm^2 V^{-1} s^{-1}) when measured with similar carrier concentrations. On the growth oxide, the maximum electric field is limited by the maximum output voltage of the measurement system and the high threshold voltage of the devices. Therefore, transfer of the synthetic WSe_2 onto a thinner oxide could show improved mobility under larger electric fields, corresponding to larger carrier concentrations. Additionally, improvements in the mobility are expected through transferring the WSe_2 to hBN, which has been demonstrated previously for graphene.[133, 216] Finally, optimization of the synthesis of this large-area WSe_2 is necessary to control defect concentrations in the samples, which would reduce trapping of charge carriers, lower the threshold voltage, and increase the carrier concentration at a given value of V_{bg}.

5.3 Considerations for High Temperature Heterostructure Synthesis

While the synthesis methods described in the previous sections result in wafer-scale, highly uniform material, it is critical to understand their applicability to heterostructure growth. In particular, at high temperature (>800 °C) interdiffusion of chalcogen atoms becomes a primary concerns. Previous studies have suggested that the transition metal selenides are unstable when exposed to sulfur at high temperature.[217]

To provide insight into the stability of the TMDs during high temperature growth of heterostructures, $MoSe_2$ flakes on SiO_2 were exposed to sulfur vapor at 1050 °C. Figure 5.14 (a) shows the Raman spectra before (black) and after (red) the exposure. Prior to the exposure, the primary $MoSe_2$ Raman mode is present at ~240 cm^{-1}. Following

the high temperature soak, the only Raman modes present are the E_{2g}^{1} and A_{1g} peaks of the MoS_2, suggesting complete conversion from $MoSe_2$ to MoS_2. Figure 5.14 (b) shows the corresponding PL response before and after the sulfur exposure. Prior to exposure time, the PL peak position matches the ~1.5 eV expected for $MoSe_2$. After exposure, the PL peak position shifts to the 1.85 eV expected for MoS_2.

Based on these results, it is concluded that high temperature heterostructure synthesis of a transition metal sulfide on a transition metal selenide is not possible without significant sulfur incorporation into the selenide. As a result, high temperature processes significantly limit the heterostructure combinations that may be directly synthesized. As a result, direct growth of heterostructures must be carried out at lower temperatures in order to provide maximum flexibility for the type of heterostructure.

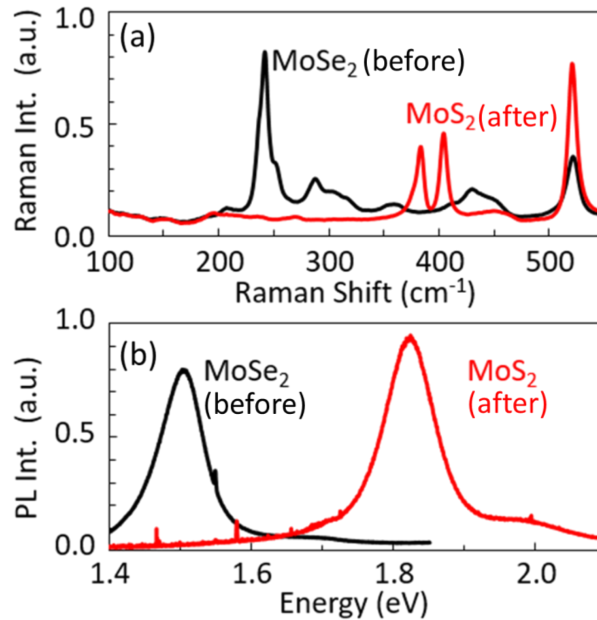

Figure 5.14. (a) Raman and (b) photoluminescence measurements for $MoSe_2$ flakes before (black lines) and after (red curves) exposure to sulfur vapor at high temperature.

CHAPTER 6

LOW TEMPERATURE SYNTHESIS OF TMDS

While the methods described in Chapter 5 provide highly-uniform, wafer-scale TMDs, the temperatures required are too high for direct synthesis of heterostructure devices. In particular, direct growth of heterostructures requires the ability to synthesize TMDs on substrates with metal contacts. As a result, the previously discussed materials are primarily applicable for transfer-based heterostructures. In order to facilitate the direct growth of vertical heterostructures, lower temperature synthesis methods were explored. In particular, synthesis was explored based on the use of H_2S plasma in both direct and remote plasmas. This chapter describes the plasma-based conversion of evaporated MoO_s thin films to MoS_2 and vapor phase growth based on the use of thermally evaporated MoO_3. In addition, a growth method based on the use of sputtered metallic transition metal sources and an H_2S plasma is described. I would like to thank MKS Instruments, Inc. for providing the equipment and manpower to carry out the experiments described in section 6.2.1.

6.1 Low Temperature Growth Methods

Three primary synthesis processes are explored in this work: (1) conversion of e-beam evaporated MoO_x films to MoS_2 using both a remote and direct plasma, (2) vapor phase reaction of thermally evaporated MoO_3 in an H_2S plasma to form MoS_2, and (3) sputter-based growth using metallic Mo or W and H_2S plasma.

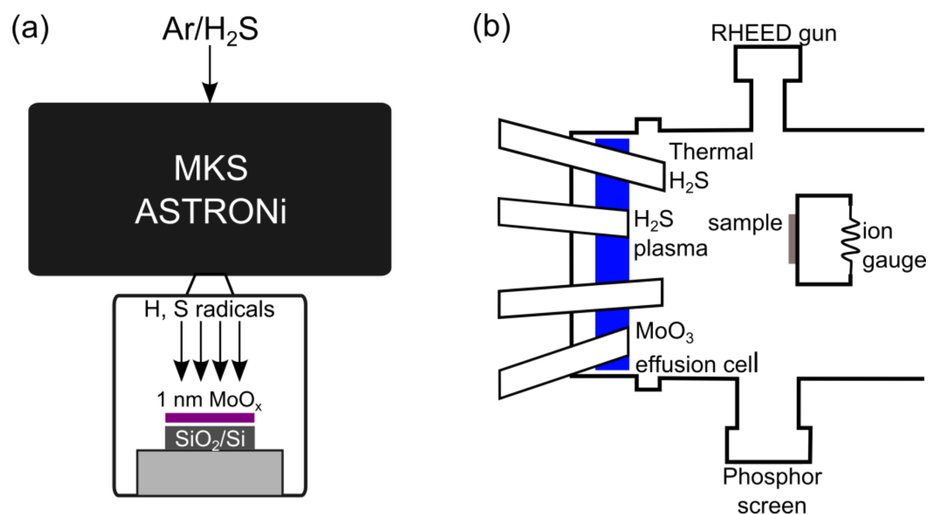

Figure 6.1. Schematic of the MoS_2 synthesis process explored. (a) Process used for remote plasma conversion. The Ar/H_2S gas mixture flows into the ASTRONi plasma source which contains the plasma. H and S radicals flow from the outlet of the plasma source into the chamber and react with the MoO_s film. (b) MBE chamber containing the direct plasma process. The chamber is outfitted with both a thermal and plasma H_2S source, as well as an effusion cell containing MoO_3 for the vapor phase growth method.

Process (1) is modeled after the MoS_2 synthesis process described in Chapter 5.[183] Briefly, a 1 nm Mo thin film is deposited on 270 nm thermal SiO_2 using e-beam evaporation at a rate of 0.3 Å/s. After exposure to air, the film naturally oxidizes resulting in a combination of MoO_2 and MoO_3, referred to as the MoO_x film. This film is then loaded into the respective chamber for each plasma process. The remote plasma process uses an MKS Instruments ASTRONi remote toroidal plasma source, which is directly mounted above a stainless steel chamber pumped out by a roughing pump, as shown in Figure 6.1 (a). The sample is placed on a chuck which can be independently heated to temperatures up to 450 °C. The process uses a mixture of 4% H_2S in Ar as the feed gas.

The direct plasma-based conversion occurs within an MBE system that uses a pure H_2S plasma as one of the sources, as shown in Figure 6.1 (b). The base pressure of the system is ~10^{-8} Torr, with a liquid nitrogen cooling shroud used to freeze out

contaminants. After the Mo thin film is loaded into the chamber, the temperature of the substrate is allowed to stabilize at 400 °C. Finally, the H_2S gas flow is started and the plasma is ignited at a power of 300 W to sulfurize the sample. After exposing the Mo thin film to the plasma for 60 minutes, the sample is isolated from the plasma and the system is pumped down to remove residual H_2S while the sample cools.

Processes (2) and (3) were designed to explore the impact of transition metal reactivity on the effectiveness of plasma sulfurization. Either a single-crystal sapphire wafer or thermal SiO_2/Si was used as the growth substrate. The growth substrate was mounted on a molybdenum substrate block that can be heated as high as 800 °C for the synthesis. For process (2), MoO_3 powder was thermally evaporated using an effusion cell held at 575 °C, which impinged on the sample simultaneously with the H_2S plasma. The H_2S flow in this process is approximately 22 sccm. A thermal gas injector was also fitted to the system, allowing heated H_2S gas to be injected into the chamber to compare the plasma-based process to a purely thermal process. In addition, each of the molecular beam sources has a pneumatic shutter, allowing the precursor beam to be toggled on and off.

Process (3) relies on the use of metallic transition metal sources for TMD growth. Importantly, the use of the metallic source eliminates detrimental oxygen, potentially increasing the material quality over the MoO_3-based method. The sputtered growth is carried out in the MBE system, using the direct H_2S plasma as the sulfur source. Due to the higher pressures required for sputtering versus the creation of a molecular beam, a pulsed process is used in which the transition metal is sputtered using Ar at 20 mTorr. The power of the sputter gun is 20 W and the deposition time is 12 seconds for Mo (18

seconds for W due to the slower sputter rate), corresponding to a deposition of 0.75 ML of MoS_2 or WS_2 per pulse. Following the sputtering step, the Ar flow is restricted, causing the pressure in the chamber to drop into the molecular beam regime. During this time, the metallic film on the substrate is exposed to the H_2S plasma at 300 W for 15 minutes. The H_2S flow is approximately 11 sccm H_2S.

6.2 Conversion of MoO_x to MoS_2

6.2.1 Remote Plasma

The remote plasma samples were processed using 4% H_2S in Ar at a flow rate of 1000 sccm. The substrate temperature was either 400 °C or 450 °C to compare the effect of temperature on the extent of reaction. Prior to H_2S exposure, one set of samples was exposed to a plasma H_2 pre-treatment to reduce the naturally oxidized MoO_x film and increase the driving force for the reaction. The H_2 pre-treatment was carried out with a flow rate of 2000 sccm H_2, a pressure of 0.5 Torr, a plasma power of 4.8 kW, and a temperature of 400 °C for 20 minutes. The H_2S exposure was either completely thermal (no plasma) or used a remote plasma source generated by an MKS Instruments (Andover, MA) ASTRONi. For both the thermal and plasma H_2S exposure, the flow rate of H_2S was 1000 sccm with a chamber pressure of 0.5 Torr and exposure time of 40 minutes. For the plasma exposure, the plasma power was 2.3kW.

Following the H_2S exposure, the chamber was purged under 1000 sccm argon flow for 40 minutes to evacuate any excess sulfur before cooling the sample to room temperature. A summary of the synthesis conditions for each sample is given in Table 1.

Table 6.1. Conditions explored for conversion of MoO_x to MoS_2.

<table>
<tr><th rowspan="2">Sample Identifier</th><th rowspan="2">H_2 Pre-treatment</th><th rowspan="2">H_2S Exposure</th><th rowspan="2">Temperature (°C)</th><th rowspan="2">Results</th><th colspan="2">FWHM (cm^{-1})</th></tr>
<tr><th>E_{2g}^1</th><th>A_{1g}</th></tr>
<tr><td>A1</td><td rowspan="4">No</td><td>Thermal</td><td>400</td><td>No MoS_2</td><td>--</td><td>--</td></tr>
<tr><td>A2</td><td rowspan="2">Plasma</td><td>450</td><td>Large-area MoS_2</td><td>16.6</td><td>10.7</td></tr>
<tr><td>A3</td><td>400</td><td>Patches of MoS_2</td><td>15.1</td><td>9.7</td></tr>
<tr><td>A4</td><td>Thermal</td><td>450</td><td>No MoS_2</td><td>--</td><td>--</td></tr>
<tr><td>B1</td><td rowspan="4">Yes</td><td rowspan="2">Plasma</td><td>450</td><td rowspan="4">Large-area MoS_2</td><td>14.8</td><td>9.8</td></tr>
<tr><td>B2</td><td>550+</td><td>6.4</td><td>6.4</td></tr>
<tr><td>B3</td><td rowspan="2">Thermal</td><td>400</td><td>11.3</td><td>8.5</td></tr>
<tr><td>B4</td><td>450</td><td>10.6</td><td>6.3</td></tr>
</table>

A representative Raman spectrum for each sample is given in Figure 6.2. Each curve is labeled with the respective sample ID, and an asterisk next to the sample ID indicates a sample which was exposed to the plasma H_2S. As noted in Table 6.1, samples with an "A" identifier were not exposed to any pre-treatment before the H_2S step, while those samples with a "B" identifier underwent a pre-treatment using H_2 plasma.

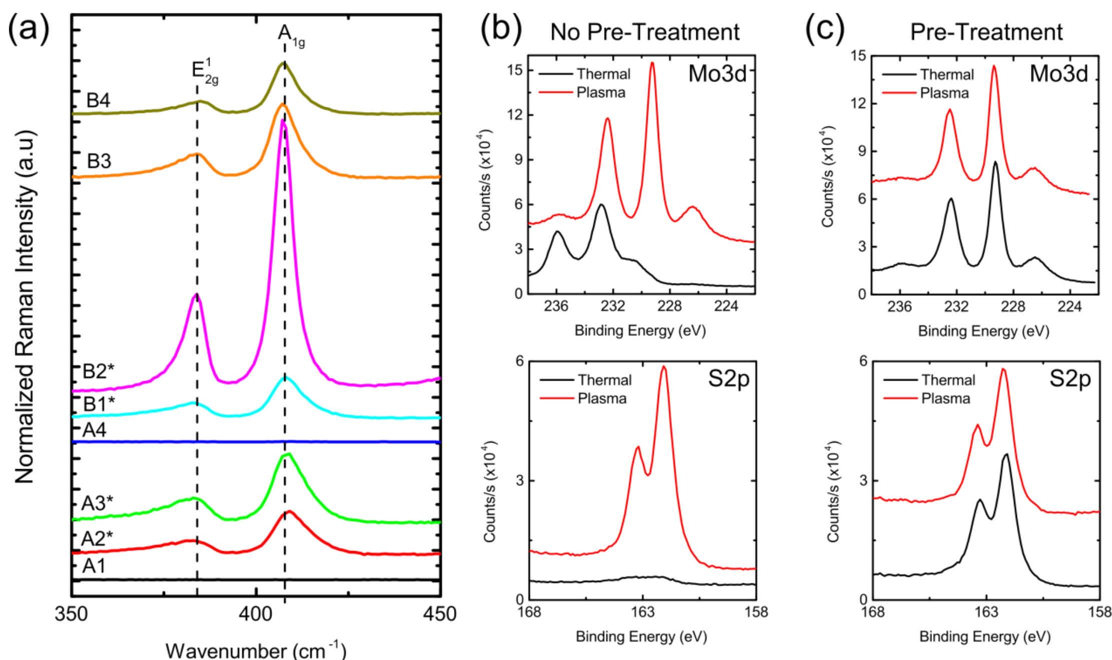

Figure 6.2. (a) Representative Raman spectra for each of the synthesis conditions explored. Samples labeled as "A" have no pre-treatment, while samples labeled as "B" underwent an H_2 plasma pre-treatment prior to H_2S exposure. Samples marked with an asterisk (*) were exposed to remote plasma H_2S, while those without an asterisk underwent the thermal H_2S process. (b) Mo3d and S2p XPS spectra for the samples without pre-treatment. The remote plasma H_2S results in effective conversion to MoS_2, while the thermal process results in minimal sulfur incorporation in the sample. (c) Mo3d and S2p XPS spectra for samples with pre-treatment. Both the thermal and plasma process result in effective conversion to MoS_2.

Figure 6.2 (a) shows representative Raman spectra for each of the synthesis conditions given in Table 1. Each curve is labeled with the respective sample ID, and an asterisk next to the sample ID indicates that the sample was processed using the H_2S remote plasma. The dashed lines represent the positions of the E_{2g}^1 and A_{1g} peaks for trilayer MoS_2, with a separation of 23.5 cm^{-1}. The presence of these two characteristic peaks in the Raman spectrum indicates the presence of MoS_2 on the sample, while the absence of the two peaks suggests there is no MoS_2 present on the sample surface.

For the samples which did not undergo the H_2 pre-treatment step (identifier A), the only samples with successful conversion to MoS_2 were the samples which were exposed to the remote H_2S plasma. The samples with only thermal H_2S did not convert from the initial MoO_x to MoS_2. In addition, the comparison of samples A2 and A3 suggests a strong temperature dependence of the efficiency of conversion. Sample A3, which was processed at a lower temperature, exhibits much weaker Raman peaks and the material is patchy rather than uniform. In contrast, sample A2, processed at a higher temperature, displays strong Raman peaks and the material is uniform across the substrate.

Interestingly, all of the samples which underwent the H_2 pre-treatment step (identifier B) resulted in conversion to MoS_2, regardless of whether the H_2S exposure was thermal or plasma-based. Further, the Raman peak separation for each sample is the same, suggesting a similar extent of reaction on each of the samples. It should be noted that sample B2 was processed at higher temperature than the other samples, resulting in the much stronger Raman peak intensity and narrower FWHM of the Raman peaks compared to the other samples.

These results suggest that the limiting factor in the conversion of MoO_x to MoS_2 is the reduction of the MoO_x to a more metallic state, which is achieved through the reaction with H radicals. Depending on the oxidation state of the molybdenum, the conversion reaction has a drastically different free energy of reaction. As a result, the oxidation state of the molybdenum is expected to significantly impact the extent of reaction with H_2S. The possible reactions and associated enthalpies of reaction are[218, 219]

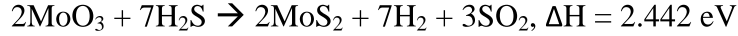

$$2MoO_3 + 7H_2S \rightarrow 2MoS_2 + 7H_2 + 3SO_2, \Delta H = 2.442 \text{ eV}$$

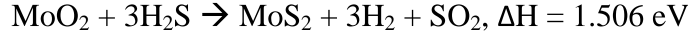

$$MoO_2 + 3H_2S \rightarrow MoS_2 + 3H_2 + SO_2, \Delta H = 1.506 \text{ eV}$$

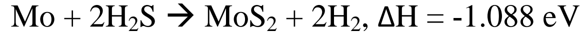

$$Mo + 2H_2S \rightarrow MoS_2 + 2H_2, \Delta H = -1.088 \text{ eV}$$

For the samples without H_2 pre-treatment, only the plasma H_2S samples were exposed to a source of H radicals, generated by splitting the H_2S molecules. The H radicals in the plasma reduce the MoO_x lowering the energetic barrier and allowing the reaction to proceed. In contrast, the energetic barrier to the conversion is too large in the case of the thermal H_2S process, resulting in the observed lack of conversion. The strong temperature dependence of the results suggests that the reduction of the MoO_x may be incomplete and the additional thermal energy in the higher temperature sample is necessary to drive the reaction. In the case of samples with H_2 plasma pre-treatment, there is an abundance of H radicals during the pre-treatment step, which readily reduce the MoO_x film prior to exposure to the H_2S. Due to the higher flow rate of H_2 for the pre-treatment step, the MoO_x film is likely reduced further compared to the plasma H_2S process for sample set A. As a result, even the lower temperature and thermal H_2S reactions have sufficient energy to drive the conversion, resulting in the presence of MoS_2 under all synthesis conditions.

To further compare the differences between the different synthesis conditions, XPS measurements were performed on representative samples from each sample set, as shown in Figure 6.2 (b) and (c). For the case without pre-treatment (Figure 6.2 (b)), the thermal sample Mo 3d spectrum is primarily made up of molybdenum oxide peaks, demonstrated by the strong peaks at 232.7 eV and 236 eV.[220] The plasma sample shows

primarily MoS_2 peaks, along with the S 2s peak at 226 eV and a small MoO_3 peak at 236 eV, suggesting either some residual MoO_3 in the film or slight re-oxidation of the sample due to atmospheric exposure. In the S 2p spectrum, the thermal H_2S process results in only a small amount of sulfur incorporation into the sample, consistent with the Raman data which indicated that there was no MoS_2 on the sample. However, the plasma H_2S sample shows a strong S 2p signal, further confirming that the plasma process more efficiently reacts sulfur with the MoO_x surface.

For the H_2 pre-treated samples (Figure 6.2 (c)), both the thermal and plasma samples are characterized primarily by the Mo $3d^{5/2}$ and $3d^{3/2}$ originating from the MoS_2 and the S 2s peak, suggesting that both the thermal and plasma processes result in a similar extent of reaction. Similarly, the S 2p spectra for the thermal and plasma processes are very similar, further suggesting that the reactions are very similar for the two samples. To calculate the stoichiometry of the MoS_2 in each sample, the area of the Mo 3d peaks from the MoS_2 was normalized by a sensitivity factor of 2.75 and the area of the sulfur peaks was normalized by a sensitivity factor of 0.54.[206] Division of the normalized sulfur peak area by the normalized Mo3d peak area results in an estimate of the stoichiometry of the sample. Using this method, the stoichiometry of the plasma H_2S sample without pre-treatment is 1.97, the stoichiometry of the pre-treated plasma sample is 1.79, and the stoichiometry of the pre-treated thermal sample is 2.03. These results further suggest that reduction of the MoO_x by H radicals plays a significant role in determining the extent of reaction in these samples.

6.2.2. Direct Plasma

To further investigate plasma-assisted sulfurization of MoS_2, sulfurization was also explored using direct plasma as part of an MBE system. Unlike the remote plasma, the direct plasma extends partially into the MBE chamber, which may change the dynamics and efficiency of reaction.

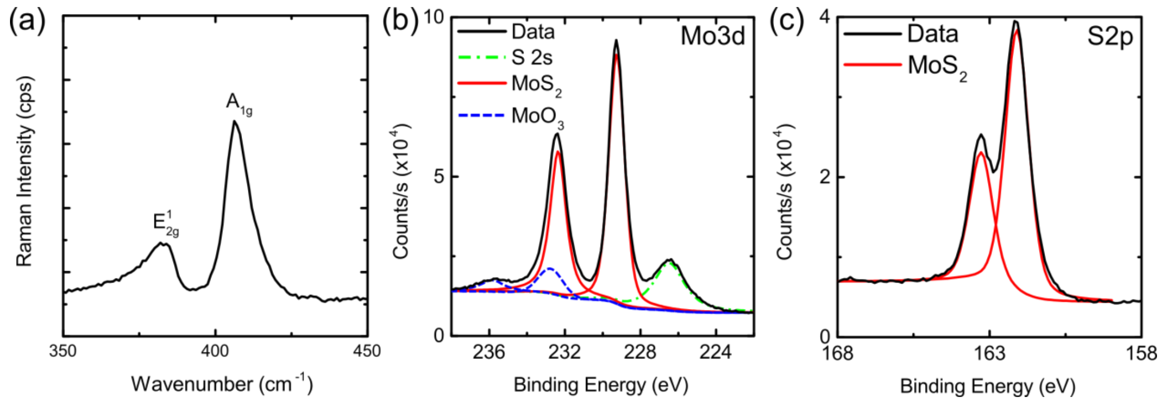

Figure 6.3. (a) Raman spectrum after conversion of MoO_x film to MoS_2 using direct plasma. (b) Mo 3d spectrum of the sample converted using direct plasma. The red curves represent the Mo $3d^{5/2}$ and Mo$3d^{3/2}$ from MoS_2 bonding and the blue curves represent the Mo $3d^{5/2}$ and Mo $3d^{3/2}$ due to MoO_3 bonding. The green curve represents the S 2s peak. (c) S 2p spectrum from the direct plasma sample. The sulfur spectrum is characterized by only two peaks, confirming that all sulfur in the sample has reacted with molybdenum.

Figure 6.3 (a) shows a representative Raman spectrum after exposure of the MoO_x film to the ECR plasma. The sample exhibits strong $E_{2g}^1$and A_{1g}peaks, confirming conversion of the film to MoS_2. The peak separation between the $E_{2g}^1$and A_{1g} is approximately 23.2 cm^{-1}, consistent with the trilayer thickness of MoS_2 expected. The FWHM of the $E_{2g}^1$and A_{1g} peaks are 11.3 cm^{-1} and 9.4 cm^{-1}, respectively. These values are similar to those obtained using the remote plasma conversion process, suggesting that

there are not significant differences in the quality of the MoS_2 created using the two processes.

Further characterization of the sample is shown in Figure 6.3 (b) and (c), which contain the Mo 3d and S 2p XPS spectra. The Mo 3d spectrum (Figure 6.3 (b)) is characterized by a strong signal from the MoS_2 (red solid curves) and a small portion of MoO_3 (blue dashed curves). The green dash-dotted curve represents the S2s peak, confirming the presence of sulfur on the sample. The S 2p spectrum (Figure 6.3 (c)) consists of a single doublet, suggesting that all of the sulfur in the sample is bonded to Mo in the sample. By taking the ratio of the normalized sulfur peak area to the normalized MoS_2 peak area, the stoichiometry of the sample is calculated as 1.79, suggesting that the sample is significantly sulfur deficient.

Comparison of the results using the direct plasma and the remote plasma processes do not reveal significant differences between the two processes. For the samples which underwent plasma H_2 pre-treatment prior to exposure to the remote H_2S plasma and the direct plasma, conversion to MoS_2 is possible at 400 °C. However, the remote H_2S plasma sample by itself is not sufficient to result in complete conversion to MoS_2 at 400 °C, suggesting that the direct plasma more efficiently converts the sample to MoS_2 at lower temperatures. One potential explanation for this is that bombardment of the sample by ionized species created by the direct plasma induces defects in the sample which lowers the energetic barrier for sulfurization.

6.3 Vapor Phase Growth of MoS_2

A second set of experiments was performed to examine the effect of molybdenum precursor reactivity on the temperature required for MoS_2 synthesis. One method uses a

vapor phase reaction between MoO_3 thermally evaporated from an effusion cell and H_2S which was either thermally injected or injected through the direct plasma. The use of thermally evaporated MoO_3 potentially changes the reaction kinetics because the precursor can be simultaneously reacted with the H_2S as the film is deposited.

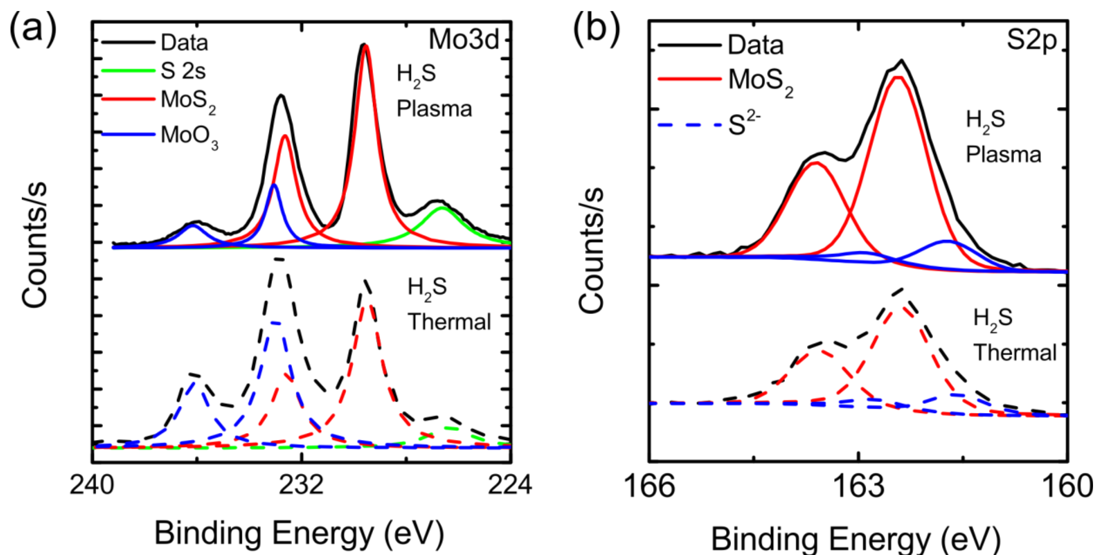

Figure 6.4. (a) Comparison of the Mo3d spectra for the plasma (solid lines) and thermal (dashed lines) vapor phase processes. While both samples exhibit a prominent peak resulting from MoO_3 in the sample, the plasma sample has a smaller MoO_3 peak, confirming that the plasma-based process results in a greater extent of reaction. (b) Comparison of the S2p spectra for the plasma and thermal processes. The red curve represents sulfur bonded to molybdenum, while the blue curve represents excess sulfur on the sample surface. The plasma sample has stronger peak intensity, indicating that more sulfur has been incorporated into the sample.

An initial set of samples compared the differences between thermally injected H_2S and plasma H_2S, both with a substrate temperature of 800 °C. Figure 6.4 shows a comparison between the (a) Mo 3d XPS spectra and (b) the S 2p XPS spectra for each of the two processes. The main difference between the two samples is the amount of MoO_3 in the samples after the growth. There are two potential sources for the MoO_3: (1)

residual unreacted MoO_3 from the vapor phase precursor, and (2) MoO_3 as a result of oxidation that occurs at grain boundaries or defects after the sample is exposed to air. From Figure 6.4 (a), it is clear that there is a smaller amount of MoO_3 in the plasma sample compared to the thermal sample. This suggests a larger extent of reaction for the plasma sample, providing evidence that for the vapor phase process, the use of plasma improves the quality of the sample. In addition, Figure 6.4 (b) shows much stronger peak intensity for the sulfur from the plasma sample compared to the thermal sample, suggesting more sulfur incorporation with the plasma-based process. Based on the XPS data, the stoichiometry of the MoS_2 within the sample was calculated based on the ratio of the normalized areas of the MoS_2 3d peaks and the S 2p peaks. It should be noted that because of the similarity in peak positions, this calculation potentially includes MoO_2 within the sample as well as the MoS_2. For the thermal sample the stoichiometry is 0.72:1 S:Mo, suggesting highly substoichiometric MoS_2 and the presence of a significant amount of MoO_2 in the sample. In the plasma sample, the stoichiometric ratio is 1.52:1 S:Mo, indicating an increase in the reaction due to the plasma.

Further evidence of the increased extent of reaction for the plasma sample can be found in the Raman data for the samples, shown in Figure 6.5. Figure 6.5 (a) shows several representative Raman spectra taken across the surface of the thermal sample, while Figure 6.5 (b) shows Raman spectra for the plasma sample. Both samples show characteristic MoS_2 peaks, confirming successful synthesis of MoS_2 using the vapor phase growth process. However, the peak separation, indicative of sample thickness, is larger for the plasma process than the thermal process. Because both samples were exposed to an identical flux of MoO_3 for the same amount of time, the larger peak

separation in the plasma sample must be a result of an increased extent of reaction for the plasma reaction. This provides further evidence that plasma-assisted synthesis results in higher quality growth than comparable thermal methods.

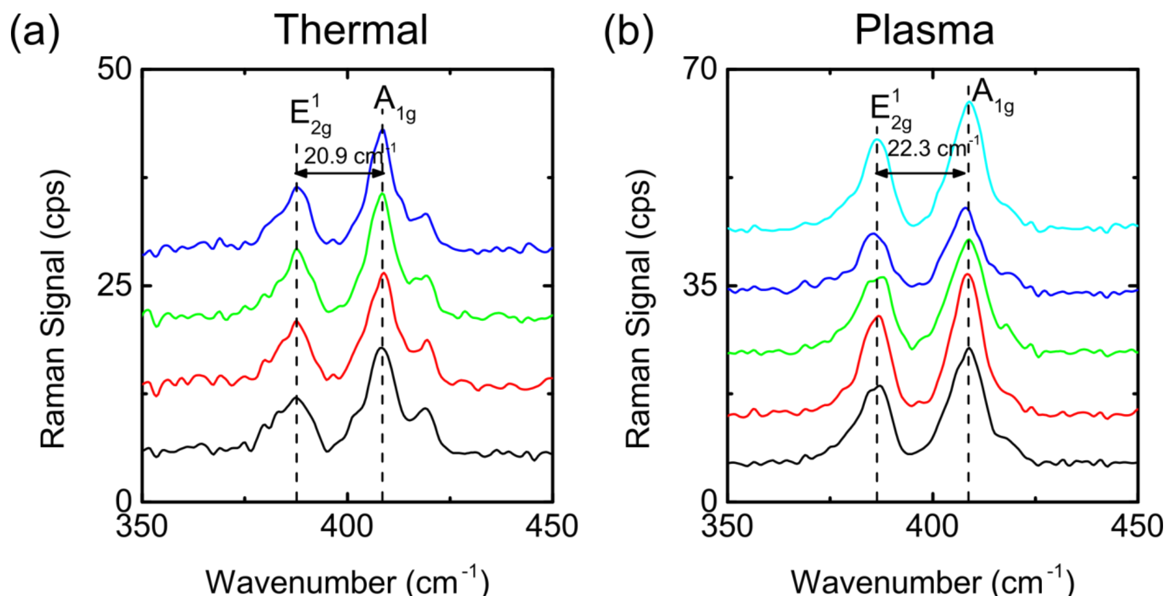

Figure 6.5. Comparison of the Raman spectra for the thermal (a) and plasma (b) vapor phase processes. Both processes result in the formation of MoS_2 on the sample surface. However, the peak separation is larger for the plasma process than the thermal process, indicating thicker MoS_2 on the plasma sample. Because the total amount of MoO_3 supplied to the sample is identical in both cases, the larger peak separation indicates that the use of plasma processing resulting in a larger extent of reaction between sulfur and MoO_3.

As an additional comparison between the thermal and plasma-assisted growth methods, RHEED patterns were captured on the two substrates, as shown in Figure 6.6. Clear streaks are visible in the RHEED pattern for both materials, indicative of the two-dimensional growth of MoS_2 on the sapphire surface.[102, 103] Despite the difference in quality, as shown by the previous XPS and Raman data, the RHEED streaks for both the thermal process and the plasma-assisted process have identical spacing. This suggests

that the MoS_2 synthesized through both the thermal and plasma processes has similar physical structure. Based on the geometry of the MBE system and the spacing between the streaks in the RHEED pattern, the lattice constant of the MoS_2 is estimated as 3.13 Å, similar to the value of 3.15 Å expected for MoS_2.[221] This result confirms that MoS_2 grows unstrained on the sapphire substrate.

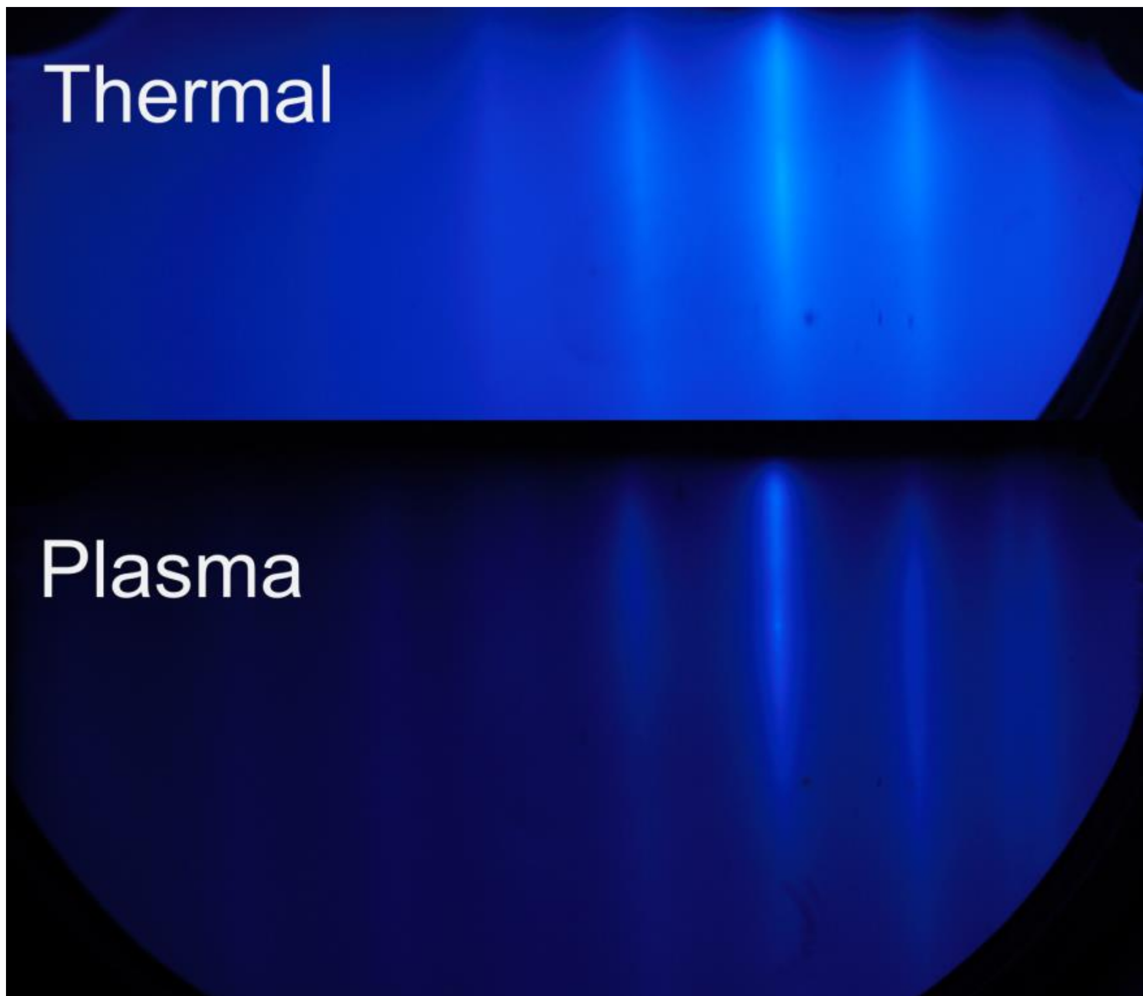

Figure 6.6. RHEED patterns measured on the thermal and plasma-assisted growths at 800 °C. The presence of streaks indicates the two-dimensional growth mode of the MoS_2. The spacing between the streaks corresponds to a lattice constant of 3.13 Å.

In an attempt to improve the quality of the plasma process, the MoO_3 vapor phase precursor was pulsed on and off every 10 minutes during the growth to provide a longer time for the sulfur plasma to react with the MoO_3. Additionally, samples were prepared at substrate temperatures of both 400 and 800 °C to measure the efficacy of the plasma process at lower temperatures. Figure 6.7 compares the (a) Mo 3d and (b) S 2p spectra for the low- and high-temperature growths. There are no clear differences between the spectra, suggesting that the lower temperature does not significantly impact the extent of reaction and suggesting that this plasma process is viable to low temperatures. In these samples, the measured stoichiometry of the MoS_2 is 1.66:1 S:Mo for the 800 °C sample, compared to 2.23:1 S:Mo in the 400 °C sample. At elevated temperatures, the MoS_2 becomes unstable in a high vacuum environment and releases sulfur into the vacuum.[222] Because the samples are cooled under vacuum rather than in a flux of H_2S plasma, it is possible that the 800 °C loses sulfur during the cooling process. As a result, the measured stoichiometry of the 800 °C sample is lower than that of the 400 °C sample.

Thermal processes at 400 °C (data not shown) do not exhibit sulfurization of the sample, providing further evidence that the plasma is necessary to achieve low-temperature growth. Subsequent runs have demonstrated the use of the low temperature plasma growth process for growth on arbitrary substrates, including gold surfaces, SiO_2, and amorphous Al_2O_3.

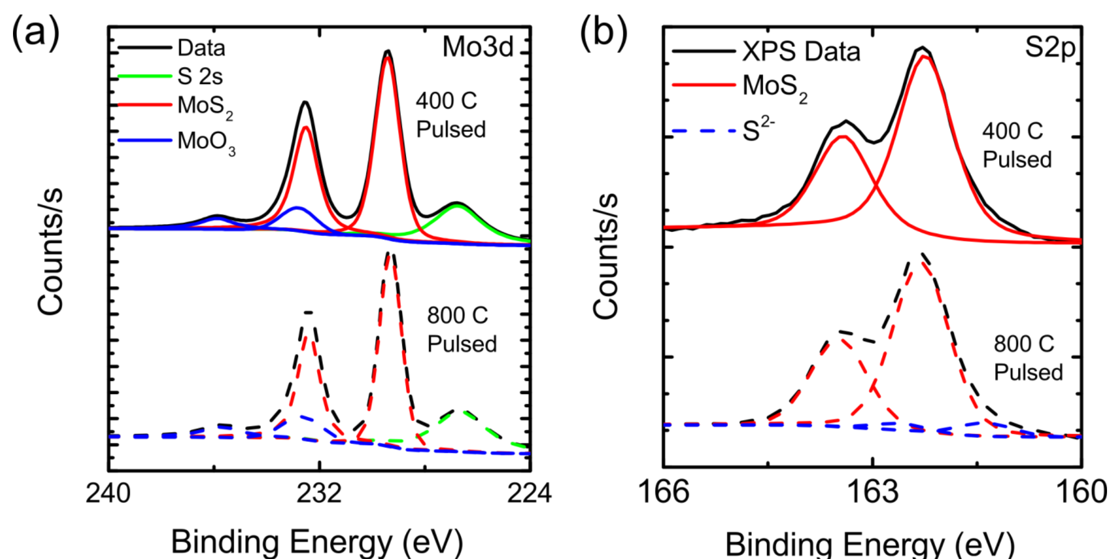

Figure 6.7. (a) Comparison of Mo3d for the pulsed MoO_3 process at 400 °C (solid) and 800 °C (dashed). The spectra are identical, suggesting that plasma processing enables low temperature processing without sacrificing material quality. (b) Comparison of S2p spectra for the low and high temperature pulsed MoO_3 processes. The high temperature sample exhibits a small amount of excess sulfur on the surface. Aside from the excess sulfur, the spectra are similar.

To evaluate the uniformity of the low-temperature MoS_2 films on sapphire, Raman mapping was performed, as shown in Figure 6.8. A map size of 500 μm x 500 μm was used, with 50 μm spacing between the points. Figure 6.8 (a) shows the positions of the E_{2g}^{1} and A_{1g}peaks in the sample, demonstrating very little variation across the area of the map and a corresponding uniform sample thickness as a function of position. Based on this data, the average peak separation is 24.1 ± 0.24 cm^{-1}. Figure 6.8 (b) shows the full-width at half maximum (FWHM) for the E_{2g}^{1} peak, while Figure 6.8 (c) shows the FWHM for the A_{1g}peak as a function of measurement position. The FWHM of the peaks is relatively uniform, indicative of uniform quality of the MoS_2 as a function of measurement position.

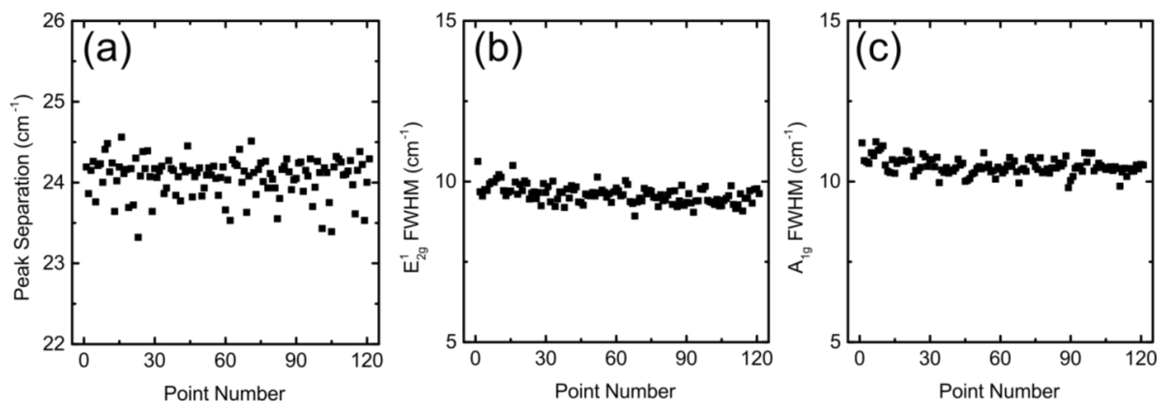

Figure 6.8. Results of Raman mapping on low-temperature pulsed MoO_3 samples. (a) Peak separation between the E^1_{2g} and A_{1g}peaks versus point number. The peak separation is relatively uniform across the sample surface, indicating a uniform sample thickness over a large area. (b) E^1_{2g} and (c) A_{1g} full width at half maximum (FWHM) versus peak position, indicating uniform quality of MoS_2 across the sample surface.

6.4 Low Temperature Growth of MoS_2 using Metallic Sources

The final growth method for low-temperature MoS_2 synthesis relies on the use of sputtered Mo rather than the MoO_3 used in the previous section. Similar to the best results obtained for the MoO_3-based method, a cyclical process is used in which a small amount of metallic Mo is sputtered onto the substrate, followed by an H_2S soak to sulfurize the material. Because the two processes are similar, differences in the synthetic MoS_2 films should only result from differences in the nature of the reaction with the Mo precursor.

Figure 6.9 shows Raman data of the MoS_2 films after synthesis, confirming the formation of MoS_2. The peak separation between the $E^1_{2g}$and A_{1g}peaks is 23.1 cm^{-1}, confirming that the sputtered growth process results in the formation of trilayer MoS_2. By extending the number of cycles in the growth, the thickness of the sample can be tailored

for specific applications. The FWHM for the $E_{2g}^{1}$and A_{1g}peaks are estimated as 9.1 cm^{-1} and 7.4 cm^{-1}, respectively.

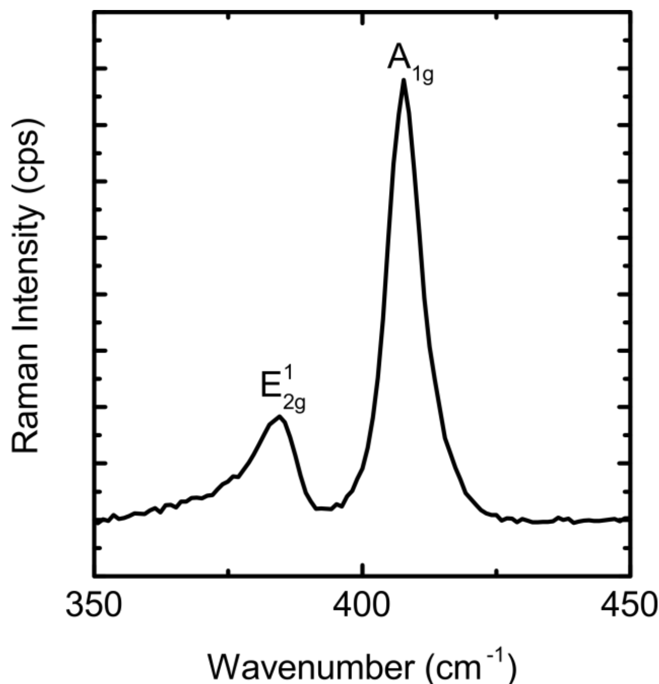

Figure 6.9. Raman spectrum of the MoS_2 grown using a sputtered Mo source and direct H_2S plasma.

Figure 6.10 shows the XPS spectrum of the MoS_2 film after synthesis on SiO_2 substrates. Part (a) shows the Mo 3d spectrum, consisting of only the S 2s peak and the doublet corresponding to the Mo 3d$^{5/2}$ and 3d$^{3/2}$ for MoS_2 bonding. Notably, there is not a significant peak corresponding to MoO_3 in the film, suggesting that the film is composed only of MoS_2. This represents an improvement over the pulsed MoO_3 method discussed above. Part (b) shows the S 2p spectrum for the MoS_2 film, confirming a successful incorporation of sulfur in the film. Based on the XPS results, the stoichiometry of the sputter-based MoS_2 is ~2.14, indicating an excess of sulfur in the films.

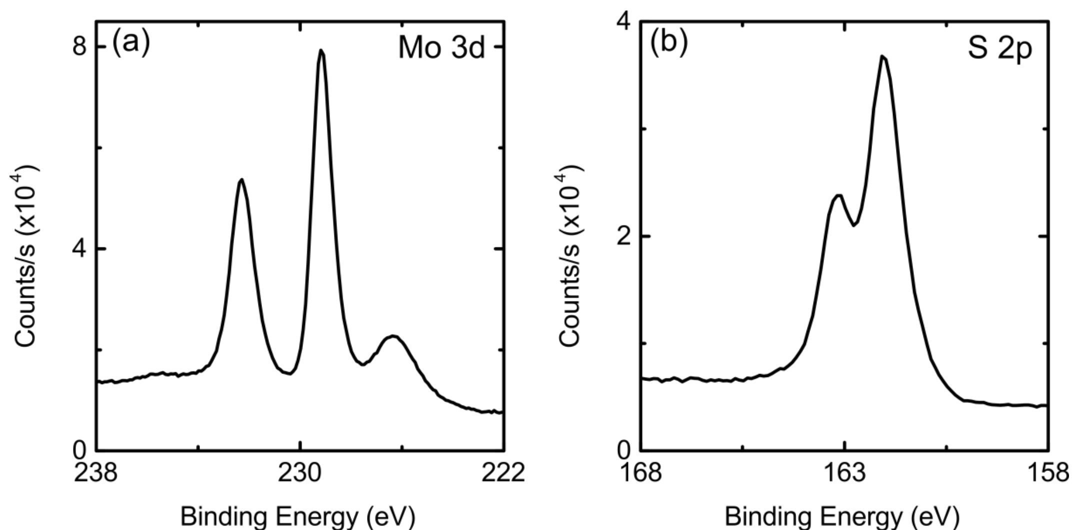

Figure 6.10. (a) Mo 3d and (b) S 2p XPS spectra for the MoS_2 grown by cyclical growth based on sputtered Mo and direct H_2S plasma at low substrate temperature.

6.5 Comparison of Low Temperature Growth Methods

Photoluminescence (PL) measurements were used to compare the characteristics of films grown using the different low-temperature growth methods, with the results shown in Figure 6.11. All of the PL spectra were collected on SiO_2 substrates to ensure differences in the PL are the result of differences in the material. The sputtered MoS_2 (black curve) and pulsed MoO_3-based MoS_2 (red curve) both exhibit PL which is characteristic of MoS_2, with the A exciton at 1.84 eV and the B exciton at 2.0 eV.

The MoS_2 grown by converting evaporated MoO_x in direct plasma H_2S (green curve) shows only a single peak at 2.0 eV. While it is difficult from the given data to deduce the exact nature of the converted film, one possible explanation for this peak is that the conversion-based approach results in strain within the film, which changes the band structure of the MoS_2.[44, 46, 223, 224] Previous DFT studies on MoS_2 suggested that

small amounts of compressive biaxial strain slightly increase the bandgap of the MoS_2, which would account for the observed shift in the PL peak.[223]

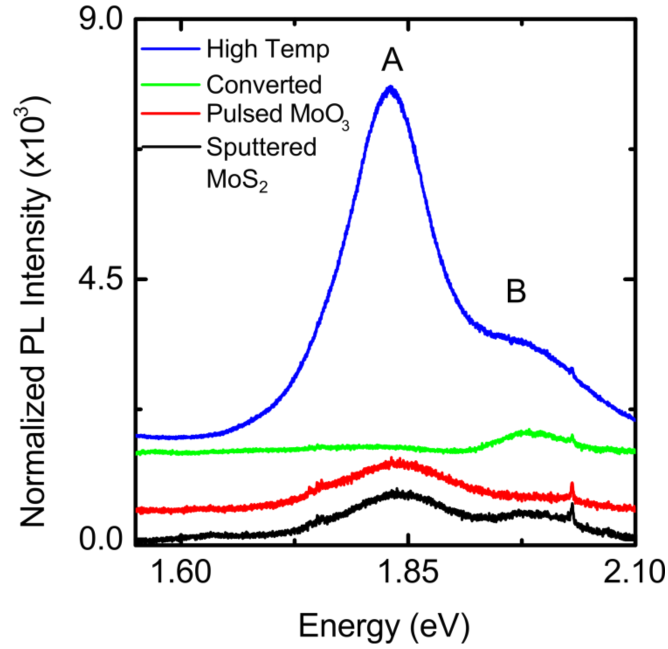

Figure 6.11. Comparison of PL response for different low temperature growth methods, including the sputtered-Mo based method (black curve), the pulsed MoO_3 method (red curve), and conversion of a thin MoO_x film using direct plasma (green curve). The PL response of a high temperature sample grown by conversion of MoO_x in sulfur vapor (blue curve) is included for comparison.

The blue line in Figure 6.11 represents MoS_2 grown by converting an evaporated MoO_x film to MoS_2 using sulfur vapor at high temperature. As expected, both the A and B excitons are present in the PL response. The biggest difference between the high temperature and lower temperature samples is that the PL intensity of the high temperature growth is significantly higher than the low temperature samples. This difference in intensity indicates that the high temperature growth results in higher quality MoS_2 than the lower temperature growths.

CHAPTER 7

STRUCTURE AND DEFECTS IN TMDS

The low temperature synthesis methods explored in Chapter 6 provide the building blocks for the creation of vertical heterostructures. Using the MBE system, it is possible to directly grow heterostructures in a transfer-free process. Two specific 2D vertical heterostructures were explored for this work: (1) MoS_2-Al_2O_3-MoS_2 based on the pulsed MoO_3 synthesis method, and (2) MoS_2-WS_2 using the sputter-based synthesis method. This chapter includes a comparison of the behavior of the layers which comprise the heterostructure in isolation to the behavior as part of the heterostructure.

7.1 MoS_2-Al_2O_3-MoS_2

Because of the requirement for direct growth of heterostructures on a variety of arbitrary substrates, it is important to understand whether the structure of the film changes depending on the growth substrate. Of particular interest is whether the grain size and crystallinity of the film are dependent on the crystalline nature of the substrate. While the films are too thin for grazing incidence x-ray diffraction (GIXRD) measurements to examine the crystal structure, some information about the crystallinity can be inferred from the Raman data of the films grown on different substrates. As observed for the high-temperature growth of MoS_2 in Chapter 5, the FWHM of the MoS_2 Raman peaks decreases as the quality of the film increases.

For the pulsed MoO_3 process, the films synthesized using 10 minute MoO_3/10 min H_2S pulses and 5 min MoO_3/10 min H_2S pulses were compared. Figure 7.1 (a) and (b) show representative Raman spectra for MoS_2 grown on sapphire (black curve),

amorphous ALD Al_2O_3 on thermal SiO_2 (red curve), and on gold contact pads (green curve) for the 10 minute MoO_3 and 5 minute MoO_3 processes, respectively. Each of the films displays the same peak separation, indicating similar sticking of the MoO_3 to each substrate.

Figure 7.1 (c) shows the FWHM for the E_{2g}^{1} and the A_{1g} peaks for each process. The FWHM of the Raman peaks does not vary significantly with the different substrates used, suggesting that the quality of the grown material is similar. However, on all substrates, the E_{2g}^{1} peak is very asymmetric, leading to the much larger FWHM of the E_{2g}^{1} peak compared to the A_{1g} peak. Previous work on WS_2 demonstrated asymmetry in the Raman spectrum of nanocrystalline WS_2 due to increased structural disorder in the material compared to single crystal samples.[225] Based on these observations, it is likely that the MoS_2 grown at low temperature using the plasma-assisted process is more nanocrystalline and of lower quality than the high-temperature MoS_2 synthesized in the tube furnace (Chapter 5).

In addition, the Raman spectrum (not shown) was collected for the 5 minute MoO_3 process with the addition of a MoO_3 seed layer. This sample was grown on ALD Al_2O_3 on SiO_2 substrates used for the complete heterostructure growth, as discussed later. The right side of Figure 7.1 (c) shows the measured FWHM of the Raman peaks, which are larger than the FWHM for the MoS_2 film by itself. The broadening of the Raman peaks after deposition of MoO_3 is indicative of interactions between the MoS_2 and MoO_3 films, including effects such as strain or doping that potentially affect heterostructure performance. In particular, MoO_3 forms a defect level which aligns with

the MoS_2 valence band, resulting in p-type doping of the MoS_2.[226] As a result, MoO_3 has previously been studied as a contact for p-type transport in MoS_2.[227]

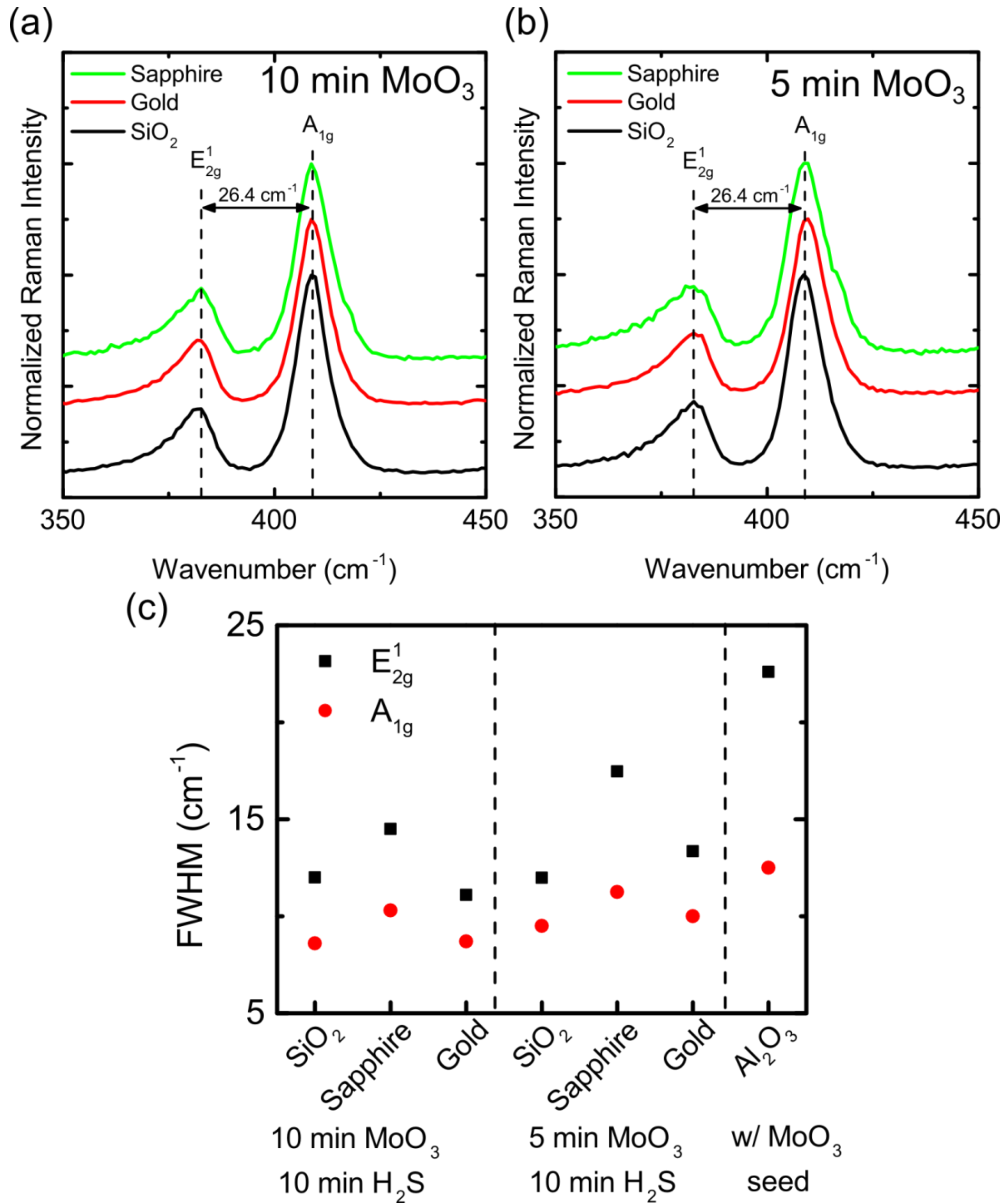

Figure 7.1 (a,b) Representative Raman spectra for growths on SiO_2 (black curve), gold (red curve), and sapphire (green curve) for the (a) 10 min MoO_3 and (b) 5 min MoO_3 pulsed growths. (c) FWHM of the Raman peaks on each substrate for the two growth methods. The FWHM for the 5 min MoO_3 pulsed growth with the addition of an MoO_3 seed layer is included as well.

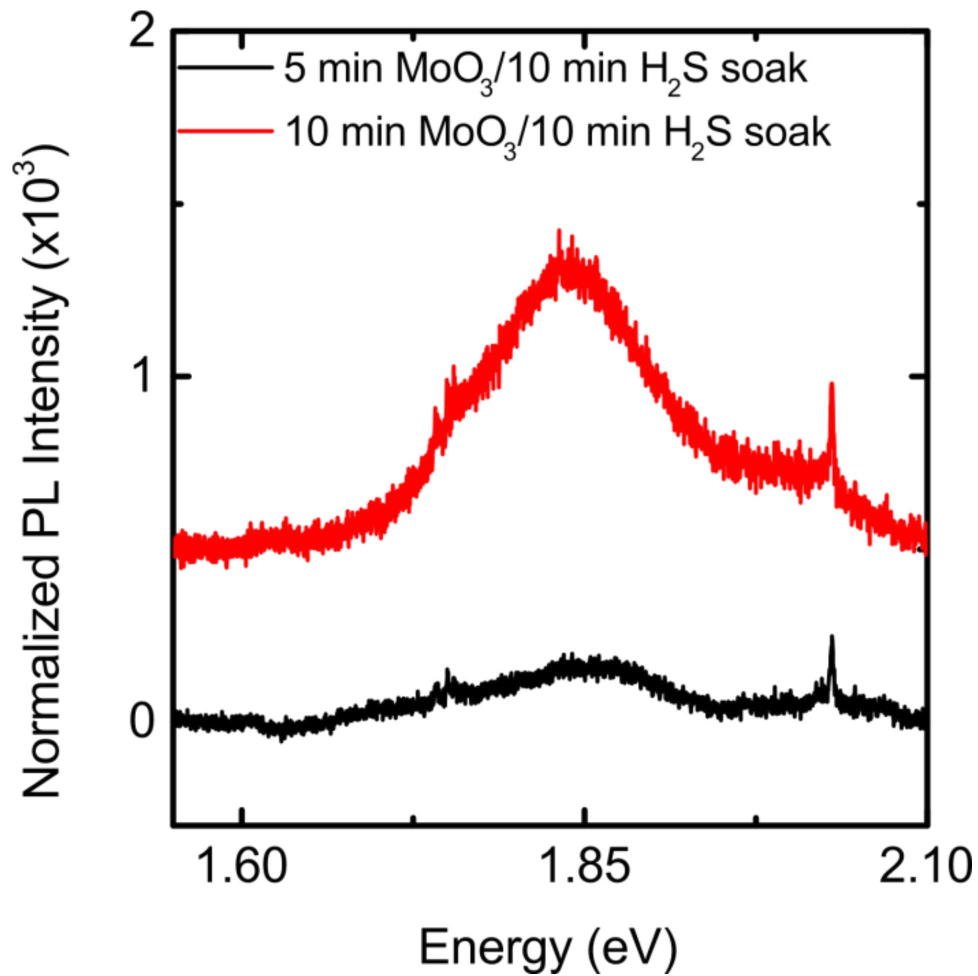

Figure 7.2. Comparison of the PL response of the 5 minute MoO_3 (black curve) and 10 minute MoO_3 (red curve) growth methods.

To provide additional information about the quality and defect structure of the MoS_2, photoluminescence data was collected for each growth method. Figure 7.2 compares the PL spectra for the 5 min MoO_3 and 10 min MoO_3 growth methods on thermal SiO_2. To ensure a good comparison, the intensity of the PL spectrum for each growth method was normalized using the intensity of the Raman peaks. Both samples exhibit the presence of the A and B excitons at 1.85 eV and 2.0 eV, respectively.

However, the PL intensity for the 5 minute MoO_3 sample is much smaller than for the 10 minute MoO_3 sample. Based on the Raman spectrum, it is expected that the two films have similar thickness. Therefore, the weaker PL signal indicates lower quality of the 5 minute MoO_3 sample. This is consistent with the Raman measurements from the two samples, in which the FWHM of the 5 minute MoO_3 samples was slightly larger than that of the 10 minute MoO_3 samples. A second contributing factor to the difference in PL response is the stoichiometry of the films. The 5 minute MoO_3 films are substoichiometric, resulting in n-type doping of the film, while the 10 minute MoO_3 films are superstoichiometric, resulting in p-type doping. Previous studies of the relationship between doping and PL response of MoS_2 suggested that p-type doping results in increased PL intensity, while n-type doping suppresses the PL response.[17, 228, 229]

Growth of MoS_2-Al_2O_3-MoS_2 heterostructures was based on the pulsed MoO_3 method using H_2S plasma sulfurization at 400 °C. The bottom layer was grown using pulse times of 5 minutes of MoO_3 exposure followed by 10 minutes of H_2S soak to sulfurize the MoO_3, with a total of four pulses. Prior to the first MoO_3 pulse, the growth substrate was exposed to the H_2S plasma for 10 minutes. The resulting thickness is expected to be 4-5 layers of MoS_2.

After the final H_2S pulse for the bottom layer, the H_2S flow was turned off and an additional two minutes of MoO_3 was deposited onto the bottom layer MoS_2 to serve as a seeding layer for the Al_2O_3 interlayer. 45 cycles of ALD Al_2O_3 were deposited at 250 °C for an estimated thickness of ~4.5 nm. After Al_2O_3 deposition, the top layer MoS_2 was grown following the same method as the bottom layer, without the MoO_3 seeding layer.

The properties of the MoS_2-Al_2O_3-MoS_2 heterostructure were explored in order to understand the influence of interlayer interactions on device performance. Figure 7.3 (a) and (b) show the Mo3d and S2p spectra after deposition of the bottom layer (BL) of MoS_2 (black curve), the deposition of the MoO_3 seed prior to ALD deposition (red curve), and after deposition of the top layer of MoS_2 to complete the entire heterostructure. To account for differences in signal intensity between the measurements, each spectrum was normalized by the maximum height in the spectrum (either the Mo $3d^{5/2}$ or the S $2p^{3/2}$ peak). The binding energy was adjusted using the peak position for adventitious carbon to account for any charging which occurred during the measurements.

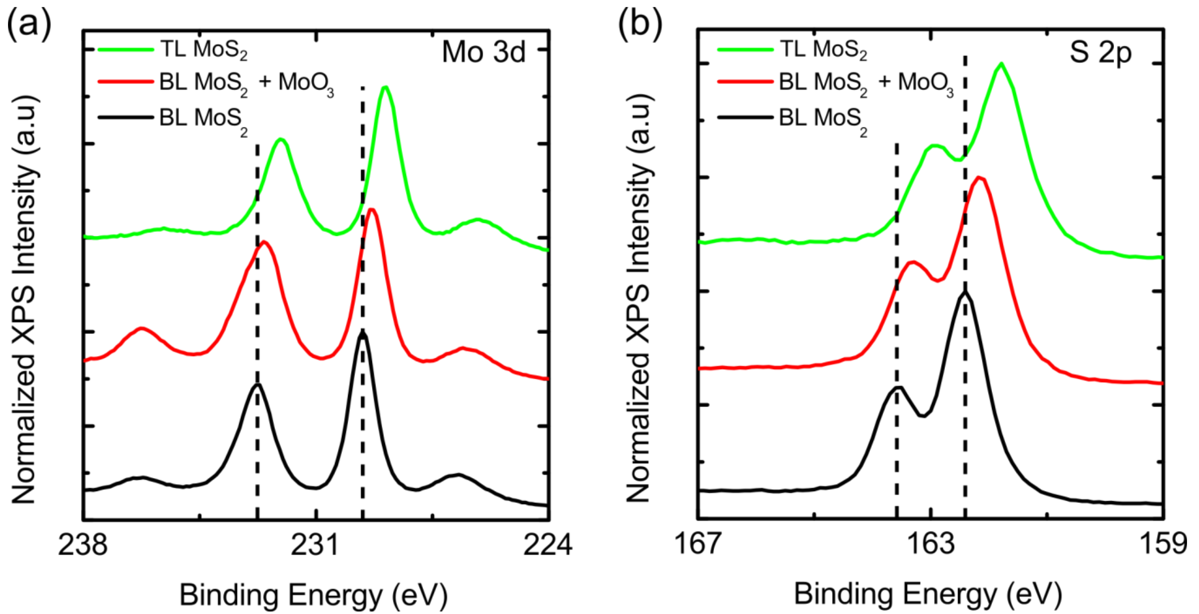

Figure 7.3. XPS comparison of the (a) Mo 3d and (b) S 2p spectra at different steps during growth of the MoS_2-Al_2O_3-MoS_2 heterostructure. The black curve was measured after deposition of the bottom layer MoS_2, the red curve represents the bottom layer of MoS_2 with the addition of a MoO_3 seeding layer, and the green curve was measured after growth of the top layer of MoS_2.

Comparison of the red and black curves reveals the effect of the MoO_3 seeding layer on the bottom layer of MoS_2 in the heterostructure. As expected, the red curve displays a much larger MoO_3 peak at 236 eV, which mainly results from the MoO_3 seeding layer. The MoS_2 $3d^{5/2}$ peak at approximately 229 eV remains unchanged, indicating no chemical effects of the MoO_3 deposition on the bottom layer of MoS_2. However, both the Mo 3d and the S 2s peaks from the sample shift to lower binding energy compared to the bottom layer MoS_2, potentially indicating electronic interactions between the MoO_3 and MoS_2 layers. After completion of the heterostructure, the XPS spectrum (green curve) looks similar to the bottom layer of MoS_2 prior to deposition of the MoO_3 seed. The only noticeable difference is an additional shift of the peaks to lower binding energy, suggesting a further effect from electronic interactions through the heterostructure, potentially between the top and bottom layers of MoS_2.

Depth profiling was used to confirm the structure of the MoS_2-Al_2O_3-MoS_2 heterostructure. Figure 7.4 shows the XPS depth profile of the heterostructure. For the sample measured, the heterostructure was grown on an amorphous ALD Al_2O_3 layer on thermal SiO_2. The figure shows the calculated atomic percentage for each elemental species in the sample as a function of the sputtering time, calculated by integrating the total peak area for the element and normalizing by the sensitivity factor for the given element. It is important to note that because the MoS_2 layers and Al_2O_3 interlayer are thinner than the sampling depth of the XPS, each measurement point contains data which is a convolution of multiple layers of the heterostructure.

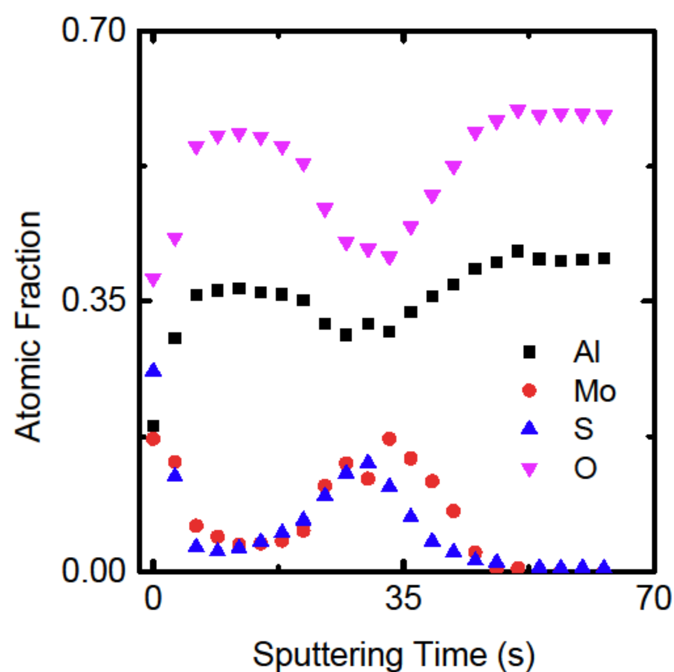

Figure 7.4. XPS depth profiling of the MoS_2-Al_2O_3-MoS_2 heterostructure.

The XPS depth profiling reveals the successful growth of a delineated MoS_2-Al_2O_3-MoS_2 structure. At the initial measurement point (0 seconds), a strong signal is present from both Mo and S, corresponding to the top layer of MoS_2. There is also a significant contribution from Al and O as a result of the signal from the interlayer Al_2O_3 under the MoS_2. Between 0 seconds and 6 seconds, the Mo and S signals decrease with sputtering, while the Al and O signals increase as the top layer of MoS_2 is removed. Between 6 seconds and 21 seconds, the Mo and S signals are at a minimum and the Al and O signals are a maximum until the Al_2O_3 interlayer is sputtered off of the sample. The Mo and S signals increase again as the interlayer is removed between 25 and 35 seconds into the depth profile. Finally, the Mo and S signals decrease to zero when the bottom layer is removed, leaving only the Al_2O_3 substrate underneath. Note that the S

signal decreases more rapidly than the Mo signal due to the preferential sputtering of sulfur.[230]

Importantly, no significant sulfur signal remains after the heterostructure is sputtered off of the substrate, demonstrating that the growth process does not incorporate large amounts of sulfur into the Al_2O_3. Sulfur incorporation into the Al_2O_3, especially into the interlayer, potentially alters the electrical performance of the device, increasing the leakage current through the dielectric and decreasing the breakdown voltage.

7.2 MoS_2-WS_2

The inclusion of two sputter guns in the MBE system allows growth of both MoS_2 and WS_2 via the sputtered growth method (Section 6.4) without exposing the sample to atmosphere in between growths. As a result, the heterostructure is expected to have contamination-free interfaces. MoS_2-WS_2 heterostructures were grown on gold, sapphire, and amorphous oxide substrates (Al_2O_3 on SiO_2). The WS_2 and MoS_2 were grown according to the process described in Section 6.4, in which a small amount of the transition metal is sputtered onto the substrate, followed by a soak in H_2S to sulfurize the metal. For these heterostructures, WS_2 serves as the bottom layer and MoS_2 serves as the top layer. The van der Waals gap is used as the interlayer.

Because the MoS_2-WS_2 heterostructure lacks an interlayer barrier to physically separate the two TMDs, it is necessary to understand the potential interactions that occur between the MoS_2 and WS_2 which could alter the expected performance of the heterostructure. Previous reports have suggested that heterostructures in which the TMD layers contain the same chalcogen are more strongly influenced by interactions than heterostructure with different chalcogens in the TMDs. To provide some information

about the nature of the interactions, Raman and PL measurements were collected on individual layers of MoS_2 and WS_2 as well as on the MoS_2-WS_2 heterostructure.

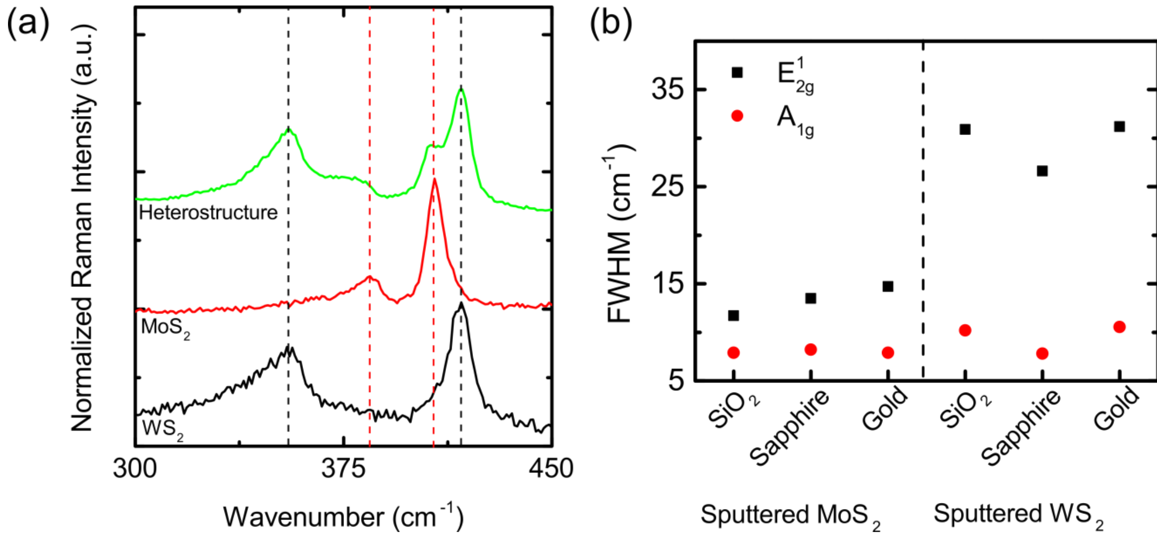

Figure 7.5. (a) Raman spectra of the individual WS_2 film (black curve), the individual MoS_2 film (red curve), and the MoS_2-WS_2 heterostructure (green curve). (b) Raman FWHM comparison of grown of the MoS_2 and WS_2 films used for the heterostructure on SiO_2, sapphire, and gold substrates.

Figure 7.5 (a) compares the Raman spectra of the individual TMDs and the heterostructure. The WS_2 film (black curve) shows the characteristic E_{2g}^1 and A_{1g} modes of WS_2, present at 355 cm^{-1} and 417 cm^{-1}. The peak separation of ~62 cm^{-1} between the two modes is consistent with previously measured values for few-layer WS_2.[231] The MoS_2 film (red curve) is characterized by the presence of the E_{2g}^1 and A_{1g}peaks at 384.6 cm^{-1} and 407.7 cm^{-1}, respectively. The peaks separation of 23.1 cm^{-1} indicates that the MoS_2 film within the heterostructure consists of trilayer MoS_2. In the heterostructure sample (green curve), the Raman spectrum is composed of a combination of the Raman active modes from both the MoS_2 and WS_2. The strong peaks in the heterostructure Raman spectrum are the WS_2 peaks located at 355 cm^{-1} and 417 cm^{-1}, while the MoS_2

peaks exhibit lower intensity and result in the formation of broad shoulders next to the WS_2 peaks. There is not a significant shift in the peak positions of either the MoS_2 or WS_2 peaks in the heterostructure compared to the individual TMDs on SiO_2, suggesting that direct heterostructure growth does not result in significant strain or doping as a result of interactions between the TMDs within the heterostructure.

Figure 7.5 (b) explores the growth of MoS_2 and WS_2 using the sputtered metallic sources on a variety of substrates. The figure shows the FWHM of the two strong Raman modes characteristic of each material for growth on SiO_2, sapphire, and gold. For the MoS_2, there are only small differences in the FWHM between the different substrates explored. This suggests a similar quality of grown material between the different substrates, with the growth on SiO_2 potentially having slightly better crystallinity than the films on the sapphire and gold substrates. For the WS_2 film, the growths on SiO_2 and gold have similar FWHM, suggesting a similar film quality on the two amorphous substrates. The FWHM measured on the sapphire substrate is significantly smaller than the other two substrates, indicating that the crystalline nature of the sapphire may increase the quality of the synthetic WS_2.

Figure 7.6 compares the PL spectra for the individual TMD films and the heterostructure film. The WS_2 and MoS_2 PL data were collected on SiO_2 substrates to provide high quality data, while the heterostructure PL spectrum was collected on Al_2O_3 on SiO_2. In order to subtract the influence of the Al_2O_3 from the heterostructure PL data, a sample of WS_2 was prepared on an identical Al_2O_3 on SiO_2 substrate. A baseline for the Al_2O_3 was created by subtracting the PL of the WS_2 on SiO_2 from the WS_2 on Al_2O_3. This baseline was then subtracted from the heterostructure PL data.

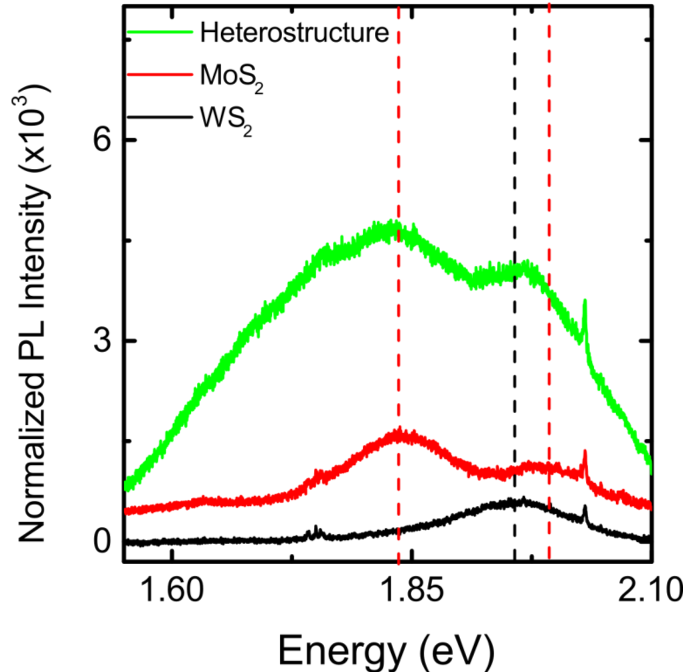

Figure 7.6. PL measurements taken on individual WS_2 (black curve) and MoS_2 (red curve) films, as well as the MoS_2-WS_2 heterostructure (green curve).

The WS_2 PL spectrum (black curve) contains only a single peak at ~1.96 eV, which is consistent with previous PL measurements on few-layer WS_2.[231] This peak corresponds to the A exciton which results from the direct band gap transition at the K-point. The intensity is relatively weak as a result of the transition between direct and indirect band gap in few-layer WS_2. The MoS_2 PL spectrum (red curve) shows both the A exciton at ~1.84 eV and the B exciton at ~2 eV. The heterostructure PL spectrum (green curve) also is mainly characterized by two peaks, which appear to be the result of contributions from both the materials. The lower energy peak at 1.84 eV represents the response of the MoS_2 film within the heterostructure, while the higher energy peak at 1.97 eV lies between the individual PL peaks of the MoS_2 B exciton and the WS_2 A

exciton. Therefore, this peak appears to be a convolution of these two peaks, resulting in the slight shift of the peak from either of the individual films. The presence of the characteristics of both the MoS_2 and WS_2 layers in the heterostructure sample confirms the presence of well-defined MoS_2 and WS_2 in the structure, without any significant interactions which alter the band structure of the materials.

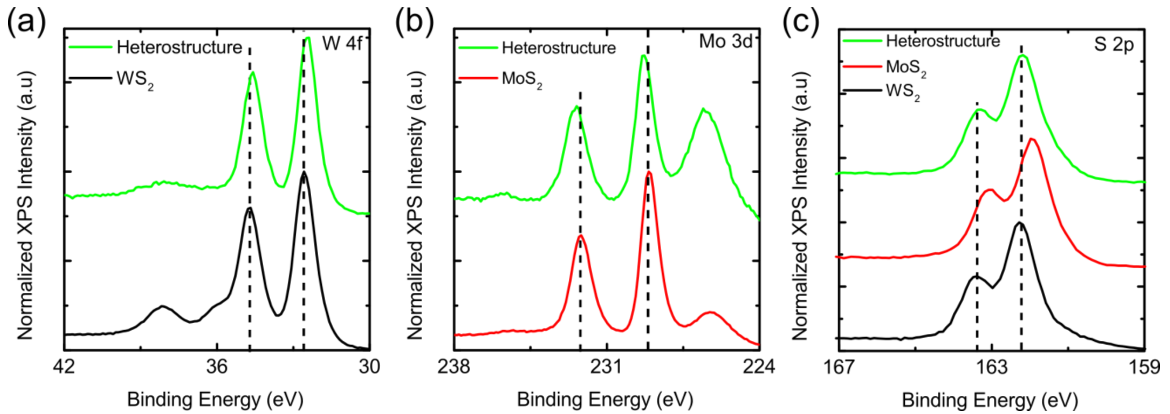

Figure 7.7. XPS comparison of the (a) Mo 3d, (b) W 4f, and (c) S 2p spectra in the MoS_2/WS_2 heterostructure. The black (red) curve represents an individual WS_2 (MoS_2) film, while the green curve was measured on the heterostructure.

XPS data were collected for the isolated MoS_2 and WS_2 layers as well as the MoS_2/WS_2 heterostructure. Figure 7.7 compares the (a) Mo 3d, (b) W 4f, and (c) S 2p spectra for the individual TMD films and the heterostructure. The peak positions for each sample were shifted based on the adventitious carbon peak in the C 1s spectrum to account for potential charging of the samples. In Figure 7.7 (a) the Mo 3d spectrum for both the individual MoS_2 layer (red curve) and the heterostructure (green curve) are composed of the S 2s peak at 226.3 eV and the Mo 3d doublet from the MoS_2 peak. There are two main differences between the individual MoS_2 and the heterostructure XPS

spectra. First, the S 2s peak relative to the MoS_2 doublet is much stronger in the heterostructure sample. This is because the S 2s signal is a combination of the sulfur in the MoS_2 and the WS_2 layers, resulting in a larger sulfur signal than in the individual MoS_2 sample. The second difference is a shift in the entire spectrum to higher binding energy by approximately 0.2 eV. This shift is indicative of interlayer interactions which alter the electronic structure of the MoS_2 in the heterostructure compared to the individual MoS_2 layer.

The W 4f spectrum (Figure 7.7 (b)) reveals interesting information about the stability of the WS_2 layer. In the isolated WS_2 layer (black curve), two doublets are present. The larger doublet results from tungsten bound to sulfur in the WS_2, while the weaker doublet suggests the presence of WO_3 in the sample. In comparison, the heterostructure sample (green curve) displays on the WS_2 doublet, without any indication of oxidation. In the heterostructure sample, the MoS_2 is grown immediately after the WS_2 layer without exposing the sample to the environment. As a result, the MoS_2 provides a passivation of the WS_2 and prevents oxidation. Because significant oxidation of the MoS_2 is not observed, these results suggest a higher stability of the MoS_2 compared to the WS_2. As observed in the Mo 3d spectrum, the W 4f exhibits a binding energy shift for the heterostructure compared to the individual WS_2 layer, providing further evidence of an electronic interaction between the MoS_2 and WS_2 in the heterostructure. Interestingly, the W 4f spectrum shifts oppositely the MoS_2 sample, with a 0.1 eV shift to lower binding energy, indicating charge transfer which occurs between the MoS_2 and WS_2.

Figure 7.7 (c) shows the S 2p spectrum for each of the samples. To compare the shape of the sulfur peaks, the intensity of the sulfur peaks was normalized by the height

of the S $2p^{3/2}$ peak for each of the samples. Therefore, the peaks look similar despite the increased sulfur signal from the heterostructure. The peak position for the heterostructure sample (green curve) is between that for the WS_2 sample (black curve) and the MoS_2 sample (red curve). These shifts in peak position further suggest electronic interactions between the layers in the heterostructure.

7.3 Fermi Level Pinning in Low-Temperature TMDs

To further explore the effect of defects on the behavior of the low-temperature TMDs, electrical characterization was performed. Both FETs and metal oxide semiconductor capacitors (MOSCAPs) were fabricated from the TMD films.

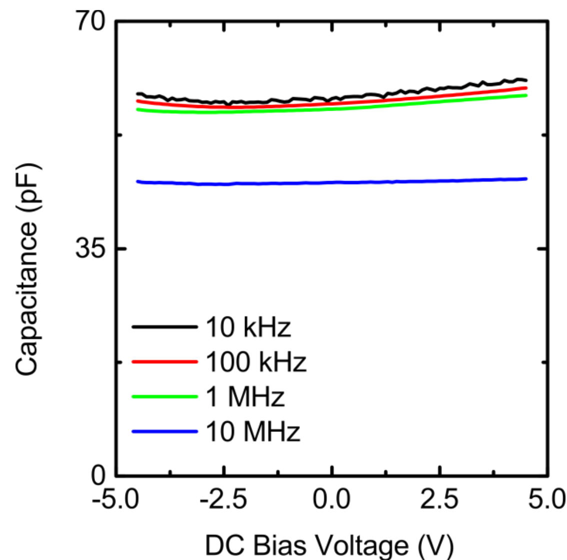

Figure 7.8. Capacitance versus DC bias voltage measured at several frequencies for the 10 min MoO_3 pulsed samples.

MOSCAPs were fabricated by growing MoS_2 using 10 minute MoO_3 pulses and 10 minute H_2S pulses. The MoS_2 film was grown on gold contacts, followed by e-beam evaporation of 1 nm Al to serve as an ALD seed layer. Ninety cycles of ALD were then

deposited for a total thickness of approximately 10 nm Al_2O_3. Gold was deposited on top of the Al_2O_3 film to provide top contacts. The capacitance-voltage measurements for several different frequencies are summarized in Figure 7.8. At all frequencies, the DC voltage does not have any effect on the value of the capacitance. Previous studies using similar devices on exfoliated or CVD MoS_2 measured a conventional *C-V* curve on the material with clear accumulation and depletion regions. Therefore, the lack of a change in capacitance with DC voltage in these measurements suggests that the Fermi level in the low-temperature MoS_2 is pinned due to defects or interface states. This type of behavior has been reported in III-V MOSCAPs in which there is a high density of interface states.[232, 233] Similar Fermi level pinning was observed in MOSCAPs fabricated with sputtered MoS_2 and WS_2.

FETs were fabricated to provide additional information about the electrical quality of the low temperature films. However, due to Fermi level pinning and high defect densities, the transfer curves of the material (not shown) exhibit almost no current modulation. Instead, two-terminal temperature-dependent conductivity measurements were performed.

The variable range hopping (VRH) is used to describe conduction in the low-temperature MoS_2 samples. Generally, VRH results from conduction which is defect-dominated, with the conduction path resulting from "hopping" of charge carriers between defect sites. Because the rate of trapping is temperature dependent, the conductivity also depends on the temperature. For a two-dimensional semiconductor, the conductivity for VRH is proportional to[234-236]

$$\sigma(T) = \sigma_0 T^{0.8} exp\left[-\left(\frac{T_0}{T}\right)^{1/3}\right] \quad (7.1)$$

where T_0 is a fitting parameter which is given by

$$T_0 = \frac{13.8}{k_B N(E_F)\xi^2} \tag{7.2}$$

where k_B is Boltzmann's constant, $N(E_F)$ is the density of states at the Fermi level, and ξ is the localization length. A smaller value of the localization length suggests that charge carriers are more confined at a certain location.

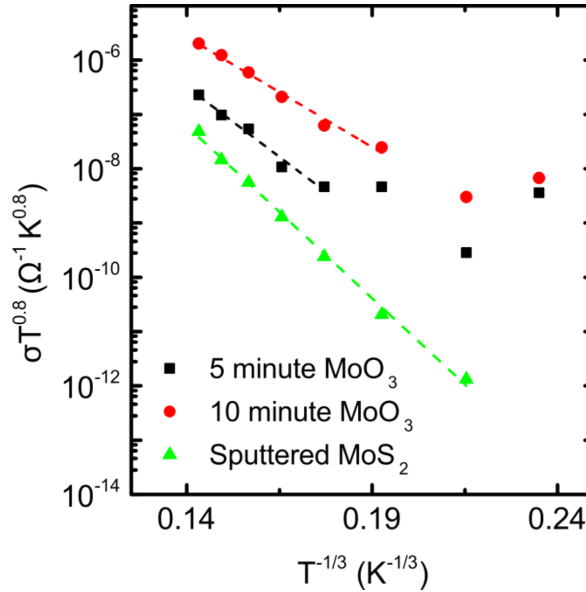

Figure 7.9. Temperature dependence of conductivity for 5 minute MoO_3 (black squares), 10 minute MoO_3 (red circles), and sputtered Mo (green triangles) based synthesis methods for MoS_2. The dashed lines indicate linear fits to the data to extract the value of T_0.

Figure 7.9 compares the temperature dependence of three different growth methods for MoS_2: (1) pulsed MoO_3 using 5 minute MoO_3/10 minute H_2S pulses, (2) pulsed MoO_3 using 10 minute MoO_3/10 minute H_2S pulses, and (3) MoS_2 grown using the sputtered Mo source. The figure plots $\sigma T^{0.8}$ on a logarithmic scale versus $T^{-1/3}$. For all three samples, the semi-log plot is linear, confirming that VRH is the dominant

conduction mechanism in these films. Based on the slope of the curves, the value of T_0 can be extracted for each growth method. The average values of T_0 are 5.7×10^5, 7.6×10^5, and 3.1×10^6 for the 5 minute MoO_3/10 minute H_2S, the 10 minute MoO_3/10 minute H_2S, and the sputtered MoS_2, respectively. These values of T_0 are similar to those measured previously for TMDs.[234, 237, 238]

Based on Equation 7.2, the extracted values of T_0 can be related to the localization length and density of states in the materials. The values of T_0 for the 5 minute and 10 minute MoO_3 growth methods are similar, suggesting a similar localization length in the samples. The slight difference is potentially due to worse fitting of the 5 minute MoO_3 sample data or a somewhat different density of defect states in the two samples near the Fermi level.

Assuming a similar density of states near the Fermi level in these samples, the larger value of T_0 in the sputtered MoS_2 sample suggests a shorter localization length. A shorter localization length suggests that hopping transport between defects is more limited in the sputtered MoS_2 sample, which is also consistent with the observed lower conductivity of the sputtered MoS_2 sample.

CHAPTER 8

PERFORMANCE OF 2D VERTICAL HETEROSTRUCTURES

Two-terminal tunneling devices were fabricated using the MoS_2-Al_2O_3-MoS_2 and the MoS_2-WS_2 heterostructures described in Chapter 7. Measurement of these devices helps build an understanding of the impact of structural disorder, defects, and interlayer interactions on the tunneling characteristic of the devices. This chapter discusses the electronic behavior of each heterostructure and compares the performance of the experimental devices with simulations of each structure based on the theoretical model explained previously. Finally, the theoretical model is used to predict the performance of devices incorporating higher quality materials based on process optimization.

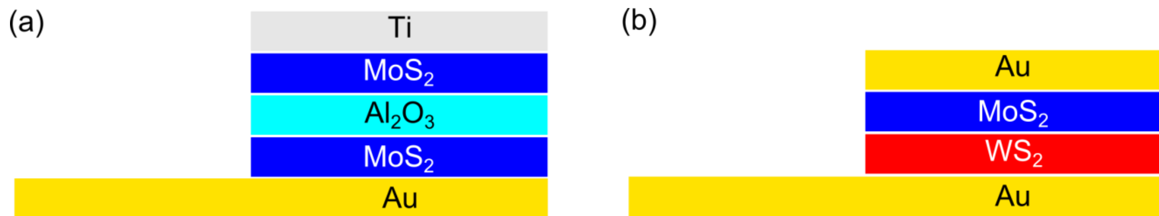

Figure 8.1. Schematics of the heterostructures explored for the (a) MoS_2/Al_2O_3/MoS2 and (b) MoS_2/WS_2 heterostructures.

Figure 8.1 shows a schematic of the devices, which are characterized only by vertical transport through the heterostructure. The device consists of the heterostructure sandwiched between two metal contacts, with a large bottom contact in order to facilitate probing for electrical measurement. In particular, this work explores the electrical

behavior of (a) $MoS_2/Al_2O_3/MoS_2$ and (b) MoS_2/WS_2 heterostructures. A completely vertical structure was chosen to eliminate the effect of lateral transport through the TMD layers. Without significant improvements in material quality, the resistance due to lateral transport is expected to dominate the device behavior, while the completely vertical structure allows study of the tunneling characteristic of the devices even with poor material quality.

8.1 Tunneling in MoS_2-Al_2O_3-MoS_2 Heterostructures

The MoS_2-Al_2O_3-MoS_2 heterostructures were grown by the process described in Chapter 7 on gold contacts. Direct growth of the heterostructures provides clean interfaces throughout the heterostructure and prevents contamination issues that can arise during transfer. Following growth of the heterostructure, Ti top contacts were deposited using a lift-off process to create the complete device. To prevent possible damage to the heterostructure, the MoS_2-Al_2O_3-MoS_2 layers were left as blanket films.

I-V characteristics were collected on several device sizes, ranging from 10 μm x 10 μm squares to 100 x 100 μm squares. Figure 8.2 (a) shows the current density for each device size, obtained by dividing the measured current by the area of the device. The shape of the current-voltage characteristic is exponential, confirming that that charge carriers are tunneling through the Al_2O_3 interlayer. Because the device size is much larger than the expected coherence length, it is expected that the current density should be relatively independent of device size, as is the case for the data in the figure. However, there are two small changes in the tunneling characteristic as the device size increases. First, the current density displays a linear characteristic in the low voltage range for the smallest devices. Second, the "turn-on" of the device shifts to higher voltages with

increasing device size. Because the device sizes are significantly larger than the coherence length in these devices, this shift is not likely to be due to a change in tunneling between the MoS_2 layers. Instead, the shift may be a result of a size-dependent series resistance which stretches out the current-voltage characteristic in the larger devices. Because the heterostructure layers are not patterned, another factor may be edge currents from the perimeter of the contact which make up a greater fraction of the current density for the smaller device sizes.

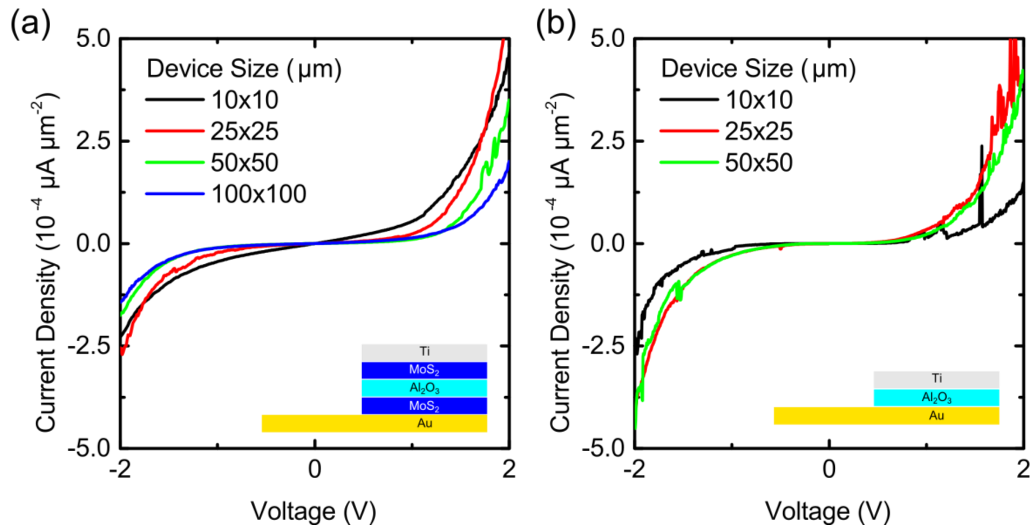

Figure 8.2. (a) Size dependence of the current density measured for the MoS_2-Al_2O_3-MoS_2 heterostructures. (b) Measured current density for various device sizes for an Au-Al_2O_3-Ti control sample.

To rule out the possibility of only metal-to-metal tunneling within the heterostructure and confirm that the MoS_2 layers are involved in tunneling, a control sample was fabricated with the MoO_3 seeding layer and 45 cycles of ALD Al_2O_3. Figure 8.2 (b) shows the current density versus voltage for each device size for the control sample. The current density measured for the control sample is of the same order of

magnitude as in the heterostructure device, confirming that the tunneling in the heterostructure device occurs only through the Al_2O_3 interlayer. If the current in the heterostructure was due to metal-to-metal tunneling, the current for the control sample would be much larger than the current in the heterostructure due to the thicker tunnel barrier for metal-to-metal tunneling, comprised of the entire MoS_2-Al_2O_3-MoS_2 stack.

Comparison of the shape of the current-voltage characteristics for the heterostructure versus control samples reveals a similar shape for both structures. This similarity is indicative of tunneling in the heterostructure which behaves in the limit of no momentum conservation. In other words, there is significant scattering within the heterostructure which prevents the observation of resonant tunneling or steep-slope behavior. In order to provide more insight into the behavior of the heterostructure and understand the influence of the metal contacts on the tunneling characteristic, the heterostructure device was simulated.

To further explore the behavior of the vertical heterostructure, the experimental results were compared to simulations. In order to match the experimental results, Fermi level pinning must be included in the simulation. The Fermi level pinning within the heterostructure arises because the active area of the heterostructure device is grown directly on an Au contact and capped with a Ti contact. As a result, the Fermi levels within the bottom and top MoS_2 layers are determined by the interaction of the MoS_2 with the Au and Ti contacts, respectively.

As discussed in Chapter 1, previous studies have determined that the Au-MoS_2 interface results in pinning of the Fermi level 0.12 eV below the conduction band edge.[114] Therefore, for the bottom layer of MoS_2 an interface density of states was included to pin

the Fermi level of the bottom layer. Similarly, the Fermi level for the top layer MoS_2 is expected to be pinned near the conduction band edge due to the Ti-MoS_2 interface. Experimentally, the Schottky barrier height for the Ti-MoS_2 contact has been measured to be 65 meV.[197] To match these previous experiments, an interface density of states was included which pins the Fermi level 0.065 eV below the conduction band edge of the top layer MoS_2. Figure 8.3 compares the measured (green solid line) and simulated transfer curves (black dashed line). The black dashed line shows the simulated curve for the MoS_2-Al_2O_3-MoS_2 heterostructure using a coherence length of 1 nm. The two curves are almost identical, confirming that Fermi level pinning dominates the performance of the device.

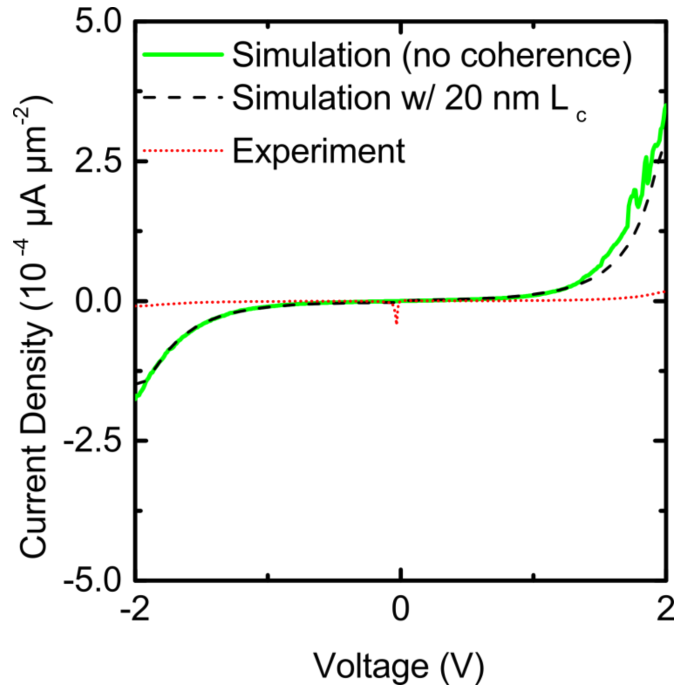

Figure 8.3. Comparison of experimentally measured (green line) with simulated transfer curves (red dotted and black dashed lines) on MoS_2-Al_2O_3-MoS_2 heterostructures. The black dashed line represents a 1 nm coherence length indicative of low quality devices and matches the experimental data well. The red dotted line uses a 20 nm coherence length to predict the performance of higher-quality devices.

While the experimentally measured current-voltage characteristic in the MoS_2-Al_2O_3-MoS_2 heterostructures is indicative of poor material quality, the comparison to simulated tunneling currents provides important validation of the device design. Most importantly, the results verify that the choice of contact metals can be used to tune the device performance. Because Fermi level pinning occurs at the contacts, the band alignment in the heterostructure can be tuned by choosing metals which pin the Fermi levels in the two layers at different values. In the Au-Ti devices described above, the difference in the Fermi level pinning of the two layers only 55 meV. As a result, a small applied voltage is expected to result in complete band alignment, which is the necessary condition for resonant tunneling behavior. To confirm this behavior, a high-quality heterostructure was simulated with the inclusion of momentum conservation, as shown by the red dotted curve in Figure 8.3. For this simulation, a coherence length of 20 nm was used. The simulated current-voltage characteristic for the high-quality heterostructure exhibits NDR with only a small applied bias voltage.

To predict the potential for tuning of the NDR peak position through the choice of contact metals, the heterostructure behavior was simulated for a variety of common metals, as shown in Figure 8.4. The Fermi level pinning for each metal was based on the experimentally measured Schottky barrier height for the metal-MoS_2 contact. In the plot, each curve is labeled by the choice of bottom and top contacts (i.e., Au-Ti represents an Au bottom contact and a Ti top contact). Au is used as the bottom contact for most of the simulations because of the capability to directly grow the heterostructure on gold. Other metals potentially undergo reactions with sulfur during growth, requiring the use of an inert bottom contact.

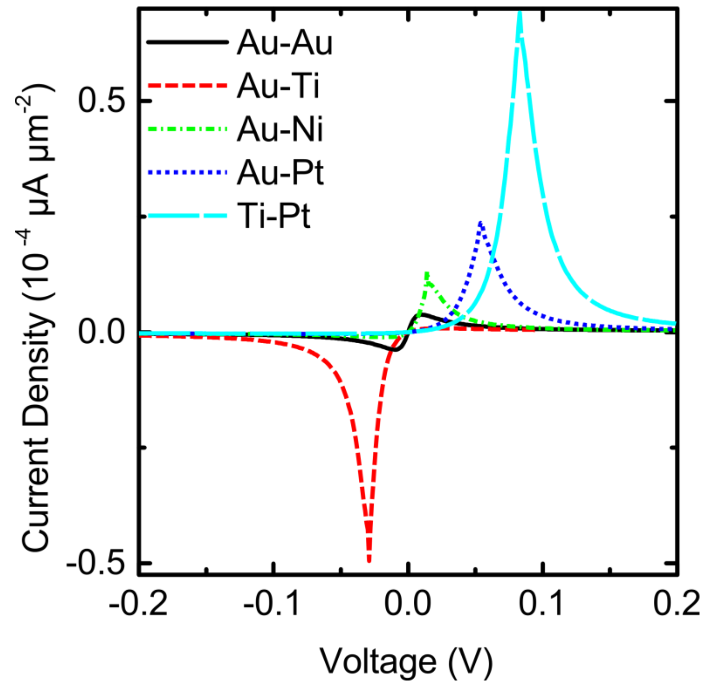

Figure 8.4. Simulation of the current-voltage characteristic for vertical MoS_2-Al_2O_3-MoS_2 heterostructures using different combinations of contact metals. The NDR peak position is tunable based on Fermi level pinning at the metal-MoS_2 interface.

For symmetric contacts (i.e. Au-Au, shown by the black solid curve in Figure 8.4), weak NDR regions are observed for both bias polarities at small voltages. Because the zero bias offset state for symmetric contacts represents perfect band alignment, momentum conservation results in the observed decrease in current at low voltages. However, for asymmetric contacts, the NDR peak position is tunable based on the difference in the location of the pinned Fermi level between the contact-MoS_2 interfaces. For the explored devices, the difference in Fermi levels in the Au-Ni (green dash-dotted curve) and Au-Ti (red dashed curve) devices are similar, but have opposite signs. As a result, the devices exhibit NDR peaks at similar voltage magnitudes but in the opposite polarities. The Fermi level difference in the Au-Pt device (dark blue dotted curve) is slightly larger than these other two devices, resulting in a shift of the NDR peak to higher

voltage. As a better demonstration of this effect, a simulation is included for a Ti-Pt device (light blue long-dashed curved), representing the largest difference in Fermi level pinning out of the explored metals. As expected, the NDR peak for this device is present at the largest magnitude of voltage.

A secondary effect of the shift in the NDR peak position is a change in the peak current observed for the devices. As the bias voltage increases, the energetic area of states which potentially contribute to the tunneling current also increases. Therefore, for NDR peaks at higher voltages, additional energetic states contribute to tunneling and the observed peak current increases.

8.2 MoS_2-WS_2 Heterostructures

The MoS_2-WS_2 heterostructure was grown on gold bottom contacts by the sputtering-based growth in the MBE system as described in Chapter 7. For these structures, the WS_2 film was deposited first, followed immediately by growth of the MoS_2 film. The thickness of each film is expected to be trilayer, resulting in a total heterostructure thickness of ~4-5 nm. Following heterostructure growth, gold top contacts were deposited on the heterostructure using a liftoff process.

Figure 8.5 shows the measured current-voltage response two devices based on the MoS_2-WS_2 heterostructures. In Device 1 (black solid curve), the current scales linearly with the applied bias voltage, indicating that the response of the heterostructure is only resistive. This type of behavior is indicative of a high defect density in the grown heterostructure. Because the MoS_2-WS_2 heterostructure lacks an interlayer barrier, it is likely that there is a defect-dominated conduction path through the heterostructure. The current contribution due to this defect path is much larger than the expected current due

to the tunneling through the devices. In addition, the resistance conduction path is independent of voltage, resulting in the linear current-voltage characteristic observed.

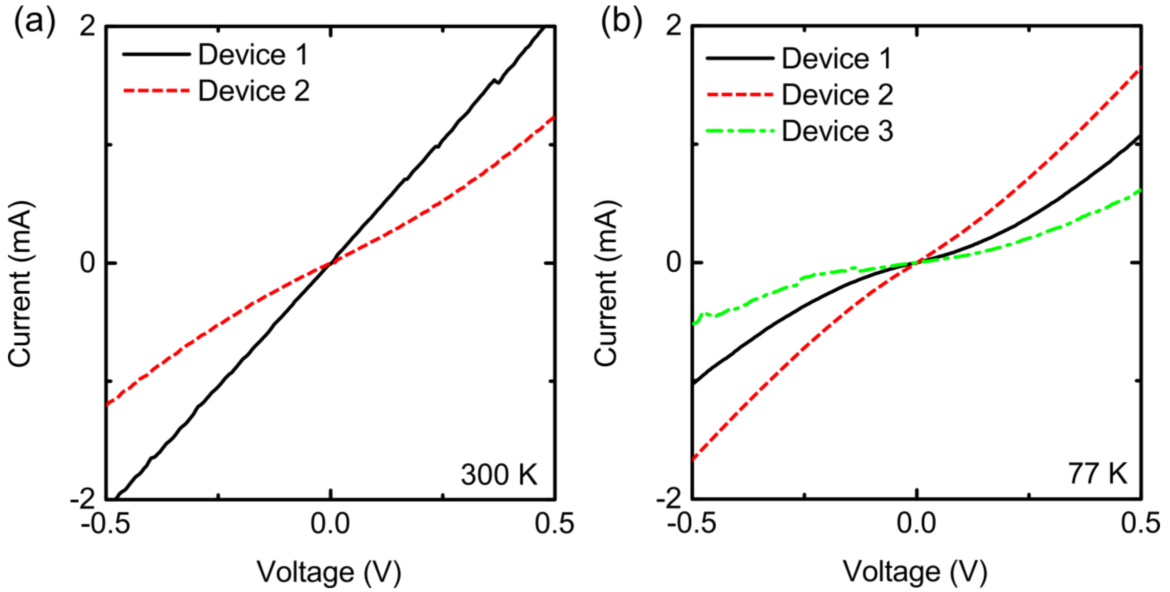

Figure 8.5. Experimentally measured current-voltage characteristics for two MoS_2-WS_2 heterostructure devices. (a) Tunneling current measured at 300 K. (b) Tunneling current measured at 77 K.

Interestingly, Device 2 (red dashed curve) shows similar high current density to Device 1. However, the current-voltage characteristic shows a small degree of nonlinearity. This nonlinear response indicates some degree of tunneling behavior in the device. However, the large currents indicate a strong influence of defects on the overall response of the devices.

Low temperature measurements at 77 K were used to further explore the behavior of the MoS_2-WS_2 heterostructures, with the goal of freezing out the defects in the material and observing better tunneling characteristics. Figure 8.5 (b) shows the measured current-voltage behavior of three MoS_2-WS_2 devices at low temperature.

Devices 1 and 2 (black solid and red dashed curves) in the figure are the same devices shown in Figure 8.5 (a) at room temperature, while Device 3 (green dash-dotted curve) is an identical device. With the exception of Device 2, which shows slightly higher current at low temperature compared to room temperature, Devices 1 and 3 exhibit a decreased current at low temperature. In addition, all three devices show varying degrees of nonlinearity in the low temperature measurements. The high variation in the device performance between the three identical devices is likely due to differences in the incorporated defects between the growths.

Comparison of the low temperature and room temperature measurements on Device 1 provide evidence that the room temperature device performance is dominated by defect conduction. At low temperature, the device shows a decreased current and nonlinear behavior, compared to the linear characteristic observed at room temperature. The nonlinear characteristic at lower temperatures arises from the freeze out of defects, resulting in lower defect-based conduction. As a result, more of the nonlinear tunneling characteristic between the MoS_2 and WS_2 films is observed.

One method to improve tunneling in these heterostructures is the insertion of an interlayer, such as Al_2O_3 or hBN, between the MoS_2 and WS_2 layers to break the conductive filament formed by defects in the two materials. However, the current density in the device will decrease as the interlayer increases in thickness. In addition, depending on the amount of Fermi level pinning in the device, it is also possible that the coupling of the TMD layers through the interlayer capacitance will alter the device behavior. For these reasons, it is also important to develop growth recipes which reduce the defect densities in the TMDs so that the van der Waals gap can be used as a tunneling barrier.

CHAPTER 9

SUMMARY AND FUTURE WORK

Transition metal dichalcogenides are interesting candidates for application to next-generation electronic devices. TMDs are useful in a variety of applications, including digital electronics, flexible electronics, sensors, photovoltaics and analog devices. In particular, vertical heterostructures composed of two dimensional materials have interesting applications in both digital and analog electronics. Using a gate-controlled structure, both resonant tunneling and steep-slope behavior are possible depending on the band alignment of the 2D material electrodes in the heterostructures. Simulations based on the Bardeen transfer Hamiltonian were used to evaluate the potential of these 2D vertical heterostructure. The results demonstrate that resonant tunneling between TMDs creates a much narrower and stronger NDR peak than similar graphene-based devices. In addition, because of the band structure of the TMDs compared to graphene, the TMD-based devices are predicted to be more robust to scaling or device-to-device variations. Compared to previous resonant tunneling devices based on III-V materials, TMD-based resonant tunneling transistors result in much higher peak-to-valley ratios due to the lack of quantized subbands.

Using the theoretical model, the potential for steep-slope behavior in the MoS_2-WSe_2 system was demonstrated for the first time. By changing the gate work functions, it is possible to tune the MoS_2-WSe_2 ITFET for low threshold voltage in both n- and p-type configurations, suggesting that complementary logic can be built using a single heterostructure. Using the MoS_2-WSe_2 ITFET, a number of design parameters which

affect device performance were explored. In particular, the results suggest that TMD-based ITFETs can be scaled to the 5 nm node without significantly impacting the subthreshold slope or saturation current in the device. Based on the simulations, realistic device performance is expected to be limited by rotational misalignment between the electrodes and defects in the material.

Implementation of TMDs for high-performance applications requires synthesis techniques which: (1) create uniform films across the wafer scale, (2) are compatible with conventional CMOS processing techniques, especially in terms of the synthesis temperature, and (3) incorporate small defect densities. Highly uniform, wafer-scale growth of both MoS_2 and WSe_2 were demonstrated using evaporated metal thin films exposed to chalcogens at a high temperature in a tube furnace. To address the need for low-temperature synthesis, plasma-assisted processing was demonstrated which meets criteria (1) and (2), with the building blocks in place for further process optimization to target requirement (3). The most promising low temperature synthesis method is based on a growth method in which a small amount of transition metal or transition metal oxide is deposited on the substrate, followed by a soak in H_2S plasma to sulfurize the deposited transition metal. Using this method, growth at 400 °C was demonstrated on arbitrary substrates for both MoS_2 and WS_2. Temperature-dependent conductivity measurements on the low temperature synthesis reveal conduction based on variable range hopping, indicative of the poor electrical quality of the material.

The low-temperature, plasma-assisted growth process was used for the direct growth of heterostructures containing MoS_2. The first heterostructure considered in this work consisted of MoS_2-Al_2O_3-MoS_2 stacks created with direct growth rather than

tranfsers. Physical characterization of the heterostructure confirmed the proper stacking of the heterostructure, with no evidence of interdiffusion between the layers. Completely vertical devices were created from the MoS_2-Al_2O_3-MoS_2 heterostructure in order to assess the electrical performance of the devices. Characteristic tunneling behavior was observed in the devices with a characteristic that suggests small coherence lengths and a high amount of scattering within the structure. The experimentally measured current-voltage characteristic was compared to simulation to explore the effect of Fermi level pinning on device performance. Finally, simulations were used to predict the performance of high quality devices. These simulations demonstrated the potential to use the metal contacts to the heterostructure to achieve NDR peaks at low voltage, with a tunable position based on the contact metal choice.

MoS_2-WS_2 heterostructures were also explored. A notable difference between these heterostructures and the MoS_2-Al_2O_3-MoS_2 heterostructures is the lack of an interlayer tunnel barrier. The MoS_2-WS_2 heterostructure demonstrated a linear current-voltage characteristic, indicating a resistive behavior of the film, rather than tunneling behavior between the MoS_2 and WS_2 films. It is likely that the current transport in the MoS_2-WS_2 heterostructure is defect-dominated, resulting in a conductive filament through the entire thickness of the heterostructure which results in the observed characteristic. Low temperature measurements recovered nonlinearity in the current-voltage characteristic, confirming that defects dominate the current voltage characteristic at room temperature. Simulations including Fermi level pinning were used to predict the performance of higher-quality MoS_2-WS_2 heterostructure devices.

9.1 Future Work

This thesis laid the ground work necessary for the realization of large-area 2D vertical heterostructures. However, there is a large amount of additional work necessary in order to improve the material quality and create high-performance devices.

9.1.1 Optimization of Low Temperature Growth

The first area of future exploration is the optimization of the growth recipes used for low temperature growth of materials. Analysis of sample stoichiometry reveals that the grown films are not stoichiometric, resulting in the incorporation of a large number of defects in the film which alter or degrade the performance of heterostructure devices. The stoichiometry of the grown films can be improved by tuning the flux of the chalcogen to better match the deposition rate of the transition metal or by adding vacuum anneals of the material prior to removal from the MBE chamber. In addition, the relationship between the deposition rate of the TMD and the resulting grain size should be explored in order to maximize the size of the grains. Both of these factors will help increase the coherence length in vertical heterostructures and provide more ideal electrical performance.

As part of the growth optimization, the crystal structure of films grown on a variety of substrates should be explored. This thesis compared the growth on sapphire, amorphous oxide, and gold substrates at a high level. This work should be followed by a more in depth study of the crystal structure of TMDs grown on metal and oxide through the use of TEM and cross-sectional TEM to understand variations in the grain size or stacking of the layers grown on different materials.

9.1.2 In-Depth Defect Characterization

To continue building the relationship between defects, Fermi level pinning, and device performance, extensive defect characterization is necessary. Analysis of MOSCAP structures provides a powerful method to compare the defects induced by different growth methods and assist in recipe optimization. Importantly, it is expected that improvements in the quality of the grown TMDs can reduce the effect of Fermi level pinning on the MOSCAP response. In this case, conventional capacitance-voltage and conductance-frequency measured can be used to probe the energy level, density, and time constant of the defect states. The measured defect response using MOSCAPs can be used to predict the performance of different recipes in heterostructures. These measurements are also useful in further understanding the interactions between the TMD and metal contacts in vertical heterostructures, which can in turn be used to improve the overall device design.

9.1.3 Heterostructures with Lateral Transport

The realization of the steep-slope tunneling transistors discussed in this work will require devices that incorporate both lateral and vertical transport. As discussed earlier, it is expected that lateral transport in TMDs will result in a series resistance which degrades the electrical transport. One alternative approach to address these concerns is the creation of hybrid graphene/TMD heterostructures, in which graphene is used for lateral transport and the TMDs determine the vertical transport properties. Because graphene is highly conductive, its use as a channel material results in lower series resistance compared to a similar TMD channel.

Several investigations are necessary in order to realize these hybrid graphene/TMD heterostructures. As with the completely vertical heterostructures, a direct growth method is desirable for the best interfacial quality within the heterostructures. Therefore, it is necessary to understand the effect of direct MoS_2 growth on graphene. In particular, the stability of the graphene channels when exposed to the direct H_2S plasma must be investigated. Current injection between graphene channels and TMD layers should also be investigated to understand whether the graphene affects vertical transport in the hybrid structure. In addition, a number of processes need to be developed and refined in order to create high quality gated structures. As one example, residue free patterning is necessary because the cleaning methods for 2D materials are limited compared to conventional cleaning or descum processes.

9.1.4 Interlayer Coupling in Heterostructures

Another important area of research is in the coupling of the TMD layers used for the creation of vertical heterostructures. While a tunnel barrier (Al_2O_3, hBN, etc.) can be used to break the coupling between the layers, this method also results in reduced tunneling current because of the increased thickness of the barrier. However, it has not been experimentally demonstrated that the vdW gap is a sufficient tunnel barrier in these devices. Further exploration of the coupling in different TMD structures is necessary in order to understand how the band structures of the materials change depending on the stacking.

APPENDIX A

EXPERIMENTAL BACKGROUND

This chapter describes the experimental apparatus used for the synthesis and characterization of the TMDs used for this work. The first section describes the tube furnaces which are used for the reaction of thin films of transition metals with high temperature chalcogen vapor. The second section includes a description of the MBE system which is used for synthesis of TMD vertical heterostructures. The third section of the chapter explores the physical and electrical characterization techniques used to compare various synthesis recipes, including the defect structure and field-effect mobility.

A.1 High Temperature Tube Furnaces

Two furnaces were used for synthesis of 2D materials in this work. The first system is a CVD Equipment (Central Islip, NY) tube furnace used for sulfurization experiments. The sample for sulfurization is placed on a graphite stage close to the contact point of a thermocouple which is used to monitor the stage temperature. The chamber is heated by infrared bulbs, with a maximum temperature of 1100 °C. Gas sources for Ar, H_2, and CH_4 are plumbed to the system, with mass flow controllers to allow for variable flow rates of each gas source. There are two sources of sulfur on the system: (1) sulfur powder contained within a lecture bottle, which is heated to 150 °C, and connected to the main chamber through heated gas lines. In order to use the sulfur powder, the vacuum valve is completely closed to place the chamber into a static environment. Following this, a pneumatic valve on the lecture bottle is opened and the

vapor pressure of the heated sulfur powder fills the chamber with a small amount of sulfur. (2) Dimethyl sulfide (DMS) liquid is contained within a bubbler. A mass flow controller on the outlet of the bubbler controls DMS flow through the rest of the system. Because of the high vapor pressure of DMS liquid at room temperature, no additional carrier gas is necessary on the DMS. For most processes, the DMS gas flow is diluted with Ar to provide a gas mixture which is less than 10% DMS. The gas mixture flows through an MKS Instruments ASTRONi toroidal plasma source prior to reaching the chamber, which is used to dissociate the DMS and create more reactive sulfur radicals.

The second furnace used in this work is a CVD Equipment FirstNano EasyTube 3000 advanced CVD system. This furnace consists of both a cylindrical tube and a load lock which isolates the tube from the outside environment. The sample stage consists of coated graphite, with three thermocouples embedded within the stage to monitor the temperature. A number of gas sources are plumbed to the furnace, with Ar, CH_4, and H_2 used in this work. Infrared bulbs are used to heat the sample stage up to a maximum temperature of 1100 °C.

A.2 Molecular Beam Epitaxy

A molecular beam epitaxy (MBE) system was used for the growth of vertical heterostructures. The base pressure of the system is on the order of $10^{-8} – 10^{-9}$ Torr. The system can accommodate up to eight molecular sources, allowing for the growth of several different 2D materials in a single system. Isolation of these molecular sources is achieved via a wagon wheel which is cooled using chilled water at a temperature of 8 °C. Each molecular beam has a shutter which can be used to interrupt the flow of an individual source during growth. For this work, the MBE is outfitted with (1) an effusion

(Knudsen) cell used for evaporation of either MoO_3 or Se; (2) a direct plasma source used for H_2S plasma sulfurization; (3) a thermal gas injector used for H_2S thermal sulfurization; (4) two sputter guns used for Mo and W sputtering; and (5) a gas injector for Ar flow in sputtering processes.

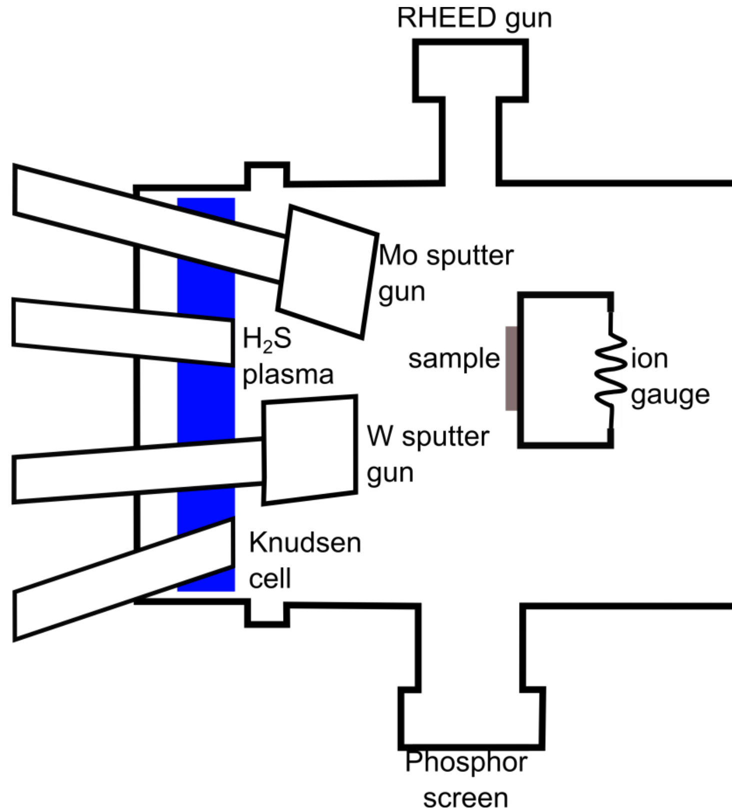

Figure A.1. Schematic of the MBE system used for TMD growth.

A schematic of the interior of the MBE system is shown in Figure A.1. The sample is mounted on a rotatable carousel, with an ion gauge (the flux gauge) mounted opposite the sample. The flux gauge allows the flux of each molecular beam to be measured prior to starting growth of each 2D material. The flux is represented by the beam equivalent pressure (BEP), which is the difference in the reading on the flux gauge

with the shutter in front of a given molecular source open versus closed. A liquid nitrogen cooling shroud lines the inner wall of the chamber. During growth, this shroud is kept at liquid nitrogen temperatures to freeze out contaminants. A second ion gauge (the background ion gauge) is mounted at the rear of the chamber to monitor the background pressure in the chamber during growth.

A RHEED gun and phosphor screen allow for some characterization of the grown 2D material *in situ*. By analyzing the pattern created by the RHEED gun, important details about the crystalline structure of the material can be determined, including the lattice constant of the grown material. For the RHEED technique, a monoenergetic 10 keV electron source is directed at a glancing angle (~1°) upon a crystal surface, with the reflected signal impingent on a phosphor screen to provide detection of the signal. Due to the low angle used for RHEED, the normal component of the electron energy is small, resulting in a shallow penetration depth. As a result, the information depth for RHEED is limited to only the first few atomic layers.

Similar to other diffraction techniques, the Ewald's sphere representation provides a method of determining the observed RHEED pattern for a given crystal structure, as shown in Figure A.2. In general, a reciprocal lattice is constructed which consists of a mesh of points for a bulk material with three dimensional periodicity. To determine the diffraction pattern based on the reciprocal lattice, a sphere is constructed with a circumference which passes through the origin and whose radius is the incident wavevector. The diffraction pattern is given by the intersection of the sphere with the reciprocal lattice. In the case of RHEED, the shallow penetration depth creates a loss of periodicity in the direction normal to the sample surface and essentially only a single

plane of atoms is considered. Due to the inverse relationship between distances in real space and reciprocal space, the infinite spacing between planes normal to the surface results in the development of continuous rods in reciprocal space.

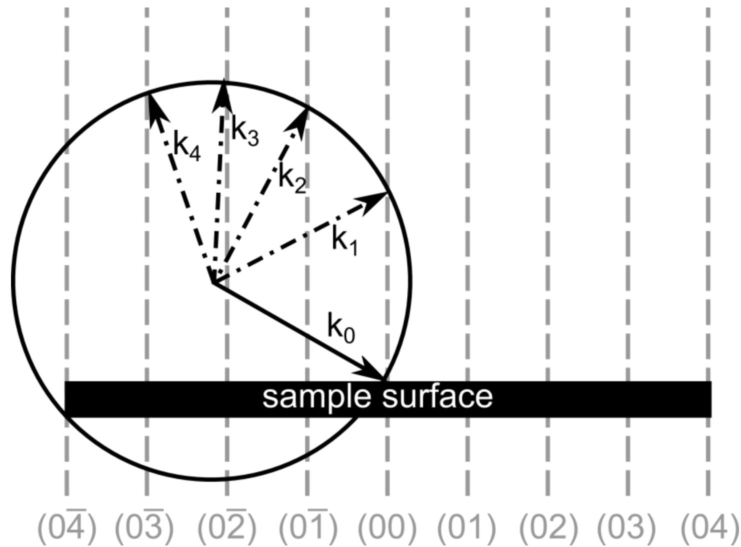

Figure A.2. Ewald sphere representation of a RHEED pattern. The intersections of the Ewald sphere with the reciprocal lattice determine the pattern of streaks which will occur.

As another consideration, the high energy of the electrons used for RHEED results in a wavevector significantly larger than the spacing of reciprocal lattice rods for most materials. As a result, the Ewald sphere can be approximated as a plane perpendicular to the electron wavevector which intersects the (00) rod largely along its length. Coupled with nonidealities in real measurements, this typically results in a diffraction spectrum which is characterized by streaks rather than well-defined spots. Using the diffraction spectrum, it is possible to determine the crystal structure of the grown material *in situ*. For example, a polycrystalline surface with randomly oriented grains results in a RHEED spectrum characterized by concentric arcs, with a spotty

pattern produced in samples with large grains. In contrast, an amorphous surface results in a diffuse diffraction pattern. A rough surface produces a spotty RHEED pattern.

In addition to the crystal structure, the spacing of the streaks in the diffraction spectrum allows calculation of the lattice constant of the grown material. The lattice spacing of the material, *a*, is

$$a = \frac{1}{\sqrt{h^2+k^2+l^2}} \frac{\lambda L}{t} \tag{A.1}$$

where *h*, *k,* and *l* represent the Miller indices of the crystallographic direction measured, λ is the wavelength of the electrons, *L* is the distance between the sample and the phosphor screen, and *t* is the spacing between diffraction streaks in the RHEED pattern.

A.3 Characterization Techniques

One of the challenges with the synthesis of few-layer TMDs is proper characterization of the materials, including measuring the thickness and uniformity of the TMD, the composition of the film, and developing an understanding of the nature of defects in the film. This section discusses some of the common techniques used to understand the nature of TMD films, including both physical and electrical characterization methods.

A.3.1 Physical Characterization Methods

Raman spectroscopy is a commonly used technique for characterizing thin films of TMDs. In general, when light impinges on a sample, the result is characterized by both Rayleigh (elastic) scattering, which comprises the bulk of the interaction, and inelastic scattering which is a much smaller portion of the signal. The inelastically scattered light is collected to form the Raman signal of a sample.

Raman analysis of TMDs generally relies on two primary vibrational modes: the E_{2g}^{1} mode, composed of in-plane vibrations, and the A_{1g} mode, resulting from out-of-plane vibrations. As the TMD thickness changes, the E_{2g}^{1} mode is relatively unaffected, as the presence of additional layers does not strongly affect in-plane vibrations. However, the A_{1g} vibration is dampened by the interactions with additional TMD layers, resulting in a blue shift of the Raman peak.[191, 239] In transition metal sulfides, the E_{2g}^{1} and the A_{1g} modes have strong intensities and are located at distinct positions.[212, 220] As a result, the peak separation between the two modes is a good indicator of the thickness of few-layer sulfide samples. For example, the separation between the E_{2g}^{1} and the A_{1g} peaks in MoS_2 varies strongly from 19 cm^{-1} in monolayer samples to a saturation value of approximately 25 cm^{-1} in bulk samples, resulting from a thickness of approximately five or more layers.[191] Because of the sensitivity of the Raman peak separation to the thickness of the TMD sample, Raman mapping across large and small scales is an excellent method for evaluating the thickness uniformity of transition metal sulfide materials.

However, for transition metal selenides, the E_{2g}^{1} and the A_{1g} modes are degenerate, resulting in only a single characteristic peak which is difficult to use for thickness determination.[209] However, the Raman spectrum shows a strong dependence on the illumination wavelength used for the measurement. For example, in WSe_2, the E_{1g}, B_{2g}^{1}, and a number of second-order Raman peaks are visible for few-layer samples, but not bulk or monolayer samples, under 488 nm illumination.[207, 208, 210, 212, 213] The presence and shape of these peaks can be used to determine the thickness and uniformity of WSe_2 samples.

X-ray photoelectron spectroscopy (XPS) is another useful technique for probing the structure of TMDs. XPS is an extremely surface-sensitive measurement technique which measures photoelectrons emitted from atoms within the first few nanometers of a sample upon interaction with an incident x-ray signal. These photoelectrons are characterized by a kinetic energy (*KE*) which is equal to

$$KE = E_{xray} - BE_{electron} - \Phi \qquad \text{(A.2)}$$

where E_{xray} is the energy of the incident x-ray, *BE* represents the binding energy of the electron to the atom, and Φ represents the work function of the sample. Importantly, the binding energy is characteristic of the element and orbital the electron originated from. Additionally, the binding energy is affected by the electronegativity difference between bonded elements, providing a measure of the chemical state of each element in a sample. Bonding to a more electronegative element typically results in a shift of the signal to higher binding energies.

For few-layer TMD samples, the sampling depth of photoelectrons is greater than the thickness of the TMD, allowing the entire thickness of the TMD film to be measured using XPS. As a result, XPS measurements of thin-film TMDs are useful for determining the stoichiometry of the TMD, which can be related to the electrical performance of devices and provides some insights into the defect structure of the material. For example, a substoichiometric TMD film is likely to contain high concentrations of chalcogen vacancies, which result in electron doping of the TMD. Conversely, an overstoichiometric film will contain chalcogen interstitials or transition metal vacancies which contribute holes to the film.

For characterizing and comparing synthesis processes, XPS measurements provide crucial information about the nature of the film and the completeness of reaction. Because the binding energy for chemical species depends on the electronic and bonding environment, the XPS spectrum for TMDs can be used to determine the different chemical states of the transition metal and chalcogen atoms in the material. For example, the XPS peak for metallic Mo $3d^{5/2}$ occurs at a binding energy of 228.0 eV, while the MoS_2 $3d^{5/2}$ peak is present at 229.0 eV.[220] Further, the MoO_3 3d peaks occur at approximately 233 eV ($3d^{5/2}$) and 236 eV ($3d^{3/2}$). Because a large number of precursors used in TMD growth contain the transition metal or chalcogen complexed with other species, such as O, CO, and Cl, any remaining fractions of the precursor ligands are expected to result in changes in the binding energy for those atoms. Therefore, XPS spectra can be used to analyze the extent of reaction during synthesis as well as identify and quantify any oxidation occurring in the samples. Finally, shifts in the peak binding energies when TMDs are in different environments, such as encapsulated in a dielectric or with a thin metal film deposited on top (i.e., material under electrical contacts), can be used to identify and characterize interactions between TMDs and other materials.

For this work, a Thermo (Waltham, MA) K-alpha XPS system is used. This system has a monochromated Kα X-ray source and a hemispherical analyzer. Measurements were taken using Constant Analyzer Energy (CAE) mode with 50 eV pass energy and 0.1 eV step size with a 400 µm spot size. The Thermo K-alpha system contains a flood gun which provides ions to the sample to negate the effects of charging during measurement. The use of the flood gun allows XPS measurement on insulating substrates, such as the SiO_2 and sapphire substrates used in this work.

A.3.2 Electrical Characterization

As a complement to the physical characterization of TMDs, electrical characterization can provide fundamental information about charge carrier mobility, defect densities, and defect energies, which can be used to evaluate and optimize synthesis processes. Combined with physical characterization techniques, electrical characterization can be used to provide important insights into the atomic-scale defect structures in TMD materials.

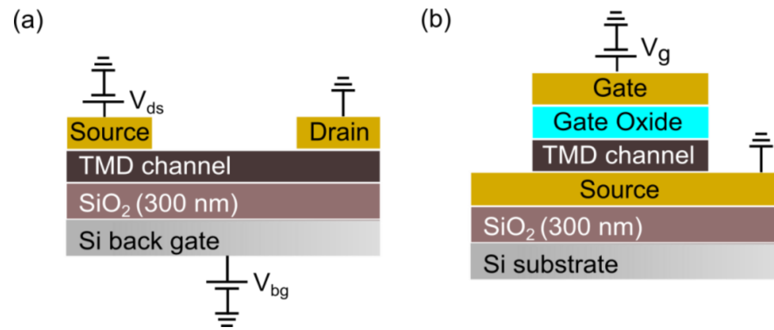

Figure A.3. (a) Schematic of back-gated field-effect transistor structure (FET) used for mobility evaluation. (b) Schematic of metal-oxide-semiconductor capacitor (MOSCAP) structure used for defect characterization

A common structure used for basic electrical characterization of TMDs is the back-gated field-effect transistor (FET), shown in Figure A.3 (a). The transfer curve of an FET is determined by fixing the source-drain bias (V_{ds}) and sweeping the back-gate voltage (V_{bg}) while measuring the source-drain current (I_d). The coupling of the gate to the channel results in the accumulation of either holes or electrons in the channel, depending on the gate bias. As the carrier concentration changes, the conductivity of the material also changes, resulting in a change in the source-drain current with changing gate voltage.

Using the transfer curve, the field-effect mobility is calculated according to $\mu_{FE} = \frac{dI_d}{dV_g}\frac{L}{WC_gV_{ds}}$, where $\frac{dI_d}{dV_g}$ represents the transconductance (derivative of the transfer curve), L and W are the channel length and width, respectively, and C_g is the gate capacitance. In general, higher quality samples display higher mobilities as a result of decreased scattering due to lower defect densities within the material. It has also been shown that the mobility in TMD samples depends strongly on the thickness of the sample, with the mobility generally decreasing as the thickness decreases.[113] Combined with the physical characterization of TMDs, electrical characterization allows critical connections to be established between the defect or grain structure of a material and its electrical performance within devices. For example, the measured mobility of CVD MoS_2 ranges from 0.02 – 30 $cm^2 V^{-1} s^{-1}$,[91, 95-98] which is much lower than the theoretical maximum, indicating that additional improvements in material quality are necessary to increase the mobility. In addition, the wide range measured for similar material indicates that different defects incorporated during the synthesis process likely alter the mobility of the samples.

The MOSCAP structure, schematically shown in Figure A.3 (b), provides a more direct measurement of the defect structure in TMDs. In particular, characterization of the MOSCAP structure provides an estimate of the shape and width of the band tails in TMDs. In a general sense, band tails form in TMDs as the result of an inhomogeneous potential distribution. This potential distribution can be caused by trapped charges in chalcogen vacancies within the TMD[240] , can form at the TMD-substrate or TMD-dielectric interfaces,[234] or can result from structural defects within the TMD including dislocations and grain boundaries.[81]

Two types of measurements are typically used to characterize band tails in semiconductors: (1) standard capacitance and (2) AC conductance measurements. Both of these techniques have been previously used to study the band tail states present in exfoliated[188] and CVD[97] MoS_2 samples.

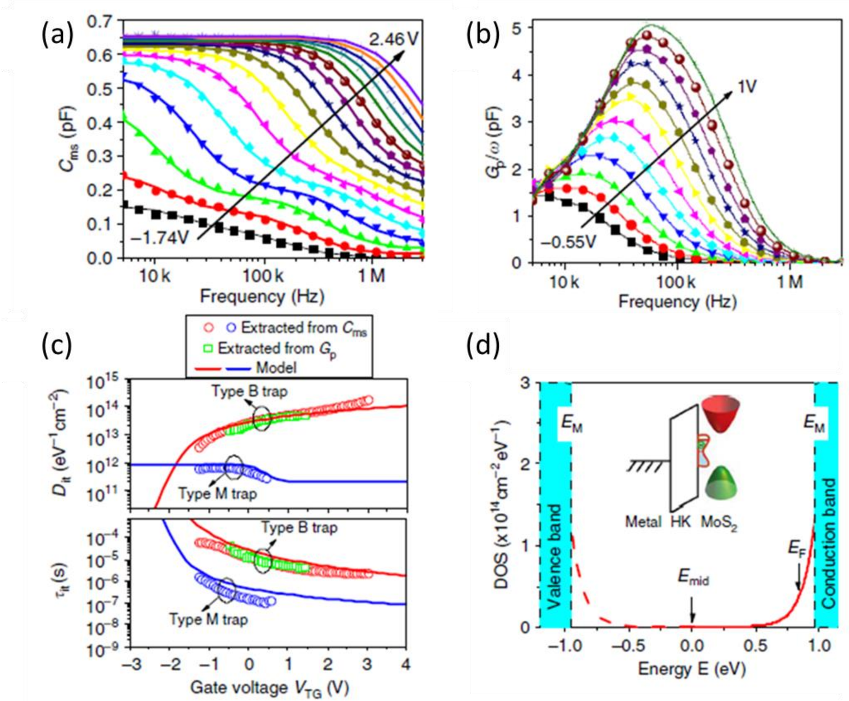

Figure A.4. (a) Capacitance and (b) Conductance measurements used to extract band tail states in MoS_2 samples. (c) Extracted density and time constants of type M and type B traps. (d) The extracted band tails in the MoS_2. Reprinted by permission from Macmillan Publishers Ltd: *Nature Communication*, reference 97, copyright 2014.

Figure A.4 details the determination of band-tail states in CVD MoS_2 using a combination of capacitance and conductance measurements.[97] Figure A.4 (a) shows the measured capacitance versus frequency for CVD MoS_2 at a number of different bias voltages. The presence of two humps at different frequencies indicates the presence of two types of traps in the MoS_2 with different time constants. Figure A.4 (b) shows the measured conductance as a function of frequency. Based on the data in Figure A.4 (a)

and (b), the density of trap states (D_{it}) and the time constant (τ_{it}) of each type of trap can be extracted, with the results shown in Figure A.4 (c).

In order to analyze the capacitance and conductance results, a generalized circuit model is used. In the work of Zhu *et al.*, a parallel model is assumed where the capacitance of the device is in parallel with branches consisting of the resistance and capacitance related to defect states.[97] Also included in the model are contributions from series resistance and the oxide capacitance. Two different defect states are assumed, with one consisting of band tail states (referred to as the "B" state) and the other including mid-gap states (referred to as the "M" state). Based on this model, the total impedance of the device is represented by[97]

$$Z = (Y_{itB} + Y_{itM} + i\omega C_s)^{-1} + (i\omega C_{ox})^{-1} + r_s \quad \text{(A.3)}$$

where ω is the angular frequency used for the measurements, C_s represents the capacitance of the TMD layer, C_{ox} represents the oxide capacitance. r_s is the series resistance in the circuit, and $Y_{itB(M)}$ is the admittance of the corresponding trap state, defined as

$$Y_{itB(M)} = \left[\frac{\tau_{itB(M)}}{C_{itB(M)}} + \frac{1}{i\omega C_{itB(M)}}\right]^{-1} \quad \text{(A.4)}$$

where $\tau_{itB(M)}$ is the time constant of the given trap. $C_{itB(M)}$ represents the capacitance of the trap and is related to the trap density by $C_{itB(M)} = eD_{itB(M)}$. When conducting capacitance measurements, two different models are generally used to represent the measured data: (1) a series model consisting of a series capacitor and resistor, or (2) a parallel model with the capacitance and conductance in parallel. Using model (1), the series capacitance and the impedance are related by

$$C_s = -\frac{1}{\omega * \mathrm{Im}[Z]} \quad \text{(A.5)}$$

Based on the above equations, the measured data can be fit to extract the density of trap states and the time constant.

An alternative method to extract the defect density is fitting of the conductance using model (2). The conductance and trap density are related by

$$\frac{G_p(\omega)}{\omega} = \frac{eD_{itB}}{2\omega\tau_{itB}} \ln[1 + (\omega\tau_{itB})^2] \quad \text{(A.6)}$$

However, the conductance is dominated by the density of states of the more prominent trap state, so that model (2) is not generally applicable to determine the properties of multiple trap states.

Based on the extracted values for D_{it} and τ_{it}, the band tail states for the CVD MoS_2 are extracted, as shown in Figure A.4 (d). Due to the large width of the band tail states, the electronic behavior of devices fabricated using currently available synthetic TMDs are expected to be significantly influenced by these band tails.

REFERENCES

1. Huang, J. K.; Pu, J.; Hsu, C. L.; Chiu, M. H.; Juang, Z. Y.; Chang, Y. H.; Chang, W. H.; Iwasa, Y.; Takenobu, T.; Li, L. J. Large-Area Synthesis of Highly Crystalline WSe_2 Monolayers and Device Applications. *ACS Nano* 2014, 8, 923-930.

2. Benhida, S.; Bernede, J. C.; Pouzet, J.; Barreau, A. Optimization of the Technique of Synthesis of WSe_2 Thin-Films by Solid-State Reaction between W and Se Thin-Films. *Thin Solid Films* 1993, 224, 39-45.

3. Ahn, S.; Kim, K.; Yoon, K. $MoSe_2$ formation from selenization of Mo and nanoparticle derived $Cu(In,Ga)Se_2$/Mo films. *Conference Record of the 2006 IEEE 4th World Conference on Photovoltaic Energy Conversion, Vols 1 and 2* 2006, 506-508.

4. Late, D. J.; Huang, Y.-K.; Liu, B.; Acharya, J.; Shirodkar, S. N.; Luo, J.; Yan, A.; Charles, D.; Waghmare, U. V.; Dravid, V. P.; Rao, C. N. R. Sensing Behavior of Atomically Thin-Layered MoS_2 Transistors. *ACS Nano* 2013, 7, 4879-4891.

5. Li, H.; Yin, Z.; He, Q.; Li, H.; Huang, X.; Lu, G.; Fam, D. W. H.; Tok, A. I. Y.; Zhang, Q.; Zhang, H. Fabrication of Single- and Multilayer MoS_2 Film-Based Field-Effect Transistors for Sensing NO at Room Temperature. *Small* 2012, 8, 63-67.

6. Liu, B.; Chen, L.; Liu, G.; Abbas, A. N.; Fathi, M.; Zhou, C. High-Performance Chemical Sensing Using Schottky-Contacted Chemical Vapor Deposition Grown Monolayer MoS_2 Transistors. *ACS Nano* 2014, 8, 5304-5314.

7. Perkins, F. K.; Friedman, A. L.; Cobas, E.; Campbell, P. M.; Jernigan, G. G.; Jonker, B. T. Chemical Vapor Sensing with Monolayer MoS_2. *Nano Lett.* 2013, 13, 668-673.

8. Sarkar, D.; Liu, W.; Xie, X.; Anselmo, A. C.; Mitragotri, S.; Banerjee, K. MoS_2 Field-Effect Transistor for Next-Generation Label-Free Biosensors. *ACS Nano* 2014, 8, 3992-4003.

9. Tsai, M.-Y.; Tarasov, A.; Razavi Hesabi, Z.; Taghinejad, H.; Campbell, P. M.; Joiner, C.; Adibi, A.; Vogel, E. M. Flexible MoS_2 field-effect transistors for gate-tunable piezoresistive strain sensors. *ACS Applied Materials & Interfaces* 2015, 7, 12850-12855.

10. He, Q.; Zeng, Z.; Yin, Z.; Li, H.; Wu, S.; Huang, X.; Zhang, H. Fabrication of Flexible MoS_2 Thin-Film Transistor Arrays for Practical Gas-Sensing Applications. *Small* 2012, 8, 2994-2999.

11. Salvatore, G. A.; Munzenrieder, N.; Barraud, C.; Petti, L.; Zysset, C.; Buthe, L.; Ensslin, K.; Troster, G. Fabrication and Transfer of Flexible Few-Layers MoS_2 Thin Film Transistors to Any Arbitrary Substrate. *ACS Nano* 2013, 7, 8809-8815.

12. Yoon, J.; Park, W.; Bae, G. Y.; Kim, Y.; Jang, H. S.; Hyun, Y.; Lim, S. K.; Kahng, Y. H.; Hong, W. K.; Lee, B. H.; Ko, H. C. Highly Flexible and Transparent Multilayer MoS_2 Transistors with Graphene Electrodes. *Small* 2013, 9, 3295-3300.

13. Chen, Y. Y.; Gholipour, M.; Chen, D. In *Flexible transition metal dichalcogenide field-effect transistors: A circuit-level simulation study of delay and power under bending, process variation, and scaling*, 2016 21st Asia and South Pacific Design Automation Conference (ASP-DAC), 25-28 Jan. 2016; 2016; pp 761-768.

14. Xu, K.; Wang, Z. X.; Du, X. L.; Safdar, M.; Jiang, C.; He, J. Atomic-layer triangular WSe_2 sheets: synthesis and layer-dependent photoluminescence property. *Nanotechnology* 2013, 24, 465705.

15. Ross, J. S.; Klement, P.; Jones, A. M.; Ghimire, N. J.; Yan, J. Q.; Mandrus, D. G.; Taniguchi, T.; Watanabe, K.; Kitamura, K.; Yao, W.; Cobden, D. H.; Xu, X. D. Electrically tunable excitonic light-emitting diodes based on monolayer WSe_2 p-n junctions. *Nature Nanotechnology* 2014, 9, 268-272.

16. Kim, I. S.; Sangwan, V. K.; Jariwala, D.; Wood, J. D.; Park, S.; Chen, K.-S.; Shi, F.; Ruiz-Zepeda, F.; Ponce, A.; Jose-Yacaman, M.; Dravid, V. P.; Marks, T. J.; Hersam, M. C.; Lauhon, L. J. Influence of Stoichiometry on the Optical and Electrical Properties of Chemical Vapor Deposition Derived MoS_2. *ACS Nano* 2014, 8, 10551-10558.

17. Nan, H. Y.; Wang, Z. L.; Wang, W. H.; Liang, Z.; Lu, Y.; Chen, Q.; He, D. W.; Tan, P. H.; Miao, F.; Wang, X. R.; Wang, J. L.; Ni, Z. H. Strong Photoluminescence Enhancement of MoS_2 through Defect Engineering and Oxygen Bonding. *ACS Nano* 2014, 8, 5738-5745.

18. Splendiani, A.; Sun, L.; Zhang, Y. B.; Li, T. S.; Kim, J.; Chim, C. Y.; Galli, G.; Wang, F. Emerging Photoluminescence in Monolayer MoS_2. *Nano Lett.* 2010, 10, 1271-1275.

19. Mak, K. F.; Lee, C.; Hone, J.; Shan, J.; Heinz, T. F. Atomically Thin MoS_2: A New Direct-Gap Semiconductor. *Phys. Rev. Lett.* 2010, 105, 136805.

20. Mak, K. F.; He, K. L.; Lee, C.; Lee, G. H.; Hone, J.; Heinz, T. F.; Shan, J. Tightly bound trions in monolayer MoS_2. *Nat. Mater.* 2013, 12, 207-211.

21. Yin, Z. Y.; Li, H.; Li, H.; Jiang, L.; Shi, Y. M.; Sun, Y. H.; Lu, G.; Zhang, Q.; Chen, X. D.; Zhang, H. Single-Layer MoS_2 Phototransistors. *ACS Nano* 2012, 6, 74-80.

22. Choi, W.; Cho, M. Y.; Konar, A.; Lee, J. H.; Cha, G. B.; Hong, S. C.; Kim, S.; Kim, J.; Jena, D.; Joo, J.; Kim, S. High-Detectivity Multilayer MoS_2 Phototransistors with Spectral Response from Ultraviolet to Infrared. *Advanced Materials* 2012, 24, 5832-5836.

23. Tsai, D. S.; Lien, D. H.; Tsai, M. L.; Su, S. H.; Chen, K. M.; Ke, J. J.; Yu, Y. C.; Li, L. J.; He, J. H. Trilayered MoS_2 Metal-Semiconductor-Metal Photodetectors: Photogain and Radiation Resistance. *Ieee J Sel Top Quant* 2014, 20.

24. Yu, W. J.; Liu, Y.; Zhou, H. L.; Yin, A. X.; Li, Z.; Huang, Y.; Duan, X. F. Highly efficient gate-tunable photocurrent generation in vertical heterostructures of layered materials. *Nature Nanotechnology* 2013, 8, 952-958.

25. Perea-Lopez, N.; Elias, A. L.; Berkdemir, A.; Castro-Beltran, A.; Gutierrez, H. R.; Feng, S. M.; Lv, R. T.; Hayashi, T.; Lopez-Urias, F.; Ghosh, S.; Muchharla, B.; Talapatra, S.; Terrones, H.; Terrones, M. Photosensor Device Based on Few-Layered WS_2 Films. *Advanced Functional Materials* 2013, 23, 5511-5517.

26. Esmaeili-Rad, M. R.; Salahuddin, S. High Performance Molybdenum Disulfide Amorphous Silicon Heterojunction Photodetector. *Sci Rep-Uk* 2013, 3.

27. Ye, Y.; Ye, Z. L.; Gharghi, M.; Yin, X. B.; Zhu, H. Y.; Zhao, M.; Zhang, X. Exciton-related electroluminescence from monolayer MoS_2. *Conf Laser Electr* 2014.

28. Fontana, M.; Deppe, T.; Boyd, A. K.; Rinzan, M.; Liu, A. Y.; Paranjape, M.; Barbara, P. Electron-hole transport and photovoltaic effect in gated MoS_2 Schottky junctions. *Sci Rep-Uk* 2013, 3, 1634.

29. Britnell, L.; Ribeiro, R. M.; Eckmann, A.; Jalil, R.; Belle, B. D.; Mishchenko, A.; Kim, Y. J.; Gorbachev, R. V.; Georgiou, T.; Morozov, S. V.; Grigorenko, A. N.; Geim,

A. K.; Casiraghi, C.; Castro Neto, A. H.; Novoselov, K. S. Strong Light-Matter Interactions in Heterostructures of Atomically Thin Films. *Science* 2013, 340, 1311-1314.

30. Eda, G.; Maier, S. A. Two-Dimensional Crystals: Managing Light for Optoelectronics. *ACS Nano* 2013, 7, 5660-5665.

31. Lin, J. D.; Li, H.; Zhang, H.; Chen, W. Plasmonic enhancement of photocurrent in MoS_2 field-effect-transistor. *Appl. Phys. Lett.* 2013, 102.

32. Feng, J.; Qian, X. F.; Huang, C. W.; Li, J. Strain-engineered artificial atom as a broad-spectrum solar energy funnel. *Nat Photonics* 2012, 6, 865-871.

33. Sundaram, R. S.; Engel, M.; Lombardo, A.; Krupke, R.; Ferrari, A. C.; Avouris, P.; Steiner, M. Electroluminescence in Single Layer MoS_2. *Nano Lett.* 2013, 13, 1416-1421.

34. Baugher, B. W. H.; Churchill, H. O. H.; Yang, Y. F.; Jarillo-Herrero, P. Optoelectronic devices based on electrically tunable p-n diodes in a monolayer dichalcogenide. *Nature Nanotechnology* 2014, 9, 262-267.

35. Pospischil, A.; Furchi, M. M.; Mueller, T. Solar-energy conversion and light emission in an atomic monolayer p-n diode. *Nature Nanotechnology* 2014, 9, 257-261.

36. Wang, C. A.; Chien, J. C.; Fang, H.; Takei, K.; Nah, J.; Plis, E.; Krishna, S.; Niknejad, A. M.; Javey, A. Self-Aligned, Extremely High Frequency III-V Metal-Oxide-Semiconductor Field-Effect Transistors on Rigid and Flexible Substrates. *Nano Lett.* 2012, 12, 4140-4145.

37. Yoon, C.; Cho, G.; Kim, S. Electrical Characteristics of GaAs Nanowire-Based MESFETs on Flexible Plastics. *IEEE Trans. Electron Devices* 2011, 58, 1096-1101.

38. Zhou, H.; Seo, J. H.; Paskiewicz, D. M.; Zhu, Y.; Celler, G. K.; Voyles, P. M.; Zhou, W. D.; Lagally, M. G.; Ma, Z. Q. Fast flexible electronics with strained silicon nanomembranes. *Sci Rep-Uk* 2013, 3.

39. Nathan, A.; Ahnood, A.; Cole, M. T.; Lee, S.; Suzuki, Y.; Hiralal, P.; Bonaccorso, F.; Hasan, T.; Garcia-Gancedo, L.; Dyadyusha, A.; Haque, S.; Andrew, P.; Hofmann, S.; Moultrie, J.; Chu, D. P.; Flewitt, A. J.; Ferrari, A. C.; Kelly, M. J.; Robertson, J.;

Amaratunga, G. A. J.; Milne, W. I. Flexible Electronics: The Next Ubiquitous Platform. *Proc. IEEE* 2012, 100, 1486-1517.

40. Phan, H. D.; Kim, Y.; Lee, J.; Liu, R.; Choi, Y.; Cho, J. H.; Lee, C. Ultraclean and Direct Transfer of a Wafer-Scale MoS_2 Thin Film onto a Plastic Substrate. *Advanced Materials* 2016, 1603928-n/a.

41. Late, D. J.; Liu, B.; Matte, H. S. S. R.; Dravid, V. P.; Rao, C. N. R. Hysteresis in Single-Layer MoS_2 Field Effect Transistors. *ACS Nano* 2012, 6, 5635-5641.

42. Kim, H. U.; Kim, H.; Ahn, C.; Kulkarni, A.; Jeon, M.; Yeom, G. Y.; Lee, M. H.; Kim, T. In situ synthesis of MoS_2 on a polymer based gold electrode platform and its application in electrochemical biosensing. *Rsc Adv* 2015, 5, 10134-10138.

43. Chai, Y.; Su, S.; Yan, D.; Ozkan, M.; Lake, R.; Ozkan, C. S. Strain Gated Bilayer Molybdenum Disulfide Field Effect Transistor with Edge Contacts. *Sci Rep-Uk* 2017, 7, 41593.

44. Conley, H. J.; Wang, B.; Ziegler, J. I.; Haglund, R. F.; Pantelides, S. T.; Bolotin, K. I. Bandgap Engineering of Strained Monolayer and Bilayer MoS_2. *Nano Lett.* 2013, 13, 3626-3630.

45. Johari, P.; Shenoy, V. B. Tuning the Electronic Properties of Semiconducting Transition Metal Dichalcogenides by Applying Mechanical Strains. *ACS Nano* 2012, 6, 5449-5456.

46. Lloyd, D.; Liu, X.; Christopher, J. W.; Cantley, L.; Wadehra, A.; Kim, B. L.; Goldberg, B. B.; Swan, A. K.; Bunch, J. S. Band Gap Engineering with Ultralarge Biaxial Strains in Suspended Monolayer MoS_2. *Nano Lett.* 2016, 16, 5836-5841.

47. Nguyen, C. V.; Hieu, N. N.; Ilyasov, V. V. Band Gap Modulation of Bilayer MoS_2 Under Strain Engineering and Electric Field: A Density Functional Theory. *J Electron Mater* 2016, 45, 4038-4043.

48. Yang, L.; Cui, X.; Zhang, J.; Wang, K.; Shen, M.; Zeng, S.; Dayeh, S. A.; Feng, L.; Xiang, B. Lattice strain effects on the optical properties of MoS_2 nanosheets. *Sci Rep-Uk* 2014, 4, 5649.

49. Liu, Z. Y.; Qi, D. P.; Guo, P. Z.; Liu, Y.; Zhu, B. W.; Yang, H.; Liu, Y. Q.; Li, B.; Zhang, C. G.; Yu, J. C.; Liedberg, B.; Chen, X. D. Thickness-Gradient Films for High Gauge Factor Stretchable Strain Sensors. *Advanced Materials* 2015, 27, 6230-6237.

50. Park, M.; Park, Y. J.; Chen, X.; Park, Y. K.; Kim, M. S.; Ahn, J. H. MoS_2-Based Tactile Sensor for Electronic Skin Applications. *Advanced Materials* 2016, 28, 2556.

51. Bardeen, J.; Brattain, W. H. The Transistor, A Semi-Conductor Triode. *Phys Rev* 1948, 74, 230-231.

52. Bardeen, J.; Brattain, W. H. Physical Principles Involved in Transistor Action. *Phys Rev* 1949, 75, 1208-1225.

53. Steehler, J. K. Understanding Moore's Law—Four Decades of Innovation (David C. Brock, ed.). *J Chem Educ* 2007, 84, 1278.

54. Conwell, E. M. Properties of Silicon and Germanium: II. *Proceedings of the IRE* 1958, 46, 1281-1300.

55. Dawon, K. Electric field controlled semiconductor device. Google Patents: 1963.

56. Gray, P. V. The silicon-silicon dioxide system. *Proc. IEEE* 1969, 57, 1543-1551.

57. Kilby, J. S. Miniaturized electronic circuits. Google Patents: 1964.

58. Mistry, K.; Allen, C.; Auth, C.; Beattie, B.; Bergstrom, D.; Bost, M.; Brazier, M.; Buehler, M.; Cappellani, A.; Chau, R.; Choi, C. H.; Ding, G.; Fischer, K.; Ghani, T.; Grover, R.; Han, W.; Hanken, D.; Hattendorf, M.; He, J.; Hicks, J.; Huessner, R.; Ingerly, D.; Jain, P.; James, R.; Jong, L.; Joshi, S.; Kenyon, C.; Kuhn, K.; Lee, K.; Liu, H.; Maiz, J.; McIntyre, B.; Moon, P.; Neirynck, J.; Pae, S.; Parker, C.; Parsons, D.; Prasad, C.; Pipes, L.; Prince, M.; Ranade, P.; Reynolds, T.; Sandford, J.; Shifren, L.; Sebastian, J.; Seiple, J.; Simon, D.; Sivakumar, S.; Smith, P.; Thomas, C.; Troeger, T.; Vandervoorn, P.; Williams, S.; Zawadzki, K. In *A 45nm Logic Technology with High-k+Metal Gate Transistors, Strained Silicon, 9 Cu Interconnect Layers, 193nm Dry Patterning, and 100% Pb-free Packaging*, 2007 IEEE International Electron Devices Meeting, 10-12 Dec. 2007; 2007; pp 247-250.

59. Clauss, F. J. *Solid lubricants and self-lubricating solids*. Elsevier: 2012.

60. Ubaldini, A.; Jacimovic, J.; Ubrig, N.; Giannini, E. Chloride-Driven Chemical Vapor Transport Method for Crystal Growth of Transition Metal Dichalcogenides. *Cryst Growth Des* 2013, 13, 4453-4459.

61. Bougouma, M.; Batan, A.; Guel, B.; Segato, T.; Legma, J. B.; Reniers, F.; Delplancke-Ogletree, M. P.; Buess-Herman, C.; Doneux, T. Growth and characterization of large, high quality $MoSe_2$ single crystals. *J Cryst Growth* 2013, 363, 122-127.

62. Brown, B. E. The Crystal Structures of WTe_2 and High-Temperature $MoTe_2$. *Acta Crystallogr* 1966, 20, 268-&.

63. Wieting, T. J.; Grisel, A.; Lévy, F. Interlayer bonding and localized charge in $MoSe_2$ and α-$MoTe_2$. *Physica B+C* 1980, 99, 337-342.

64. Hla, S. W.; Marinkovic, V.; Prodan, A.; Musevic, I. STM/AFM investigations of β-$MoTe_2$, α-$MoTe_2$, and WTe_2. *Surf Sci* 1996, 352, 105-111.

65. Revolinsky, E.; Beerntsen, D. Electrical Properties of α- and β-$MoTe_2$ as Affected by Stoichiometry and Preparation Temperature. *J Phys Chem Solids* 1966, 27, 523-&.

66. Revolinsky, E.; Beerntsen, D. Electrical Properties of the $MoTe_2$-WTe_2 and $MoSe_2$-WSe_2 Systems. *J. Appl. Phys.* 1964, 35, 2086-&.

67. Upadhyayula, L. C.; Loferski, J. J.; Wold, A.; Giriat, W.; Kershaw, R. Semiconducting Properties of Single Crystals of N and P-Type Tungsten Diselenide (WSe_2). *J. Appl. Phys.* 1968, 39, 4736.

68. Vellinga, M. B.; de Jonge, R.; Haas, C. Semiconductor to metal transition in $MoTe_2$. *J Solid State Chem* 1970, 2, 299-302.

69. Davey, B.; Evans, B. L. Optical Properties of $MoTe_2$ and WSe_2. *Phys Status Solidi A* 1972, 13, 483-&.

70. Conan, A.; Bonnet, A.; Amrouche, A.; Spiesser, M. Semiconducting Properties and Band-Structure of $MoTe_2$ Single-Crystals. *J Phys-Paris* 1984, 45, 459-465.

71. Conan, A.; Delaunay, D.; Bonnet, A.; Moustafa, A. G.; Spiesser, M. Temperature-Dependence of the Electrical-Conductivity and Thermoelectric-Power in $MoTe_2$ Single-Crystals. *Physica Status Solidi B-Basic Research* 1979, 94, 279-286.

72. Novoselov, K. S.; Jiang, D.; Schedin, F.; Booth, T. J.; Khotkevich, V. V.; Morozov, S. V.; Geim, A. K. Two-dimensional atomic crystals. *P Natl Acad Sci USA* 2005, 102, 10451-10453.

73. Radisavljevic, B.; Radenovic, A.; Brivio, J.; Giacometti, V.; Kis, A. Single-layer MoS_2 transistors. *Nature Nanotechnology* 2011, 6, 147-150.

74. Wang, Q. H.; Kalantar-Zadeh, K.; Kis, A.; Coleman, J. N.; Strano, M. S. Electronics and Optoelectronics of Two-Dimensional Transition Metal Dichalcogenides. *Nat. Nanotechnol.* 2012, 7, 699-712.

75. Riflikova, M.; Martonak, R.; Tosatti, E. Pressure-induced gap closing and metallization of $MoSe_2$ and $MoTe_2$. *Phys. Rev. B* 2014, 90.

76. Gabuda, S. P.; Kozlova, S. G.; Ryzhikov, M. R.; Fedorov, V. E. Transition from 2-D Semiconductor to 1-D Metal State and Electron Density Distribution in Nanolayered MoX_2 (X = S, Se, Te). *J Phys Chem C* 2012, 116, 20651-20655.

77. Kuc, A.; Zibouche, N.; Heine, T. Influence of quantum confinement on the electronic structure of the transition metal sulfide TS_2. *Phys. Rev. B* 2011, 83.

78. Han, S. W.; Kwon, H.; Kim, S. K.; Ryu, S.; Yun, W. S.; Kim, D. H.; Hwang, J. H.; Kang, J. S.; Baik, J.; Shin, H. J.; Hong, S. C. Band-gap transition induced by interlayer van der Waals interaction in MoS_2. *Phys. Rev. B* 2011, 84.

79. Eda, G.; Yamaguchi, H.; Voiry, D.; Fujita, T.; Chen, M. W.; Chhowalla, M. Photoluminescence from Chemically Exfoliated MoS_2. *Nano Lett.* 2011, 11, 5111-5116.

80. Santosh, K. C.; Roberto, C. L.; Rafik, A.; Robert, M. W.; Kyeongjae, C. Impact of intrinsic atomic defects on the electronic structure of MoS_2 monolayers. *Nanotechnology* 2014, 25, 375703.

81. Zhou, W.; Zou, X. L.; Najmaei, S.; Liu, Z.; Shi, Y. M.; Kong, J.; Lou, J.; Ajayan, P. M.; Yakobson, B. I.; Idrobo, J. C. Intrinsic Structural Defects in Monolayer Molybdenum Disulfide. *Nano Lett.* 2013, 13, 2615-2622.

82. Zou, X. L.; Liu, Y. Y.; Yakobson, B. I. Predicting Dislocations and Grain Boundaries in Two-Dimensional Metal-Disulfides from the First Principles. *Nano Lett.* 2013, 13, 253-258.

83. Elias, A. L.; Perea-Lopez, N.; Castro-Beltran, A.; Berkdemir, A.; Lv, R. T.; Feng, S. M.; Long, A. D.; Hayashi, T.; Kim, Y. A.; Endo, M.; Gutierrez, H. R.; Pradhan, N. R.; Balicas, L.; Houk, T. E. M.; Lopez-Urias, F.; Terrones, H.; Terrones, M. Controlled Synthesis and Transfer of Large-Area WS_2 Sheets: From Single Layer to Few Layers. *ACS Nano* 2013, 7, 5235-5242.

84. Nguyen, N. T.; Berseth, P. A.; Lin, Q. Y.; Chiritescu, C.; Cahill, D. G.; Mavrokefalos, A.; Shi, L.; Zschack, P.; Anderson, M. D.; Anderson, I. M.; Johnson, D. C. Synthesis and Properties of Turbostratically Disordered, Ultrathin WSe_2 Films. *Chem Mater* 2010, 22, 2750-2756.

85. Bernede, J. C.; Pouzet, J.; Manai, N.; Benmouais, A. Structural Characterization of Synthesized Molybdenum Ditelluride Thin-Films. *Mater Res Bull* 1990, 25, 31-42.

86. Srivastava, S. K.; Guettari, N.; Bernede, J. C. Growth of textured nonstoichiometric $MoTe_2$ films from Mo/Te layers and their use as precursor in the synthesis of $MoTe_{2-x}S_x$ films. *Solid State Commun* 2004, 132, 601-606.

87. Kong, D. S.; Wang, H. T.; Cha, J. J.; Pasta, M.; Koski, K. J.; Yao, J.; Cui, Y. Synthesis of MoS_2 and $MoSe_2$ Films with Vertically Aligned Layers. *Nano Lett.* 2013, 13, 1341-1347.

88. Wang, H. T.; Kong, D. S.; Johanes, P.; Cha, J. J.; Zheng, G. Y.; Yan, K.; Liu, N. A.; Cui, Y. $MoSe_2$ and WSe_2 Nanofilms with Vertically Aligned Molecular Layers on Curved and Rough Surfaces. *Nano Lett.* 2013, 13, 3426-3433.

89. Yu, J. H.; Lee, H. R.; Hong, S. S.; Kong, D.; Lee, H.-W.; Wang, H.; Xiong, F.; Wang, S.; Cui, Y. Vertical Heterostructure of Two-Dimensional MoS_2 and WSe_2 with Vertically Aligned Layers. *Nano Lett.* 2015, 15, 1031-1035.

90. Zhan, Y. J.; Liu, Z.; Najmaei, S.; Ajayan, P. M.; Lou, J. Large-Area Vapor-Phase Growth and Characterization of MoS_2 Atomic Layers on a SiO_2 Substrate. *Small* 2012, 8, 966-971.

91. Kang, K.; Xie, S. E.; Huang, L. J.; Han, Y. M.; Huang, P. Y.; Mak, K. F.; Kim, C. J.; Muller, D.; Park, J. High-mobility three-atom-thick semiconducting films with wafer-scale homogeneity. *Nature* 2015, 520, 656-660.

92. Eichfeld, S. M.; Hossain, L.; Lin, Y.-C.; Piasecki, A. F.; Kupp, B.; Birdwell, A. G.; Burke, R. A.; Lu, N.; Peng, X.; Li, J.; Azcatl, A.; McDonnell, S.; Wallace, R. M.; Kim, M. J.; Mayer, T. S.; Redwing, J. M.; Robinson, J. A. Highly Scalable, Atomically Thin WSe_2 Grown via Metal–Organic Chemical Vapor Deposition. *ACS Nano* 2015, 9, 2080-2087.

93. Xia, J.; Huang, X.; Liu, L. Z.; Wang, M.; Wang, L.; Huang, B.; Zhu, D. D.; Li, J. J.; Gu, C. Z.; Meng, X. M. CVD synthesis of large-area, highly crystalline $MoSe_2$ atomic layers on diverse substrates and application to photodetectors. *Nanoscale* 2014, 6, 8949-8955.

94. Wang, X. L.; Gong, Y. J.; Shi, G.; Chow, W. L.; Keyshar, K.; Ye, G. L.; Vajtai, R.; Lou, J.; Liu, Z.; Ringe, E.; Tay, B. K.; Ajayan, P. M. Chemical Vapor Deposition Growth of Crystalline Monolayer $MoSe_2$. *ACS Nano* 2014, 8, 5125-5131.

95. Najmaei, S.; Liu, Z.; Zhou, W.; Zou, X.; Shi, G.; Lei, S.; Yakobson, B. I.; Idrobo, J.-C.; Ajayan, P. M.; Lou, J. Vapour Phase Growth and Grain Boundary Structure of Molybdenum Disulphide Atomic Layers. *Nat. Mater.* 2013, 12, 754-759.

96. van der Zande, A. M.; Huang, P. Y.; Chenet, D. A.; Berkelbach, T. C.; You, Y. M.; Lee, G. H.; Heinz, T. F.; Reichman, D. R.; Muller, D. A.; Hone, J. C. Grains and grain boundaries in highly crystalline monolayer molybdenum disulphide. *Nat. Mater.* 2013, 12, 554-561.

97. Zhu, W.; Low, T.; Lee, Y. H.; Wang, H.; Farmer, D. B.; Kong, J.; Xia, F. N.; Avouris, P. Electronic transport and device prospects of monolayer molybdenum disulphide grown by chemical vapour deposition. *Nat. Commun.* 2014, 5, 3087.

98. Lee, Y. H.; Zhang, X. Q.; Zhang, W. J.; Chang, M. T.; Lin, C. T.; Chang, K. D.; Yu, Y. C.; Wang, J. T. W.; Chang, C. S.; Li, L. J.; Lin, T. W. Synthesis of Large-Area MoS_2 Atomic Layers with Chemical Vapor Deposition. *Advanced Materials* 2012, 24, 2320-2325.

99. Lu, X.; Utama, M. I. B.; Lin, J. H.; Gong, X.; Zhang, J.; Zhao, Y. Y.; Pantelides, S. T.; Wang, J. X.; Dong, Z. L.; Liu, Z.; Zhou, W.; Xiong, Q. H. Large-Area Synthesis of Monolayer and Few-Layer $MoSe_2$ Films on SiO_2 Substrates. *Nano Lett.* 2014, 14, 2419-2425.

100. Shaw, J.; Zhou, H.; Chen, Y.; Weiss, N.; Liu, Y.; Huang, Y.; Duan, X. Chemical vapor deposition growth of monolayer $MoSe_2$ nanosheets. *Nano Res.* 2014, 7, 1-7.

101. Boscher, N. D.; Carmalt, C. J.; Parkin, I. P. Atmospheric pressure chemical vapor deposition of WSe_2 thin films on glass - highly hydrophobic sticky surfaces. *Journal of Materials Chemistry* 2006, 16, 122-127.

102. Aretouli, K. E.; Tsipas, P.; Tsoutsou, D.; Marquez-Velasco, J.; Xenogiannopoulou, E.; Giamini, S. A.; Vassalou, E.; Kelaidis, N.; Dimoulas, A. Two-dimensional semiconductor $HfSe_2$ and $MoSe_2/HfSe_2$ van der Waals heterostructures by molecular beam epitaxy. *Appl. Phys. Lett.* 2015, 106.

103. Barton, A. T.; Yue, R.; Anwar, S.; Zhu, H.; Peng, X.; McDonnell, S.; Lu, N.; Addou, R.; Colombo, L.; Kim, M. J.; Wallace, R. M.; Hinkle, C. L. Transition metal dichalcogenide and hexagonal boron nitride heterostructures grown by molecular beam epitaxy. *Microelectronic Engineering* 2015, 147, 306-309.

104. Diaz, H. C.; Chaghi, R.; Ma, Y. J.; Batzill, M. Molecular beam epitaxy of the van der Waals heterostructure $MoTe_2$ on MoS_2: phase, thermal, and chemical stability. *2D Materials* 2015, 2.

105. Vishwanath, S.; Liu, X.; Rouvimov, S.; Basile, L.; Lu, N.; Azcatl, A.; Magno, K.; Wallace, R. M.; Kim, M.; Idrobo, J.-C.; Furdyna, J. K.; Jena, D.; Xing, H. G. Controllable growth of layered selenide and telluride heterostructures and superlattices using molecular beam epitaxy. *J Mater Res* 2016, FirstView, 1-11.

106. Yuan, X.; Tang, L.; Liu, S. S.; Wang, P.; Chen, Z. G.; Zhang, C.; Liu, Y. W.; Wang, W. Y.; Zou, Y. C.; Liu, C.; Guo, N.; Zou, J.; Zhou, P.; Hu, W. D.; Xiu, F. X. Arrayed van der Waals Vertical Heterostructures Based on 2D GaSe Grown by Molecular Beam Epitaxy. *Nano Lett.* 2015, 15, 3571-3577.

107. Yue, R. Y.; Barton, A. T.; Zhu, H.; Azcatl, A.; Pena, L. F.; Wang, J.; Peng, X.; Lu, N.; Cheng, L. X.; Addou, R.; McDonnell, S.; Colombo, L.; Hsu, J. W. P.; Kim, J.; Kim, M. J.; Wallace, R. M.; Hinkle, C. L. $HfSe_2$ Thin Films: 2D Transition Metal Dichalcogenides Grown by Molecular Beam Epitaxy. *ACS Nano* 2015, 9, 474-480.

108. Zuo, Z.; Xu, Z. G.; Zheng, R. J.; Khanaki, A.; Zheng, J. G.; Liu, J. L. In-situ epitaxial growth of graphene/h-BN van der Waals heterostructures by molecular beam epitaxy. *Sci Rep-Uk* 2015, 5.

109. Aretouli, K. E.; Tsoutsou, D.; Tsipas, P.; Marquez-Velasco, J.; Aminalragia Giamini, S.; Kelaidis, N.; Psycharis, V.; Dimoulas, A. Epitaxial 2D $SnSe_2$/ 2D WSe_2 van der Waals Heterostructures. *ACS Applied Materials & Interfaces* 2016, 8, 23222-23229.

110. Hussain, S.; Singh, J.; Vikraman, D.; Singh, A. K.; Iqbal, M. Z.; Khan, M. F.; Kumar, P.; Choi, D.-C.; Song, W.; An, K.-S.; Eom, J.; Lee, W.-G.; Jung, J. Large-area, continuous and high electrical performances of bilayer to few layers MoS_2 fabricated by RF sputtering via post-deposition annealing method. *Sci Rep-Uk* 2016, 6, 30791.

111. Ahn, C.; Lee, J.; Kim, H. U.; Bark, H.; Jeon, M.; Ryu, G. H.; Lee, Z.; Yeom, G. Y.; Kim, K.; Jung, J.; Kim, Y.; Lee, C.; Kim, T. Low-Temperature Synthesis of Large-Scale Molybdenum Disulfide Thin Films Directly on a Plastic Substrate Using Plasma-Enhanced Chemical Vapor Deposition. *Advanced Materials* 2015, 27, 5223-5229.

112. Lince, J. R.; Carré, D. J.; Fleischauer, P. D. Schottky-barrier formation on a covalent semiconductor without Fermi-level pinning: The metal-MoS_2(0001) interface. *Phys. Rev. B* 1987, 36, 1647-1656.

113. Das, S.; Chen, H. Y.; Penumatcha, A. V.; Appenzeller, J. High Performance Multilayer MoS_2 Transistors with Scandium Contacts. *Nano Lett.* 2013, 13, 100-105.

114. Kaushik, N.; Nipane, A.; Basheer, F.; Dubey, S.; Grover, S.; Deshmukh, M. M.; Lodha, S. Schottky barrier heights for Au and Pd contacts to MoS_2. *Appl. Phys. Lett.* 2014, 105, 113505.

115. Gong, C.; Colombo, L.; Wallace, R. M.; Cho, K. The Unusual Mechanism of Partial Fermi Level Pinning at Metal-MoS_2 Interfaces. *Nano Lett.* 2014, 14, 1714-1720.

116. Zhong, H. X.; Quhe, R. G.; Wang, Y. Y.; Ni, Z. Y.; Ye, M.; Song, Z. G.; Pan, Y. Y.; Yang, J. B.; Yang, L.; Lei, M.; Shi, J. J.; Lu, J. Interfacial Properties of Monolayer and Bilayer MoS_2 Contacts with Metals: Beyond the Energy Band Calculations. *Sci Rep-Uk* 2016, 6.

117. Smyth, C. M.; Addou, R.; McDonnell, S.; Hinkle, C. L.; Wallace, R. M. Contact Metal–MoS_2 Interfacial Reactions and Potential Implications on MoS_2-Based Device Performance. *The Journal of Physical Chemistry C* 2016, 120, 14719-14729.

118. Guo, Y.; Liu, D.; Robertson, J. Chalcogen vacancies in monolayer transition metal dichalcogenides and Fermi level pinning at contacts. *Appl. Phys. Lett.* 2015, 106, 173106.

119. Liu, D.; Guo, Y.; Fang, L.; Robertson, J. Sulfur vacancies in monolayer MoS_2 and its electrical contacts. *Appl. Phys. Lett.* 2013, 103, 183113.

120. Geim, A. K.; Grigorieva, I. V. Van der Waals heterostructures. *Nature* 2013, 499, 419-425.

121. Campbell, P. M.; Tarasov, A.; Joiner, C. A.; Ready, W. J.; Vogel, E. M. Band structure effects on resonant tunneling in III-V quantum wells versus two-dimensional vertical heterostructures. *J. Appl. Phys.* 2016, 119, 024503.

122. de la Barrera, S. C.; Gao, Q.; Feenstra, R. M. Theory of Graphene–Insulator–Graphene Tunnel Junctions. *JVST B* 2014, 32, 04E101.

123. Feenstra, R. M.; Jena, D.; Gu, G. Single-Particle Tunneling in Doped Graphene-Insulator-Graphene Junctions. *J. Appl. Phys.* 2012, 111, 043711.

124. Zhao, P.; Feenstra, R. M.; Gu, G.; Jena, D. SymFET: A Proposed Symmetric Graphene Tunneling Field-Effect Transistor. *IEEE Trans. Electron Devices* 2013, 60, 951-957.

125. Campbell, P. M.; Tarasov, A.; Joiner, C. A.; Ready, W. J.; Vogel, E. M. Enhanced Resonant Tunneling in Symmetric 2D Semiconductor Vertical Heterostructure Transistors. *ACS Nano* 2015, 9, 5000-5008.

126. Li, M.; Esseni, D.; Snider, G.; Jena, D.; Grace Xing, H. Single Particle Transport in Two-Dimensional Heterojunction Interlayer Tunneling Field Effect Transistor. *J. Appl. Phys.* 2014, 115, 074508.

127. Li, M. O.; Esseni, D.; Nahas, J. J.; Jena, D.; Xing, H. G. Two-Dimensional Heterojunction Interlayer Tunneling Field Effect Transistors (Thin-TFETs). *Electron Devices Society, IEEE Journal of the* 2015, 3, 200-207.

128. Chang, L. L.; Esaki, L.; Tsu, R. Resonant Tunneling in Semiconductor Double Barriers. *Appl. Phys. Lett.* 1974, 24, 593-595.

129. Esaki, L.; Tsu, R. Superlattice and Negative Differential Conductivity in Semiconductors. *IBM J. Res. Dev.* 1970, 14, 61-65.

130. Tsu, R.; Esaki, L. Tunneling in a Finite Superlattice. *Appl. Phys. Lett.* 1973, 22, 562-564.

131. Yan, R. S.; Fathipour, S.; Han, Y. M.; Song, B.; Xiao, S. D.; Li, M. D.; Ma, N.; Protasenko, V.; Muller, D. A.; Jena, D.; Xing, H. G. Esaki Diodes in van der Waals Heterojunctions with Broken-Gap Energy Band Alignment. *Nano Lett.* 2015, 15, 5791-5798.

132. Roy, T.; Tosun, M.; Cao, X.; Fang, H.; Lien, D.-H.; Zhao, P.; Chen, Y.-Z.; Chueh, Y.-L.; Guo, J.; Javey, A. Dual-Gated MoS_2/WSe_2 van der Waals Tunnel Diodes and Transistors. *ACS Nano* 2015, 2071-2079.

133. Britnell, L.; Gorbachev, R. V.; Geim, A. K.; Ponomarenko, L. A.; Mishchenko, A.; Greenaway, M. T.; Fromhold, T. M.; Novoselov, K. S.; Eaves, L. Resonant Tunnelling and Negative Differential Conductance in Graphene Transistors. *Nat. Commun.* 2013, 4, 1794.

134. Roy, T.; Liu, L.; de la Barrera, S.; Chakrabarti, B.; Hesabi, Z.; Joiner, C.; Feenstra, R.; Gu, G.; Vogel, E. Tunneling Characteristics in Chemical Vapor Deposited Graphene–Hexagonal Boron Nitride–Graphene Junctions. *Appl. Phys. Lett.* 2014, 104, 123506.

135. Britnell, L.; Gorbachev, R. V.; Jalil, R.; Belle, B. D.; Schedin, F.; Mishchenko, A.; Georgiou, T.; Katsnelson, M. I.; Eaves, L.; Morozov, S. V.; Peres, N. M. R.; Leist, J.; Geim, A. K.; Novoselov, K. S.; Ponomarenko, L. A. Field-Effect Tunneling Transistor Based on Vertical Graphene Heterostructures. *Science* 2012, 335, 947-950.

136. Xue, J. M.; Sanchez-Yamagishi, J.; Bulmash, D.; Jacquod, P.; Deshpande, A.; Watanabe, K.; Taniguchi, T.; Jarillo-Herrero, P.; Leroy, B. J. Scanning tunnelling microscopy and spectroscopy of ultra-flat graphene on hexagonal boron nitride. *Nat. Mater.* 2011, 10, 282-285.

137. Cao, J.; Cresti, A.; Esseni, D.; Pala, M. Quantum simulation of a heterojunction vertical tunnel FET based on 2D transition metal dichalcogenides. *Solid-State Electronics* 2016, 116, 1-7.

138. Sarkar, D.; Xie, X.; Liu, W.; Cao, W.; Kang, J.; Gong, Y.; Kraemer, S.; Ajayan, P. M.; Banerjee, K. A subthermionic tunnel field-effect transistor with an atomically thin channel. *Nature* 2015, 526, 91-95.

139. Liang, X. L.; Sperling, B. A.; Calizo, I.; Cheng, G. J.; Hacker, C. A.; Zhang, Q.; Obeng, Y.; Yan, K.; Peng, H. L.; Li, Q. L.; Zhu, X. X.; Yuan, H.; Walker, A. R. H.; Liu, Z. F.; Peng, L. M.; Richter, C. A. Toward Clean and Crackless Transfer of Graphene. *ACS Nano* 2011, 5, 9144-9153.

140. Her, M.; Beams, R.; Novotny, L. Graphene transfer with reduced residue. *Phys Lett A* 2013, 377, 1455-1458.

141. Kim, K.; Yankowitz, M.; Fallahazad, B.; Kang, S.; Movva, H. C. P.; Huang, S.; Larentis, S.; Corbet, C. M.; Taniguchi, T.; Watanabe, K.; Banerjee, S. K.; LeRoy, B. J.; Tutuc, E. van der Waals Heterostructures with High Accuracy Rotational Alignment. *Nano Lett.* 2016.

142. Lin, Y. C.; Ghosh, R. K.; Addou, R.; Lu, N.; Eichfeld, S. M.; Zhu, H.; Li, M. Y.; Peng, X.; Kim, M. J.; Li, L. J.; Wallace, R. M.; Datta, S.; Robinson, J. A. Atomically thin resonant tunnel diodes built from synthetic van der Waals heterostructures. *Nat. Commun.* 2015, 6, 7311.

143. Nikam, R. D.; Sonawane, P. A.; Sankar, R.; Chen, Y.-T. Epitaxial growth of vertically stacked p-MoS_2/n-MoS_2 heterostructures by chemical vapor deposition for light emitting devices. *Nano Energy* 2017, 32, 454-462.

144. Choudhary, N.; Park, J.; Hwang, J. Y.; Chung, H. S.; Dumas, K. H.; Khondaker, S. I.; Choi, W. B.; Jung, Y. Centimeter Scale Patterned Growth of Vertically Stacked Few Layer Only 2D MoS_2/WS_2 van der Waals Heterostructure. *Sci Rep-Uk* 2016, 6, 25456.

145. Chen, J. Y.; Zhou, W.; Tang, W.; Tian, B. B.; Zhao, X. X.; Xu, H.; Liu, Y. P.; Geng, D. C.; Tan, S. J. R.; Fu, W.; Loh, K. P. Lateral Epitaxy of Atomically Sharp WSe_2/WS_2 Heterojunctions on Silicon Dioxide Substrates. *Chem Mater* 2016, 28, 7194-7197.

146. Jung, Y.; Shen, J.; Sun, Y.; Cha, J. J. Chemically Synthesized Heterostructures of Two-Dimensional Molybdenum/Tungsten-Based Dichalcogenides with Vertically Aligned Layers. *ACS Nano* 2014, 8, 9550-9557.

147. Aymerich-Humet, X.; Serra-Mestres, F.; Millán, J. A Generalized Approximation of the Fermi–Dirac Integrals. *J. Appl. Phys.* 1983, 54, 2850-2851.

148. Lam, K. T.; Seol, G.; Guo, J. Operating Principles of Vertical Transistors Based on Monolayer Two-Dimensional Semiconductor Heterojunctions. *Appl. Phys. Lett.* 2014, 105.

149. Bardeen, J. Tunnelling from a Many-Particle Point of View. *Phys. Rev. Lett.* 1961, 6, 57.

150. Gottlieb, A. D.; Wesoloski, L. Bardeen's Tunnelling Theory as Applied to Scanning Tunnelling Microscopy: A Technical Guide to the Traditional Interpretation. *Nanotechnology* 2006, 17, R57.

151. Duke, C. B. *Tunneling in Solids*. Academic Press: 1969.

152. Vogel, E. M.; Ahmed, K. Z.; Hornung, B.; Henson, W. K.; McLarty, P. K.; Lucovsky, G.; Hauser, J. R.; Wortman, J. J. Modeled tunnel currents for high dielectric constant dielectrics. *IEEE Trans. Electron Devices* 1998, 45, 1350-1355.

153. Yoder, P. D.; Grupen, M.; Smith, R. K. Demonstration of Intrinsic Tristability in Double-Barrier Resonant Tunneling Diodes With the Wigner Transport Equation. *IEEE Trans. Electron Devices* 2010, 57, 3265-3274.

154. Kane, E. O. Thomas-Fermi Approach to Impure Semiconductor Band Structure. *Phys Rev* 1963, 131, 79-&.

155. Mehmetoglu, T. Analytical evaluation of charge carrier density of organic materials with Gauss density of states. *J Comput Electron* 2014, 13, 960-964.

156. Sun, J. P.; Haddad, G. I.; Mazumder, P.; Schulman, J. N. Resonant Tunneling Diodes: Models and Properties. *Proc. IEEE* 1998, 86, 641-661.

157. Broekaert, T. P. E.; Lee, W.; Fonstad, C. G. Pseudomorphic $In_{0.53}Ga_{0.47}As$/AlAs/InAs Resonant Tunneling Diodes with Peak-to-Valley Current Ratios of 30 at Room Temperature. *Appl. Phys. Lett.* 1988, 53, 1545-1547.

158. Ismail, K.; Meyerson, B. S.; Wang, P. J. Electron Resonant Tunneling in Si/SiGe Double Barrier Diodes. *Appl. Phys. Lett.* 1991, 59, 973-975.

159. See, P.; Paul, D. J.; Hollander, B.; Mantl, S.; Zozoulenko, I. V.; Berggren, K. F. High Performance Si/$Si_{1-x}Ge_x$ Resonant Tunneling Diodes. *IEEE Electron Device Lett.* 2001, 22, 182-184.

160. See, P.; Paul, D. J. The Scaled Performance of Si/$Si_{1-x}Ge_x$ Resonant Tunneling Diodes. *IEEE Electron Device Lett.* 2001, 22, 582-584.

161. Luo, L. F.; Beresford, R.; Wang, W. I. Interband Tunneling in Polytype GaSb/AlSb/InAs Heterostructures. *Appl. Phys. Lett.* 1989, 55, 2023-2025.

162. Haddad, G. I.; Reddy, U. K.; Sun, J. P.; Mains, R. K. The Bound-State Resonant Tunneling Transistor (BSRTT): Fabrication, D.C. I–V Characteristics and High-Frequency Properties. *Superlattices Microstruct.* 1990, 7, 369-374.

163. Capasso, F.; Kiehl, R. A. Resonant Tunneling Transistor with Quantum Well Base and High-Energy Injection: A New Negative Differential Resistance Device. *J. Appl. Phys.* 1985, 58, 1366-1368.

164. Reed, M. A.; Frensley, W. R.; Matyi, R. J.; Randall, J. N.; Seabaugh, A. C. Realization of a Three-Terminal Resonant Tunneling Device: The Bipolar Quantum Resonant Tunneling Transistor. *Appl. Phys. Lett.* 1989, 54, 1034-1036.

165. Mazumder, P.; Kulkarni, S.; Bhattacharya, M.; Sun, J. P.; Haddad, G. I. Digital Circuit Applications of Resonant Tunneling Devices. *Proc. IEEE* 1998, 86, 664-686.

166. Fobelets, K.; VanHoof, C.; Genoe, J.; Stake, J.; Lundgren, L.; Borghs, G. High-Frequency Capacitance of Bipolar Resonant Tunneling Diodes. *J. Appl. Phys.* 1996, 79, 905-910.

167. Bowen, R. C.; Klimeck, G.; Lake, R. K.; Frensley, W. R.; Moise, T. Quantitative Simulation of a Resonant Tunneling Diode. *J. Appl. Phys.* 1997, 81, 3207-3213.

168. Klimeck, G.; Bowen, R. C.; Boykin, T. B. Off-Zone-Center or Indirect Band-Gap-like Hole Transport in Heterostructures. *Phys. Rev. B* 2001, 63, 195310.

169. Sakr, S.; Warde, E.; Tchernycheva, M.; Julien, F. H. Ballistic Transport in GaN/AlGaN Resonant Tunneling Diodes. *J. Appl. Phys.* 2011, 109, 023717.

170. Sakuraba, M.; Takahashi, K.; Murota, J. Room-Temperature Resonant Tunneling Diode with High-Ge-Fraction Strained $Si_{1-x}Ge_x$ and Nanometer-Order Ultrathin Si. *ECS Trans.* 2010, 33, 379-387.

171. Xia, J. B. Theory of Hole Resonant Tunneling in Quantum-Well Structures. *Phys. Rev. B* 1988, 38, 8365-8370.

172. Moise, T. S.; Kao, Y. C.; Katz, A. J.; Broekaert, T. P. E.; Celii, F. G. Experimental Sensitivity Analysis of Pseudomorphic InGaAs/AlAs Resonant-Tunneling Diodes. *J. Appl. Phys.* 1995, 78, 6305-6317.

173. Inata, T.; Muto, S.; Nakata, Y.; Sasa, S.; Fujii, T.; Hiyamizu, S. A Pseudomorphic $In_{0.53}Ga_{0.47}As$/AlAs Resonant Tunneling Barrier with a Peak-to-Valley Current Ratio of 14 at Room-Temperature. *Jpn J Appl Phys 2* 1987, 26, L1332-L1334.

174. Nowak, E. J. Maintaining the benefits of CMOS scaling when scaling bogs down. *IBM J. Res. Dev.* 2002, 46, 169-180.

175. Appenzeller, J.; Lin, Y. M.; Knoch, J.; Avouris, P. Band-to-band tunneling in carbon nanotube field-effect transistors. *Phys. Rev. Lett.* 2004, 93, 196805.

176. Choi, W. Y.; Park, B. G.; Lee, J. D.; Liu, T. J. K. Tunneling field-effect transistors (TFETs) with subthreshold swing (SS) less than 60 mV/dec. *IEEE Electron Device Lett.* 2007, 28, 743-745.

177. Jeon, K.; Loh, W. Y.; Patel, P.; Kang, C. Y.; Oh, J.; Bowonder, A.; Park, C.; Park, C. S.; Smith, C.; Majhi, P.; Tseng, H. H.; Jammy, R.; Liu, T. J. K.; Hu, C. M. Si Tunnel Transistors with a Novel Silicided Source and 46mV/dec Swing. *S Vlsi Tech* 2010, 121-122.

178. Kim, S. H.; Kam, H.; Hu, C. M.; Liu, T. J. K. Germanium-Source Tunnel Field Effect Transistors with Record High I_{ON}/I_{OFF}. *2009 Symposium on VLSI Technology, Digest of Technical Papers* 2009, 178-179.

179. Krishnamohan, T.; Kim, D.; Raghunathan, S.; Saraswat, K. Double-Gate Strained-Ge Heterostructure Tunneling FET (TFET) With Record High Drive Currents and < 60mV/dec Subthreshold slope. *Int El Devices Meet* 2009, 947-949.

180. Leonelli, D.; Vandooren, A.; Rooyackers, R.; Verhulst, A. S.; De Gendt, S.; Heyns, M. M.; Groeseneken, G. Performance Enhancement in Multi Gate Tunneling Field Effect Transistors by Scaling the Fin-Width. *Jpn J Appl Phys* 2010, 49, 04DC10.

181. Lu, Y. R.; Bangsaruntip, S.; Wang, X. R.; Zhang, L.; Nishi, Y.; Dai, H. J. DNA functionalization of carbon nanotubes for ultrathin atomic layer deposition of high κ dielectrics for nanotube transistors with 60 mV/decade switching. *J Am Chem Soc* 2006, 128, 3518-3519.

182. Mayer, F.; Le Royer, C.; Damlencourt, J. F.; Romanjek, K.; Andrieu, F.; Tabone, C.; Previtali, B.; Deleonibus, S. Impact of SOI, $Si_{1-x}Ge_x$OI and GeOI substrates on CMOS compatible Tunnel FET performance. *Int El Devices Meet* 2009, 163-166.

183. Tarasov, A.; Campbell, P. M.; Tsai, M.-Y.; Hesabi, Z. R.; Feirer, J.; Graham, S.; Ready, W. J.; Vogel, E. M. Highly Uniform Trilayer Molybdenum Disulfide for Wafer-Scale Device Fabrication. *Adv. Funct. Mater.* 2014, 24, 6389-6400.

184. Jeon, J.; Jang, S. K.; Jeon, S. M.; Yoo, G.; Jang, Y. H.; Park, J. H.; Lee, S. Layer-controlled CVD growth of large-area two-dimensional MoS_2 films. *Nanoscale* 2015, 7, 1688-1695.

185. Campbell, P. M.; Tarasov, A.; Joiner, C. A.; Tsai, M.-Y.; Pavlidis, G.; Graham, S.; Ready, W. J.; Vogel, E. M. Field-effect transistors based on wafer-scale, highly uniform few-layer p-type WSe_2. *Nanoscale* 2016, 8, 2268-2276.

186. Chiu, M. H.; Zhang, C. D.; Shiu, H. W.; Chuu, C. P.; Chen, C. H.; Chang, C. Y. S.; Chen, C. H.; Chou, M. Y.; Shih, C. K.; Li, L. J. Determination of band alignment in the single-layer MoS_2/WSe_2 heterojunction. *Nat. Commun.* 2015, 6, 7666.

187. Komsa, H. P.; Kotakoski, J.; Kurasch, S.; Lehtinen, O.; Kaiser, U.; Krasheninnikov, A. V. Two-Dimensional Transition Metal Dichalcogenides under Electron Irradiation: Defect Production and Doping. *Phys. Rev. Lett.* 2012, 109.

188. Chen, X. L.; Wu, Z. F.; Xu, S. G.; Wang, L.; Huang, R.; Han, Y.; Ye, W. G.; Xiong, W.; Han, T. Y.; Long, G.; Wang, Y.; He, Y. H.; Cai, Y.; Sheng, P.; Wang, N. Probing the electron states and metal-insulator transition mechanisms in molybdenum disulphide vertical heterostructures. *Nat. Commun.* 2015, 6, 6088.

189. Seabaugh, A. C.; Zhang, Q. Low-Voltage Tunnel Transistors for Beyond CMOS Logic. *Proc. IEEE* 2010, 98, 2095-2110.

190. Nikonov, D. E.; Young, I. A. Overview of Beyond-CMOS Devices and a Uniform Methodology for Their Benchmarking. *Proc. IEEE* 2013, 101, 2498-2533.

191. Lee, C.; Yan, H.; Brus, L. E.; Heinz, T. F.; Hone, J.; Ryu, S. Anomalous Lattice Vibrations of Single- and Few-Layer MoS_2. *ACS Nano* 2010, 4, 2695-2700.

192. Li, H.; Zhang, Q.; Yap, C. C. R.; Tay, B. K.; Edwin, T. H. T.; Olivier, A.; Baillargeat, D. From Bulk to Monolayer MoS_2: Evolution of Raman Scattering. *Advanced Functional Materials* 2012, 22, 1385-1390.

193. Laskar, M. R.; Ma, L.; Kannappan, S.; Sung Park, P.; Krishnamoorthy, S.; Nath, D. N.; Lu, W.; Wu, Y.; Rajan, S. Large area single crystal (0001) oriented MoS_2. *Appl. Phys. Lett.* 2013, 102, -.

194. Fuhrer, M. S.; Hone, J. Measurement of mobility in dual-gated MoS_2 transistors. *Nature Nanotechnology* 2013, 8, 146-147.

195. Park, W.; Park, J.; Jang, J.; Lee, H.; Jeong, H.; Cho, K.; Hong, S.; Lee, T. Oxygen environmental and passivation effects on molybdenum disulfide field effect transistors. *Nanotechnology* 2013, 24.

196. Bao, W. Z.; Cai, X. H.; Kim, D.; Sridhara, K.; Fuhrer, M. S. High mobility ambipolar MoS_2 field-effect transistors: Substrate and dielectric effects. *Appl. Phys. Lett.* 2013, 102.

197. Qiu, H.; Pan, L. J.; Yao, Z. N.; Li, J. J.; Shi, Y.; Wang, X. R. Electrical characterization of back-gated bi-layer MoS_2 field-effect transistors and the effect of ambient on their performances. *Appl. Phys. Lett.* 2012, 100.

198. Liu, W.; Kang, J. H.; Sarkar, D.; Khatami, Y.; Jena, D.; Banerjee, K. Role of Metal Contacts in Designing High-Performance Monolayer n-Type WSe_2 Field Effect Transistors. *Nano Lett.* 2013, 13, 1983-1990.

199. Cowley, A. M.; Sze, S. M. Surface States and Barrier Height of Metal-Semiconductor Systems. *J. Appl. Phys.* 1965, 36, 3212-3220.

200. Chen, J.-R.; Odenthal, P. M.; Swartz, A. G.; Floyd, G. C.; Wen, H.; Luo, K. Y.; Kawakami, R. K. Control of Schottky Barriers in Single Layer MoS_2 Transistors with Ferromagnetic Contacts. *Nano Lett.* 2013, 13, 3106-3110.

201. Jariwala, D.; Sangwan, V. K.; Lauhon, L. J.; Marks, T. J.; Hersam, M. C. Emerging Device Applications for Semiconducting Two-Dimensional Transition Metal Dichalcogenides. *ACS Nano* 2014, 8, 1102-1120.

202. Dankert, A.; Langouche, L.; Kamalakar, M. V.; Dash, S. P. High-Performance Molybdenum Disulfide Field-Effect Transistors with Spin Tunnel Contacts. *ACS Nano* 2014, 8, 476-482.

203. Liu, H.; Si, M.; Najmaei, S.; Neal, A. T.; Du, Y.; Ajayan, P. M.; Lou, J.; Ye, P. D. Statistical Study of Deep Submicron Dual-Gated Field-Effect Transistors on Monolayer Chemical Vapor Deposition Molybdenum Disulfide Films. *Nano Lett.* 2013, 13, 2640-2646.

204. Liu, Y.; Tan, C.; Chou, H.; Nayak, A.; Wu, D.; Ghosh, R.; Chang, H.-Y.; Hao, Y.; Wang, X.; Kim, J.-S.; Piner, R.; Ruoff, R. S.; Akinwande, D.; Lai, K. Thermal Oxidation of WSe_2 Nanosheets Adhered on SiO_2/Si Substrates. *Nano Lett.* 2015, 15, 4979-4984.

205. Yamamoto, M.; Dutta, S.; Aikawa, S.; Nakaharai, S.; Wakabayashi, K.; Fuhrer, M. S.; Ueno, K.; Tsukagoshi, K. Self-Limiting Layer-by-Layer Oxidation of Atomically Thin WSe_2. *Nano Lett.* 2015, 15, 2067-2073.

206. Wagner, C. D.; Davis, L. E.; Zeller, M. V.; Taylor, J. A.; Raymond, R. H.; Gale, L. H. Empirical Atomic Sensitivity Factors for Quantitative-Analysis by Electron-Spectroscopy for Chemical-Analysis. *Surf Interface Anal* 1981, 3, 211-225.

207. del Corro, E.; Terrones, H.; Elias, A.; Fantini, C.; Feng, S. M.; Nguyen, M. A.; Mallouk, T. E.; Terrones, M.; Pimenta, M. A. Excited Excitonic States in 1L, 2L, 3L, and Bulk WSe_2 Observed by Resonant Raman Spectroscopy. *ACS Nano* 2014, 8, 9629-9635.

208. Luo, X.; Zhao, Y. Y.; Zhang, J.; Toh, M. L.; Kloc, C.; Xiong, Q. H.; Quek, S. Y. Effects of lower symmetry and dimensionality on Raman spectra in two-dimensional WSe_2. *Phys. Rev. B* 2013, 88.

209. Sahin, H.; Tongay, S.; Horzum, S.; Fan, W.; Zhou, J.; Li, J.; Wu, J.; Peeters, F. M. Anomalous Raman spectra and thickness-dependent electronic properties of WSe_2. *Phys. Rev. B* 2013, 87, 165409.

210. Terrones, H.; Del Corro, E.; Feng, S.; Poumirol, J. M.; Rhodes, D.; Smirnov, D.; Pradhan, N. R.; Lin, Z.; Nguyen, M. A. T.; Elias, A. L.; Mallouk, T. E.; Balicas, L.;

Pimenta, M. A.; Terrones, M. New First Order Raman-active Modes in Few Layered Transition Metal Dichalcogenides. *Sci Rep-Uk* 2014, 4, 4215.

211. Zhao, W. J.; Ghorannevis, Z.; Amara, K. K.; Pang, J. R.; Toh, M.; Zhang, X.; Kloc, C.; Tan, P. H.; Eda, G. Lattice dynamics in mono- and few-layer sheets of WS_2 and WSe_2. *Nanoscale* 2013, 5, 9677-9683.

212. Tonndorf, P.; Schmidt, R.; Bottger, P.; Zhang, X.; Borner, J.; Liebig, A.; Albrecht, M.; Kloc, C.; Gordan, O.; Zahn, D. R. T.; de Vasconcellos, S. M.; Bratschitsch, R. Photoluminescence emission and Raman response of monolayer MoS_2, $MoSe_2$, and WSe_2. *Opt Express* 2013, 21, 4908-4916.

213. Li, H.; Lu, G.; Wang, Y. L.; Yin, Z. Y.; Cong, C. X.; He, Q. Y.; Wang, L.; Ding, F.; Yu, T.; Zhang, H. Mechanical Exfoliation and Characterization of Single- and Few-Layer Nanosheets of WSe_2, TaS_2, and $TaSe_2$. *Small* 2013, 9, 1974-1981.

214. Pradhan, N. R.; Rhodes, D.; Memaran, S.; Poumirol, J. M.; Smirnov, D.; Talapatra, S.; Feng, S.; Perea-Lopez, N.; Elias, A. L.; Terrones, M.; Ajayan, P. M.; Balicas, L. Hall and field-effect mobilities in few layered p-WSe_2 field-effect transistors. *Sci. Rep.* 2015, 5, 8979.

215. Zhou, H. L.; Wang, C.; Shaw, J. C.; Cheng, R.; Chen, Y.; Huang, X. Q.; Liu, Y.; Weiss, N. O.; Lin, Z. Y.; Huang, Y.; Duan, X. F. Large Area Growth and Electrical Properties of p-Type WSe_2 Atomic Layers. *Nano Lett.* 2015, 15, 709-713.

216. Dean, C. R.; Young, A. F.; Meric, I.; Lee, C.; Wang, L.; Sorgenfrei, S.; Watanabe, K.; Taniguchi, T.; Kim, P.; Shepard, K. L.; Hone, J. Boron nitride substrates for high-quality graphene electronics. *Nature Nanotechnology* 2010, 5, 722-726.

217. Mahjouri-Samani, M.; Lin, M.-W.; Wang, K.; Lupini, A. R.; Lee, J.; Basile, L.; Boulesbaa, A.; Rouleau, C. M.; Puretzky, A. A.; Ivanov, I. N.; Xiao, K.; Yoon, M.; Geohegan, D. B. Patterned arrays of lateral heterojunctions within monolayer two-dimensional semiconductors. *Nat. Commun.* 2015, 6, 7749.

218. Jain, A.; Hautier, G.; Moore, C. J.; Ong, S. P.; Fischer, C. C.; Mueller, T.; Persson, K. A.; Ceder, G. A high-throughput infrastructure for density functional theory calculations. *Comp Mater Sci* 2011, 50, 2295-2310.

219. Jain, A.; Hautier, G.; Ong, S. P.; Moore, C. J.; Fischer, C. C.; Persson, K. A.; Ceder, G. Formation enthalpies by mixing GGA and GGA plus U calculations. *Phys. Rev. B* 2011, 84.

220. Spevack, P. A.; Mcintyre, N. S. A Raman and XPS Investigation of Supported Molybdenum Oxide Thin-Films .2. Reactions with Hydrogen-Sulfide. *J Phys Chem-Us* 1993, 97, 11031-11036.

221. Young, P. A. Lattice parameter measurements on molybdenum disulphide. *Journal of Physics D: Applied Physics* 1968, 1, 936.

222. Donarelli, M.; Bisti, F.; Perrozzi, F.; Ottaviano, L. Tunable sulfur desorption in exfoliated MoS_2 by means of thermal annealing in ultra-high vacuum. *Chem Phys Lett* 2013, 588, 198-202.

223. López-Suárez, M.; Neri, I.; Rurali, R. Band gap engineering of MoS_2 upon compression. *J. Appl. Phys.* 2016, 119, 165105.

224. Castellanos-Gomez, A.; van der Zant, H. S. J.; Steele, G. A. Folded MoS_2 layers with reduced interlayer coupling. *Nano Res.* 2014, 7, 572-578.

225. Chung, J. W.; Dai, Z. R.; Adib, K.; Ohuchi, F. S. Raman scattering and high resolution electron microscopy studies of metal-organic chemical vapor deposition-tungsten disulfide thin films. *Thin Solid Films* 1998, 335, 106-111.

226. K. C, S.; Longo, R. C.; Addou, R.; Wallace, R. M.; Cho, K. Electronic properties of MoS_2/MoO_x interfaces: Implications in Tunnel Field Effect Transistors and Hole Contacts. *Sci Rep-Uk* 2016, 6, 33562.

227. Chuang, S.; Battaglia, C.; Azcatl, A.; McDonnell, S.; Kang, J. S.; Yin, X.; Tosun, M.; Kapadia, R.; Fang, H.; Wallace, R. M.; Javey, A. MoS_2 P-type Transistors and Diodes Enabled by High Work Function MoO_x Contacts. *Nano Lett.* 2014, 14, 1337-1342.

228. Wei, X.; Yu, Z.; Hu, F.; Cheng, Y.; Yu, L.; Wang, X.; Xiao, M.; Wang, J.; Wang, X.; Shi, Y. Mo-O bond doping and related-defect assisted enhancement of photoluminescence in monolayer MoS_2. *Aip Adv* 2014, 4, 123004.

229. Mouri, S.; Miyauchi, Y.; Matsuda, K. Tunable Photoluminescence of Monolayer MoS_2 via Chemical Doping. *Nano Lett.* 2013, 13, 5944-5948.

230. Baker, M. A.; Gilmore, R.; Lenardi, C.; Gissler, W. XPS investigation of preferential sputtering of S from MoS_2 and determination of MoS_x stoichiometry from Mo and S peak positions. *Appl Surf Sci* 1999, 150, 255-262.

231. Song, J.-G.; Park, J.; Lee, W.; Choi, T.; Jung, H.; Lee, C. W.; Hwang, S.-H.; Myoung, J. M.; Jung, J.-H.; Kim, S.-H.; Lansalot-Matras, C.; Kim, H. Layer-Controlled, Wafer-Scale, and Conformal Synthesis of Tungsten Disulfide Nanosheets Using Atomic Layer Deposition. *ACS Nano* 2013, 7, 11333-11340.

232. Shahrjerdi, D.; Oye, M. M.; Holmes, A. L.; Banerjee, S. K. Unpinned metal gate/high-κ GaAs capacitors: Fabrication and characterization. *Appl. Phys. Lett.* 2006, 89.

233. Ali, A.; Madan, H. S.; Kirk, A. P.; Zhao, D. A.; Mourey, D. A.; Hudait, M. K.; Wallace, R. M.; Jackson, T. N.; Bennett, B. R.; Boos, J. B.; Datta, S. Fermi level unpinning of GaSb (100) using plasma enhanced atomic layer deposition of Al_2O_3. *Appl. Phys. Lett.* 2010, 97.

234. Ghatak, S.; Pal, A. N.; Ghosh, A. Nature of Electronic States in Atomically Thin MoS_2 Field-Effect Transistors. *ACS Nano* 2011, 5, 7707-7712.

235. Mott, N. F.; Davis, E. A. *Electronic processes in non-crystalline materials*. OUP Oxford: 2012.

236. VanKeuls, F. W.; Hu, X. L.; Jiang, H. W.; Dahm, A. J. Screening of the Coulomb interaction in two-dimensional variable-range hopping. *Phys. Rev. B* 1997, 56, 1161-1169.

237. Utama, M. I. B.; Lu, X.; Zhan, D.; Ha, S. T.; Yuan, Y.; Shen, Z.; Xiong, Q. Etching-free patterning method for electrical characterization of atomically thin $MoSe_2$ films grown by chemical vapor deposition. *Nanoscale* 2014, 6, 12376-12382.

238. Roy, A.; Movva, H. C. P.; Satpati, B.; Kim, K.; Dey, R.; Rai, A.; Pramanik, T.; Guchhait, S.; Tutuc, E.; Banerjee, S. K. Structural and Electrical Properties of $MoTe_2$ and $MoSe_2$ Grown by Molecular Beam Epitaxy. *Acs Applied Materials & Interfaces* 2016, 8, 7396-7402.

239. Molina-Sanchez, A.; Wirtz, L. Phonons in single-layer and few-layer MoS_2 and WS_2. *Phys. Rev. B* 2011, 84.

240. Qiu, H.; Xu, T.; Wang, Z. L.; Ren, W.; Nan, H. Y.; Ni, Z. H.; Chen, Q.; Yuan, S. J.; Miao, F.; Song, F. Q.; Long, G.; Shi, Y.; Sun, L. T.; Wang, J. L.; Wang, X. R. Hopping transport through defect-induced localized states in molybdenum disulphide. *Nat. Commun.* 2013, 4.

VITA

PHILIP M. CAMPBELL was born on May 14, 1991 in Poughkeepsie, New York. He received his Bachelor of Science in Electrical Engineering from the University of Texas at Dallas in August 2012. He received a Master of Science in Materials Science and Engineering from the University of Texas at Dallas in August 2013. While at the University of Texas at Dallas, he was supervised by Yves Chabal. His master's thesis studied the functionalization of Si(111) surfaces using organic molecules to create double tunnel junctions. After leaving the University of Texas at Dallas, he joined Eric Vogel's research group at the Georgia Institute of Technology in June 2013.